DOCTOR OF PHILOSOPHY

Improving multi-phase flow modelling of CO_2/brine/rock systems using van Genuchten's empirical model

Onoja, Michael

Award date:
2019

Awarding institution:
Coventry University

Improving multi-phase flow modelling of CO_2/brine/rock systems using van Genuchten's empirical model

By

Michael Ugbede Onoja

A thesis submitted in partial fulfilment of the University's requirements for the Degree of Doctor of Philosophy

July 2019

Faculty of Engineering, Environment and Computing

Content removed on data protection grounds

Certificate of Ethical Approval

Applicant:

Michael Ugbede Onoja

Project Title:

Improving multi-phase flow modelling of CO_2/brine/rock systems using van Genuchten's empirical model

This is to certify that the above named applicant has completed the Coventry University Ethical Approval process and their project has been confirmed and approved as Low Risk

Date of approval:

03 May 2019

Project Reference Number:

P90345

Abstract

In recent years, assessing the safety and feasibility of long-term geological CO_2 sequestration (GCS) usually relies on model-based forecasting of the sub-surface behaviour of CO_2. In the application of two-phase flow in porous media, numerical simulations are usually implemented using empirical formulations by either Brooks-Corey (BC) or van Genuchten (vG) to describe the transport properties in a CO_2/brine/rock system. The forward modelling of GCS is often prompted by uncertainties in fluid flow and transport processes, which are majorly governed by structural complexity resulting from the sedimentary properties of the porous media. Since flow characteristics can vary within the reservoir and sealing formation, this thesis investigates the consequences of sedimentary heterogeneities, such as gradation, cementation, interbedded argillaceous units, in the storage formation on the transport and flow processes of CO_2/brine systems.

The study focuses on CO_2 storage in siliciclastic aquifers and examines the effects of the dynamic representation of grain-scale heterogeneities on multiphase fluid flow during geological CO_2 storage. This was implemented by relating a number of sedimentary processes and structures in the reservoir and caprock formation to the constitutive functions of relative permeability and capillary pressure using the van Genutchten's empirical model. A set of continuum-scale numerical simulations was conducted to investigate the impact of variability in these constitutive functions using simulators that are based on Darcy-flow physics. Firstly, the pore geometry parameter, which is an empirical constant in both BC and vG model, was described for different clastic rocks using numerical validation of statistical data from soil physics. This enables the adaptability of the pore geometry parameter to the type of clastic rock, thus proposing a new methodology for the effective characterisation of the pore geometry parameter for different clastic rocks. The effect of key parameters in the vG empirical model, such as the pressure strength coefficient, the pore geometry parameter and the connate saturation (wetting and non-wetting), on GCS was also incorporated in the numerical investigations.

Trapping mechanisms such as structural, residual and dissolution are assessed in this thesis using Bunter Sandstone Formation (Chapter 4), Mercia Mudstone Group (Chapter 5) and Utsira Sandstone Formation (Chapter 6) as case studies. Results showed that relative permeability assumptions have a significant impact on the afore listed trapping mechanisms as well as the pore pressure distribution within the reservoir and caprock formation. It argues for the adequate representation of small-scale heterogeneities in large-scale forward modelling of CO_2 storage, especially when describing the capillary pressure and relative permeability functions. The characterisation of the pore gemetry parameter serves as a formative tool for describing capillary pressure and relative permeability heterogeneities that could arise from sedimentary structures in clastic reservoir formations and their subsequent impact on CO_2/brine transport processes in a porous medium.

Acknowledgement

I would like to thank my supervisors Seyed Shariatipour, Adrian Wood and John Williams for all the guidance they have provided on this project. My gratitude goes to the British Geological Survey (Nottingham) for providing access to research facilities during a six-week visit and to all members of the CO_2 Storage Team for technical discussions and providing useful recommendation during the numerical study that was conducted there. I would also like to thank the Faculty Research Centre for Fluid and Complex Systems as well as the Doctoral College for supporting my research mobility across the UK and several other European countries. The students and staff in Maudslay House with whom I have spent many days in the office and shared a cuppa are all thanked. Special thanks goes to my family, The Onojas, The Cireasas and The Azubuikes, for the encouragement through the years.

This project is dedicated to my wife, Annamaria Onoja, with a heartfelt appreciation for her love and unwavering support during this experience. Multumesc Frumos Ufedo Mi.

Nomenclature

Symbols:

K Intrinsic permeability
k Effective permeability
k_r Relative permeability
k_r^0 Endpoint relative permeability
P Pressure
P_c Capillary pressure
P_e Capillary entry pressure
S Saturation
S_e Effective or Normalised saturation
S_w Wetting saturation
S_n Non-wetting saturation
S_{wr} Residual wetting saturation
S_{nr} Residual non-wetting saturation
S_{nc} Critical non-wetting saturation
S_{nt} Trapped non-wetting saturation
S_{hy} Non-wetting saturation at flow reversal
C Land trapping coefficient
N_c Capillary number
ρ Density
v Velocity
μ Viscosity
ϕ Porosity
g Gravity acceleration
Λ Phase mobility
σ Interfacial tension
R Pore throat radius
θ Contact angle
λ Brook-Corey's pore size distribution index
n van Genuchten's pore geometry parameter
m van Genuchten's pore geometry parameter
P_g van Genuchten's pressure scaling parameter
α van Genuchten's pressure strength coefficient

Subscripts:

α Incompressible Newtonian fluid
w Wetting fluid
n Non-wetting fluid
c Capillary
e Entry or Displacement
$ceqn$ Capillary at equilibrium
max Maximum

Abbreviations:

CCS Carbon Capture and Storage
GCS Geological CO_2 Sequestration
BC Brooks-Corey
vG van Genuchten
REV Representative Elementary Volume
IFT Interfacial Tension
EOR Enhanced Oil Recovery
EOS Equation of State

Table of Contents

List of Figures

List of Tables

CHAPTER 1

Background and Theoretical Framework

1.1 Carbon Capture and Storage (CCS)

CCS, a three-step process that involves the capture, transport and storage of carbon dioxide [CO_2], is considered as a key strategy for decarbonisation of the power and industrial sectors in order to mitigate the severe consequences of climate change (IPCC 2014). This is because the components of integrated CCS systems currently exist and are in use by the petroleum industry, based on the fact that the technology was inspired by the utilisation of CO_2 in Enhanced Oil Recovery, CO_2-EOR (Gozalpour et al. 2005, Kovscek and Cakici 2005). There is significant research aimed at enhancing the implementation and cost of CO_2 capture systems across three broadly classified technologies: pre-combustion (Rubin et al. 2007, Figueroa et al. 2008, Jansen et al. 2015), post-combustion (Lin and Chen 2011, Padurean et al. 2011, Versteeg and Rubin 2011), and oxy-fuel combustion (Wall et al. 2009, Scheffknecht et al. 2011, Senior et al. 2013). The next stage in the CCS value chain after capture is transporting the CO_2 to sinks for either permanent storage or use in CO_2-EOR. For large-scale integrated CCS facilities, pipelines and ships are economical means of CO_2 transportation to the point of storage (IPCC 2005). Large-scale integrated CCS facilities are defined as facilities involving the capture, transport, and storage of CO_2 at a scale of at least 0.8 $MtCO_2$/yr for a coal-based power plant, or 0.4 $MtCO_2$/yr for other emissions-intensive industrial facilities (GCCSI 2018).

Permanent sequestration of CO_2 can be achieved through a variety of strategies, mainly mineral carbonation, oceanic, and underground geological storage. In the CCS framework, geological sequestration is the most prominent for large-scale projects, out of potential options that include deep ocean storage and mineral carbonation (IPCC 2005). By mid-2018, 17 large-scale CCS facilities were in operation around the world, four of which utilised deep saline formations for storage while the rest were used for EOR before subsequent permanent storage. These four CCS facilities that utilised deep saline formations are the Illinois CCS project in the USA, which started injecting in 2017 (DOE - Fossil Energy 2017); the Quest CCS project in Canada, which started injecting in 2015 (Rock et al. 2017); the Snøhvit CCS project in Norway, which started injecting in 2008 (Hansen et al. 2013); and the Sleipner CCS project in Norway, which started injection in 1996 (Singh et al. 2010). A comprehensive list of all CCS facilities in operation as well as those in construction and early/advanced development is available in the projects database of the Global CCS Institute (GCCSI 2018). Ample practical engineering and scientific knowledge has been generated from these large-scale CCS deployments as well as numerous smaller-scale

CCS field experiments and technology demonstrations (Eiken et al. 2011, Aimard et al. 2007, Preston et al. 2005, Dance 2013, Hovorka et al. 2011). This has successively stimulated research using CO_2 flow modelling datasets to identify potential risks associated with CO_2 injection as well as possible storage capacity of proposed sinks for geological CO_2 storage.

1.2 Geological CO_2 Storage (GCS)

Various investigations on subsurface storage media have identified sedimentary rocks such as clastics, carbonates, and coal as ideal media for CO_2 storage (van der Meer 1992, Bergman and Winter 1995, Freund and Ormerod 1997, Hitchon et al. 1999). Options considered as storage sinks include saline aquifers, depleted oil and gas reservoirs, unmineable coal seams, hydrate storage and CO_2 within enhanced geothermal systems (Bachu 2000). Common factors taken into consideration when accessing suitable formations for CO_2 sequestration include the volumetric storage efficiency, *i.e.* the bulk mass of CO_2 stored per unit reservoir volume, and the sealing integrity (Bachu 2008). For GCS, CO_2 is injected into the formation in its supercritical state, at temperatures and pressures above 31.1°C and 7.39MPa, respectively. Supercritical CO_2 ($scCO_2$) is neither a gas nor a liquid but exhibits properties similar to both fluid states. In other words, it is dense like a liquid and viscose like a gas. This results in a massive volume compression from the standard pressure conditions of CO_2, thus increasing the reservoir volume available for sequestration. CO_2 encounters greater pressures at depth which preferentially increases its density, allowing for efficient pore filling and reducing the contrast in buoyancy between the gas and *in situ* fluids (Benson and Cole 2008). The gas attains and maintains a supercritical state at geological depths greater than 800 metres as a result of the geothermal gradient.

A considerable body of scientific knowledge have identified that deep saline aquifers and depleted oil and gas reservoirs are the most promising options for large scale CCS deployment (Benson and Surles 2006, Koide et al. 1992, Holt et al. 1995). However, deep saline aquifers offer the highest storage capacity (Bachu and Adams 2003, Wickstrom et al. 2006). The geological storage of CO_2 usually proceeds via various trapping mechanisms during CO_2 plume evolution. These can broadly be distinguished as chemical and physical trapping mechanisms:

1.2.1 Chemical trapping mechanisms

Chemical trapping refers to the immobilisation of a CO_2 plume as a result of geochemical reactions between the gas, the formation water, and the rock mineralogy. This trapping mechanism is a very slow form of CO_2 confinement initiated by CO_2 dissolution in formation water and onward precipitating kinetic reactions. As CO_2 plume migrates through the reservoir formation, some of it dissolves in formation water in a process known as *solubility trapping*. The rate of CO_2 dissolution in formation water varies directly with the pressure and inversely with temperature and salinity (Spycher et al. 2003, Duan and Sun 2003, Koschel et al. 2006). The dissolution of CO_2 in formation water leads to acidic conditions through the production of proton which invariably lowers the pH of the aqueous phase ($H_2O + CO_2 \leftrightarrow H_2CO_3 \leftrightarrow HCO_3^- + H^+$). This acidic condition in the reservoir enhances the possibility of chemical reactions with the carbonate minerals present in the formation ($X_2^+ + HCO_3^- \leftrightarrow XCO_3 + H^+$), where X could be Calcium, Magnesium, or Iron. The resulting precipitation of carbonates, which serves as a permanent solid fix for CO_2, is referred to as *mineral trapping* (Bachu et al. 1994).

1.2.2 Physical trapping mechanisms

Physical trapping is the principal means of geological CO_2 confinement and is usually characterised by the structure of the sedimentary basin (Zhang and Song 2014). This type of trapping mechanism includes hydrostatic, hydrodynamic, and residual-gas trapping. *Static traps* are closed hydrogeological structures which provide boundary restrictions for the buoyant migration of CO_2 plume. They are usually a function of rock orientations as well as depositional and diagenetic lithological variations in the reservoir, otherwise referred to as sedimentary structures and processes (Boggs 2006). Static traps are often referred to as structural traps and could be either anticlines or faults; and stratigraphic traps, which refers to to pinch-outs, reefs, and unconformities (Figure 1.1). Diapiric traps such as mud diapirs and salt domes can also be classified as static traps. Figure 1.2 depicts various CO_2 trapping mechanims in an aquifer.

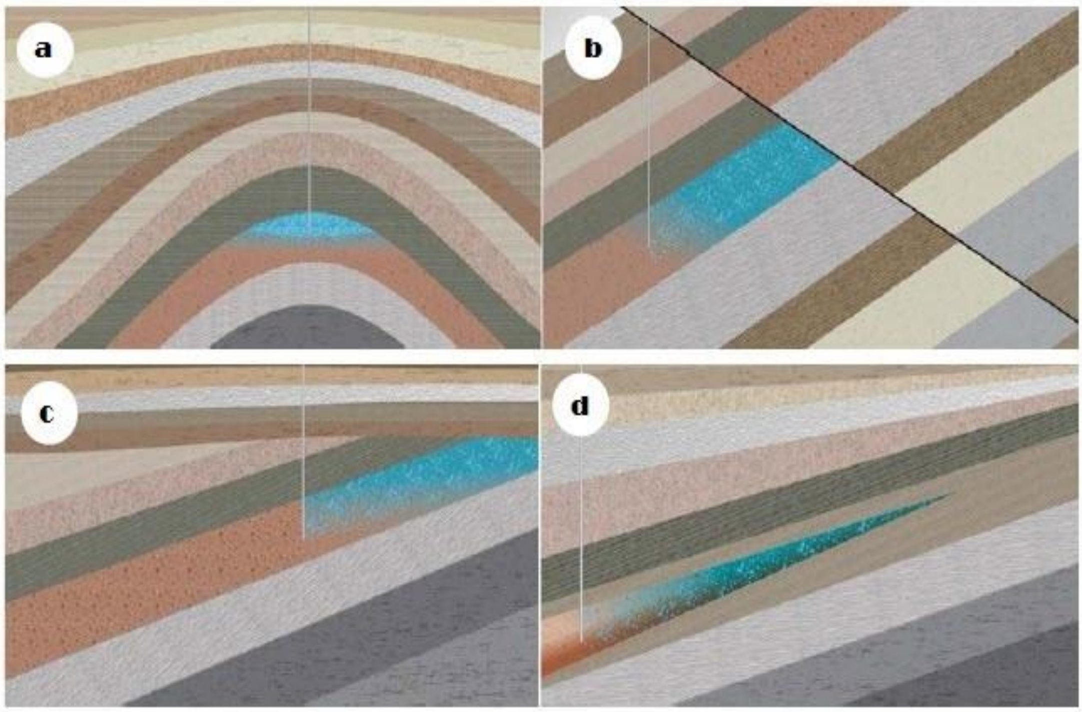

Figure 1.1: Illustration of structural and stratigraphic traps. a) anticline b) fault trap c) angular unconformity d) pinch-out. [Source: IPCC (2005)]

At the onset of CO_2 injection, the movement of CO_2 plume as a gravity current in the reservoir will gradually lead to up-dip deceleration and subsequent isolation and immobilization of CO_2 bubbles in pore spaces. This isolation is regarded, in literature, as “snap-off” of CO_2 plume in the trailing edge. Dullien (1991) attributed this “snap-off” to wettability and capillary effects in the porous media. Such trapping mechanisms are referred to as *residual or capillary traps* and it generally occurs as water imbibes into CO_2 plume, especially after injection stops (Benson and Cole 2008).

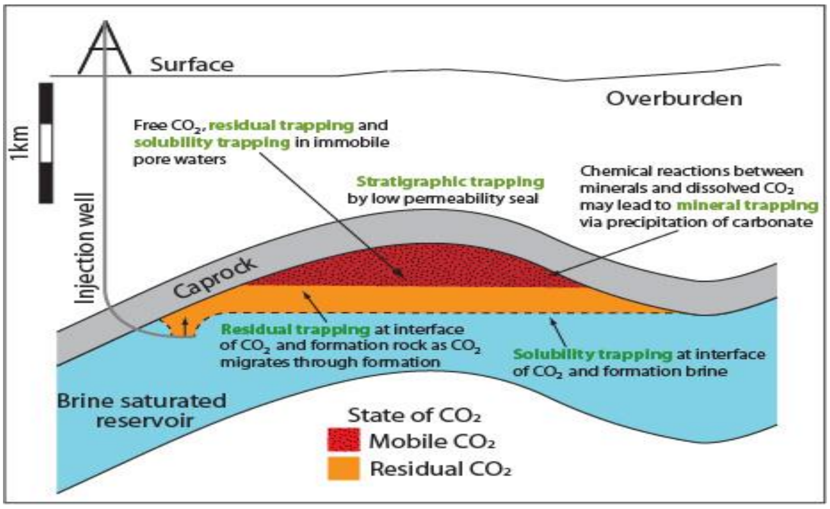

Figure 1.2: Graphic of CO_2 trapping mechanisms in saline aquifer. [Source: UKCCSRC (2012)]

Another trapping mechanism that can prevent the upward movement of CO_2 is the hydrodynamic movement of formation water down permeable reservoir beds (Selley and Sonnenberg 2014). A high hydrodynamic force of downdip water flow over the buoyant force of up-dip CO_2 flow will halt the migration of CO_2 plume and entrap the gas within the bed. These traps occur as part of other trapping mechanisms and storage in deep saline aquifers are more conducive to them. Hydrodynamic traps can proceed within static closures or without any permeability barrier and they exhibit tilted or inclined CO_2-water interfaces caused by differences in water pressure associated with water flow (Hubbert 1953). The security of the trapped CO_2 increases overtime as different types of traps become significant after the onset of CO_2 injection in the geological formation (Figure 1.3). Physical traps dominate during CO_2 injection and these traps are influenced by the structures and processes in sediment formation, which are mostly portrayed in features such as the rock heterogeneity.

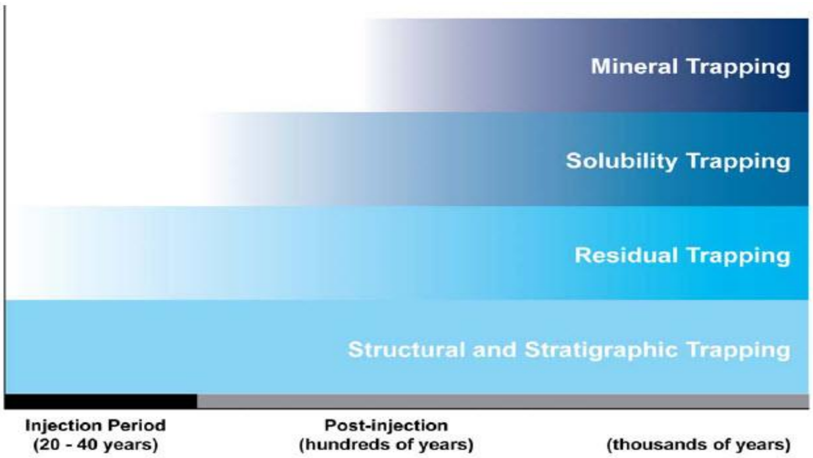

Figure 1.3: Trapping mechanisms with rising degree of storage security. [Source: IPCC (2005)]

1.2.3 Rock heterogeneity

Rock heterogeneity is prevalent in geological formations and exists at every scale: pore-scale (~µm), grain scale (~0.1 to 10 cm), and field scale (> 10 cm). These different scales result in complexities when solving multiphase flow problems. Grain scale heterogeneity, which is the focus of this study, implies sedimentary structures resulting from the spatial distribution and deposition of rock particles prior to lithification. These structures include cross bedding, graded bedding, laminated bedding, ripple marks in bedforms, and synsedimentary folds and faults (Boggs 2006). NB: Bedding is the arrangement of sedimentary rocks in strata or layers that have lithological, textural, or structural unity that distinguishes them from the strata above or below.

In recent years, assessing the safety and feasibility of long-term GCS usually relies on model-based forecasting of the sub-surface behaviour of CO_2. These models simulate complex geological processes which aid in the design of injection schemes as well as the assessment of storage capacities in target locations. Often, simulation studies are prompted by uncertainties in fluid flow and transport processes, with an increasing number focusing on aquifers due to the scarcity of history matching data in these reservoirs. As noted by Bachu (2008), Krevor et al. (2012) and IPCC (2005), there are a number of key physical and chemical processes that work in concert to help ensure the efficacy of deep geological CO_2 storage over time. Increasing the level of detail in geological modelling for simulation models is essential for producing meaningful and accurate results (Van De Graaff and Ealey 1989). In the absence of site-specific data, synthetic reservoir models are constructed using a wide range of hypotheses and used for investigative purposes in GCS. A common assumption in these models is that a sharp interface exists between a reservoir rock and an overlying sealing rock, commonly referred to as the caprock. The reservoir and caprock are two distinct sedimentary formations that are readily distinguished by their petrophysical properties, which include porosity (ϕ), permeability (K), relative permeability (k_r), capillary pressure (P_c), and saturation (S). Pore-size distribution, which is a function of grain-scale heterogeneity, is a component of these properties (Lucia 2007).

Sedimentary structures are particularly abundant in siliciclastic sedimentary rocks such as reservoir sandstones and sealing mudstones. A threshold division on the basis of grain size is used as the starting point to classify and name siliciclastic sediments and sedimentary rocks e.g. the Udden-Wentworth grain scale (Wentworth 1922). In clastic formations, reservoir rocks typically comprise coarse- and medium-grained sediments while sealing rocks are usually very fine-grained sedimentary rocks. In most reservoir simulation studies, the assumption of a distinct interface between the caprock and the reservoir rock ignores the deposition of intermediary-sized sediments at this interface. This may not always be true of actual geological formations. A common example is the interface between Sherwood Sandstone Group and the overlying Mercia Mudstone Group where transitional lithologies usually exist (Seedhouse and Racey 1997, Newell and Shariatipour 2016). Shariatipour et al. (2016a) demonstrated that the occurrence of such geological structures can affect various trapping mechanisms within the reservoir as well as influence CO_2 plume migration and the estimation of storage capacity and volume of the aquifer. In their contribution, Shariatipour et al. (2016a) focused on the influence of static properties of flow and transport process such as the porosity and permeability of the rock media, neglecting the dynamic properties *i.e.* the capillary pressure and relative permeability.

A number of studies using numerical models acknowledge the importance of constitutive $P_c - k_r - S$ relationship on multiphase fluid flow during GCS (Fleet et al. 2004, Ennis-King and Paterson 2005, Juanes et al. 2006, Obi and Blunt 2006, Burton et al. 2009, Kopp et al. 2009, Zhao et al. 2018, Gershenzon et al. 2017, Debbabi et al. 2017, Li et al. 2018). It has been suggested that capillary heterogeneity provides a new trapping mechanism in carbon sequestration, referred to as local capillary trapping (Saadatpoor et al. 2010). Capillary heterogeneity is also known to be an important parameter affecting multiphase flow of CO_2 and brine, affecting properties such as saturation profile, capillary pressure and relative permeability (Kuo and Benson 2015). It is therefore imperative that reservoir simulations adequately model rock heterogeneities and describe dynamic flow properties at the grain scale for greater precision in predictive analyses.

1.3 Thesis Overview

1.3.1 Aims and Objectives

Assessing the risks associated with CO_2 geological sequestration entails identifying the formation's petrophysical properties and their relationships. Since flow characteristics within the reservoir/seal interface could differ from the bulk properties of the entire corresponding formation, the main aim of this study is to investigate the consequences of pore-scale heterogeneity in the storage formation on the transport and flow processes of CO_2/brine systems. The heterogeneity mentioned in this text will be described in P_c and k_r functions for CO_2/brine/rock systems using a constitutive empirical model that is based on grain-size variation. The focal point of analysis is to characterise the implications of micro-heterogeneities on dynamic two-phase behaviour in porous siliciclastic media in terms of the pore geometry index. The relevance of the pore geometry index in the predictive analysis of CO_2/brine transport processes during geo-sequestration is highlighted in the next chapter. The more specific aspects of this work addresses the following questions:

- Which empirical correlation used to describe relative permeability and capillary pressure functions in GCS will be most efficient in modelling their heterogeneities?
- Between static and dynamic properties for multiphase fluid flow, which property is predominant during CO_2 sequestration in aquifers?
- What are the implications of grain-scale heterogeneities in saline porous media on the overall performance of CO_2 storage in the reservoir domain?

The analysis presented in this study considers only displacement processess during CO_2 injection. The overall aim is to understand how the inclusion of P_c and k_r heterogeneities in models that show permeability variations will contradict results that otherwise exclude them. This work has three main objectives. First is the introduction of a parameterisation scheme that essentially describes grain-scale heterogeneity in siliciclastic rocks. The second objective is adopting this scheme in an empirical model that adequately describes the constitutive $P_c - k_r - S_w$ relationship, where S_w is the wetting saturation. It is presumed that this model can be fit to available relative permeability curves that are obtained experimentally. The third objective is the numerical implementation of capillary pressure and relative permeability curves in various reservoir simulation models for investigative purposes.

1.3.2 Thesis structure

The structure of this thesis follows the outlined objectives. **Chapter 2** contains the major theoretical section of the study and is divided into two main parts. The first part recalls the mathematical formulation of flow at the Darcy scale, including the two-phase flow model as well as capillarity and fluid conductivity in porous media. The second gives a brief overview of hysteresis in capillary pressure and relative permeability functions and reviews the major constitutive empirical models used to describe these functions in reservoir simulation studies. Investigative elements of the study are shown in Chapters 3, 4, 5 and 6. **Chapter 3** proposes a parameterisation scheme to be used for describing dynamic flow properties in siliciclastic sedimentary rocks. Numerical implementation of the scheme is presented in Chapters 4, 5 and 6. A range of two-dimensional (2D) and three-dimensional (3D) simulations using the commercial reservoir simulation software ECLIPSE are conducted across these chapters to investigate the effect of various sedimentary structures and processes on the overall CO_2 storage performance.

Chapter 4 investigates the effect of gradational contact at the reservoir/seal interface and the gradual change in clast size within the aquifer, duly represented by constitutive $P_c - k_r - S_w$ curves, on CO_2 storage capacity and pressurisation in the reservoir model. Other parameters such as cemented sand layers, and the structural orientation of the caprock (flat vs dome) are also introduced in order to study their influence on the results. Here two 3D reservoir models based on the Triassic Bunter Sandstone Formation, southern North Sea Basin, United Kingdom is employed for the exercise. **Chapter 5** explores the effects of sedimentary heterogeneities in sealing formations, such as the Mercia Mudstone Group, on the predictive analysis of GCS. Using a 2D axisymmetric model, the chapter also examines the effect of boundary conditions on the final results. **Chapter 6** builds on this regime, using the parameterisation scheme to investigate the CO_2 plume migration through intra-reservoir mudstone baffles and high-permeability channels, with the Utsira Formation sandstone as a case study. The aforementioned formations are located in the North Sea Basin, which is believed to have significant potential for storing CO_2 for climate change mitigation (Chadwick et al. 2004). These are clastic formations that show sedimentary heterogeneity in various forms, where the storage formations have already been identified as suitable options for CO_2 storage. In the first instant, the Bunter Sandstone Formation show sedimentary heterogeneity, in the form of gradational changes in the sandstone, within the storage unit. The proceeding case study, i.e. the Mercia Mudstone Group, is used to elaborate on the impact of such gradation in the sealing unit on CO_2 storage performance. The is due to the fact that the base of the Mercia Mudstone Group shows gradational changes in mudrock within the East Midlands Shelf, the Cheshire Basin, and the Stafford Basin. Finally, the Utsira Sandstone Formation shows a different orientation of sedimentary heterogeneity where sandstone units alternate with mudstone units within the storage domain.

Chapter 7 summarises the results obtained in this study, presenting concluding remarks and outlining some perspectives for future work.

CHAPTER 2

Mathematics of multiphase flow in porous media

2.1 Introduction

The mathematical illustration of multiphase flow in porous media requires appropriate governing equations for the conservation of fluids mass and the momentum as well as other constitutive equations. Geological CO_2 sequestration in deep saline aquifers entail two-phase flow processes that describe the interaction between injected CO_2, brine and rock matrix. The classical description of such flow phenomena ignores changes in thermo-physical properties and assumes fluids are incompressible and immiscible (Bear 1972). The rock structure, pressure, temperature, and salinity are primary controls on fluid interaction in a porous medium. Fluid properties such as viscosity, density, contact angle and interfacial tension, which are all affected by pressure, temperature and salinity, can be identified as secondary variables. Irreducible water and residual CO_2 saturations together with the relative permeability may then be considered as tertiary variables as these are in turn controlled by the fluid properties (Bachu and Bennion 2008). Due to the uncertainty that surrounds activities of subsurface engineering, numerical simulators based on finite difference, finite volume and finite element methods, which capture the flow phenomena occurring in the porous media, are mostly employed (Aarnes et al. 2007).

The complete description of the two-phase flow behaviour representing the CO_2 sequestration is characterised by a system of hydrodynamic model. One of the key components of this model is the capillary function which describes the relationship between the water saturation and the capillary pressure. A complimentary constitutive relationship is given by the relative permeability function, describing the ability of each fluid phase to flow in the porous medium as a function of the phase saturation. Both functions are strongly non-linear and are used to describe the complex interplay of capillary, gravitational and viscous forces which affect multiphase flow in porous media. Their form depends principally on the geometrical characteristics of the pore space and the properties of the fluid-fluid and fluid-solid interfaces (surface tension). Equations of motion are generally partial differential equations that combine an expression of mass with these constitutive relationships. The essential descriptors that need to be included in a typical reservoir engineering study to design the geo-sequestration of carbon include the reservoir model, the fluid model and the flow model. The reservoir model indicates the static model, which includes distribution of petrophysical properties such as porosity, permeability, facies, thickness and existing barriers or conduits to fluid flow. Building one requires substantial geological data, which can be obtained from core analysis, well logs, experimental investigations and seismic profiles (Kelkar et al. 2002).

The fluid model is required to design simultaneous flow of supercritical CO_2 ($scCO_2$) and formation brine using the constitutive relative permeability and capillary pressure functions which depend on the path and history of saturation (Dullien 1991). This chapter introduces the governing equations describing the behaviour of a gas-water system, their flow characteristics and the constitutive functions in fluid flow and transport processes.

2.2 Governing equations

The relevant physical processes for flow simulation are accessible at various observation scales ranging from the microscale of the pore channels to the macroscale of the reservoir. Mathematical models applied at each scale represent the principles of conservation of basic quantities such as mass, momentum and energy. The exact form of the governing equations, however, may differ substantially between the scales. In some cases, the model describing processes at a macroscopic scale is attainable from the equations relevant at a microscopic scale by an appropriate averaging procedure. Alternatively, the governing equations can be formulated at the larger scale, based on phenomenological considerations (Szymkiewicz 2013). Two basic scales typically described in porous media are the pore scale and the Darcy scale (Figure 2.1):

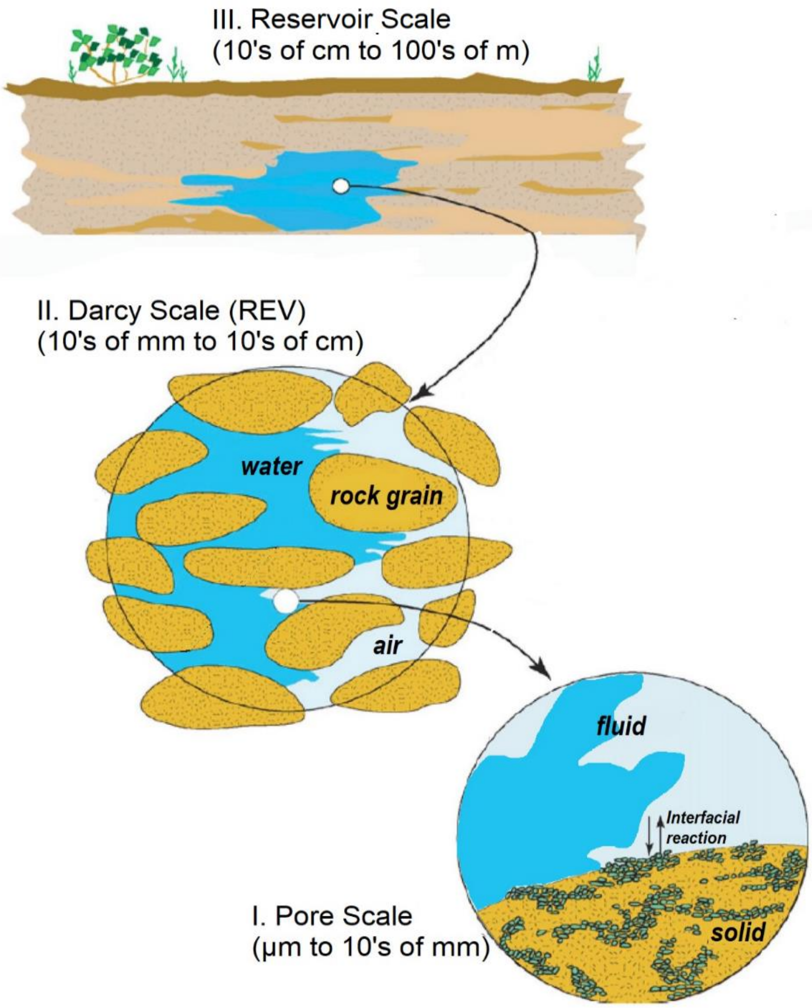

Figure 2.1: Observation scales in a porous medium. [Adapted from Wood et al. (2007)]

At the pore scale, the characteristic spatial dimension is the size of a single pore, which in granular media is approximately proportional to the grain size. The flow field in the pore space is described by the Navier-Stokes equations (Temam 1979), which solves incompressible Newtonian flow with appropriate conditions at the fluid-solid and fluid-fluid interactions (e.g. Blunt et al. 2013, Krevor et al. 2015):

$$-\nabla P + \mu\nabla^2 v = \rho\left(\frac{\partial v}{\partial t} + v \cdot \nabla v\right), \tag{2.1}$$

$$\nabla \cdot v = 0 \tag{2.2}$$

where ρ is the fluid density, v is the volumetric flux velocity, μ is dynamic viscosity, P is fluid pressure, and g is the gravity acceleration.

At the Darcy scale, each spatial point corresponds to a representative elementary volume (REV) containing a sufficient number of pores occupied by two or more fluid phases. Navier-Stokes equations are not suitable for the practical description of spatial domains hence the governing equations describing the behaviour of immiscible and incompressible phases, such as CO_2-brine systems, are formulated at the continuum or Darcy scale (Helmig et al. 2010). A rigorous averaging of the Navier-Stokes equations yields the extended Darcy equation, also referred to as Darcy's law (Hubbert 1956):

$$v_\alpha = -\frac{k_\alpha}{\mu_\alpha}(\nabla P_\alpha - \rho_\alpha g) \tag{2.3}$$

where α is the incompressible Newtonian fluid $\equiv w \; or \; n$; w and n represent wetting and non-wetting phase respectively; k is the effective permeability tensor for the fluid phase:

$$k_\alpha = K k_{r\alpha} \tag{2.4}$$

where k_r is the scalar relative permeability coefficient, assuming values from zero to one, and K is the absolute/intrinsic permeability of the rock. Effective permeability is a measure of the conductance for a fluid phase in a porous medium saturated with more than one fluid. Intrinsic permeability is independent of fluid properties and specifies the ability of a porous medium to permit fluid flow through its effective porosity.

An alternative representation of two-phase flow in porous media at the Darcy-scale is:

$$v_\alpha = -K\Lambda_\alpha(\nabla P_\alpha - \rho_\alpha g) \tag{2.5}$$

where Λ_α is the phase mobility = $k_{r\alpha}/\mu_\alpha$

The governing equations for CO_2/brine/rock systems are derived from the mass conservative principle applied to the Darcy's law within saturation and pressure constraints. The balance of mass for phases and interfaces holds for each phase in the continuity equation for two-phase flow in porous media:

$$\frac{\partial}{\partial t}(\rho_\alpha S_\alpha \phi) + \nabla(\rho_\alpha v_\alpha) = 0 \tag{2.6}$$

where ϕ is the porosity assumed constant, and S is the phase saturation that indicates the fraction of void space occupied by the fluid phase at any point within the REV.

Substituting the Darcy equation (2.5) into the Mass Balance equation (2.6) for each phase results in the following system of coupled partial differential equations (Hassanizadeh and Gray 1993):

$$\frac{\partial}{\partial t}(\rho_w S_w \phi) - \nabla[\rho_w \Lambda_w K(\nabla P_w - \rho_w g)] = 0 \tag{2.7}$$

$$\frac{\partial}{\partial t}(\rho_n S_n \phi) - \nabla[\rho_n \Lambda_n K(\nabla P_n - \rho_n g)] = 0 \tag{2.8}$$

Using the chain substitution rule, the storage term for each phase can be expanded to show explicitly the contributions related to the fluid compressibility and saturation change:

$$\frac{\partial}{\partial t}(\rho_\alpha S_\alpha \phi) = S_\alpha \phi \frac{\partial P_\alpha}{\partial t} + \rho_\alpha \phi \frac{\partial S_\alpha}{\partial t} \tag{2.9}$$

For the non-wetting phase, $$\frac{\partial}{\partial t}(\rho_\alpha S_\alpha \phi) = S_\alpha C_\alpha \phi \frac{\partial P_\alpha}{\partial t} + \rho_\alpha \phi \frac{\partial S_\alpha}{\partial t} \tag{2.10}$$

For the wetting phase, $$\frac{\partial}{\partial t}(\rho_\alpha S_\alpha \phi) = S_\alpha C_\alpha \phi \frac{\partial}{\partial t}\frac{1}{\beta_\alpha} + \rho_\alpha \phi \frac{\partial S_\alpha}{\partial t} \tag{2.11}$$

where C_α is compressibility coefficient, β_α is formation volume factor for α.

Compressibility coefficient for water: $$C_w = \rho_w \beta_w \tag{2.12}$$

Compressibility coefficient for gas: $$C_g = \rho_g / P_g \tag{2.13}$$

The fluid saturation of porous medium is constrained through the expression of saturation-dependent functions through the wetting phase saturation, S_w:

$$S_w + S_n = 1 \tag{2.14}$$

Another relationship that is specific to fluid pairs and the porous medium is the correlation between the wetting saturation (S_w) and the capillary pressure (P_c), *i.e.* the difference in the fluid pressures, where P_c is assumed a function of S_w:

$$P_c \equiv P_c(S_w) = P_n - P_w \tag{2.15}$$

Eq. 2.14 and 2.15 are closure equations for the systems of Eq. 2.3 – 2.11. Eq. 2.15 is implicitly assumed to account for all effects and processes that influence the equilibrium distribution of fluids, such as surface tension, presence of fluid-fluid interfaces, wettability of solid surfaces, grain size distribution, and microscale heterogeneities. All of these effects are lumped into the P_c – S_w relationship (Reeves and Celia 1996, Held and Celia 2001). This relationship depends on the flow dynamics or hysteresis, *i.e.* the history and the rate of change of saturation. Under a simple assumption of no heat and mass transfer, as well as no compressibility and rheological factors, pore scale flow will be governed by the interaction of capillary, viscous and gravitational forces. The validity of a conventional two-phase flow model requires the accuracy of capillary pressure and relative permeability functions. The latter has been shown to be an approximate description of the aggregate impact of multi-fluid displacement at pore-scale (Benson et al. 2013).

2.3 Two-phase flow characteristics

Multi fluids in contact in a porous medium generate buoyancy pressure, resulting from density differential between them and the column height of the least dense fluid (Leverett 1941). As illustrated in the previous section, capillary pressure is the pressure difference that exists across the interface of the fluids in contact. This pressure is analogous to the force required to push a fluid droplet through a pore throat. It is higher for smaller pore diameter and it increases linearly with the interfacial tension between the wetting and non-wetting fluids (Brown 2000).

By definition, the capillary pressure at equilibrium ($P_{ceqn} \approx P_n - P_w$; *where* $P_n > P_w$) is always positive (Leverett 1941). For non-wetting fluids (oil or CO_2) to accumulate in a water-wet reservoir, the buoyancy force that drives them into the pores must overcome the capillary force that was formed between the displacing fluid and the original fluid. Since the largest pore throats have least capillary resistance, the non-wetting fluid first occupies the largest pores. Subsequently, the buoyancy pressure increases with increasing column height of the non-wetting fluid thereby resulting in the gas migration into smaller and smaller pore throats. The pressure required to push the non-wetting fluid into these pores is called the capillary entry or displacement pressure (Hassler and Brunner 1945). At the onset of flow, fluid conductance, a measure of how effectively fluids are transported through a medium, is highly dependent on the permeability of the porous media. Since the permeability is a function of the pore characteristics in sedimentary formations (Krause et al. 2013), the pore structure not only controls the pressure transmitted to the rock but also has a significant effect on hydraulic conductivity in multiphase systems. The relative permeability is a functional parameter when assessing fluid conductance in such systems. It provides an empirical description of the reduction in fluid flow due to surface-tension effects between the fluids, and the chemical interaction between fluids and the mineralogy of the rock matrix (Burnside and Naylor 2014).

Structural trapping is driven by spatial distribution in capillary entry pressures at specific water saturation values. For sealing systems in GCS, the caprock integrity is dependent on the magnitude of the displacement pressure acting along the reservoir-seal interface (Shukla et al. 2010). The maximum CO_2 column that can be retained by the seal (*i.e.* the capillary sealing capacity) is determined by its smallest pore throat radius (Zhang et al. 2016). Similarly, the ultra low hydraulic permeability of caprocks such as shales translates to very small pore throats commonly portrayed by pore size distribution of micro-pores (pore width < 2nm) and meso-pores (2nm to 50 nm) (Kuila and Prasad 2013, Pommer and Milliken 2015). Capillary leakage occurs when the capillary breakthrough pressure of the caprock is exceeded and pressure-driven flow breaches the rock matrix (Wollenweber et al. 2010). In such scenarios the leakage rate becomes a function of the relative permeability of the fluid within the multiphase system (Hildenbrand et al. 2002). This makes the CO_2 capillary breakthrough pressure and relative permeability important control measures when implementing CO_2 sequestration projects. Capillary pressures and relative permeabilities are both functions of the formation's heterogeneity, defined by properties such as partial distribution of sediments, faults and fractures, and cemented layers, and they rely particularly on the saturation path, *i.e.* hysteresis, during CO_2 storage. The relationship between the variables of flow resistance and reservoir fluid migration is expressed by the Young-Laplace law:

$$P_e \approx \frac{2\sigma \cos\theta}{R_{max}} \tag{2.16}$$

where P_e is the capillary entry pressure or the minimum displacement pressure required for a non-wetting fluid to displace a wetting fluid in the maximum pore throat radius, R_{max}; σ is the interfacial tension between the wetting and non-wetting fluids, and θ is the wettability, expressed by the angle of contact which the fluid interface forms with the solid. The following sub-sections give a brief overview of wettability and interfacial tension in the context of geological CO_2 storage (GCS).

2.3.1 Wettability

When considering a fluid-rock system, it is crucial to consider the wetting character of the rock, which describes the preferential affinity of one of the fluids to the rock surface. Wettability usually involves the measurement of contact angles of a gas/liquid/solid system. Young (1805) first described the contact angle in multiphase systems at thermodynamic equilibrium as a function of three interfacial tensions: solid/gas (σ_{sg}), solid/liquid (σ_{sl}), and gas/liquid (σ_{lg}).

$$\cos\theta = \frac{\sigma_{sg} - \sigma_{sl}}{\sigma_{lg}} \tag{2.17}$$

Contact angles << 90 indicate high wettability while those >> 90 indicate low wettability. Treiber and Owens (1972) considered three common cases of wettability for hydrocarbon systems as, water-wet (0° ≤ θ < 75°), intermediate-wet (75°≤ θ <105°), and oil-wet (105° ≤ θ < 180°). Subsequently, Iglauer et al. (2015) used a bigger catalog for contact angles to explicitly describe the wettability of CO_2/brine systems as illustrated in Table 2.1:

Contact Angle relative to brine, θ (°)	***Description***
0-30	Significantly water wet
30-60	Moderately water wet
60-90	Weakly water wet
90	Neutrally wet
90-120	Weakly CO_2 wet
120-150	Moderately CO_2 wet
150-180	Significantly CO_2 wet

Table 2.1: Contact angles for wettability of CO_2/brine/rock systems

The common approach in fluid distribution is a preferential coating of the wetting phase on the surface of the rock grains, occupying fissures and the smallest pores, while the non-wetting phase exists as droplets in the centre of the pores (Benson et al. 2013). For multiphase flow in porous media, the fundamentals of capillary forces in wettability of porous media are two displacement processes: imbibition and drainage (see Section 2.4).

CO_2/brine system generally indicates a water-wet system and during CO_2 injection, contact angles for CO_2-wettability and water wettability are representated by the advancing contact angle, θ_a, and the receding contact angle, θ_r, respectively. It is essential to characterise these contact angles as a function of temperature, pressure, salinity and mineralogy of the formation. With the premonition that reservoir rock minerals in water saturated aquifers are predominantly water-wet (McCaffery 1972, Hansen et al. 2000), the notion that dense (pressurized) CO_2 can alter the water-wettability of various organic and inorganic substances has been investigated in various literature. Espinoza and Santamarina (2010) reported that at supercritical conditions, deionized water will preferentially wet a rock surface compared to brine of 200g NaCl/kg (~10°) and the water-wettability decreases as pressure increases. An increase in contact angle with pressure was also reported for mica and quartz, rock minerals which predominantly occur in shale and sandstone respectively, in a number of studies, e.g. Farokhpoor et al. (2013), Iglauer et al. (2015), Chiquet et al. (2007), Broseta et al. (2012), Wang et al. (2013), Jung and Wan (2012), Arif et al. (2016), and Saraji et al. (2014). The authors observed that at GCS relevant conditions, high CO_2 pressures result in wettability variation from water-wet to intermediate-wet with mica showing a more prominent wettability alteration. If this wettability evolution holds for other representative shale minerals, the impact of wettability on the capillary sealing efficiency will largely depend on the burial depths of the caprock. This takes into account the fact that $scCO_2$ sequestration in increasing depths is synonymous with pressure elevation, leading to a conclusion that reservoirs with lower pressures exhibit better capillary sealing efficiency (Bachu 2003).

In regard to temperature effects, Arif et al. (2016) and Broseta et al. (2012) observed a decrease in CO_2-brine-mica contact angles with increasing temperature. Observations on CO_2-brine-quartz contact angles, however, showed two different trends. These were a slight increase in advancing contact angle of CO_2-brine-quartz with increasing temperature (Farokhpoor et al. 2013, Sarmadivaleh et al. 2015) and a significant decrease in contact angles with increasing temperature (Saraji et al. 2014, Iglauer et al. 2012, Bikkina 2011). This begs the question of the influence of other parameters such as the surface contaminants (Mahadevan 2012, Bikkina 2012) and surface roughness (Wang et al. 2013). A comparison of contact angles for mica and quartz show higher values for θ_a and θ_r of $scCO_2$-brine-mica systems over $scCO_2$-brine-quartz systems. This can be attributed to the effect of surface roughness on CO_2 adhesion to mineral surfaces following Wang et al.'s (2013) observation that mica surfaces are the easiest to cleave onto due to nanometer-smooth surfaces, as opposed to quartz surfaces. It should also be noted that dissolution reactions that could occur during CO_2 sequestration can lead to changes in surface smoothness. The trend for pressure alteration reported in most literature can be readily attributed to increasing CO_2 density and CO_2 adsorption with pressure. Likewise, it can be inferred that if surface contaminants and surface roughness are neglected, the trend for temperature alteration will be solely attributed to CO_2 density and CO_2 adsorption, which decrease with increasing temperature (Busch et al. 2008, Kang et al. 2011).

2.3.2 Interfacial tension

Interfacial tension (IFT) is largely influenced by *in situ* reservoir conditions of pressure, temperature and salinity**.** An absence of interfacial tension in any fluid system indicates zero capillary pressure. Technically, this is unrealistic for fluids in contact in a reservoir formation. Generally, the magnitude of IFT alterations resulting from *in situ* reservoir conditions depends on the density difference between the two phases, for example IFT between gaseous CO_2 and brine is higher than that between scCO_2 and brine (Bennion and Bachu 2008). Studies by Hebach et al. (2002) and Chun and Wilkinson (1995) on the IFT of CO_2/water systems, under the assumption of significant water-wettability, show IFT values for scCO_2/water interactions to typically range from 20 – 50 mN/m. Although these authors did not take into account the influence of salinity, a linear relationship between the increase in IFT and salinity was observed by Okasha and Alshiwaish (2009) and Chalbaud et al. (2006). This trend could be attributed to increments in the surface tension of aqueous solutions of salts as concentration of the solute along a given isotherm increases (Ali et al. 2006). For a given salinity, however, an increase in temperature decreases the surface tension of the aqueous solution. Nevertheless, at GCS relevant conditions, interfacial tension decreases as pressure is increased along a given isotherm for both CO_2/pure water and CO_2/brine systems (Chiquet et al. 2007). Generally, IFT rises with temperature, except near the critical point, and decreases with increasing CO_2 solubility. According to Li et al. (2012), at conditions relevant to GCS the IFT ranges from 20 mN/m (at low temperature, low salinity, and high pressure conditions) to 55 mN/m (at high temperature, high salinity, and low pressure conditions).

2.4 Hysteresis model

In a multiphase system saturation may change in two directions simultaneously, indicated by two terms: drainage and imbibition (Land 1968). In CO_2/brine systems, the conventional definition of drainage implies the decreasing wetting phase saturation due to CO_2 injection into the brine saturated rock. Imbibition indicates increasing wetting phase saturation after flow reversal where brine flushes back into the rock partially saturated with CO_2 (Burnside and Naylor 2014). During fluid flow the saturation path depends on the saturation history, allowing capillary pressure and relative permeability to alternate between drainage and imbibition curves. This is referred to as hysteresis and usually results from a number of inter-dependent pore scale mechanisms during drainage and imbibition (Spiteri et al. 2008). For example, the presence of chemical heterogeneities and surface roughness can lead to “contact angle hysteresis” where the advancing brine has higher angle of contact in comparison to the receding CO_2 (Juanes et al. 2006). Drainage and imbibition usually occurs at the leading edge and the trailing edge of the CO_2 plume, respectively. During imbibition the continuous CO_2 plume is disturbed at the trailing edge by encroaching brine, leading to the snap-off and isolation of CO_2 phase into bubbles and ganglia and subsequent immobilisation (Figure 2.2). This is referred to as residual trapping at the reservoir (continuum) scale, where significant non-wetting phase remains in the pore space.

Hysteresis effect is assessable through the magnitude of non-wetting trapping upon flow reversal. Capillary pressure hysteresis and relative permeability hysteresis indicates the dependence of capillary functions ($P_c - S_w$) and relative permeability functions ($k_r - S_w$), respectively, on the rate of change of saturation. Land's (1968) model, developed for the prediction of trapped non-wetting saturation as a function of initial non-wetting saturation, is currently the most widely applied empirical model for quantifying the amount of residual non-wetting phase. The Land model is defined as:

$$S_{nt} = \frac{S_{hy}}{1+C \cdot S_{hy}} \tag{2.18}$$

$$C = \frac{1}{S_{nt,max}} - \frac{1}{S_{n,max}} \tag{2.19}$$

where S_{nt} is the trapped non-wetting saturation, S_{hy} is the non-wetting saturation at the flow reversal, $S_{n,max}$ is the maximum non-wetting saturation, $S_{nt,max}$ is the maximum trapped non-wetting saturation, and C is the Land trapping coefficient. Land's equation serves as the basis for many hysteresis models currently employed in continuum-scale investigations (Killough 1976, Carlson 1981, Lenhard and Parker 1987, Larsen and Skauge 1998, Lenhard and Oostrom 1998, Blunt 2000, Beygi et al. 2015).

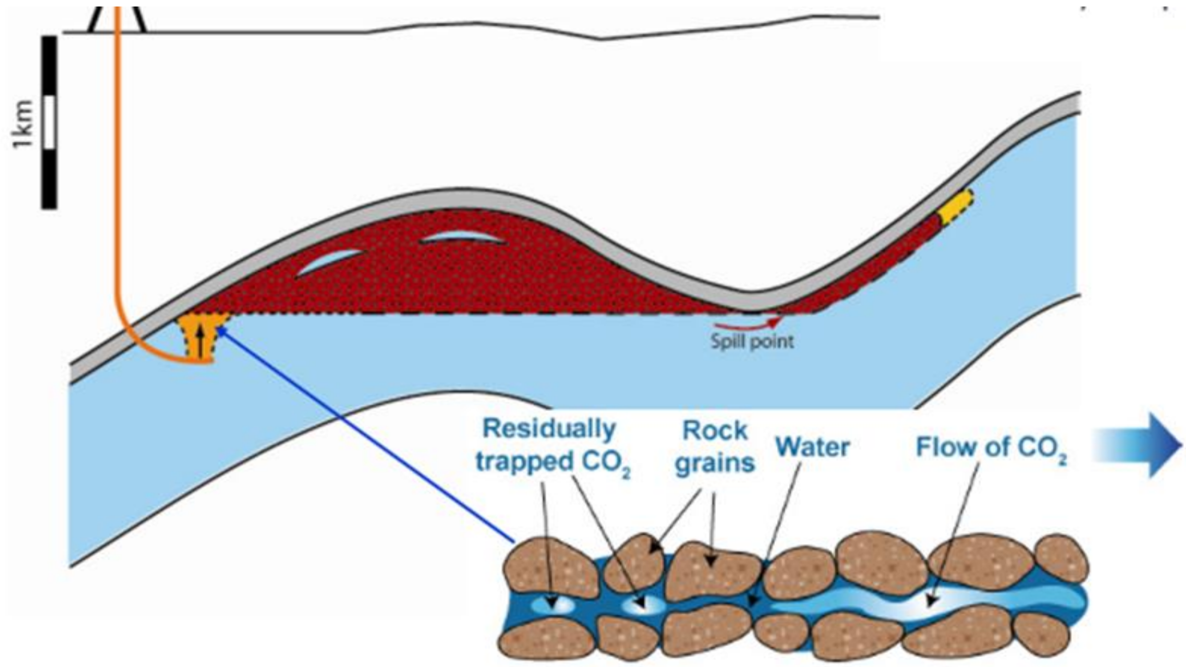

Figure 2.2: Snap-off of the tail of CO_2 plume and subsequent residual trapping during up-dip migration. [Source: Burnside and Naylor (2014)]

2.4.1 Capillary functions (P_c – S_w curves)

Capillary functions determine the hydrostatic distribution of fluids in the porous media. Capillary pressure measurements, developed from drainage situations, include three major laboratory techniques; mercury injection method (Purcell 1949), porous diaphragm method (Christoffersen and Whitson 1995, Reitsma and Kueper 1994), and centrifugal method (Chen and Ruth 1995, Hassler and Brunner 1945, O'Meara et al. 1992). The shape of the capillary pressure curve depends on the interconnection of the pores and the sorting of the pore sizes (Thomeer 1960). Experimental measurement techniques for P_c – S_w curves are time consuming (Li and Horne 2002), hence a more convenient way for describing this constitutive function for either drainage or imbibition in sedimentary formations is through analytical models (Leij et al. 1997, Leong and Rahardjo 1997, Fredlund and Xing 1994). Typical P_c – S_w *curve*s are illustrated in the figure below:

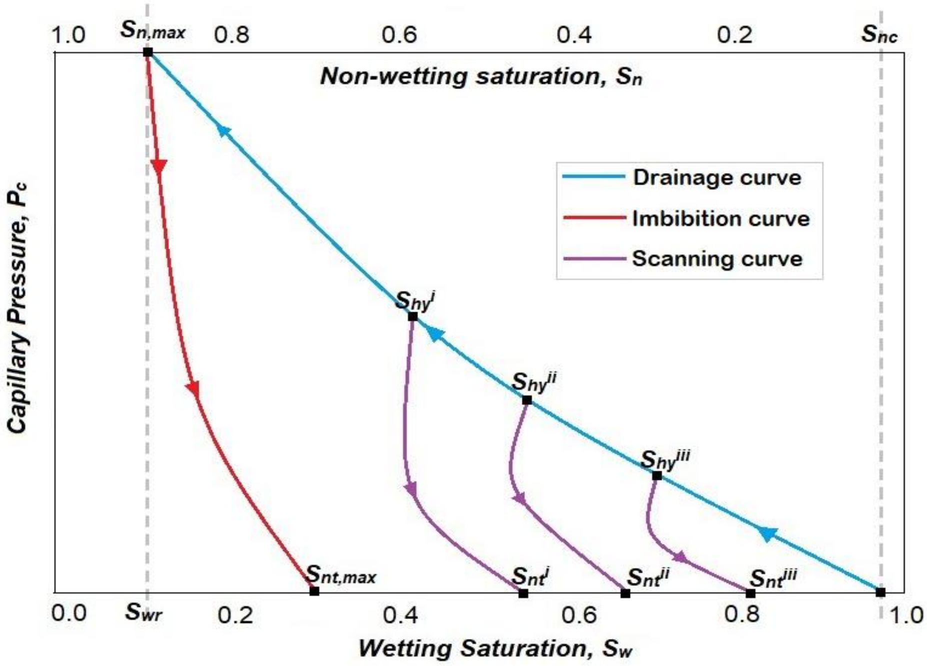

Figure 2.3: Typical capillary pressure curves in a two-phase system

In general, the capillary pressure will follow drainage curve for decreasing wetting phase saturations and the imbibition curve for increasing wetting phase saturations. The drainage curve starts at the critical non-wetting saturation, S_{nc}, or the drainage critical saturation. Critical saturation is the saturation of a fluid at which it becomes mobile as saturation is increased. For a full drainage process, the bounding drainage curve is followed to the maximum non-wetting saturation, $S_{n,max}$, which is equivalent to the residual wetting saturation, $S_{wr.}$ If an imbibition process then occurs, the bounding imbibition curve is followed from the maximum attainable non-wetting saturation to imbibition critical saturation, which corresponds to the maximum trapped non-wetting saturation, $S_{nt,max}$. However, should a reversal in the direction of saturation change occur at some intermediate point on either of the bounding curve, the path for capillary pressure trails one of the scanning curves (Killough 1976). Each scanning curve arises from a turning point on the bounding imbibition or draining curve. A scanning curve emerging from the drainage process will run from the maximum non-wetting saturation reached at the flow reversal, S_{hy}^i, to another critical non-wetting saturation, which then indicates the trapped non-wetting saturation, S_{nt}. If another drainage process commences at any point on the scanning curve, the same scanning curve is retraced until S_{hy} is reached, and further imbibition processes would occur along the appropriate scanning curves.

2.4.2 Relative permeability functions (k_r – S_w curves)

In CO_2/brine/rock systems, relative permeability functions quantify the extent to which the injected CO_2 and water interfere with each other as they migrate through the rock. The need for describing relative permeability functions in reservoir engineering is exemplified in several literature, including Chierici (1984), Eichel et al. (2005), and Sakurai et al. (2013). Relative permeability curves affect almost all of the important aspects of a storage project. For example, the spatial extent of the CO_2 plume (Doughty 2010, Cavanagh 2013), the injectivity of a well (Mathias et al. 2013, Cameron and Durlofsky 2012), extent of capillary trapping (Krevor et al. 2012, MacMinn et al. 2011), and leakage through the well or seal (Vialle et al. 2016, Espinoza and Santamarina 2017) are influenced by relative permeability.

The relationship between fluid saturation and relative permeability in a reservoir formation can be obtained in a number of ways, namely:

i) From laboratory flow experiments on rock samples,
ii) From history match and data extrapolation based on field performance, and
iii) From mathematical derivations of flow behaviour using some experimentally obtained characteristics of reservoir rocks.

Two basic experimental methods are used for determining k_r – S_w curves: steady state and unsteady state fluid flow processes (Bear 1972, Honarpour et al. 1986). In the steady state technique, a fixed ratio of both fluid phases is driven at constant rates or pressure through the rock core sample for extended durations to reach equilibrium (Abaci et al. 1992, Richardson et al. 1952). This implies that values are only measured when the tested sample reaches a stable or steady-state behaviour. This technique is usually regarded as the most reliable source of k_r data but requires a long time for flow stabilization and can be quite expensive (Honarpour and Mahmood 1988).

In contrast, unsteady state techniques entail the displacement of one fluid from the core by injecting another fluid, with both fluids eventually exiting the core. Since flow and pressure stabilisation are not required, unsteady-state experiments are quicker. However, this technique is limited to displacements where the assumptions based on Buckley-Leverett theory (Buckley and Leverett 1942) is fulfilled by ignoring capillary pressure, and does not generate relative permeabilities for the total saturation level (Benson et al. 2013). Furthermore, although the laboratory measurements offer the only direct method for determining relative permeability characteristics applicable to field problems, representative rock samples of a reservoir may not be readily available. A few limitations also exist for other options used to derive relative permeability functions. For example, past reservoir performance is not readily available for CO_2 storage in aquifers and the relative permeability characteristics obtainable from hydrocarbon production data may be inadequate for EOR and CO_2 storage process. The mathematical techniques developed by Purcell (1949), along with the Kozeny-Carman equation (Carman 1956), are commonly used to derive relative permeability from experimental measurements and theoretical arguments. The resulting mathematical expressions are mostly computed with respect to the wetting saturation, S_w. For example, Rose and Bruce (1949) defined mathematical correlation between the relative permeability to the wetting phase, k_{rw}, based on the Kozeny-Carman equation and experimental data for capillary retention curve, as:

$$k_{rw} = S_w \left(\frac{P_e}{P_c}\right)^2 \tag{2.20}$$

Rapoport and Leas (1951) described the relative permeability to the wetting phase, based on surface energy relations and the Kozeny-Carman equation, as:

$$k_{rw} = \frac{(S_w)^3}{\left({}^{A_w}/_{A}\right)^3} \tag{2.21}$$

Gates and Lietz (1950) described the relative permeability to the wetting phase, based on the capillary pressure curve using the Purcell model, as:

$$k_{rw} = \frac{\int_0^{S_w} \frac{dS_w}{(P_c)^2}}{\int_0^{100} \frac{dS_w}{(P_c)^2}} \tag{2.22}$$

Fatt and Dykstra (1951) described another expression for relative permeability to wetting phase by using Purcell's method and introducing a saturation-dependent function for pore radius, *b*, in the form:

$$k_{rw} = \frac{\int_0^{S_w} \frac{dS_w}{(P_c)^{2(1+b)}}}{\int_0^{100} \frac{dS_w}{(P_c)^{2(1+b)}}} \tag{2.23}$$

where P_c is the capillary pressure associated with given values for the wetting phase saturation, S_w; P_e is the capillary pressure of the maximum sized pore which is completely filled under the given condition of saturation, A_w is the total surface area of the wetting system, and A is the total surface area of the solid system, *i.e.* the total grain surface. In practice, the k_r – S_w relation is an empirical parameter that depends on the specific context in which it is applied. For example, water flooding during oil recovery requires water injection into the reservoir (an imbibition process), while for CO_2 storage in water-bearing formations CO_2 is injected into the reservoir (a drainage process).

2.4.3 The coupled P_c – k_r – S_w relationship

For utilisation in geo-models, the hydraulic properties are expressed as analytical functions, often called parametric models. The main hypothesis of these analytical functions for multi-phase flow are illustrated in terms of the effective or normalised saturation of the fluid phase, $S_{e\alpha}$:

$$S_{e\alpha} = \frac{S_\alpha - S_{\alpha r}}{1 - S_{wr} - S_{nr}} \tag{2.24}$$

where S_α is the fluid phase saturation, $S_{\alpha r}$ is the residual saturation of the fluid phase, S_{nr} is the residual non-wetting saturation, and S_{wr} is the residual wetting saturation. The parameters at the base of this normalised saturation, S_{nr} and S_{wr}, are determined by the flow dynamics. For example, for the primary drainage curve, S_{nr} = 0; for primary imbibition (wetting) curve, S_{nr} = $S_{nr,max}$; and for other imbibition (wetting) curves S_{nr} = S_{nt}.

$S_{nr,max}$ is an input parameter that defines the maximum residual non-wetting saturation in analytical model. It varies inversely with porosity, ϕ, and generally taken as a constant material property. A typical formulation by Holtz (2002) is described below:

$$S_{nr,max} = -0.9696\phi + 0.5473 \tag{2.25}$$

In the absence of direct experimental measurement of the capillary pressure-saturation, mathematical models for capillary pressure data become a reliable technique to describe flow characteristics in a porous media. The most commonly used empirical formulation for capillary pressure data in porous media are models by Brooks and Corey (1964) and van Genutchten (1980). P_c – S_w curves are typically convex for BC models and S-shaped for vG models (Figure 2.4). Brooks-Corey (BC) model describe a plateau that ends with a non-zero capillary entry pressure while the van Genuchten (vG) model illustrate a steep slope that connects the endpoint (usually zero) to the plateau region (Li et al. 2013).

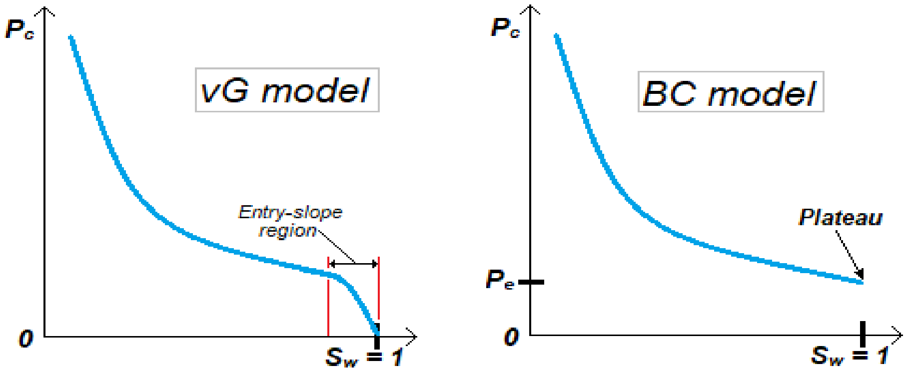

Figure 2.4: P_c – S_w curves for vG and BC analytical models

Capillary pressure curves measured using the experimental mercury injection technique usually have an entry-slope region similar to vG models although the capillary pressure at S_w = 1 is usually non zero. Nothwithstanding the starting point capillary pressure in vG models at S_w = 1 can be zero or non zero. The BC model introduces a well-defined capillary entry pressure value, P_e, which is associated with the largest pore throat radius through the relation of Young-Laplace law (Eq. 2.16) and shows good agreement with experimental data:

For $P_c > P_e$;
$$S_{ew} = \left(\frac{P_c}{P_e}\right)^{-\lambda} \tag{2.26}$$

$$P_c = P_e\,(S_{ew})^{-\frac{1}{\lambda}} \tag{2.27}$$

For $P_c \leq P_e$;
$$S_{ew} = 1 \tag{2.28}$$

where λ is the pore size distribution index is an empirical constant with values typically ranging from 0.2 to 4.2 for fine- to coarse- clast textures (Brooks and Corey 1964).

In contrast, the vG function for $P_c – S_w$ relations does not explicitly account for P_e but describes a continous function by introducing a pressure scaling parameter, P_g, which is related to the average size of the pores. This pressure scaling parameter is quite different from the P_e and is usually larger than the P_e (Morel-Seytoux et al. 1996). The van Genutchen model for $P_c – S_w$ relations is computed as:

For $P_c > 0$; $$S_{ew} = [1 + (\alpha P_c)^n]^{-m} \tag{2.29}$$

$$S_{ew} = \left[1 + \left(\frac{P_c}{P_g}\right)^n\right]^{-m} \tag{2.30}$$

For $P_c \leq 0$; $$S_{ew} = 1 \tag{2.31}$$

where n and m are pore geometry/model parameters, related by the assumption that $m = 1 - {}^{1}/_{n}$ or $m = 1 - {}^{2}/_{n}$; and α (Pa^{-1}) is assumed to be roughly the inverse of P_g and can be estimated from observed $P_c – S_w$ data.

In water wet systems, k_{rw} depends only on the amount of mobile water ($S_w - S_{wr}$) present, while k_{rn} depends on the amount of non-wetting phase present. Recalling the relationship between effective permeability and relative permeability in Eq. 2.4, if the effective permeability is said to be a function of the pore size distribution, the wettability, and the saturation history of the rock-fluid system, the same can be said of the relative permeability value. It becomes easier to discuss relative permeability – saturation behaviour if effective saturation units are used rather than the pore saturation units:

$$k_{ew} = \frac{k_w}{k_{w,s_{ew=1}}} \tag{2.32}$$

$$k_{en} = \frac{k_n}{k_{n,s_{ew=0}}} \tag{2.33}$$

where k_{ew} and k_{en} is the effective permeability normalised for the wetting and non-wetting phase, respectively; k_w and k_n is the effective permeability of wetting phase and non-wetting phase at a given wetting phase saturation, respectively; $k_{w,s_{ew=1}}$is the effective wetting phase permeability at effective wetting phase saturation equal to 1; and $k_{n,s_{ew=0}}$ is the effective non-wetting phase permeability at effective wetting phase saturation equal to 0.

The relationship for normalised effective permeabilities phase and effective wetting saturation given in Eq. 2.32 & 2.33 can be used to directly represent the relative permeabilities of the fluid phases. This is because the base of the normalised effective permeabilities, $k_{w,s_{ew=1}}$ and $k_{n,s_{ew=0}}$, correspond to the absolute permeability, K, of each fluid phase in the porous media. Note that when the effective wetting saturation, S_{ew}, equals zero, the effective non-wetting saturation, S_{en}, equals one and vice versa. Consequently the following relationships apply:

$$k_{ew} = \frac{k_w}{k_{w,s_{ew=1}}} = \frac{k_w}{k} = k_{rw} \tag{2.34}$$

$$k_{en} = \frac{k_n}{k_{n,s_{ew=0}}} = \frac{k_n}{k} = k_{rn} \tag{2.35}$$

Early works by Burdine (1953) and Mualem (1976), using the mean hydraulic pore radius concept of Kozeny-Carman, led to the following generalised drainage relationships for describing the relative permeability for both the wetting and non-wetting phase:

$$k_{rw:dr} = \frac{k_w}{k_{w,S_{ew}=1}} = (S_{ew})^a \left(\frac{\int_0^{S_{ew}} \left(\frac{1}{P_c}\right)^x \cdot dS_{ew}}{\int_0^1 \left(\frac{1}{P_c}\right)^x \cdot dS_{ew}} \right)^{b^2} \tag{2.36}$$

$$k_{rn:dr} = \frac{k_n}{k_{n,S_{ew}=0}} = (1 - S_{ew})^a \left(\frac{\int_{S_{ew}}^1 \left(\frac{1}{P_c}\right)^x \cdot dS_{ew}}{\int_0^1 \left(\frac{1}{P_c}\right)^x \cdot dS_{ew}} \right)^{b} \tag{2.37}$$

In the above equations, the portions that involve the ratio of integrals of $(1/P_c)^x \cdot dS_{ew}$ represent flow area changes, while $(S_{ew})^a$ represent flow path length changes. When the pore size distribution index, λ, is known, both models provide the following closed-form analytical solutions:

$$k_{rw:dr} = (S_{ew})^y \tag{2.38}$$

$$k_{rn:dr} = (1 - S_{ew})^a \, [1 - (S_{ew})^z]^b \tag{2.39}$$

The unknown power functions a, b, x, y and z, are defined based on the model as illustrated in Table 2.2:

Model	**a**	**b**	**x**	**y**	**z**
Burdine	2	1	2	$3 + 2/\lambda$	$1 + 2/\lambda$
Mualem	0.5	2	1	$2.5 + 2/\lambda$	$1 + 1/\lambda$

Table 2.2: Parameters used in Burdine (1953) and Mualem (1976) relative permeability models

Using a combination of Purcell and Burdine, Corey (1954) described a simple mathematical expression for drainage gas-liquid relative permeability thus:

$$k_{rw} = (S_{ew})^4 \tag{2.40}$$

$$k_{rn} = (1 - S_{ew})^2 . [1 - (S_{ew})^2] \tag{2.41}$$

As seen in Eq. 2.40 and 2.41, Corey model assumes that the pore gemetry parameter, λ, in Burdine's model equals 2. To this end, curves identified as $\lambda = 2$ are often called Corey curves. Although Burdine's (1953) and Mualem's (1976) generalised expressions may be valid for estimating relative permeabilities to the wetting phase, they may fall short of purpose for adequately quantifying non-wetting relative permeabilities in CO_2 storage operations. This is because in describing the relative permeability to both the wetting saturation (S_w) and non-wetting saturation (S_n), the corresponding relative permeability endpoints, designated as k_{rw}^0 and k_{rn}^0 respectively, have to be considered. Eq. 2.34 and 2.35 assume that both k_{rw}^0 and k_{rn}^0 equal unity. While this assumption is valid for k_{rw}^0 in completely water-wet CO_2/brine/rock systems, it will be invalid for k_{rn}^0 where the irreducible wetting saturation is not be equal to zero. It is necessary, therefore, to relate k_{rn}^0 to S_{wr} as these parameters are expected to be inversely proportional to each other since S_{wr} acts to reduce the cross-sectional area of non-wetting fluid flow. Hence both parameters should show some effect of pore size distribution. Although k_{rn} is not necessary for measuring the entrapped non-wetting phase, S_{nt}, it is an important parameter for evaluating injectivity and evolving flow rates. Hence the presentation of $k_{r(CO_2)}$, S_{nt}, and $S_{n,max}$ is the best evidence base currently available for assessing the CO_2 storage security (Burnside and Naylor 2014). It becomes necessary in GCS operations to discount the normalised non-wetting permeability, k_{en}, to obtain a corresponding relative peremability, k_{rn}, at absolute permeability equals unity. For this purpose, k_{rn}^0 which accounts for the maximum relative permeability to the non-wetting phase is introduced in Eq. 2.35 as shown below:

$$k_{en} = \frac{k_n}{k_{rn}^0 \cdot k_{n,S_{ew}=0}} = \frac{k_n}{k_{rn}^0 \cdot k} = \frac{k_{rn}}{k_{rn}^0} \tag{2.42}$$

The drainage functions for non-wetting relative permeability can then be computed as:

$$k_{rn:dr} = k_{rn}^0 \cdot (1 - S_{ew})^a \, [1 - (S_{ew})^z]^b \tag{2.43}$$

Value for k_{rn}^0 is usually obtained from core-flooding experiments (e.g. Dria et al. 1993). In the absence thereof, however, the following relationship for k_{rn}^0 has been proposed for $S_{wr} < 0.5$ by Standing (1975):

$$k_{rn}^0 = 1.31 - (2.62 * S_{wr}) + (1.1 * S_{wr}^2) \tag{2.44}$$

A reasonable good fit for experimental data on $k_{r(CO_2)}$ is often achieved with Eq. 2.43 through proper choice of the values for the end-point relative permeability (Bennion and Bachu 2008, Perrin and Benson 2010, Krevor et al. 2012). The functionality of Eq. 2.43 is however limited due to its inability to duplicate the observed behaviour of many rock-fluid systems. Nevetheless, Corey's (1954) proposition creates the opportunity for better reconciliation of calculated and measured relative permebility curves when the exponents *a* and *b* in Eq. 2.43 are modified. Direct analytical computations of $P_c - k_r - S_w$ relationships for GCS predictive simulations typically entail the wetting and non-wetting phase relative permeability curves proposed by Burdine (1953) and Mualem (1976), integrated to the arbitrary capillary functions of van Genuchten (1980) and Brooks & Corey (1964). A modified version of coupled Brooks-Corey-Burdine model, where the exponents *y* and *z* (see Table 2.2) are designated as Corey exponents, has been referred to as Brooks-Corey – variable Corey (BC-vC) model in literature (Oostrom et al. 2016). Here, values for the "Corey exponents" typically depend on the fit to experimental data (Krevor et al. 2012, Bennion and Bachu 2008). The Burdine formula can be integrated analytical to the vG capillary function if $m = 1 - 2/n$:

$$k_{rw} = (S_{ew})^a \left[1 - \left(1 - (S_{ew})^{1/m}\right)^m\right] \tag{2.45}$$

$$k_{rn} = k_{rn}^0 \cdot (1 - S_{ew})^a \left[1 - (S_{ew})^{1/m}\right]^m \tag{2.46}$$

The Mualem formula can be integrated analytical to the vG capillary function if $m = 1 - 1/n$:

$$k_{rw} = (S_{ew})^a \left[1 - \left(1 - (S_{ew})^{1/m}\right)^m\right]^2 \tag{2.47}$$

$$k_{rn} = k_{rn}^0 \cdot (1 - S_{ew})^a \left[1 - (S_{ew})^{1/m}\right]^{2m} \tag{2.48}$$

Between the two relative permeability models coupled to the vG function, Mualem's approach was found to be more applicable to a wider variety of sediments than Burdines's formulation (van Genuchten and Nielsen 1985). Few examples of studies that employed analytical models in subsurface engineering include: Poe (2014) and Clarkson et al. (2016) on performance of production wells; Ebigbo et al. (2007) and Nordbotten et al. (2004) on gas leakage through abandoned wells; Gor et al. (2013) and Rutqvist et al. (2008) on geomechanical analysis of the reservoir-caprock system; Doughty (2010) and Espinet et al. (2013) on CO_2 plume behaviour during GCS; and finally Liu et al. (2011), Xu et al. (2010), and Pruess and Muller (2009) on reactive transport processes.

2.5 Numerical implementation

The governing equations of two-phase fluid flow and of constitutive models for capillary pressure and relative permeability are implemented in numerical simulators to investigate subsurface flow problems. Examples of continuum-scale simulators commonly used to reproduce coupled multiphase flow and reactive transport processes related to CO_2/brine/rock systems include: Schlumberger's ECLIPSE (Schlumberger 2017), Lawrence Berkeley National Laboratory's TOUGH2-ECO$_2$N (Pruess 2005), Pacific Northwest National Laboratory's STOMP-CO_2 (White et al. 2012), and Los Alamos National Laboratory's PFLOTRAN (Lichtner et al. 2015). These models are based on established implementation of Darcy's law for fluid flow in heterogeneous porous media. They solve conservative equations for component mass (*i.e.* water, CO_2 and salt) and energy by expressing them as partial differential equations on a structured grid. The reservoir simulators allow solution of large sets of finite-difference equations describing two- and three-dimensional (2D and 3D) multiphase flow using one or more of three linearisation schemes widely used in petroleum reservoir simulation, namely the Fully Implicit (FI), Implicit Pressure Explicit Saturation (IMPES) and Adaptive Implicit Method (AIM). Coats (1987) provides a general description of these formulations. ECLIPSE consists of two modules: ECLIPSE 100, a fully implicit black oil simulator with gas condensate option; and ECLIPSE 300, a compositional simulator that can be run in FI, IMPES and AIM modes. TOUGH2-ECO$_2$N, STOMP-CO_2 and PFLOTRAN use integral finite differences to achieve spatial discretisation with a fully implicit treatment of fluid flux.

Modelling of CO_2 sequestration requires pressure-volume-temperature (PVT) and phase equilibria properties of the CO_2/brine/rock system. A few models have been developed in the form of equations of state for both CO_2 and brine across a range of temperature, pressure, and salinity that is applicable to GCS. The equation of state (EOS) is a collection of constitutive equations that describe the phase conditions, phase compositions, phase densities, and phase equilibria (Perrot 1998). It is a semi-empirical functional relationship between temperature, pressure, volume, and internal enthalpy of a pure substance. The most famous EOS is the van der Waals EOS (van der Waals 1910). However, reservoir simulators widely employ one of three more accurate EOS for subsurface engineering, *i.e.* the Peng-Robinson EOS (Peng and Robinson 1976), Redlich-Kwong EOS (Redlich and Kwong 1949), and Redlich-Kwong-Soave EOS (Soave 1972). Thermodynamic properties of CO_2 in these simulators are usually computed via tabular interpolation of Span and Wagner's (1996) equation of state for CO_2 while thermodynamic properties of brine are calculated using American Association of Mechanical Engineers' (ASME) steam table formulations (Harvey et al. 2014).

The Darcy-based modelling approach has been employed in a number of studies on GCS in aquifers. For example,

a) Orsini et al. (2014) and Zhang et al. (2017) used PFLOTRAN to conduct an analysis on CO_2 storage performance for a potential storage site located off the coast of Italy, and to evaluate the interplay between heterogeneity and reactive transport processes in predicting CO_2 storage performance, respectively;

b) Pruess and Nordbotten (2011) and Mathias et al. (2013) used TOUGH2-ECO$_2$N to examine the long-term behaviour of CO_2 stored beneath a sloping caprock, and to perform sensitivity analysis on CO_2 injectivity in association with relative permeability functions, respectively;

c) Shariatipour et al. (2016) used ECLIPSE 300 and Ashraf (2014) used ECLIPSE 100 to assess the viability of the CO_2 downhole mixing technique, and to investigate the impact of heterogeneity on aquifer pressure, respectively; and

d) Nguyen et al. (2016) and Mishra et al. (2014) used STOMP-CO_2 to investigate the impact of CO_2/brine transport process on a formation's geomechanical properties, and to calibrate pressure response resulting from CO_2 storage in the Mount Simon formation, respectively.

The main difference between these simulators is that ECLIPSE uses analytical derivatives to solve solutions of non-linear problem while the others only use numerical differentiation. This offers significant computational time-saving compared to standard linear solvers (Williams et al. 2018). Brooks-Corey, van Genuchten, Mualem and Burdine formulations described in Section 2.4.3 govern the majority of P_c – k_r – S_w relations implemented in the reservoir models. Four coupled constitutive models are commonly utilised in GCS analysis: van Genutchen – Mualem (vG-M) model (Gor et al. 2013, Doughty 2010, Doughty et al. 2008), Brooks-Corey – Burdine (BC-B) model (Class et al. 2009, Kolditz et al. 2012, Rasmusson et al. 2015), van Genutchen – Corey (vG-C) model (Alkan et al. 2010, Kim et al. 2012), and van Genutchen – Mualem-Corey (vG-MC) model (Birkholzer et al. 2009, Zhou et al. 2010, Espinet et al. 2013, Giorgis et al. 2007, Middleton et al. 2012, Rutqvist et al. 2008). In vG-MC, the coupled Mualem-Corey formulation is used to compute relative permeabilities where Mualem (1976) describes the relative permeability to the wetting fluid, and Corey (1954) defines the relative permeability to the non-wetting fluid. This is the most widely used model for describing hysteretic relations during scCO_2 injection; hence, this thesis implements the vG-MC model and conducts numerical simulations using the ECLIPSE suite. The next chapter elaborates on this model, introducing a possible parameterisation scheme for describing hysteretic functions in siliciclastic formations during reservoir-scale simulations.

CHAPTER 3*

vG parameterisation scheme

In the application of two-phase flow in porous media within the context of CO_2 sequestration, a non-wetting phase is used to displace a wetting phase residing *in-situ* to the maximum extent through a network of pore conduits. The storage performance of this physical process can be assessed through numerical simulations where transport properties are usually described using the Brooks & Corey (BC) or van Genuchten (vG) model. The empirical constant, namely the pore geometry index, is a primary parameter in both of these models and experimental evidence shows a variation in the value of this parameter. It is, therefore, essential to cast this empirical constant into a ternary diagram for all types of clastic porous media to demarcate the efficiency of two-phase flow processes in terms of the pore geometry index (PGI). In doing so, this approach can be used as a tool for designing more efficient processes, as well as for the normative characterisation of two-phase flow, taking into consideration the predominance of capillary pressure or relative permeability effects. This concept is based on the existence of a PGI estimation for clastic sediments, for which the value for 12 sediment mixtures fall between 1.01 and 3.00. Statistical data obtained from soil physics is used for developing and validating numerical models where a good match is observed in numerical simulations.

This chapter presents theoretical observations and continuum-scale numerical simulation results of a PGI characterisation for the prediction of the hydraulic properties of clastic reservoir rocks. The effect of key parameters in the vG empirical model, such as the pressure strength coefficient and the PGI, is incorporated into the simulation analysis. In this chapter, a new methodology for the effective characterisation of PGI for different clastic rocks is proposed.

---

* The content of this chapter has been extracted from the following paper:

Onoja, M.U., Ahmadinia, M., Shariatipour, S.M., and Wood, A.M. (2019) Characterising the role of parametric functions in the van Genuchten empirical model on CO_2 storage performance. *International Journal of Greenhouse Gas Control* **88**, 233 – 250. https://doi.org/10.1016/j.ijggc.2019.06.004

The candidate set the scientific scope of the work, devised and developed the methodology, performed all data analysis and wrote the text. Masoud Ahmadinia wrote the MATLAB-code coupled to ECLIPSE for numerical simulation. Seyed Shariatipour and Adrian Wood provided guidance during the design of this part of the project and feedback on the manuscript.

Minor adaptations have been performed to streamline the layout of the thesis.

3.1 Introduction

Relative permeability [k_r] and capillary pressure [P_c] functions in subsurface formations play an integral role in determining the accuracy of any numerical solution to multi-phase fluid flow. In view of the spatial variability factor associated with reservoir-scale investigations, empirical models provide a viable means of characterising P_c – k_r – S_w relations. This is because experimental methods for determining these curves are often tedious, time consuming and may only prove to be cost-effective for specific purposes (Wösten and van Genuchten 1988). Oostrom et al. (2016) conducted a comparative study on the performance of empirical models employed for CO_2 geo-storage and identified van Genuchten-Mualem-Corey (vG-MC) and Brooks-Corey-variable-Corey (BC-vC) models as the most suitable for $scCO_2$ injection simulations:

$$S_{ew} = \frac{S_w - S_{wr}}{S_{w,max} - S_{wr} - S_{nr}} \tag{3.1}$$

vG-MC:

$$P_c = P_g\left[(S_{ew})^{-1/m} - 1\right]^{1/n} \tag{3.2}$$

$$k_{rw} = (S_{ew})^{0.5}\left[1 - \left(1 - (S_{ew})^{1/m}\right)^m\right]^2 \tag{3.3}$$

$$k_{rn} = k_{rn}^0 \cdot (1 - S_{ew})^2(1 - S_{ew}^2) \tag{3.4}$$

BC-vC:

$$P_c = P_e\,(S_{ew})^{-\frac{1}{\lambda}} \tag{3.5}$$

$$k_{rw} = (S_{ew})^X \tag{3.6}$$

$$k_{rn} = k_{rn}^0 \cdot (1 - S_{ew})^2.[1 - (S_{ew})^Y] \tag{3.7}$$

The variables λ, n, and m are fitting parameters known as the pore size/geometry index, while X and Y are known as Corey exponents for the wetting and non-wetting phase, respectively. S_{ew} is the effective wetting saturation, S_w is the wetting saturation, S_{wr} is the residual wetting saturation, $S_{w,max}$ is the maximum wetting saturation, S_{nr} is the residual non-wetting saturation, P_e is the capillary entry pressure, k_{rn}^0 is the end-point relative permeability to the non-wetting phase, and P_g is the strength coefficient expressed as the inverse of the pressure scaling parameter, α. Justifications for the wide utilisation of these geometry-based empirical models include the relative ease of their implementation in numerical simulators in the absence of site-specific P_c – k_r – S_w data, as well as the relative fit of experimentally determined P_c – k_r – S_w curves to the BC-vC model through λ, X and Y e.g. Bachu (2013), Krevor et al. (2012), and Perrin and Benson (2010). The use of BC-vC over vG-MC for this purpose is mainly due to the inclusion of the capillary entry pressure in the former. Nevertheless, the latter has been increasingly adopted in the numerical modelling of subsurface $scCO_2$ and brine transport within the last decade, e.g. Yamamoto and Doughty (2011), Doughty (2010), Zhou et al. (2010), Middleton et al. (2012), Birkholzer et al. (2015), Liu et al. (2011), Okwen et al. (2011), and Pruess and Nordbotten (2011). Most of these studies, however, utilised van Genuchten model within simplified parametric descriptions of the pore geometry index [n] and the strength coefficient [P_g] which may require revision. The first important consideration is the description of n (where $n = 1/1\text{-}m$) which usually includes a generic value of $n \approx 2.0$ for sandstone aquifer and even shale aquitard as seen in Birkholzer et al. (2009), Espinet et al. (2013), and Gor et al. (2013). This assumption may not be ideal practice in geological CO_2 sequestration (GCS) since the variability in the pore size index normally provides a reasonable fit to available experimental data (Doughty et al. 2008). Smith et al.'s (2017) data for clastic samples show a close relationship between mineralogy and pore size distribution within a sample. Hence, with reference to the relationship between mineralogy and particle size as described in Figure 3.1, this infers that the value for the pore geometry parameter should not be the same for all types of sedimentary rocks.

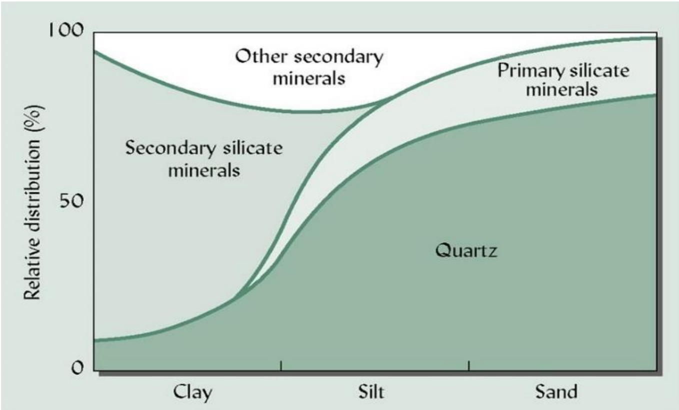

Figure 3.1: Relationship between particle size and mineralogy. [Adapted from Irons et al. (1989)]

In addition, the available experimental data for P_c and k_r in $scCO_2$/brine systems show variance in flow characteristics within clastic rocks that are located in the same reservoir formation. For example, Mercury Intrusion Porosimetry (MIP) analyses performed under the same experimental conditions on six sets of small plugs of the Heletz sandstone, obtained from well H18A of the Heletz project site at a depth of ~ 1634 m (Hingerl et al. 2016), showed variance in P_c curves despite having the same capillary entry pressure (see Figure 3.2).

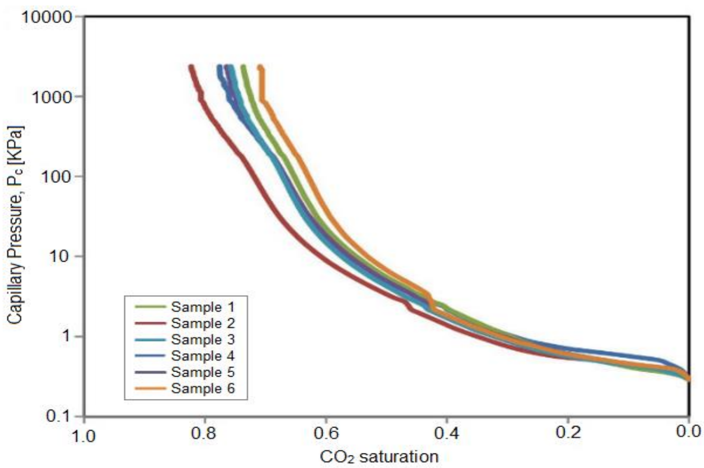

Figure 3.2: $P_c - S_w$ curve measured on six sub-samples of the Heletz sandstone using Mercury Intrusion Porosimetry. [Source: Benson et al. (2015)]

Bennion and Bachu (2008) also showed varying $k_r - S$ curves for rock samples obtained from the same formation, further highlighting the influence of the pore geometry on characteristic $P_c - k_r -$

S_w curves. Thus, the oversimplification and/or improper assumption of parameter values in empirical models used in characterising $P_c - k_r - S_w$ functions for simulating GCS can introduce errors in any subsequent predictive analysis (Mori et al. 2015). Secondly, the strength coefficient [P_g], where $P_g = 1/\alpha$, in vG-MC model has been referred to as the capillary entry pressure [P_e] in studies by Zhou et al. (2008) and Mathias et al. (2013). This is inconsistent with Van Genuchten's (1980) description of the pressure scaling parameter at the maximum pore throat radius [R_{max}] to be at least larger than the capillary entry pressure *i.e.* $\alpha P_e < 1$. According to the author, an inflection point on the capillary pressure curve is usually required to determine the value for the model's pressure scaling parameter [α]. Hence an assumption of $\alpha P_e = 1$ usually results in a wide variance between the BC's and vG's description of the flow model. Nevertheless, the introduction of capillary entry pressure is generally advisable when using the Mualem model (as is the case with vG-MC) irrespective of the parameter function used to describe the effective wetting saturation (Ippisch et al. 2006). The crucial point in applying Mualem's model is the correct evaluation of the integral:

$$\int_0^{S_{ew}} \frac{1}{P_c(S_w)} dS_w = -\int_{P_c(S_{ew})}^{\infty} \frac{1}{P_c(S_w)} \cdot \frac{dS}{dP_c} \cdot dP_c \tag{3.8}$$

If a capillary entry pressure value is not introduced in the parameterisation of the capillary pressure curve, then a decrease in the absolute value of the derivative of the capillary pressure curve $|\frac{dS}{dP_c}|$ must be faster than the increase of $\frac{1}{P_c}$ for $P_c \to 0$. These conditions are general and independent of the specific model used for capillary pressure curve. Thus, the absence of the capillary entry pressure in the vG model imposes a constraint of $n \geq 1.88$ when it is coupled to the Mualem model (Fuentes et al. 1992). However, fine-textured sediments may exhibit n-values in the range of $1 < n < 2$ (e.g. Carsel and Parrish 1988), therefore the introduction of a capillary entry pressure in the vG model is obligatory if $n < 2$ (Ippisch et al. 2006). It becomes advisable to introduce some sort of parameter equivalence between the van Genutchten and Brooks-Corey equations when describing the hydraulic properties of sedimentary formations using the vG model. This helps to quantify the capillary entry pressure during vG computations. Within accessible literature, no numerical study has been conducted to determine whether the constancy of the pore geometry parameter in a field introduces a bias in the predicted CO_2 storage performance. Besides, little information exists on the effect of using different values for *n* to represent different rock lithologies in a reservoir/seal system. To begin addressing these issues the current chapter applies linear parameter estimation techniques to fit vG's pore geometry parameter [*n*] in soil hydraulic behaviour to the rock hydraulic behaviour. This approach is implemented by comparing the different heterogeneous pore systems of sand/clay and their consolidated counterparts, sandstone/claystone, assuming the percentage composition of clastic sediments are approximal in both porous media. This should avoid discrepancies in the systematic behaviour of predicted relative permeabilities in soils and rocks. Of particular interest is information on improving the predicted values of relative permeability that do not require a large increase in experimental measurements. Rather than focus on all sedimentary rock types that are suitable for GCS, this thesis only highlights siliciclastic rocks, which have defined grain-size categories. Once estimated, the optimised model parameters will be used to investigate the relationships between sedimentary heterogeneities in siliciclastic rocks and CO_2 storage performance in aquifers. Since the $P_c - k_r - S_w$ relationship is expressed in the form of analytical functions, thus facilitating their efficient inclusion into numerical simulation models, they should enable a rapid comparison of the hydraulic properties of different siliciclastic rocks.

3.2 Assumptions and limitations of the study

The specific purpose of this chapter is to characterise the pore geometry index of vG-MC model to siliciclastic rock formations. This study adopts a classification of clastic rocks based on particle size and some sediment structures (Potter et al. 1980, Stow 1981). Herein, principles and methods used in soil mechanics are applied, utilising a limited set of predictors that focus mainly on the grain size distribution. The contribution of other effects such as the wettability of the porous medium, fluid viscosity and the interfacial tension between the fluids in contact is not considered in the parameterisation scheme. This is because the capillary number [N_c], a dimensionless number that characterises the ratio of viscous forces to interfacial tension, has been shown to only have impact on the shape of relative permeability curves at values of $N_c > 10^{-6}$ in two-phase systems (Bardon and Longeron 1980, Fulcher et al. 1985, Amaefule and Handy 1982).

$$N_c = \frac{v\mu}{\sigma} \tag{3.9}$$

where v is the Darcy velocity, μ is the viscosity of the displacing phase, and σ is the interfacial tension (IFT). For CO_2 sequestration, N_c is typically less than or approximately 10^{-6} making the flow regime capillary dominated (Krevor et al. 2012, Perrin and Benson 2010). Counter-intuitively, the higher the capillary number, the lower the effect of capillary pressure. Furthermore, Bennion and Bachu (2006) showed that at constant temperature and water salinity, the end-point relative permeability to CO_2 and the maximum endpoint CO_2 saturation increases as the IFT decreases. This trend was also seen to be identical for the effect of brine-to-CO_2 viscosity ratio on k_r curves, and is attributed to the strong dependency of both IFT and viscosity on pressure. IFT reduces by increasing pressure while CO_2 viscosity increases with increasing pressure, causing a relative decrease in brine-to-CO_2 viscosity ratio at fixed values for temperature and water salinity. Studies by Al-Khdheeawi et al. (2017) and Valle et al. (2018) have also shown that differences in reservoir wettability has varying impacts on CO_2 storage performance, with strongly water-wet reservoirs favouring residual trapping and strongly CO_2-wet reservoirs favouring dissolution trapping due to the bouyant migration of CO_2 plume and subsequently an increased contact with reservoir brine. Al-Mutairi et al. (2014) and Seyyedi et al. (2015) experimentally investigated the wettability alteration as a function of time during CO_2 flooding and concluded that increasing CO_2 concentration in brine could result in larger alteration of wettability. This can be attributed to the reduction in brine pH due to the dissolution of CO_2 in brine. The reduced pH may affect the electric charges on water–rock interfaces and, hence, alter the wetting characteristics of the surface. With respect to the wetting properties, the thesis assumes a completely wet system where the non-wetting phase invades the porous matrix at a contact angle of zero degree relative to the wetting phase. Finally, reactive transport properties and the impact of grid block resolution on the dynamic simulation is not considered herein. However, a fine scale (high resolution) grid, may, more readily emphasise the relative effect of capillary pressure and relative permeability heterogeneity on CO_2 storage performance. This is because coarse scaling (low resolution) usually result from the merging fine grid cells into a larger cell, thereupon averaging the reservoir properties within the coarse domain. This process of coarsening the fine grid is known as upgridding, while the averaging of reservoir properties within coarse cells is known as upscaling (Durlofsky 2005). NB: Detailed assumptions and limitations relating to the dynamic modelling and simulation in this thesis are indicated within respective chapters.

3.3 Description of pore geometry index [*n*] in vG model for clastic rocks

Volumetrically, siliciclastic rocks are the dominant sedimentary formations for GCS (Boggs 2009). To describe the pore geometry index in van Genuchten model for clastic rocks, it is important to first define such rocks. Clasts or rock fragments vary in size from fine clay and silt, to medium-textured sand, up to coarse-textured pebble, cobble and boulder sized clasts. Sand clasts are defined by the United States Department of Agriculture (USDA 1987) and the British Standards Institution (BSI 1990) as having a diameter of 0.06 to 2.00 mm. Silt clasts are 0.06 to 0.002 mm while clay is ≤0.002 mm. Using the Wentworth (1922) Scale, the terms 'very coarse sandstone', 'coarse sandstone', 'medium sandstone', 'fine sandstone', and 'very fine sandstone' are used (Table 3.1). However, some fine-grained sedimentary rocks are not precisely defined, while the classification of shale is more ambiguous (e.g. Picard 1971, Flemming 2000, Macquaker and Adams 2003, Potter et al. 2005). Shale has been regarded as mudrocks that show fissility, *i.e.* a strong tendency to split or break (Ingram 1953). Mudrocks exhibit a much wider grain size distribution than sandstones, with grain diameters typically ranging over five orders of magnitude, and include both silts and clays (e.g. Aplin et al. 1999, Dewhurst et al. 1998).

<table>
<tr><th>Geological size (mm)</th><th>Sediment Texture</th><th colspan="2">General term for Consolidated Rock</th></tr>
<tr><td>2.0 - 1.0</td><td>Very coarse sand</td><td colspan="2" rowspan="5">Sandstone</td></tr>
<tr><td>1.0 - 0.5</td><td>Coarse sand</td></tr>
<tr><td>0.5 - 0.25</td><td>Medium sand</td></tr>
<tr><td>0.25 - 0.125</td><td>Fine sand</td></tr>
<tr><td>0.125 - 0.0625</td><td>Very fine sand</td></tr>
<tr><td>0.0625 - 0.0313</td><td>Coarse silt</td><td rowspan="4">Siltstone</td><td rowspan="5">Mudrock (Shale)</td></tr>
<tr><td>0.0313 - 0.0156</td><td>Medium silt</td></tr>
<tr><td>0.0156 - 0.0078</td><td>Fine silt</td></tr>
<tr><td>0.0078 - 0.0039</td><td>Very fine silt</td></tr>
<tr><td>< 0.0039</td><td>Clay</td><td>Claystone</td></tr>
</table>

Table 3.1: The Wentworth scale for clastic sediments (Wentworth 1922)

Siliciclastic rocks can be classified using the soil textural triangle developed by the US Department of Agriculture (USDA 1987) and the recommended ternary diagram for naming clasts (Shepard 1954) as shown in Figure 3.3. This classification scheme can be further sub-divided into muddy sand and sandy mud (Figure 3.4) and is used to define siliciclastic rocks in Table 3.2.

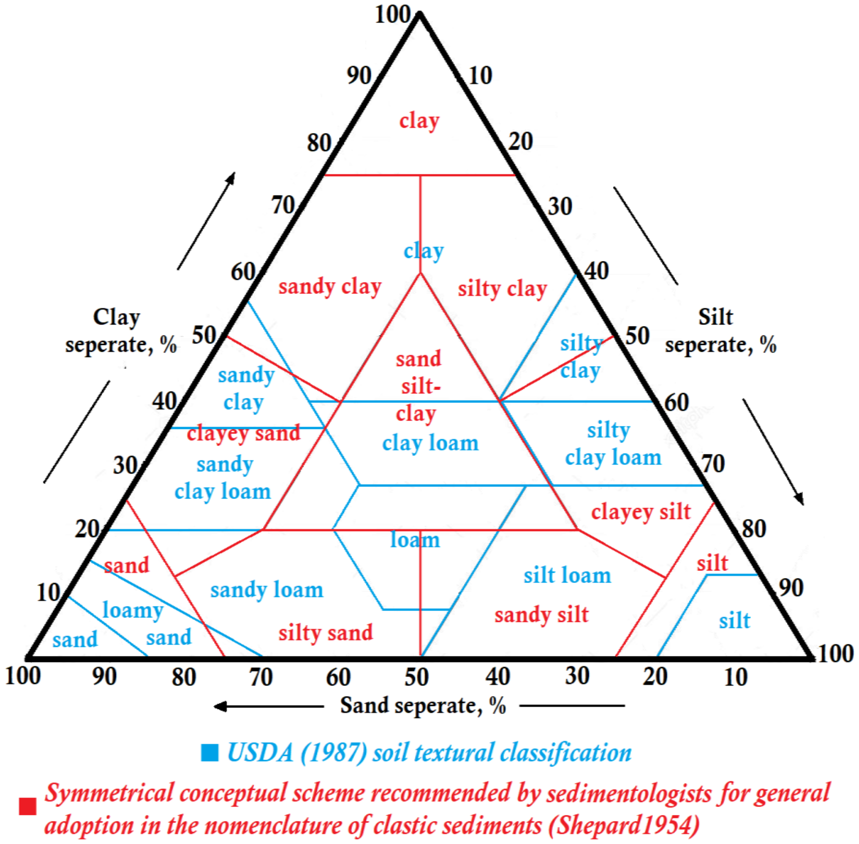

Figure 3.3: Correlation between USDA (1987) soil texture triangle and recommended conceptual scheme for the nomenclature of mixed clastic sediments. NB: See Appendix A, Figure A1 for seperate triangles.

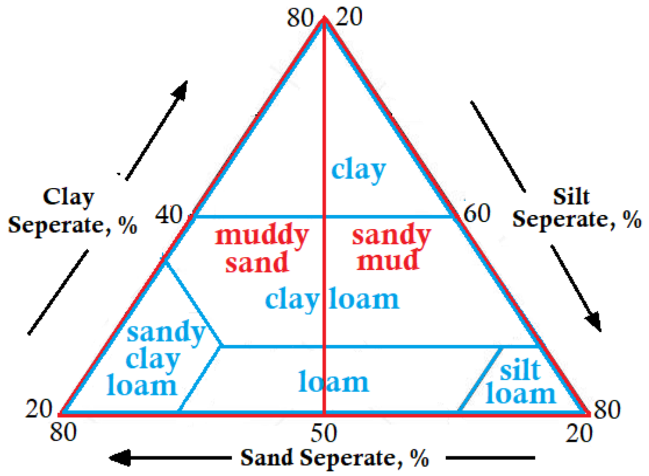

Figure 3.4: Sub-division of the sand silt-clay triangle in Figure 3.3

Recommended nomenclature for clastic sediments (from Shepard 1954)	***Equivalent textural classification (from USDA 1987)***	***Sedimentary composition (adopted from USDA 1987)***			***Proposed terminology for clastic rock in this study***	***General term for sedimentary rock in literature***
		%Sand	*%Silt*	*%Clay*		
Sand	Sand	≥ 85	Silt + 1.5Clay ≤ 15		Coarse-textured Sandstone	Sandstone
	Loamy Sand	70 - 85	Silt + 2Clay ≤ 30		Medium-textured Sandstone	
Silty Sand	Sandy Loam	≥ 50	Silt + 2Clay > 30	≤ 20	Fine-textured or Silty Sandstone	Sandstone
Clayey Sand	Sandy Clay Loam	≥ 45	< 28	20 - 35	Very Fine-textured or Clayey Sandstone	Sandstone
Sandy Silt	Silt Loam		≥ 50	< 27	Coarse-textured or Sandy Siltstone	Sandstone
Silt	Silt		≥ 80	< 12	Siltstone	Mudrock
Clayey Silt	Silty Clay Loam	< 20		27 ≤ Clay ≥ 40	Clayey Siltstone or Silty Mudstone	Mudrock
Muddy Sand*	Sandy Clay Loam + Loam + Clay Loam + Clay	≥ 50*	Clay + 2Silt ≥ 40*		Muddy Sandstone*	Sandstone
Sandy Mud*	Silt Loam + Loam + Clay Loam + Clay	20 – 45*	Clay + Silt ≥ 40*		Mudstone*	Mudrock
Sandy Clay	Sandy Clay	≥ 45		≥ 35	Sandy Claystone	Mudrock
Silty Clay	Silty Clay		≥ 40	≥ 40	Silty Claystone	Mudrock
Clay	Clay	< 45	< 40	≥ 40	Claystone	Mudrock
**Nomenclature and sedimentary composition suggested in this study*						

Table 3.2: Naming convention proposed for siliciclastic rocks

Carsel and Parrish (1988) estimated, through statistical analysis of a sample size between 46 and 1183, the spatial representation of van Genuchten's (1980) pore geometry parameter [*n*] in all twelve of USDA's soil textural classes. The application of this data provides a basis upon which associated pore geometry index for the siliclastic rocks defined in Table 3.2 are inferred in this study. Estimated vG *n*-values are extapolated for the siliciclastic rocks and shown in Table 3.3. This is a pragmatic approach based on the applicability of the vG model in both soil and rock mechanics. Fundamental to this approach, however, is the need to establish good approximations to empirical distributions for *n*-values in each siliciclastic rock shown in Table 3.3. In this regard, a senstivity analysis on *n*-values ranging from 1.01 to 3.00 is described in Section 3.5.

Siliciclastic rock	***Pore-geometry parameter, n (from Carsel and Parrish, 1988)***	***Textural classification adopted for siliclastic rocks in this study***
Coarse Sandstone	2.68	Very coarse
Sandstone	2.28	
Silty Sandstone	1.89	Coarse
Muddy Sandstone	1.56	
Clayey Sandstone	1.48	
Sandy Siltstone	1.41	Medium
Siltstone	1.37	
Mudstone	1.31	
Clayey Siltstone or Silty Mudstone	1.23	Fine
Sandy Claystone	1.23	
Silty Claystone	1.09	Very fine
Claystone	1.09	

Table 3.3: Descriptive n-values in Van Genuchten model for clastic rocks

3.4 Parameter equivalence between BC and vG models

In the vG P_c model (Eq. 3.2), the pressure scaling parameter [α], where $\alpha = 1/P_g$, the pore geometry index [*n*], the maximum wetting saturation [$S_{w,max}$], and the residual wetting saturation [S_{wr}] are independent parameters that can be estimated from experimental P_c – S_w *data*. It is convenient to express $S_{w,max} = 1$ and assume that S_{wr} (the water content where S_{ew} equals zero) is a well-defined parameter in geological CO_2 sequestration within water-wet systems. Theoretical descriptions of α in literature are usually through a parameter equivalence between BC and vG, which describes an empirical relationship between the capillary entry pressure [P_e] in BC models and the pressure-scaling parameter, α, in vG models. van Genutchen (1980) suggested that for large capillary pressure values, which will be the case in fine-textured sediments, the classical vG model reduces to the BC model where $\lambda = mn$. In an attempt to account for all sediment textures, *i.e.* from coarse to fine grained, Ippisch et al. (2006) modified the van Genutchen model to directly incorporate a capillary entry pressure value by introducing a parameter, S_c (where S_c, the saturation at cut-off point, = $[1 + (\alpha Pe)^n]^{-m}$]) but this term is restricted to fluid models where $\alpha P_e \gg 1$. Vogel and Cislerova's (1988) proposal for deriving a van Genuchten model including a capillary entry pressure introduced an arbitrary parameter, S_m (where $S_m \geq S_{w,max}$). However, this arbitrary parameter makes the author's theorem unsuitable in describing completely water wet systems and should only be considered as an additional fitting parameter that may enable a more precise description of k_r and P_c functions near saturation, especially for $n < 2$ (Vogel et al. 2000). Li et al. (2013) described a vG-type P_c model (Eq. 3.10) with the inclusion of a "threshold" non-wetting phase saturation [S_{nth}] which defines the width of the entry slope region in the vG model (Figure 2.4):

$$P_c = P_e\left(\frac{S_w - S_{wr}}{1 - S_{wr}}\right)^{-\frac{1}{\lambda}} \qquad \text{if } S_{wr} \le S_w \le 1 - S_{nth} \tag{3.10a}$$

$$P_c = \frac{P_e}{S_{nth}}\left(\frac{1 - S_{nth} - S_{wr}}{1 - S_{wr}}\right)^{-\frac{1}{\lambda}}(1 - S_w) \qquad \text{if } 1 - S_{nth} < S_w \le 1 \tag{3.10b}$$

However, Eq. 3.10 does not reflect the original van Genuchten model and is theoretically a replica of the BC model where an exception is made for the capillary pressure at a wetting saturation of unity to be equivalent to zero *i.e.* $P_{c(Swr=1)} = 0$. Morel-Seytoux et al. (1996) suggested a parameter equivalence between Brooks-Corey and van Genuchten by introducing the following mathematical expressions for coupled Mualem formulations:

$$P_e = \left(\frac{1}{\alpha}\right)\frac{(p+3)}{2p(p-1)}\left(\frac{147 + 8.1p + 0.092p^2}{55.6 + 7.4p + p^2}\right) \qquad \text{where } p = 1 + (2/m). \tag{3.11}$$

Its applicability, however, is limited as it is based on a fully defined value for the pressure scaling parameter, α, and fails to identify a relationship between the pore size index of Brooks-Corey model, λ, and van Genuchten model, n. Lenhard et al. (1989) identified this relationship in the authors' mathematical expressions for parameter equivalence between Brooks-Corey and van Genuchten for $P_c > P_e$:

$$\lambda = \frac{m}{1-m}\left(1 - Z^{\frac{1}{m}}\right) \tag{3.12}$$

where Z represents the match-point effective wetting saturation, *i.e.* midway between the saturated wetting fluid saturation and irreducible saturation, and equals 0.5. In this study, Eq. 3.12 agrees with van Genuchten's (1980) summation that λ is equivalent to the product of m and n for fine-textured sediments. This is seen in Table 3.3 for λ-values of silty mudstone, sandy claystone, silty claystone and claystone correct to one decimal place. Therefore, the parameter equivalence for BC and vG employed herein is described by:

$$\alpha = \frac{(S_{ew})^{\frac{1}{\lambda}}}{P_e} \cdot \left[(S_{ew})^{-1/m} - 1\right]^{1-m} \tag{3.13}$$

where λ is computed from Eq. 3.12.

3.5 Pore Geometry Index, *n*, sensitivity study for CO_2 geo-sequestration

A sensitivity analysis is presented here to distinguish between values for n (*i.e.* n-values) that have the same significance on *in situ* CO_2 plume shape and overall assessment of CO_2 geo-storage. Using the vG-MC model, hysteretic $P_c - k_r - S_w$ curves are computed for n-values ranging from 1.01 to 3.00, with an increment of 0.01, to account for each value of n in Table 3.3. The approach taken in this study requires realistic characterisation of parameter uncertainty, therefore, the residual wetting saturation [S_{wr}] is held constant for all values of n. This indicates a constant relative permeability to the non-wetting phase [k_{rCO2}] in the sensitivity study thus accounting for the role of the pore geometry index in CO_2 storage performance. To make the sensitivity analysis computationally tractable, the system model assumes a 200m-thick isotropic saline aquifer with axisymmetric geometry of 1km in radial length and an incompressible siliciclastic rock with homogeneous rock properties. The reservoir is initially fully saturated with brine and no-flow conditions are assumed on the lateral and vertical boundaries of the domain. A black oil simulator, ECLIPSE 100 (E100), is used to simulate injection of supercritical CO_2 ($scCO_2$) through a single injection well into the reservoir under isothermal conditions. The well is situated at the leftmost boundary (r = 0), perforated across the bottom half of the permeable reservoir, and $scCO_2$ is injected for 10 years at a constant rate of 0.3 Mt/year. The radius of the domain and injection rate of CO_2 are chosen so that the gas saturation front is far from the boundary and there is negligible effect of these parameters on the motion of saturation front during the injection period. Irreducible CO_2 saturation for drainage and imbibition are assumed to be 0 and 0.412, respectively. Other parameters used in the simulation are summarised in Table 3.4.

Parameter	***Value***
Well radius	0.5 m
Injection rate	0.3 Mt/yr
Injection duration	10 years
Porosity	0.14
Permeability	50 mD
Rock compressibility	4.5×10^{-10} Pa^{-1}
Initial pressure	10 MPa
Temperature	33°C
Brine salinity	300,000 ppm
Capillary entry pressure	1.622×10^{-3} MPa
Contact angle	0°
Interfacial tension	30 mN/m
Maximum brine saturation	1.0
Residual brine saturation	0.3
End-point relative permeability to brine	1.0
End-point relative permeability to CO_2	0.623

Table 3.4: Parameters used for the E100 simulations

In accounting for both parameter uncertainty and the role of the parameter, n, in the model, n-values are ranked based on four criteria described in Section 3.5.1. These are:

i) the shape of the plume,
ii) the maximum radial extension of the plume at the base of the reservoir model,
iii) the mobile gas fraction, and
iv) the percentage volume of residual CO_2 saturation, at the end of $scCO_2$ injection.

3.5.1 Parameter sensitivity analysis

A MATLAB code is defined and coupled to ECLIPSE for computing the P_c – k_r – S_w relations, using the vG model (see Appendix A, Algorithm A1). The code generates 200 realisations for reservoir simulation using the pore geometry spectrum n=1.10:0.01:3.00 (i.e. *n* varies from 1.10 to 3.00 with incremental intervals of 0.01). Numerical simulations of CO_2 injection for $1.01 \leq n \leq 1.09$ were truncated due to the extremely steep $P_c - S_w$ curve for these *n*-values, thus hindering CO_2 injection in the domain. Nevertheless, CO_2 injection was initiated for all other *n*-values and simulation results of injected CO_2 with time showed a linear and constant relationship for all *n*-values. This culminated in a total injected CO_2 of 3Mt in each sensitivity case for $1.10 \leq n \leq 3.00$ at the end of simulation. This was expected since the total injected CO_2 is highly sensitive to the end-point relative permeability to CO_2 (Yoshida et al. 2016), which was held constant for all *n*-values in the study. Table 3.5 and Figure 3.5 illustrate the sensitivity to *n*-values according to criteria III and IV, respectively.

Average field gas saturation range	***Pore geometry index, n***	***Siliciclastic rock***
0.02664 – 0.02655	3.00 – 2.37	Coarse sandstone
0.02654 – 0.02645	2.36 – 1.93	Sandstone
0.02644 – 0.02635	1.92 – 1.70	Silty Sandstone
0.02634 – 0.02625	1.69 – 1.56	Muddy Sandstone
0.02624 – 0.02615	1.55 – 1.45	Clayey Sandstone
0.02614 – 0.02605	1.44 – 1.38	Sandy Siltstone
0.02604 – 0.02595	1.37 – 1.32	Siltstone
0.02594 – 0.02585	1.31 – 1.28	Mudstone
0.02584 – 0.02575	1.27 – 1.24	Silty Mudstone
0.02574 – 0.02565	1.23 – 1.21	Sandy Claystone
0.02564 – 0.02555	1.20 – 1.19	Silty Claystone
0.02554 – 0.02500	1.18 – 1.10	Claystone

Table 3.5: Characterisation of the range of values for average gas stauration to the PGI range

It is evident from Figure 3.5 and Table 3.5 that the ranking of the pore geometry index is consistent with descriptive values in Table 3.3. Values in Figure 3.5 are characterised via a 0.3 percentage increase for very coarse-, coarse- and medium-textured siliciclastic rocks, and a 1- and 2-percentage increase for fine and very-fine textured siliciclastic rocks, respectively (see Table 3.3). This is based on inductive inference from failed simulation runs, for *n*-values between 1.01 and 1.09, which suggests a steepening curve in the alignment of values for *n* situated at the lower end of the spectrum, ***n=1.10:0.01:3.00***, for computed residual CO_2 saturation in Figure 3.5. Table 3.5, showing the average range with an increment value of 6×10^{-5} for mobile CO_2 saturation in the domain, supports this approach and validates the distribution of *n*-values obtained from Carsel and Parrish (1988) for various siliciclastic rocks identified in Table 3.3. Figure 3.6 depicts the effective saturation distribution for representative examples from the range for *n*-values identified in Table 3.5. A similarity in the shape of CO_2 plume at the end of injection is observed for pairs of *n* that correspond to the same siliciclastic rock. Red ticks at the domains' horizontal boundaries in Figure 3.6 illustrate plume edges at these boundaries for the defined *n*-value. The change in the shape of the CO_2 plume is attributed to the correlated structure of the rock matrix, which is described by the pore geometry parameter [*n*]. Smaller values for *n* increases the capillary resistance to buoyant migration of CO_2 plume, resulting in the preferentially lateral migration in the bottom of the modelled domain for lower n-values (Figure 3.6). Through the same capillary resistance, the rate of snap-off of CO_2 ganglia at the trailing end of the plume, i.e. the residual trapping of CO_2, also increases, resulting in the lower degree of mobile gas saturation within the domain.

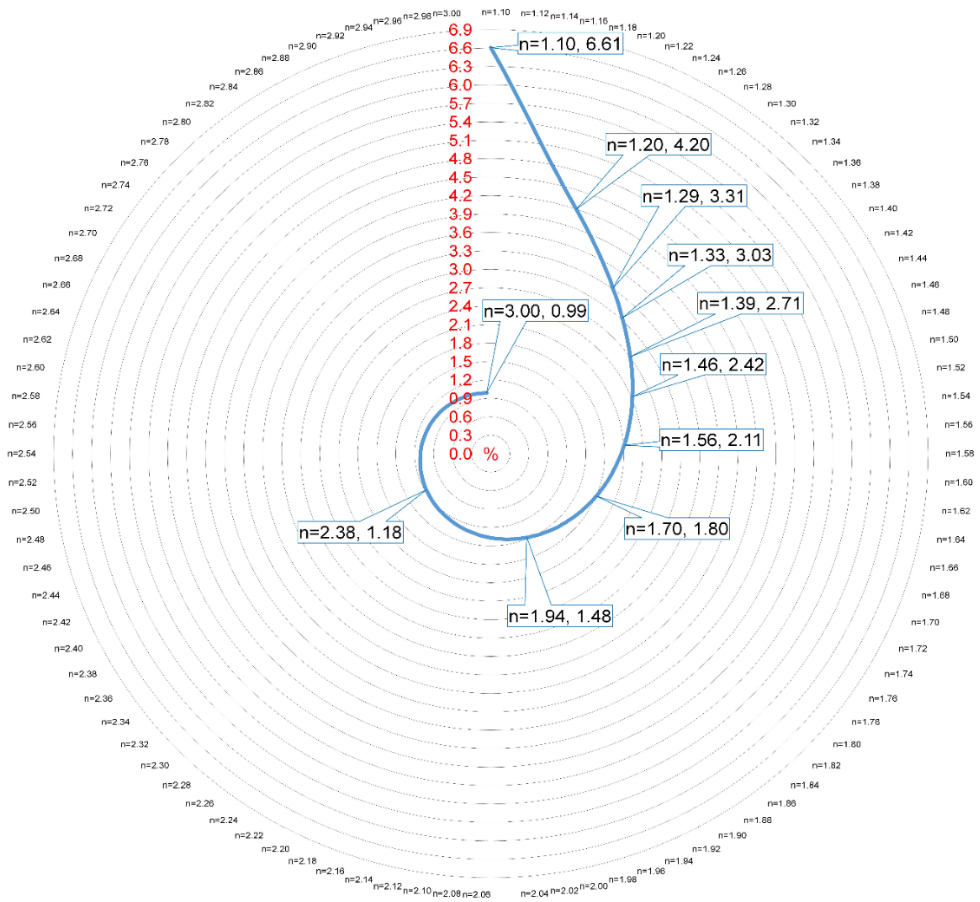

Figure 3.5: Percentage volume of residual CO_2 at the end of simulation. NB: Data outcalls show the value for n and corresponding percentage of residual CO_2 saturation while the n-values outside the ring indicate the range of values analysed.

Radial distance along bottom boundary (m)	***Highest n-value showing CO_2 saturation***
50	3.00
75	2.33
100	1.98
150	1.67
200	1.53
250	1.43
300	1.35
350	1.28
400	1.22
450	1.16
500	1.12

Table 3.6: Correlation of CO_2 plume edge along the the base of the modelled domain for n-values

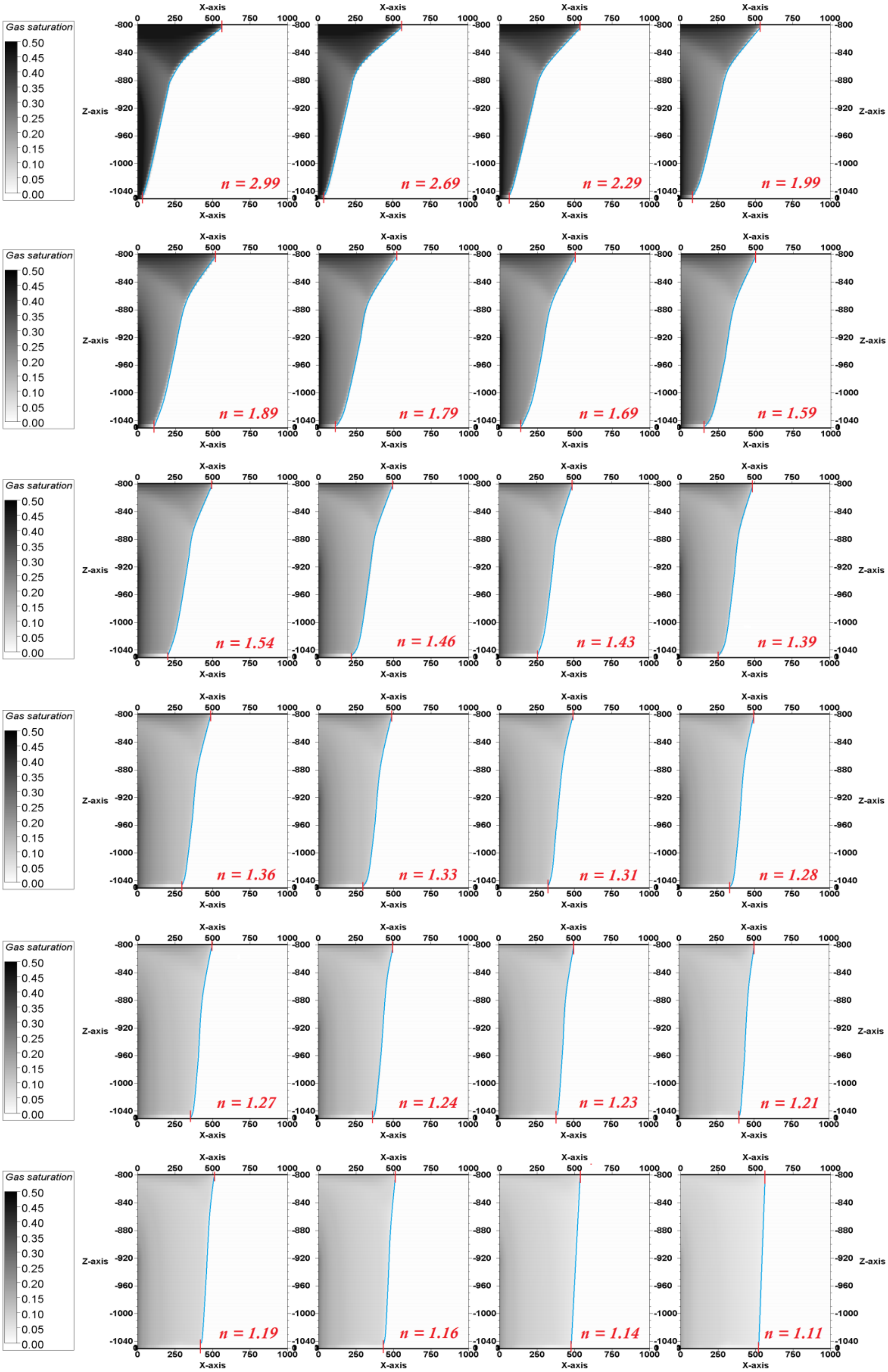

Figure 3.6: The shape of CO_2 plume for representative examples of n at the end of simulation

An assessment of plume tip sensitivity was achieved through quantifying the total gas saturation at the end of CO_2 injection, for each *n*-value, in grid blocks at designated intervals on the bottom horizontal boundary (Table 3.6). The evaluation was implemented for only the bottom boundary due to larger variation in lateral plume migration at the base of the domain as observed in Figure 3.6. To check the viability of *n*-values ranging from 1.01 to 1.09 in the description of hydraulic properties, a sensitivity study was conduction for this range at a constant $P_c - S_w$ curve. Other reservoir parameters described in Section 3.5 remain applicable within varying $k_r - S_w$ relations based on the *n*-spectrum, **1.01:0.01:1.10**. Results show that CO_2 plume shapes correspond to n = 1.11 in Figure 3.6, and the lateral migration of plume goes beyond the radial distance of 500 m in the domain at the end of a 10-year CO_2 injection period (Figure 3.7). It can be seen that the data in Table 3.6 are similar to the range of *n*-values for different siliciclastic rocks presented in Figure 3.5 and Table 3.5. This, in combination with Figure 3.7, validates the representative *n*-values adopted for this study (see Table 3.3).

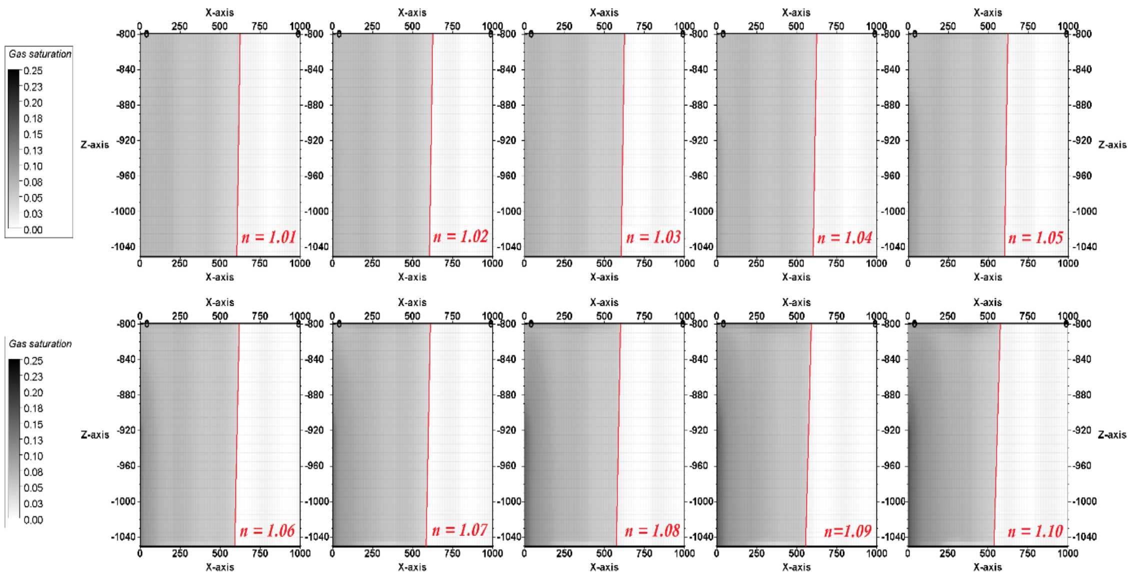

Figure 3.7: CO_2 plume shape at the end of simulation on the validity of n-values between 1.01 – 1.09 for describing hydraulic properties of siliclastic rocks

3.6 Characterising empirical functions in vG-MC for CO_2 storage

The aquifer model used in this section is a three-dimensional (3D) isothermal and homogeneous domain (Figure 3.8) discretised into 80 x 80 x 72 cells (460, 800 grid cells in total) and has dimensions of 2000 m x 2000 m x 220 m, which is comprised of a 10 m- and 210 m-thick caprock and reservoir formation, respectively. CO_2 injection was simulated using one vertical well centrally located in the model and perforated across layers 56 to 70 (approximately 60 m). The injector was set to operate at a target flow rate of 149,500 sm^3/day subject to a maximum bottom-hole pressure (BHP) of 23.62 MPa. This was specified to ensure that the hydrostatic pressure gradient in the model does not exceed the fracture pressure gradient, which was assumed to be 75% of the lithostatic pressure gradient. This and other petrophysical properties assumed for the flow simulation model are described in Table 3.7.

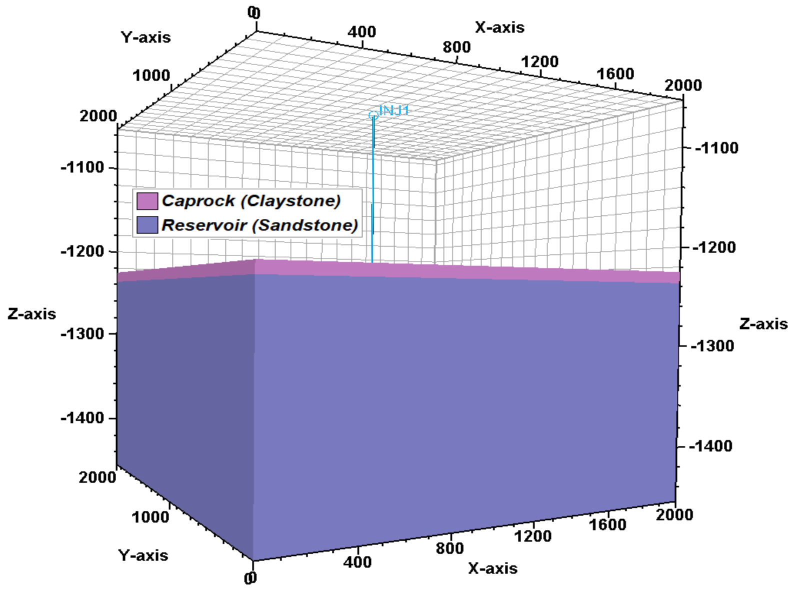

Figure 3.8: Illustration of the 3D matrix aquifer model showing the caprock and reservoir formation.

Parameter	***Value in Caprock***	***Value in Reservoir***
Porosity	0.04	0.14
Permeability (mD)	6.30×10^{-3}	150
Capillary entry pressure (KPa)	172	1.622
Residual brine saturation	0.61	0.3
End-point relative permeability to CO_2	0.121	0.623
Maximum brine saturation	1.0	
End-point relative permeability to brine	1.0	
Temperature (°C)	33	
Brine salinity (ppm)	300,000	
Hydrostatic pressure gradient (KPa/m)	12.15	
Fracture pressure gradient (KPa/m)	16.97	

Table 3.7: Petrophysical properties used for the E300 simulations

Simulations were carried out using the compositional module of ECLIPSE (E300). This section addresses the relative impact of the pore geometry parameter [n], the residual wetting saturation [S_{wr}], the maximum non-wetting residual saturation [S_{nrmax}], and the description of P_c-curve on CO_2 storage in a homogeneous saline aquifer.

3.6.1 Descriptions of P_c-curve: vG (for Pg ≠ Pe & Pg = Pe) vs BC

This section analyses the relative impact of the parametric description of capillary entry pressure in the vG model on flow simulation in a $scCO_2$/brine system. Here, Brooks-Corey description for capillary pressure is identified as the benchmark empirical model, idenitifed as *BC*, while two variations of vG's $P_c - S_w$ model are based on the following descriptions:

i) the strength coefficient [P_g] is equivalent to the capillary entry pressure [P_e]. Here the model is identified as *vG (Pg = Pe)*;

ii) the strength coefficient is <u>not</u> equal to the capillary entry pressure but a derivative of the parameter equivalence between BC and vG shown in Eq. 3.13. Here the model is identified as *vG (Pg ≠ Pe)*.

Description of the relative permeability functions are based on the Mualem-Corey model (Eq. 3.3 & 3.4) coupled to all three $P_c - S_w$ models identified herein. These capillary pressure curves are illustrated in Figure 3.9.

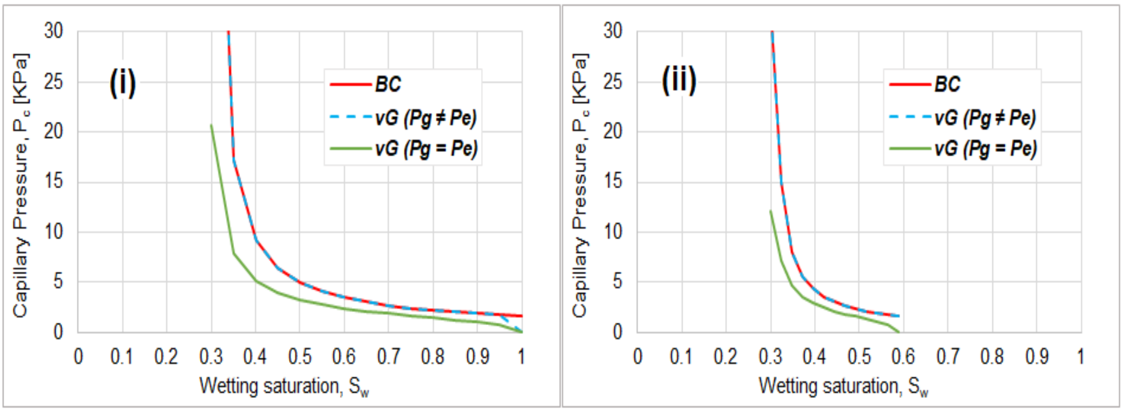

Figure 3.9: Brooks-Corey (BC) and van Genuchten (vG) capillary pressure curves for (i) drainage and (ii) imbibition in the sandstone reservoir

During flow simulation, CO_2 injection rate is seen to be constant across all three cases until the seventh year of injection when it reaches the formation's limiting pressure and reduces drastically for each case. The reduction rate varies across the cases, with *BC* showing the highest and *vG (Pg = Pe)* the lowest, thus influencing the cumulative CO_2 injected in each case (Figure 3.10).

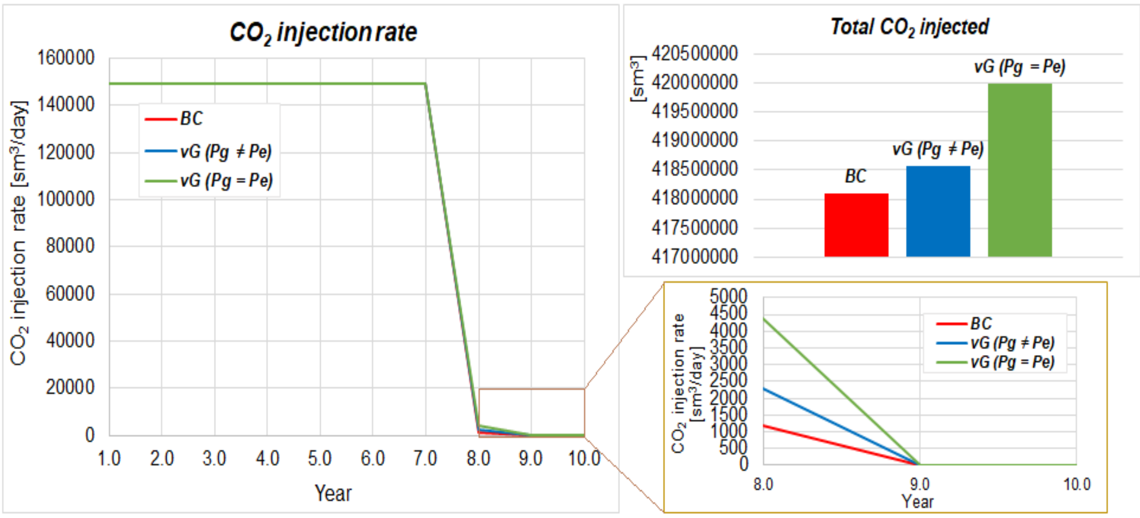

Figure 3.10: Illustration of CO_2 injection rate and total CO_2 injection during flow simulation.

The trend is attributed to the entry and exit point of the P_c drainage plot (Figure 3.9i), where exit points for *BC* and *vG (Pg ≠ Pe)* are similar and greater than the exit point for *vG (Pg = Pe)*. This translates to higher resistance to drainage flow for the former over the latter. Hence the constrast in CO_2 injection rate post-decline between *BC* and *vG (Pg ≠ Pe)* can be ascribed to their varying entry points on the P_c-curve. Although the *vG (Pg ≠ Pe)* and *BC* models are not entirely identical in terms of simulating the total CO_2 injected, the *vG (Pg ≠ Pe)* model exhibits a closer match to the *BC* model with an increase of 0.12% compared to 0.5% in the *vG (Pg = Pe)* model. In the seventh year of CO_2 injection, where the cumulative gas injected is the same for all cases, the degree of primary trapping mechanisms also shows a close similarity between the *BC* and the *vG (Pg ≠ Pe)* model (Figure 3.11). The percentage of structurally trapped CO_2 (*i.e*. mobile CO_2) is slightly higher for the *BC* model than the *vG (Pg ≠ Pe)* model because of the entry point on the P_c-curve that is higher for the former (Figure 3.9i). This impedes the bouyant migration of CO_2 plume in the *BC* model more than in the *vG (Pg ≠ Pe)* model (Figure 3.11b). However, for residual trapping, the identical P_c imbibition curves for the *vG (Pg ≠ Pe)* and *BC* models correspond to the equivalent percentage of residually trapped CO_2 in the seventh year of gas injection. The lower entry and exit points on the P_c imbibition curve for the *vG (Pg = Pe)* model results in additional capillary trapping of CO_2 (Figure 3.11c) because more water readily imbibes into the pore matrix at lower capillary pressures. Figure 3.11 indicates that the *BC* and *vG (Pg ≠ Pe)* models show an equal amount of residually trapped CO_2, which vary from the *vG (Pg = Pe)* model by approximately 2% of the total injected volume by the seventh year. This demonstrates a greater percentage error in CO_2 injection rate when the capillary entry pressure in vG is assumed to be the strength coefficient.

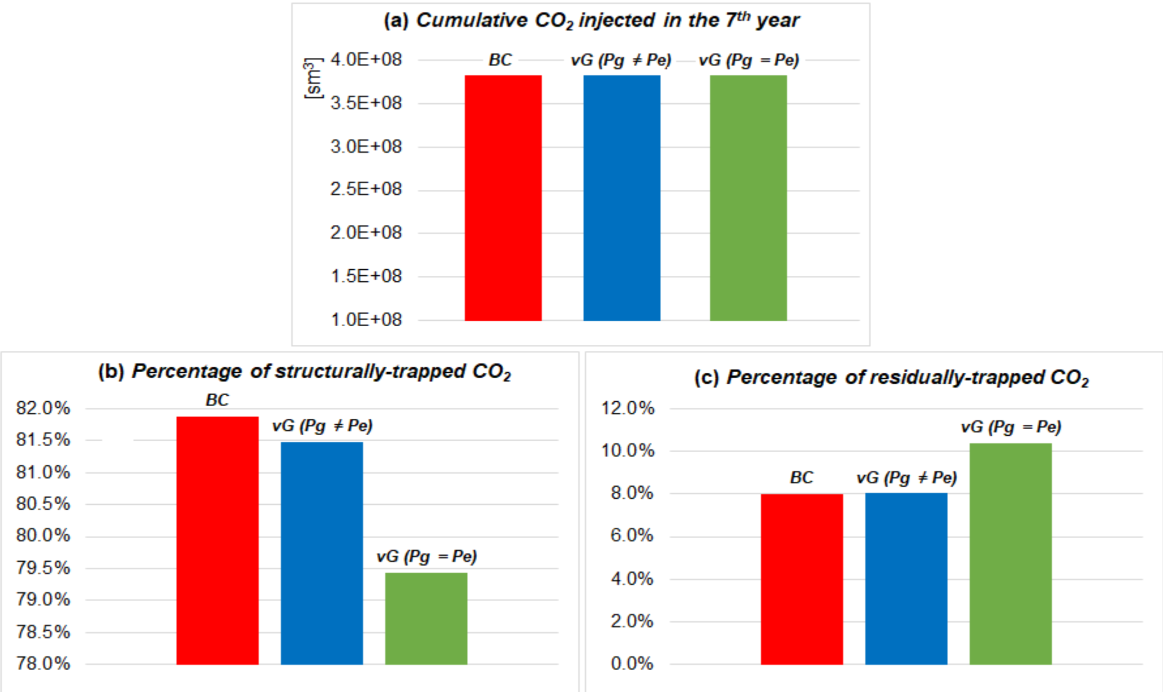

Figure 3.11: Illustration of (a) the total volume of CO_2 sequestered in the 7th year of CO_2 injection by (b) structural, and (c) capillary trapping mechanisms.

3.6.2 CO_2 storage performance: *n* vs S_{wr} vs S_{nrmax}

This section highlights the relative importance of the pore geometry parameter [*n*], the residual wetting saturation [S_{wr}], and the maximum non-wetting residual saturation [S_{nrmax}], during the predictive analysis of CO_2 sequestration. The study is initialised with the vG-MC model where *vG*

(Pg ≠ Pe) is identified as the base case, CASE0. Different variations of relative permeability and capillary pressure based on assumed values for n, S_{wr}, and S_{nrmax} (as identified in Table 3.8) are computed using the vG-MC model and defined as CASE 1, 2, 3, X, Y & Z. In order to curb the mitigating effect of relative permeability on CO_2 injectivity, these k_r and P_c functions were imputed in the top-half of the reservoir formation, high above the well perforations, while the bottom-half of the reservoir had a constant k_r and P_c functions for all cases. Table 3.8 and Figure 3.12 describe the design of the sensitivity study in this regard, where S_{wr} and S_{nrmax} values vary from 0.3 to 0.6, while n values vary from 1.56 to 2.67.

<table>
<tr><th>CASE ID (n-value)</th><th colspan="3">SUB-CASE
(Description)</th></tr>
<tr><td>CASE 0 (n=2.67)</td><td colspan="3">(S_{wr} = 0.30; S_{nrmax} = 0.30)</td></tr>
<tr><td>CASE 1 (n=2.28)</td><td rowspan="3">A
($P_c – k_r – S_w$ curves computed with representative n-value; S_{wr} = 0.30; S_{nrmax} = 0.30)</td><td rowspan="3">B
($k_r – S_w$ curve computed with representative n-value; $P_c – S_w$ curve the same as BASE’s; S_{wr} = 0.30; S_{nrmax} = 0.30)</td><td rowspan="3">C
($P_c – S_w$ curve computed with representative n-value; $k_r – S_w$ curve the same as BASE’s; S_{wr} = 0.30; S_{nrmax} = 0.30)</td></tr>
<tr><td>CASE 2 (n=1.89)</td></tr>
<tr><td>CASE 3 (n=1.56)</td></tr>
<tr><td>CASE X (n=2.67; Vary S_{wr} & S_{nrmax})</td><td>1
(S_{wr} = 0.35, S_{nrmax} = 0.35)</td><td>2
(S_{wr} = 0.40, S_{nrmax} = 0.40)</td><td>3
(S_{wr} = 0.45, S_{nrmax} = 0.45)</td></tr>
<tr><td>CASE Y (n=2.67; Constant S_{wr})</td><td>1
(S_{wr} = 0.30, S_{nrmax} = 0.40)</td><td>2
(S_{wr} = 0.30, S_{nrmax} = 0.50)</td><td>3
(S_{wr} = 0.30, S_{nrmax} = 0.60)</td></tr>
<tr><td>CASE Z (n=2.67; Constant S_{nrmax})</td><td>1
(S_{wr} = 0.40, S_{nrmax} = 0.30)</td><td>2
(S_{wr} = 0.50, S_{nrmax} = 0.30)</td><td>3
(S_{wr} = 0.60, S_{nrmax} = 0.30)</td></tr>
</table>

Table 3.8: Sensitivity study design for addressing the relative impact of n, S_{wr}, and S_{nrmax} in CO_2 storage performance

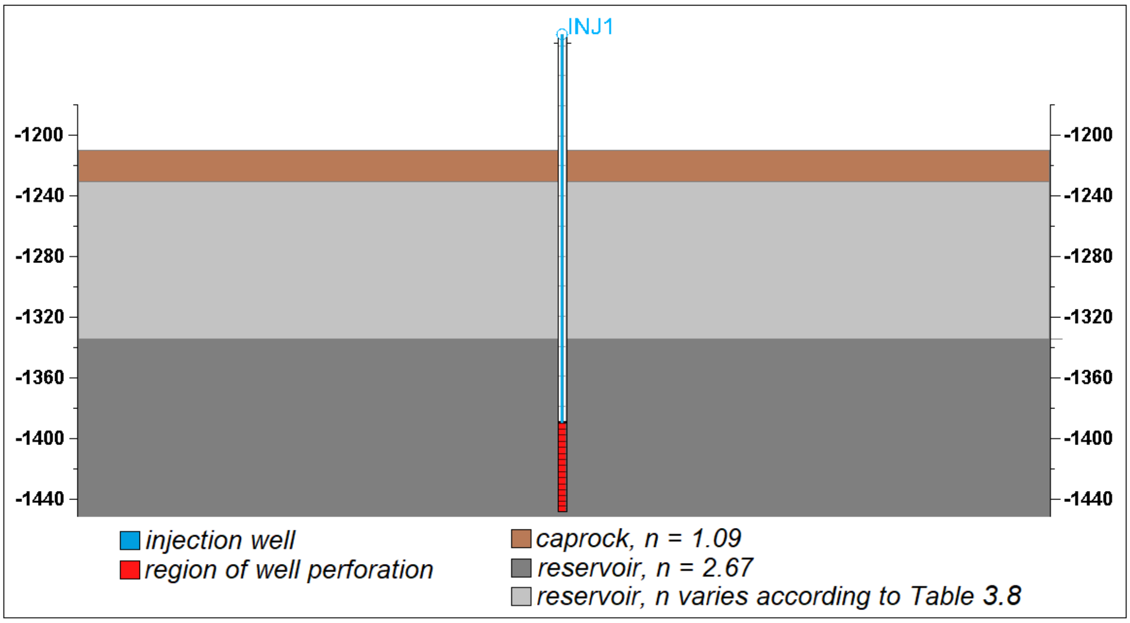

Figure 3.12: Description of segments in the reservoir for variations according to Table 3.8.

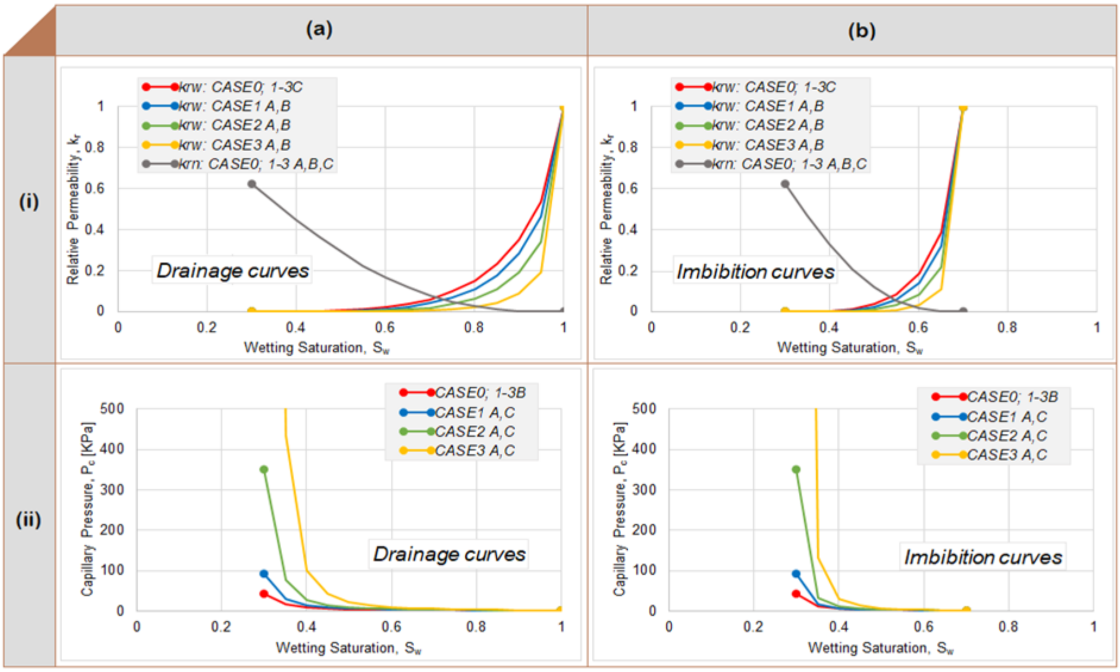

Figure 3.13: $P_c - k_r - S_w$ curves for (a) drainage and (b) imbibition in all descriptions of CASEs 0, 1, 2, & 3

Figure 3.13 shows the $P_c - k_r - S_w$ relationship computed for CASE 0, 1, 2 & 3. According to Eqs. 3.2 – 3.4, computing the non-wetting relative permeability using the vG-MC model is insensitive to the pore geometry parameter. Hence, a single representative curve for relative permeability to the non-wetting CO_2 [k_{rCO2}] exists for all cases in Figure 3.13. Nevertheless, *n* has a considerable effect on the relative permeability to the wetting phase and the capillary pressure. Conversely, S_{wr} and S_{nrmax} are seen to be significant in both functions of the relative permeability, *i.e.* k_{rw} and k_{rn}, where S_{wr} mainly influences the drainage curve, and S_{nrmax} influences the imbibition curve (Figure 3.14). Figure 3.15 – 3.20 illustrate the degree of mobile and immobile CO_2 saturation at the end of a 10-year flow simulation, quantified as structurally trapped and residually trapped CO_2 respectively.

3.6.2.1 Analysis of S_{wr}

The impact of variation in values of the residual wetting saturation [S_{wr}] are described by CASE Z and illustrated in Figure 3.15. Here the quantity of structurally trapped CO_2 at the end of simulation is highest in the base case (CASE 0) and progressively decreases in CASE Z from 1 to 3 (Figure 15a). The reverse is the case for the residual trapping of the CO_2 plume in Figure 15b, where the rate of CO_2 immobilisation in the rock matrix is seen to be directly proportional to S_{wr}. The higher the S_{wr}, the lower the measure of continuously mobile saturation of CO_2 that is available to be structurally trapped by flow barriers in the reservoir model. This is because increasing the S_{wr} increases the wettability of the rock matrix, *i.e.* its affinity to the wetting fluid. This feature is portrayed in the $k_r - S_w$ drainage curves where the intercept of both functions shift to the higher end of the wetting saturation as S_{wr} increases (Figure 14a-iii). Consequently, the displacement efficiency of the wetting phase by the invading CO_2 diminishes.

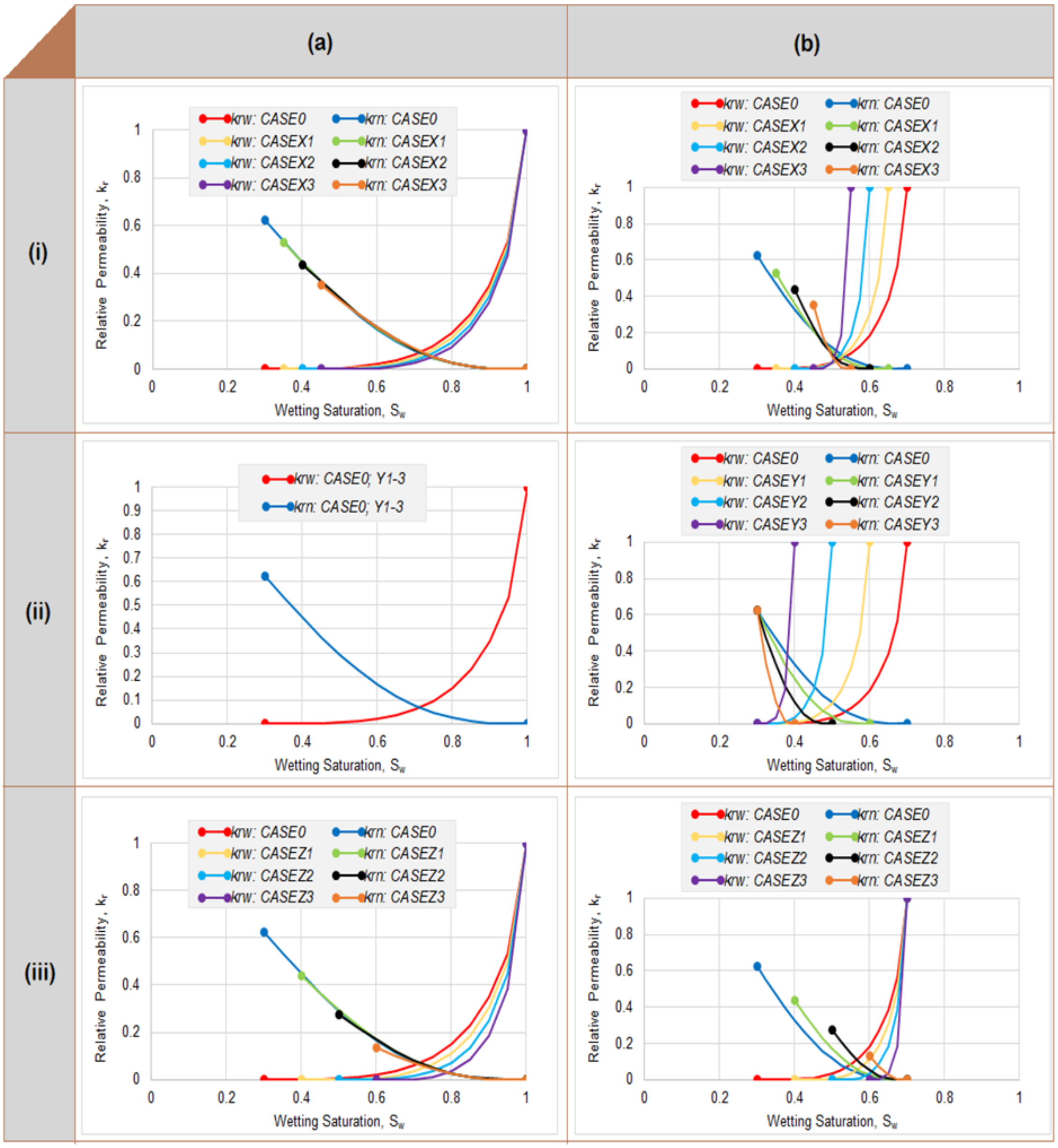

Figure 3.14: k_r – S_w curves for (a) drainage and (b) imbibition in all descriptions of CASE 0 vs i) CASE X, ii) CASE Y, and iii) CASE Z.

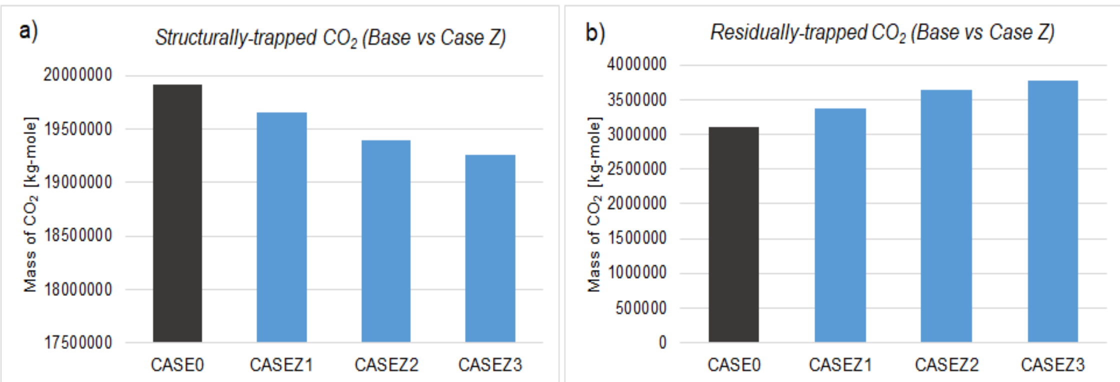

Figure 3.15: Quantity of CO_2 sequestered by (a) structural, and (b) residual trapping mechanisms at the end of gas injection for the base case and all descriptions of CASE Z.

3.6.2.2 *Analysis of S_{nrmax}*

The impact of variation in values of the maximum residual non-wetting saturation [S_{nrmax}] are described by CASE Y and illustrated in Figure 3.16. Here the quantity of structurally trapped CO_2 decreases as S_{nrmax} increases. This is mainly attributed to the capillary trapping efficiency, defined by the imbibition curves in Figure 3.14b-ii, which increases with increasing S_{nrmax} thereby inducing the immobilisation of more CO_2 particles. This invariably results in the higher quantity of mobile CO_2 for the smallest value of S_{nrmax}, *i.e.* CASE 0 (Figure 3.16a), irrespective of the single k_r – S_w drainage curve defined for CASE 0, Y1, Y2 & Y3 (Figure 3.14a-ii).

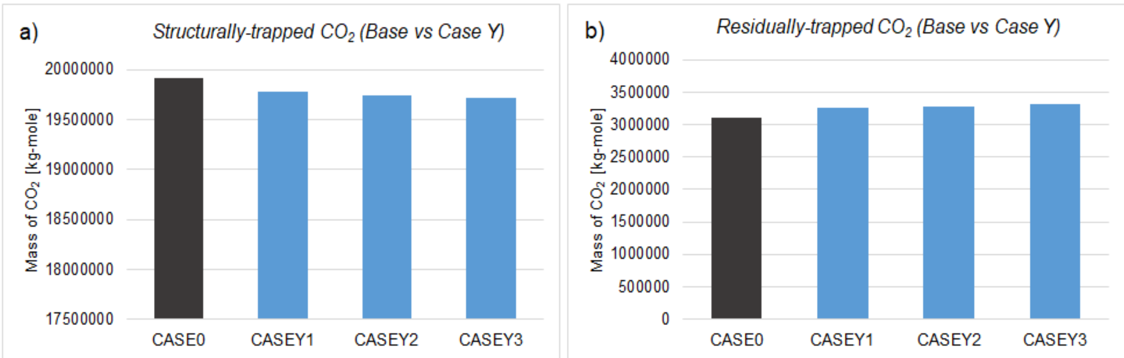

Figure 3.16: Quantity of CO_2 sequestered by (a) structural, and (b) residual trapping mechanisms at the end of gas injection for the base case and all descriptions of CASE Y.

When both values of S_{wr} and S_{nrmax} are increased simultaneously, as portrayed by CASE X in Table 3.8, the progressive decrease in the quantity of CO_2 structural trapped (see Figure 3.17a) is accredited to the increasing S_{wr}, while the increase in the residual trapping of CO_2 (see Figure 3.17b) is mainly a function of the increasing S_{nrmax}.

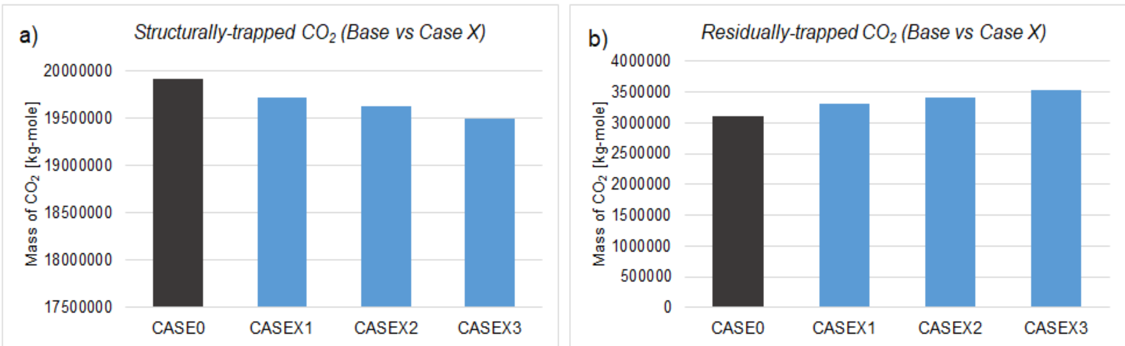

Figure 3.17: Quantity of CO_2 sequestered by (a) structural, and (b) residual trapping mechanisms at the end of gas injection for the base case and all descriptions of CASE X

The S_{wr} can be said to work in tandem with the S_{nrmax}. Figure 3.18 elaborates on this using a comparison of the mass of mobile CO_2 saturation quantified at the end of simulation for the base case and representative cases for X, Y, & Z that aids the comparability, namely: CASE X2, Y1 & Z1. Using the base case, CASE 0, as a reference point in Figure 3.18, the disparity in the mass of structurally trapped CO_2 at the end of simulation is highest in CASE X2 due to the simultaneous changes in S_{wr} and S_{nrmax}. Additionally, S_{wr} is seen to have a higher impact on the structural trapping of CO_2 than S_{nrmax} through a higher percentage change between CASE 0 and CASE Z1 than between CASE 0 and CASE Y1.

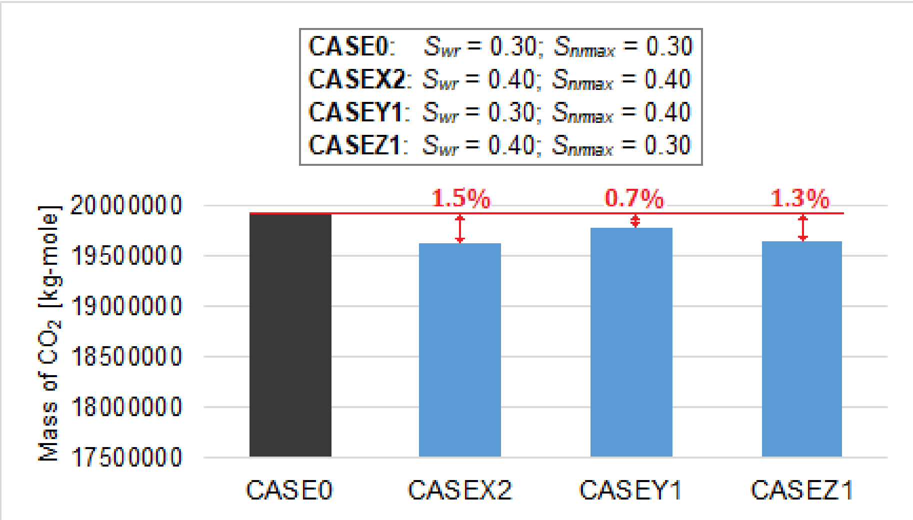

Figure 3.18: Quantity of CO_2 in mobile gas phase at the end of gas injection for CASE 0, CASE X2, CASE Y1 and CASE Z1. NB: Using the base case as a reference point, the values highlighted in red show the percentage change in mass of structurally trapped CO_2 at the end of a 10-year CO_2 injection period.

3.6.2.3 Analysis of n

All descriptions of CASE 1, 2, & 3 describe the impact of variation in values for the pore geometry index [*n*]. In the sub-categories: A, B, & C, the variance in *n* was defined by the $P_c – S_w – k_r$, $k_r – S_w$, and $P_c – S_w$ curves, respectively. This means that for cases defined by A, the variability in *n*-values was incorporated into the $k_r – S_w$, and $P_c – S_w$ curves. Cases defined by B had variance in *n*-values only incorporated into the $k_r – S_w$ curves, while the difference in *n*-values was only incorporated into the $P_c – S_w$ curves of cases defined by C. Consequently, cases B were modelled with the same $P_c – S_w$ curve of the base case, which has the highest value for *n*, while C cases were modelled with the same $k_r – S_w$ curves as the base case. Otherwise both the magnitude of capillary pressure and wetting saturation at the intercept of the $k_r – S_w$ curves are lowest in the base case, CASE 0, and increases progressively from CASE 1 to CASE 3 (Figure 3.13). This change in the shape of the relative permeability and capillary pressure curve, as a function of *n*, is attributed to the description of *n*-values in the van Genuchten model for clastic rocks, where higher values denote coarser-grained clasts (see Table 3.3). Thus coarser-grained clastic rocks, in comparison to their finer-grained counterparts, will possess a lower force of resistance to the buoyant migration of CO_2 plume and a higher relative permeability to the invading non-wetting gas. Likewise, the finer-grained rocks, in comparison to their coarser-grained counterparts, will increase the capillary trapping efficiency of the rock matrix while also reducing the relative permeability to the CO_2 plume. This explains why the mass of structurally trapped CO_2 decreases and the residual trapping efficiency increases with decreasing *n*, as illustrated in Figure 3.19.

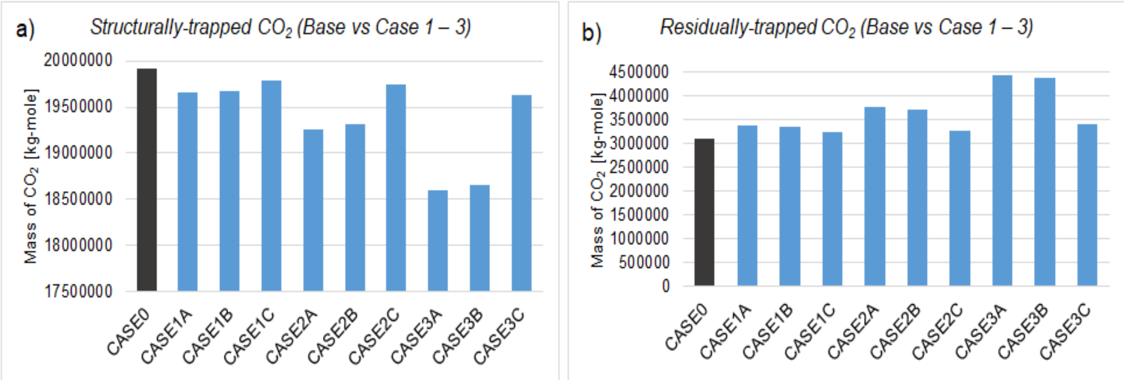

Figure 3.19: Quantity of CO_2 sequestered by (a) structural, and (b) residual trapping mechanisms at the end of gas injection for all descriptions of CASE 0, 1, 2, & 3.

The sub-categories of CASE 1, 2 & 3, *i.e.* A, B & C, also show variation in the degree of mobile and immobile CO_2 at the end of simulation. The mass of structural trapped CO_2 is greatest in sub-categorised cases of C and smallest in A. For C-cases, the relative permeability functions lead to a higher rate of CO_2 mobility, which creates a preferential flow pathway that evades the fine-grained sedimentation within the rock fabric. These fine-grained sediments serve as possible snap-off regions in the porous media. In B-cases the transport properties of *in-situ* fluids imitate movement through the fine-grained sediments even though the resistant force to plume migration, *i.e.* capillary pressure functions, is lower here than in C. Hence, the slower moving CO_2 plume results in a lesser amount of structurally trapped CO_2 due to a higher degree of residual trapping within regions of finer-grained sedimentation. The mobility of CO_2 is lowest in A-cases because the flow transport properties and resistant force imitate percolation through fine-grained sedimentation. The higher resistant force acting on slower moving CO_2 plume results in a greater resident time of the non-wetting fluid in the constricted rock matrix. This increases the rate of CO_2 ganglia that is isolated from the migrating plume, thus making residual trapping highest for sub-categorised cases of A.

3.6.2.4 The relative impact of n, S_{wr} and S_{nrmax} on the CO_2 storage performance

Quantifying the degree of structural trapping at the end of the flow simulation show that a variance in the pore geometry parameter [*n*] has a higher impact on CO_2 storage performance than a variance in the residual wetting saturation [S_{wr}] and the maximum residual non-wetting saturation [S_{nrmax}]. This is illustrated in Figure 3.20 where the bars indicating the amount of mobile CO_2 for cases with different *n* show greater variance from the base case than those for cases with different S_{wr} and S_{nrmax}. This is because the pore geometry of the rock essentially dictates the degree of residual wetting saturation and the maximum residual non-wetting saturation that could exist within its porous fabric. This accentuates the importance of the pore geometry parameter in subsurface flow simulation and the relevance of the concept of assigning different values of *n* to different sedimentary rocks. To verify this assertion, Section 3.6.3 considers the influence of *n* in an aquitard on flow performance during CO_2 sequestration.

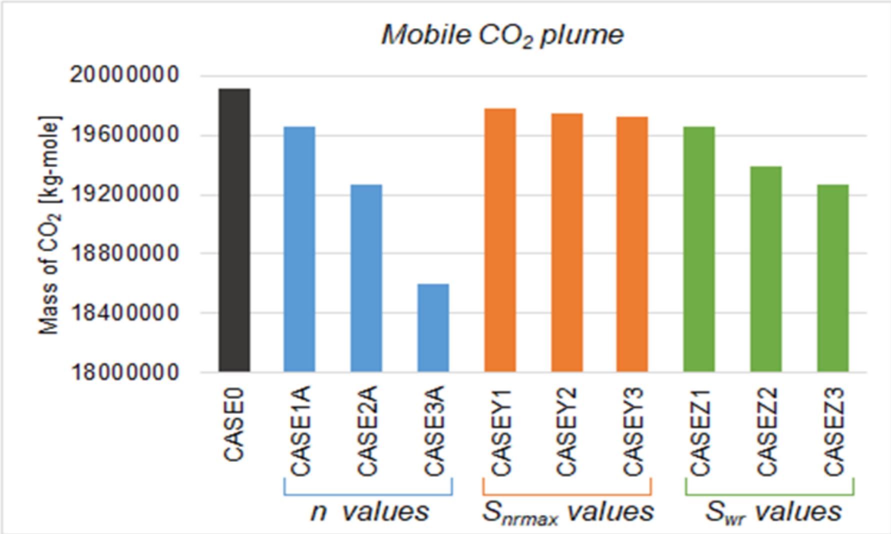

Figure 3.20: Computing the impact of n, S_{wr} and S_{nrmax} on the mass of mobile CO_2 in gas phase during a 10-year CO_2 injection period

3.6.3 Effect of *n* description in shale aquitard

Here the same injection scheme is considered for two variations of the base case. The first, CASE 0, as defined in the previous section and the second CASE V, which varies from CASE 0 through the description of the $P_c - k_r - S_w$ relationship in the caprock, where n = 1.56. The CO_2 injection rate and all other petrophysical parameters shown in Table 3.7 remain the same. Flow simulation is initialised for ten years of gas injection and an additional 40 years post gas injection. Figure 3.21 depicts the quantity of CO_2 in the caprock at the end of the simulation, where the cumulative gas injection is equivalent for both cases.

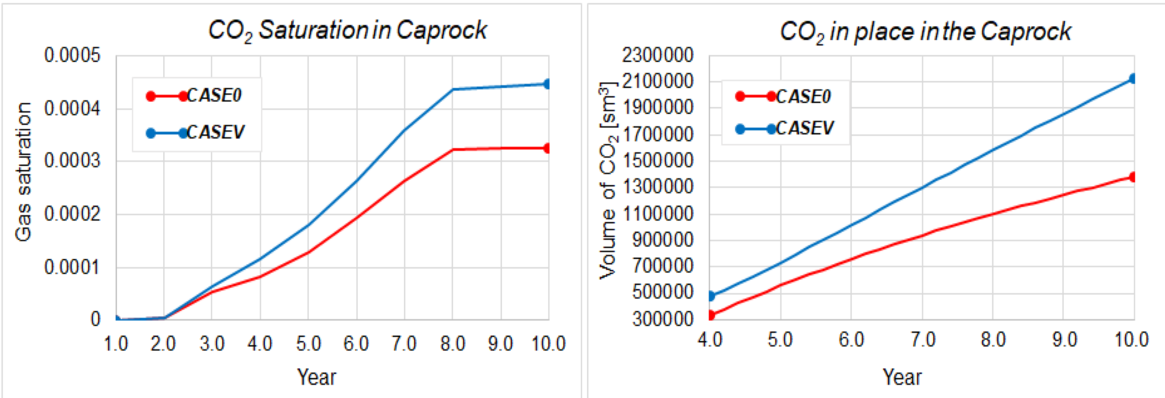

Figure 3.21: Quantity of CO_2 in caprock at the end of a 10-year flow simulation

Results show a larger quantity of CO_2 in the caprock for CASEV, which indicates a higher relative permeability to the non-wetting CO_2 in CASEV in comparison to CASE0. This is evident in the pressurisation of the caprock as illustrated in Figure 3.22, where pressure magnitude around the injection well is greater for CASEV and transmits to the top of the caprock in the said case, unlike CASE0. Hence, for multiphase flow modelling in CO_2/brine/rock systems the pore geometry parameter [*n*] can influence the degree of trapping mechanisms and the pore pressure profile in the aquifer and the aquitard. This augments the importance of the parametric description of pore geometry index in CO_2/brine flow simulation that use empirical correlations such as the Brooks-Corey or the van Genuchten model to compute the $P_c - k_r - S_w$ relationships.

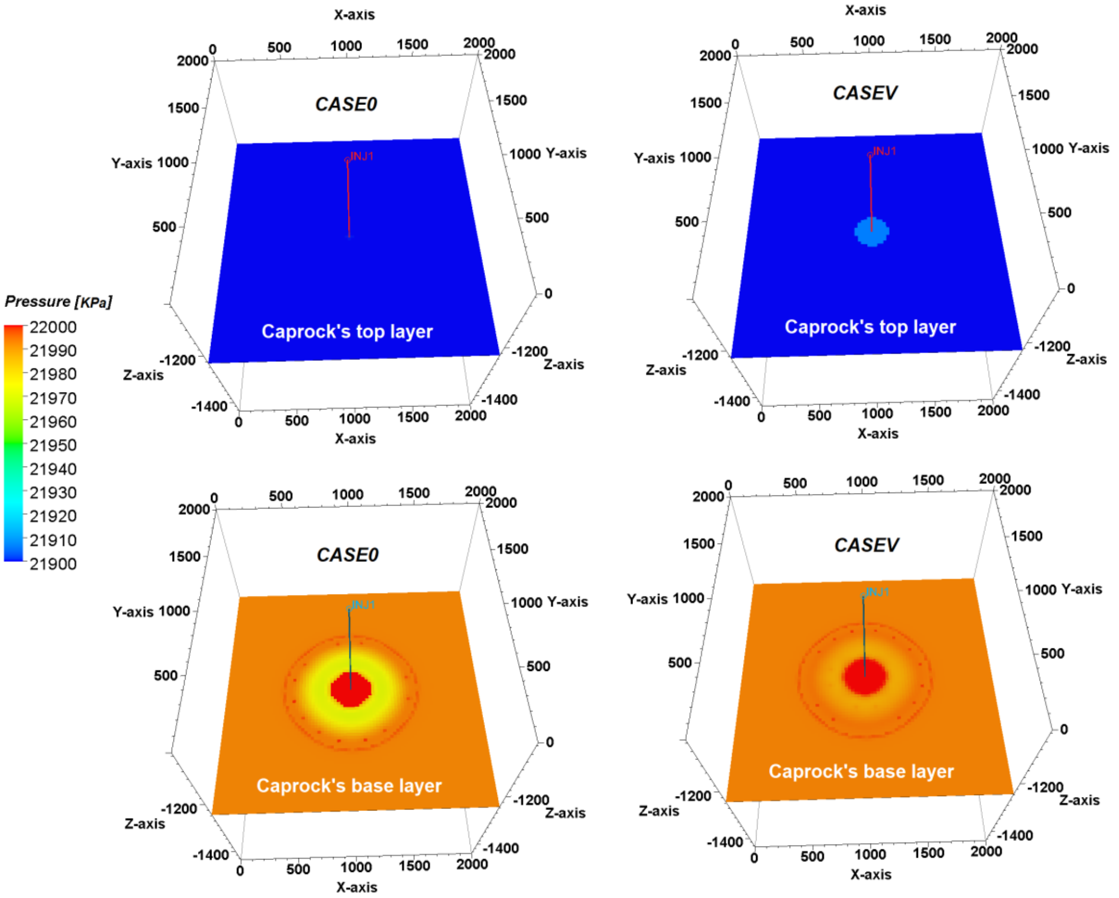

Figure 3.22: Comparison of caprock pressurisation in CASE 0 and CASE V

3.7 Summary and conclusion

The Brooks-Corey and van Genuchten models are widely used in computing $P_c - k_r - S_w$ relations for simulating CO_2 geo-sequestration. For $P_c - S_w$ curves, the BC model accounts for a non-zero capillary entry pressure while the vG model connects the entry slope of the curve to a capillary pressure of zero but fails to account for the entry capillary pressure. Capillary entry pressure [P_e] is governed by the rock's wettability, the largest pore throat radius of the rock matrix, and the interfacial tension acting between the in-situ fluids and rock surface, making it an essential parameter in the derivation of $P_c - S_w$ curves. This chapter described a relationship adopted for the equivalence in $P_c - S_w$ curves computed by both BC and vG models inorder to account for the introduction of P_e in the vG model. The study was then extended to define the pore geometry parameter [n] in the vG model for different clastic rocks. A quantitative methodology was presented here to compare the contribution of 200 n-values, ranging from 1.01 to 3.00 with an increment of 0.01, on the uncertainty of CO_2 plume evolution in a homogeneous saline aquifer. The methodology accounted for both the degree of uncertainty in each value and the application of a representative parametric value for a range of *n*. Four ranking criteria were outlined for comparing parameter roles in the uncertainty of CO_2 plume evolution at the end of a 10-year scCO_2 injection:

i) The shape of CO_2 plume.
ii) Plume edge at the bottom of the modelled domain.
iii) Fraction of mobile CO_2 saturation.
iv) Percentage volume of residual CO_2.

According to all four criteria, the pore geometry index clearly influences the uncertainty in the migration and trapping of CO_2 plume. Results showed that the parameterisation scheme for *n*-values described by Carsel and Parrish (1988) in soil physics can be applicable in rock physics. Furthermore, the primary parameters of the van Genutchen model, *i.e* the pore geometry index [*n*], the residual wetting saturation [S_{wr}] and the maximum residual non-wetting saturation [S_{nrmax}], were individually characterised to identify their relative impact on predictive analysis of CO_2 storage. Low values in *n*, S_{wr} and S_{nrmax} lead to increased gas migration while high values lead to increased immobilisation of the CO_2 plume. Among the three parameters, *n* is identified as the most significant element in the simulation and analysis of CO_2/brine flow in subsurface storage media, hence the significance of assigning defined values of *n* to different sedimentary rocks. This is because the pore geometry index dictates the degree of S_{wr} and S_{nrmax} that can exist in a rock's matrix. In realistic geological settings, the highly compacted pore geometry of finer-grained rocks will, most likely, restrict fluid perolation and increase in-situ fluid retention to a higher degree than the less compacted pore geometry of coarser-grained rocks.

Using the same *n* value when computing the $P_c – k_r – S_w$ relationship for siliciclastic rocks that make up the storage formation, such as sandstones, and those that make up the sealing formation, such as mudstones, can curb the accuracy in the forward modelling of CO_2 storage performance. In the absence of site-specific data on capillary pressure, relative permeability and pore geometry distribution, the parameterisation scheme for pore geometry index proposed in this chapter should aid in a more precise description of the hydraulic behaviour in siliciclastic rocks during numerical simulation of CO_2 storage. The proceeding chapters (4, 5 and 6) employ the optimised parameters for the vG-model in investigating various descriptions of sedimentary heterogeneities in siliciclastic rocks, and their subsequent impact on CO_2 storage performance, through numerical simulations.

CHAPTER 4[†]

Impact of gradational contact at the reservoir-seal interface and assumptions of relative permeability functions on CO_2 storage performance

The implementation of CO_2 storage in sub-surface sedimentary formations can involve decision making using relevant numerical modelling. These models are often represented by 2D or 3D grids that show an abrupt boundary between the reservoir and the seal lithologies. However, in an actual geological formation, an abrupt contact does not always exist at the interface between distinct clastic lithologies such as sandstone and shale. This chapter presents a numerical investigation of the effect of sediment-size variation on CO_2 transport processes in saline aquifers. Using the Triassic Bunter Sandstone Formation (BSF) of the Southern North Sea Basin, the impact of a gradation change at the reservoir-seal interface on CO_2 sequestration is investigated. This is of great interest because of the importance of enhanced geological detail in predictive reservoir modelling of CO_2 plume migration and the integrity of trapping mechanisms within the storage formation. The simplified strategy was to apply the *van Genutchen* formulation to establish constitutive relationships for pore geometric properties, which include capillary pressure (P_c) and relative permeability (k_r) as a function of brine saturation in the porous media.

[†] The content of this chapter has been extracted from the following paper:

Onoja, M.U., and Shariatipour, S.M. (2018) The impact of gradational contact at the reservoir-seal interface on geological CO_2 storage capacity and security. *International Journal of Greenhouse Gas Control* **72**, 1–13. https://doi.org/10.1016/J.IJGGC.2018.03.007

The candidate set the scientific scope of the work, devised and developed the methodology, performed all data analysis and wrote the text. The co-author provided guidance during the design of this part of the project and feedback on the manuscript.

Minor adaptations have been performed to streamline the layout of the thesis

4.1 Introduction

Depositional and diagenetic processes dominate reservoir heterogeneity. The sedimentology of the formation primarily influences the reservoir quality by regulating the pore system (Pettijohn et al. 1972), which governs the storage capacity and the efficiency of physical trapping mechanisms during CO_2 sequestration (Benson and Cole 2008). The physical and chemical changes that alter the characteristics of sediments after deposition are referred to as diagenesis. During transportation and deposition of sediments the clasts can be sorted, having an average grain size, and deposited in a geological sequence of sedimentary beds or strata (Hiscott 1978). Consequently, sedimentary structures such as gradational contacts and graded beds can be formed. Gradational contact describes the gradual transition in the average size of deposited clasts between conformable strata, while graded bedding refers to the vertical evolution of grain size in a stratum. These structures are reservoir-scale heterogeneities that can influence injected CO_2 flow patterns due to distinct hydraulic conductivities arising from grain-scale heterogeneities. Grain-scale heterogeneity dictates the capillary effect that governs two physical traps: stratigraphic and residual gas trapping (Bjørlykke 2010). This capillarity effect emanates from fluid and interfacial physics at the pore-scale. Hence, the effective hydraulic behaviour on any practical field-scale is dominated by the large scale spatial-arrangement of small-scale variability (Krevor et al. 2015). See Pettijohn (1957) and Haldorsen (1986) for the basics of sedimentary structures and scales of heterogeneity, respectively.

In the numerical simulation of GCS, the lithostratigraphic units of many generic reservoir models are usually interpreted from wireline logs of representative geologies, such as data from a Gamma Ray (GR) tool (Doveton 1991, Darling 2005). However, the GR log may not be able to distinguish between types of argillaceous rock, *i.e.* siltstone and claystone (Katahara 1995, Fabricius et al. 2003, Nazeer et al. 2016). Clay distribution alone cannot account for the fine-grained sediments in an actual reservoir hence it is important to assess the impact of sediment-size gradation on GCS, particularly at the reservoir-seal interface. Most models that simulate the CO_2 plume distribution are built on the premise that the stratigraphic contact between the reservoir rock and the caprock is abrupt, a sudden distinctive change in the lithology. This may not always be the case as the bedding contact between sandstone and mudstone can be gradational. For example, the Sherwood Sandstone Group shows an upward grading from coarse sandstones to siltstones, and then to the Mercia Mudstone Group (Benton et al. 2002, Newell 2017) [see Figure 4.1 for an illustration of a stratigraphic column of TRIASSIC age in the Wessex Basin area]. Nevertheless, several contemporary studies used reservoir models with geological details such as top-surface morphologies, transition zone heterogeneities, and layered reservoirs (e.g. Shariatipour et al. 2014, Newell and Shariatipour 2016, Wen and Benson 2019). These studies demonstrated that such geological detail can affect various trapping mechanisms within the reservoir as well as influence CO_2 plume migration, the estimation of storage capacity, and the volume of the aquifer. Generally, increasing the level of detail in geological modelling for simulation models is important for producing meaningful and accurate results (Van De Graaff and Ealey 1989).

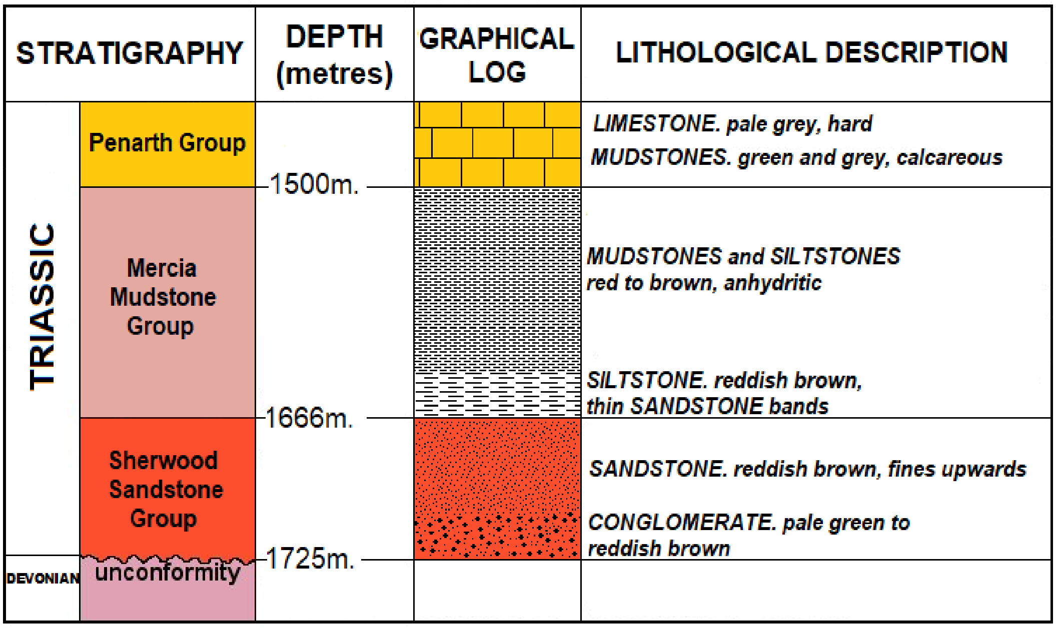

Figure 4.1: Generalised stratigraphy of the Southampton Geothermal Well showing the TRIASSIC section. [Adapted from Thomas and Holliday (1982)].

The main aim of this chapter is to investigate the variability in transport and flow processes of injected CO_2 resulting from a gradational contact at the reservoir-seal interface and the gradual change in clast-size within an aquifer. This variability is described in constitutive functions using an empirical correlation that is based on grain-size variation, *i.e.* the van Genuchten's (1980) formulation. The aim of this investigative approach is to encourage the representation of heterogeneity in capillary pressure [P_c] and relative permeability [k_r] functions during reservoir simulation. Although Saadatpoor et al. (2010) and Meckel et al. (2015) showed the influence of grain-scale heterogeneity on a reservoir-scale, their studies only emphasised the influence of capillary heterogeneity on CO_2 storage performance. The former scaled the variability of flow processes using intrinsic permeability heterogeneity with a spatially constant capillary pressure curve, while the latter introduced capillary heterogeneity by generating a capillary threshold pressure distribution based on defined median grain size. In this thesis, the capillary heterogeneity is scaled from a spatially constant threshold pressure while variation in relative permeability curves is described using the grain size. The contribution of other variables such as the wettability of the porous medium, the interfacial tension between the fluids in contact, and the diagenetic processes in the geological formation are not considered in this thesis.

4.2 Model development

The study is based upon the Triassic Bunter Sandstone Formation (BSF) of the Southern North Sea Basin (SNS) in the United Kingdom (UK) sector (Williams et al. 2013). The BSF is a reservoir unit composed predominantly of medium- to coarse-grained sandstone units of metre-scale upward coarsening regime interbedded with fine-grained sediments (Rhys 1974). It is a major gas producing reservoir in the SNS. Most of the BSF is filled with saline water and is considered to have significant CO_2 storage potential. In the UK sector, it overlies the Triassic Bunter Shale Formation and it is sealed by mudstones and evaporites of the upper Triassic Haisborough Group (Brook et al. 2003). Figure 4.2 illustrates the location map of the Bunter aquifer in the UK SNS. Structurally, Bunter sandstones contain several periclines commonly referred to as Bunter domes (Williams et al. 2013). One such Bunter dome in the UK sector was recently identified by the Energy Technologies Institute's Strategy UK CCS Storage Appraisal Project (S.SAP) as a promising candidate for CO_2 storage (James et al. 2016). This dome is penetrated by Well 44/26-01, a deep exploration well completed in 1968 with interpreted log data identifying the strata within the dome (Figure 4.3). The basis for the site development plan is an assumed supply of 7Mt/yr of CO_2 from a future terminal at Barmston on the east coast of Yorkshire, which commences operation in 2027 (James et al. 2016). The BSF within the dome is interpreted as having five intra-reservoir sandstone zones with interbedded shale and cemented sandstone layers and no seismically interpretable faults (James et al. 2016). The thickness of the BSF at the site is approximately 215 m. Refer to Williams et al. (2013) for a detailed description of the sedimentology and lithostratigraphy of this dome, hereafter referred to as the Bunter aquifer.

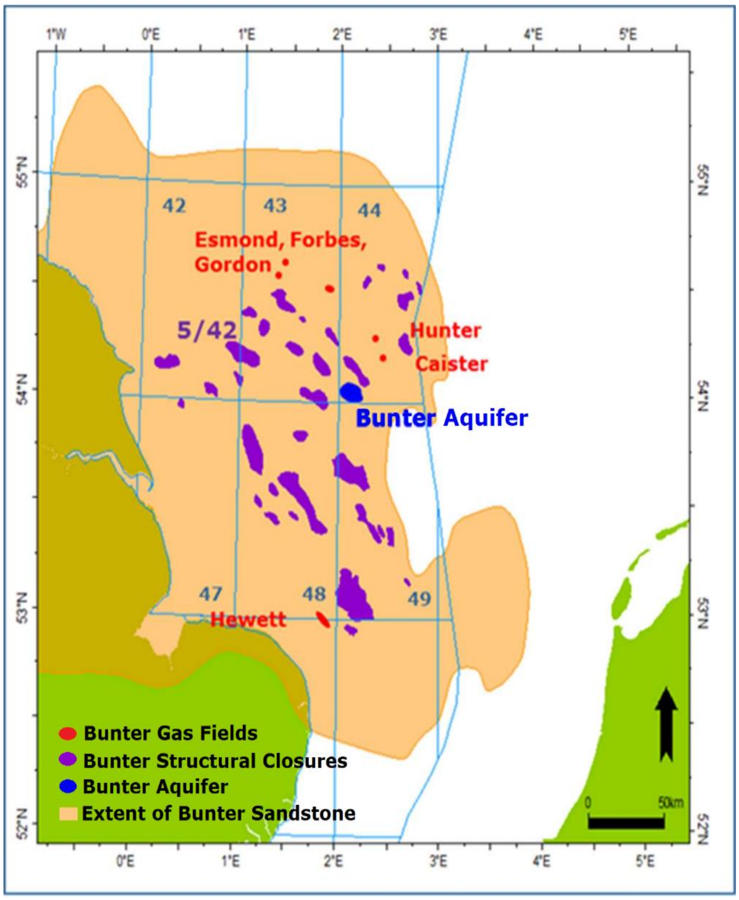

Figure 4.2: The Bunter Aquifer Location Map. [Source: James et al. (2016)]

This chapter presents a brief overview of the Bunter aquifer in order to justify the lithological modelling approach used to investigate the multiphase fluid flow regime resulting from pore scale variation in the reservoir-seal interface. Zone 1 in Figure 4.3 is assumed to be the reservoir-seal interface and henceforth referred to as the *transition zone*. As this is a generic study of CO_2 storage in deep sandstone aquifers overlain by mudstones rather than the study of a specific aquifer, the goal is to select representative characteristics for the aquifer as a base case for systematic parameter study. As such, the thickness and other aquifer characteristics are based on the log data from Well 44/26-01. In the numerical analysis presented in this chapter, two different structural models, a generic box model with flat strata and an anticline with a caprock dome, are adapted for the Bunter aquifer and defined in Sections 4.3 and 4.4, respectively.

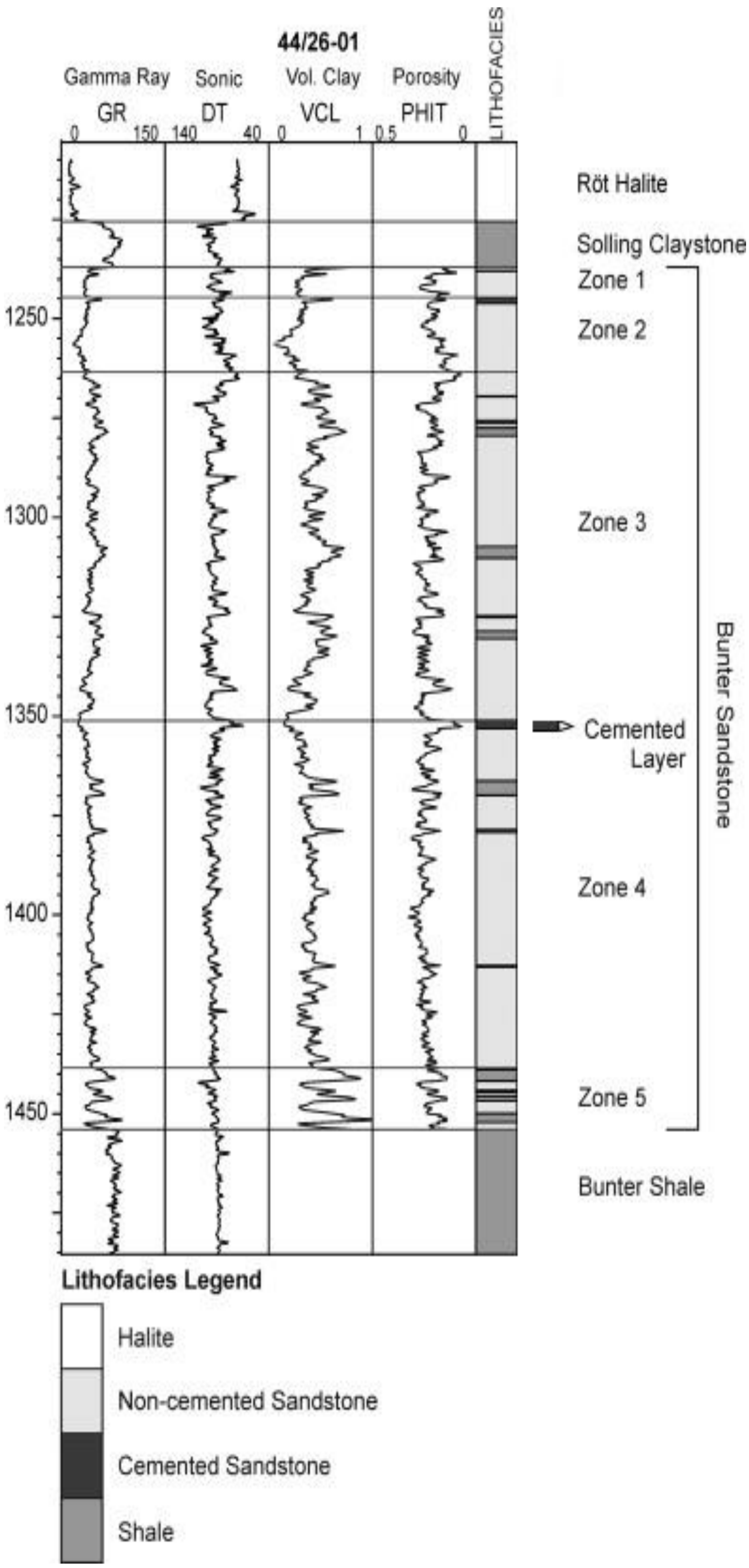

Figure 4.3: Lithostratigraphical delineation of the Bunter Sandstone in Well 44/26-01 using logging data. [Source: Williams et al. (2013)].

4.3 The generic box model

A simplified 3D static geological model with an areal of 2 km x 2 km and a thickness of 300 m is developed and discretised into a total of 544,000 active cells (n_i = 80, n_j = 80, n_k = 85) using Schlumberger's (2016) PETREL software. In this geological model the layers shown in Figure 4.3 are defined in Table 4.1 and illustrated in Figure 4.4:

Zones	***Top depth (m)***	***Number of layers***
Rot Halite	1200	4
Claystone	1225	12
R.Zone 1	1237	8
R.Zone 2	1245	10
R.Zone 3	1264	15
R.Zone 4	1350	22
R.Zone 5	1438	5
Basal Shale	1455	9

Table 4.1: Vertical grid discretisation for the modelled domain.

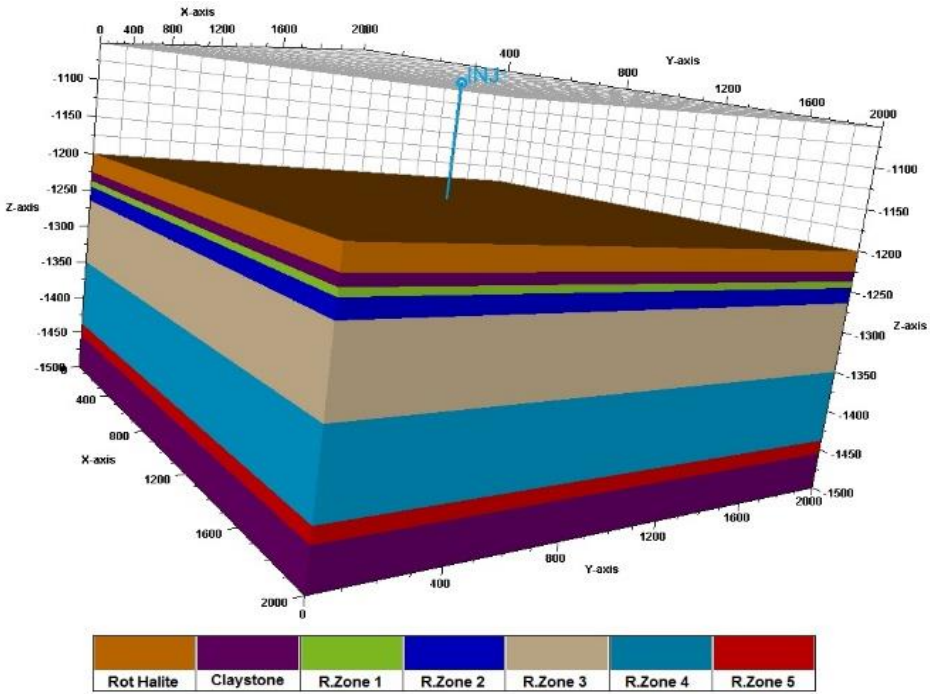

Figure 4.4: Reservoir model used for ECLIPSE simulations.

An average horizontal permeability (K_h) value of 6.5 x 10^{-3} mD is assigned to the top and base seal lithologies (after Spain and Conrad 1997) while the average K_h for the reservoir is assumed to be 233 mD. The Solling Claystone and the Rot Halite are assigned porosity values of 4% and 1%, respectively, based on the range of porosity values in the Solling, Rot, and Muschelkalk caprocks above the BSF in the southern Dutch North Sea (Spain and Conrad, 1997). The base seal and reservoir formation are assigned average porosity values of 4% and 22% respectively. Permeability anisotropy is assumed to be 0.3 since the average vertical permeabilities of the Bunter sandstone are reported to be typically some 30 % lower than the horizontal permeabilities (Noy et al. 2012). Pore fluid in the domain is modelled under an isothermal condition of 42ºC and an initial pressure of 12 MPa with a brine pore fluid gradient of 10.7 MPa/km. This implies a pore fluid density of 1.09 g/cc at a salinity of 133,000 ppm. Pressure control consideration for dynamic modelling is 75% of a lithostatic pressure gradient of 22.5 MPa/km (after Noy et al. 2012). $P_c - k_r - S_w$ relationships are generated under the assumption of a strongly water wet system with a CO_2/brine interfacial tension of 30 mN/m, following published results by Hebach et al. (2002), Chiquet et al. (2007) and Perrin and Benson (2010). Draining and imbibition curves are included allowing for the residual trapping of CO_2 to be modelled (Figure 4.5):

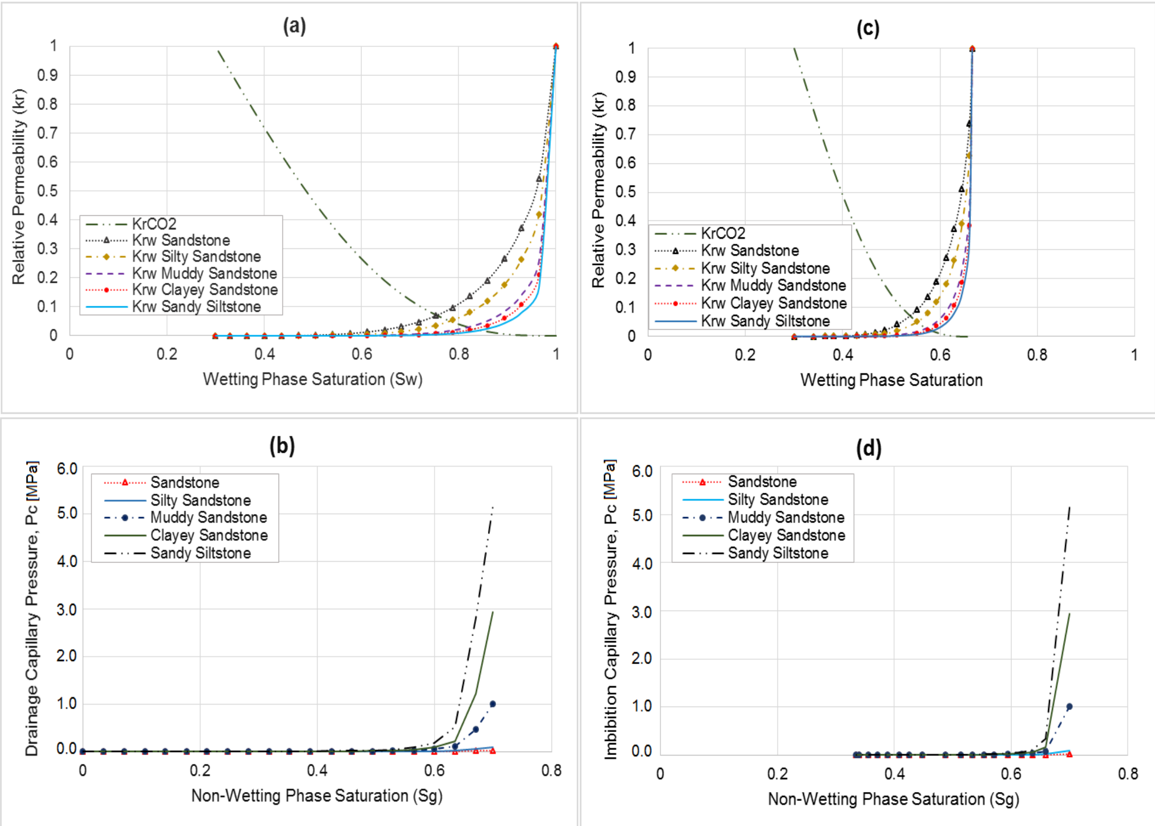

Figure 4.5: $P_c - k_r - S_w$ functions for (a) drainage relative permeability, (b) drainage capillary pressure, (c) imbibition relative permeability, and (d) imbibition capillary pressure

CO_2 saturation end points for the reservoir and seal are based on published results for the Captain Formation in the North Sea Goldeneye Field (Shell 2011) and the Colorado Group (Bennion and Bachu 2008), respectively. The capillary displacement pressure of shale is assumed to be 4.7 MPa, after Spain and Conrad's (1997) experimental investigation on the Solling Claystone in the southern Dutch North Sea. In the absence of closely related data, the maximum pore throat size in the reservoir is assumed to be 37 microns. This value falls within the range of dominant pore throat sizes of Permo-Triassic sandstones in the United Kingdom (Bloomfield et al. 2001). Numerical simulations are conducted using the compositional ECLIPSE E300 module (Schlumberger 2017). This model assumes no conductive faults, nor cemented sand layers, interbedded shale or leaky wellbores in the formation.

4.3.1 Sensitivity design

Simulation studies are conducted in aquifer systems idealised as "closed" and "open" to observe the impact of the two sedimentary structures on CO_2 storage, *i.e.* the gradational contact at the reservoir-seal interface and the gradual change in clast-size within an aquifer. The closed aquifer system is identified as Aquifer-1 while the open aquifer system is identified as Aquifer-2. The concept of graded bedding is investigated using normal grading, where the strata fines upwards, and inverse grading, where the strata coarsens upwards. Five reservoir lithologies are identified from Table 4.2: sandstone, silty sandstone, muddy sandstone, clayey sandstone, and sandy siltstone. The spatial porosity value of 22% remained the same for all the reservoir lithologies. However, permeability data for the varying lithologies were extrapolated from rock permeability values used in S.SAP's 2016 report for the intra-reservoir zones (James et al. 2016):

Rock lithology	***Rock permeability [mD]***
Sandstone (S)	233
Silty Sandstone (SiS)	223
Muddy Sandstone (MS)	219
Clayey Sandstone (CS)	195
Sandy Siltstone (SSi)	162

Table 4.2: Permeability data for reservoir rock lithologies

The plot of the sensitivity study is outlined in three phases:

- ***Phase I*** focuses on the effect of varying the dynamic properties of the rock geometry (*i.e.* the P_c – k_r – S_w functions) in the reservoir model at a constant permeability within the reservoir.
- ***Phase II*** focuses on the effect of varying the permeability values and the P_c – k_r – S_w functions in the reservoir. Simulation cases in this phase are identified by the suffix "A".
- ***Phase III*** cases, identified by the suffix "B", are modelled with variable permeability values and a single P_c – k_r – S_w function within the reservoir. This is to compare, in magnitude, the "stand-alone" effect of P_c – k_r – S_w functions over intrinsic permeability functions in the modelled domain.

For this study, permeability and porosity data are henceforth regarded as *the static functions* while P_c – k_r – S_w functions are regarded as *the dynamic functions*. The base case for the simulation regards all five reservoir zones as sandstone and is identified as CASE 1. Sensitivity cases are then labelled according to the description in Table 4.3.

4.3.1.1 Aquifer-1

Aquifer-1 is confined vertically and laterally within the modelled domain (Figure 4.4) with a reservoir pore volume of 1.93 x 10^8 m^3. This aquifer is used to investigate the impact of gradational contact and graded bedding on the reservoir's injectivity and physical trapping mechanisms. In this aquifer, a numerical simulation is initiated at an annual CO_2 injection rate of 100,000 metric tonnes through an injection well peforated in R.Zone 4 and 5. The sensitivity plots of Phase I, II and III were investigated in this aquifer.

4.3.1.2 Aquifer-2

Aquifer-2 is also confined in the vertical boundaries of the modelled domain but is assumed to have lateral aquifer connection. This aquifer is used to investigate the impact of gradational contact and graded bedding on overpressure at the reservoir-seal interface. The concept of an open aquifer is introduced in the study because closed aquifers do not communicate with other reservoirs, laterally, and as a result, may be over-pressured following the CO_2 injection (Elewaut et al. 1996). For two-phase flow in porous media, one important role the aqueous phase plays in affecting the evolution of CO_2 plume is that it serves as a pressure transmission medium within the porous media (Pruess and Nordbotten 2011). As a result, the ease with which the migrating CO_2 plume evacuates brine from the pore space will influence the pressure evolution within the formation.

<table>
<tr><th>Reservoir Zone / Case</th><th>1</th><th>2</th><th>3</th><th>4</th><th>5</th></tr>
<tr><td>1</td><td>Sandstone</td><td>Sandstone</td><td>Sandstone</td><td>Sandstone</td><td>Sandstone</td></tr>
<tr><td>2</td><td>Sandstone</td><td>Silty Sandstone</td><td>Muddy Sandstone</td><td>Clayey Sandstone</td><td>Sandy Siltstone</td></tr>
<tr><td>3</td><td>Sandy Siltstone</td><td>Clayey Sandstone</td><td>Muddy Sandstone</td><td>Silty Sandstone</td><td>Sandstone</td></tr>
<tr><td>4</td><td>Silty Sandstone</td><td colspan="4" rowspan="4">Sandstone</td></tr>
<tr><td>5</td><td>Muddy Sandstone</td></tr>
<tr><td>6</td><td>Clayey Sandstone</td></tr>
<tr><td>7</td><td>Sandy Siltstone</td></tr>
</table>

Table 4.3: Pore geometric parameters for the reservoir simulation

4.3.2 Result and discussion

4.3.2.1 Reservoir injectivity

For the simulation of gas injection, CO_2 plume was observed to rise vertically to the superjacent ultra-low permeable barrier. This buoyant migration of the plume is due to the density difference between the supercritical CO_2 and brine. Simulation results for reservoir injectivity for all three phases of the analysis show an equivalence in CO_2 injection with time for the first 13 years of injection before reaching the limiting field pressure in the fourteenth year of injection (Figure 4.6):

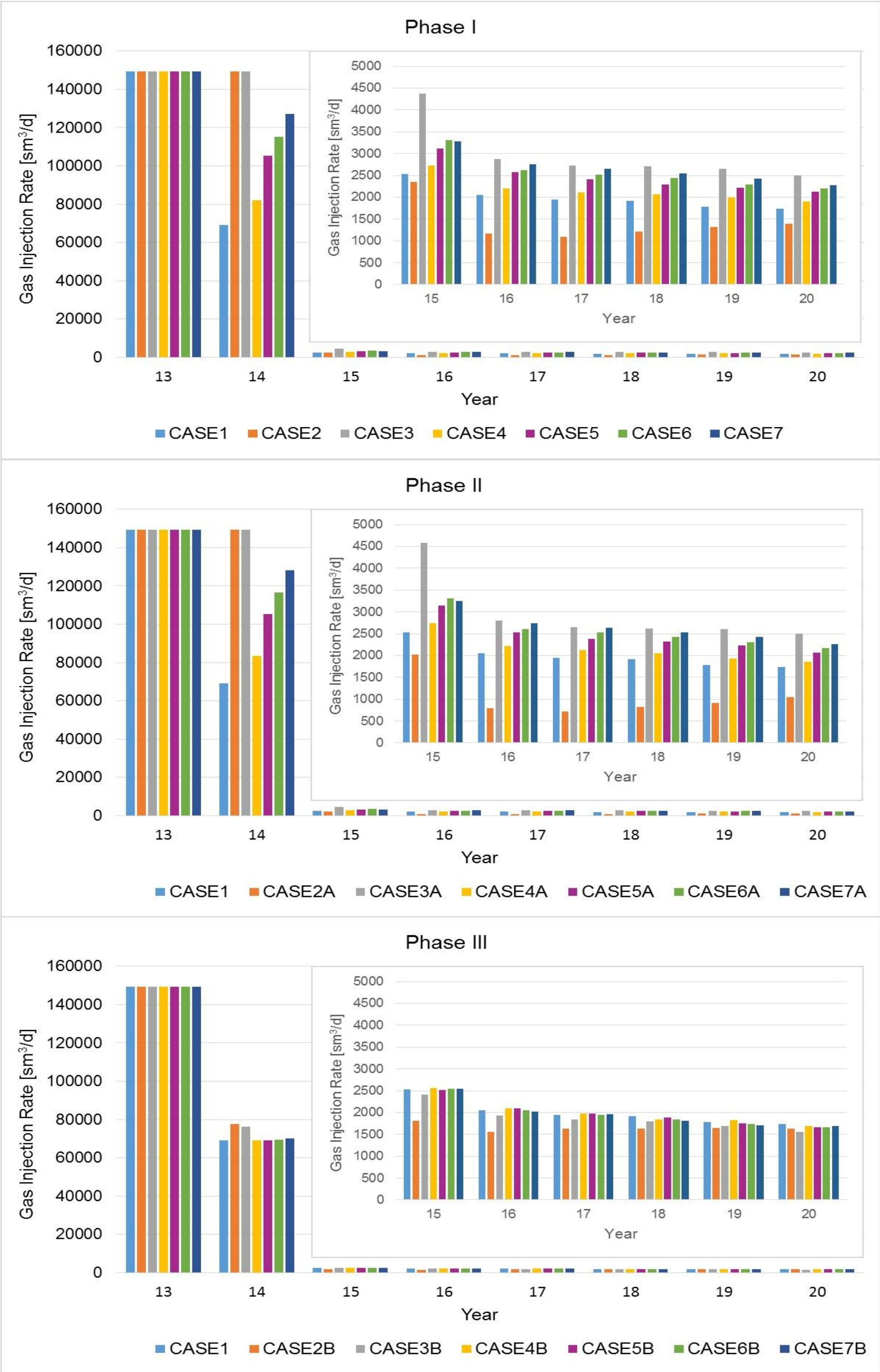

Figure 4.6: CO_2 injection rates for all sensitivity cases

The illustrations in Figure 4.6 show the importance of the $P_c - k_r - S_w$ functions on a reservoir's injectivity. Incorporating this dynamic relationship for heterogeneity at the transition zone was a major influencing factor on the reservoir injectivity as the pore fluid pressure approached the well control pressure. For gradational contact at the reservoir-seal interface, the rate of CO_2 injection into the lower part of the reservoir increases with the decrease in size of clastic sediments at the top of the reservoir. For the graded reservoir, the rate of CO_2 injection is higher for normal grading than for reverse grading. This can be seen from the fourteenth year of injection. The results indicate that the relative permeability functions predominate over permeability and porosity data when describing sedimentary heterogeneity. This is further emphasised in the comparison between the total CO_2 injected for all cases investigated. Figure 4.7 shows neglible differences in the total amount of CO_2 injected between the base case and other sensitivity cases at the end of simulation for Phase III as opposed to Phases I and II:

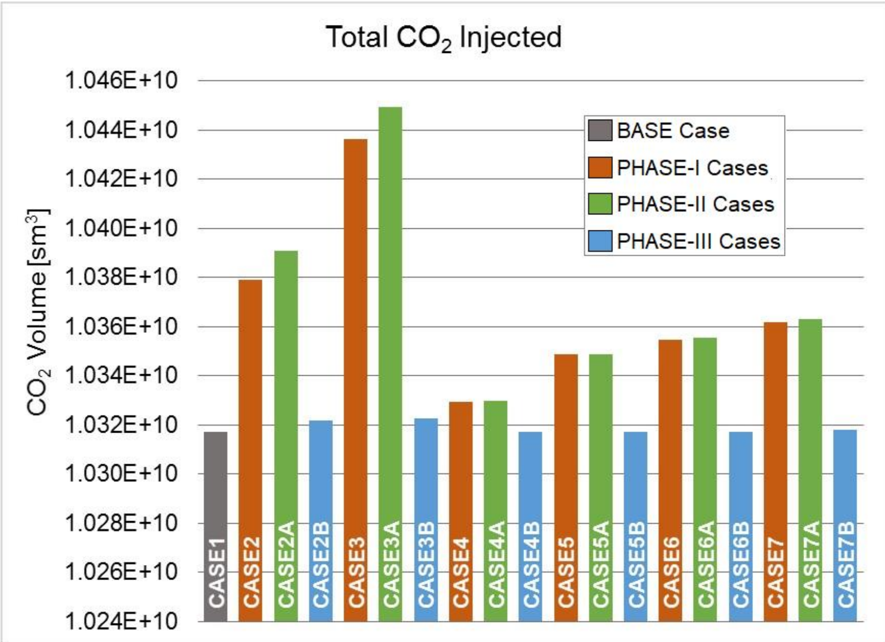

Figure 4.7: Total volume of CO_2 injected into the reservoir during Phase III analysis, compared with Phases I and II

At the end of the simulation, all cases that used the $P_c - k_r - S_w$ functions to describe hetergeneity within the model allowed for more CO_2 injection than the base case. In Figure 4.7, Cases 4 and 4A show the smallest margin in total CO_2 injection and this accounts for an additional 23,000 tonnes of CO_2 being injected into the reservoir.

4.3.2.2 Physical trapping

At the end of the injection period, the upward migration of CO_2 plume was restrained by the caprock layer in all the cases simulated. When graded bedding was integrated into the pore geometric analysis, the impact of the dynamic functions followed the trend identified in Section 4.3.2.1 and amplified the supporting role of the static parameter thereby decreasing the effective permeability to the non-wetting phase. This was attributed to the impact of the irreducible aqueous phase on the relative permeability to CO_2 within the reservoir. Figure 4.8 illustrates this impact based on the *vG-MC* model which described a constant K_{rCO2}–S_w curve for all the reservoir lithologies in this study:

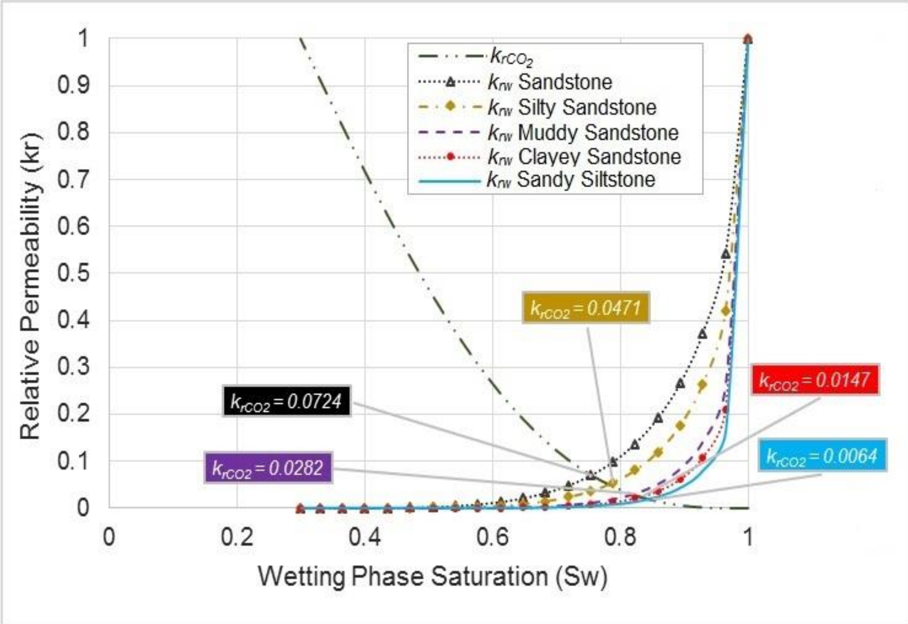

Figure 4.8: Relative permeability curves showing the values for $k_{r(CO2)}$ at the intercept of $k_{r(brine)}$ in various reservoir lithologies

Figure 4.8 shows a decreasing value of the relative permeability to CO_2 at the intercept between the non-wetting k_{rnw}–S_w curve and the variable wetting k_{rw}–S_w curves for the reservoir rocks. This resulted in a lower degree of mobile CO_2 in models that incorporated smaller clasts within the reservoir, particularly at the transition zone. The relative drag in plume movement within the constricting rock matrix led to an increase in the local capillary trapping, a trapping mechanism resulting from intrinsic capillary heterogeneity (Saadatpoor et al. 2010). This was represented by the P_c–S_w relationships in the model and explains why the impact of the static parameter on capillary trapping is not noticeable for the gradational changes investigated. Retention of CO_2 within the pore spaces is enhanced by the capillary forces acting at the pore throats. Due to the larger distribution of the capillary processes, graded bedding in the reservoir accounted for a higher degree of capillary trapping when the static and dynamic parameters were integrated. Normally graded reservoirs were seen to residually trap more CO_2 than their inversely graded counterparts. This was attributed to the gradual rise in the magnitude of capillary forces acting within normally graded stratum, as opposed to the fall in magnitude for the inversely graded stratum. Figure 4.9 shows the quantification of CO_2 trapping for all cases modelled in Aquifer-1.

It is observed in Figure 4.9a that more gas is trapped residually from the top, Case 1, to the bottom, Case 3A, of the chart. The prominence of capillary trapping within the reservoir serves to reduce the rate of CO_2 spreading at the base of the caprock, as well as increasing brine contact which is beneficial for CO_2 dissolution (Golding et al. 2011). This is noted through the lateral extent of plume migration beneath the caprock for all simulated cases which followed the trend 1 > 4 > 2 > 5 > 6 > 7 > 3 in the order Phase III > Phase I > Phase II. It suggests that the failure to include a variance in the $P_c – k_r – S_w$ functions within the reservoir domain will lead to an over estimation of bouyant drive to- and the gravity current at- the transition zone. Following this observation, the open aquifer, *i.e.* Aquifer-2, becomes only an extension of Phase II for an analysis on overpressure.

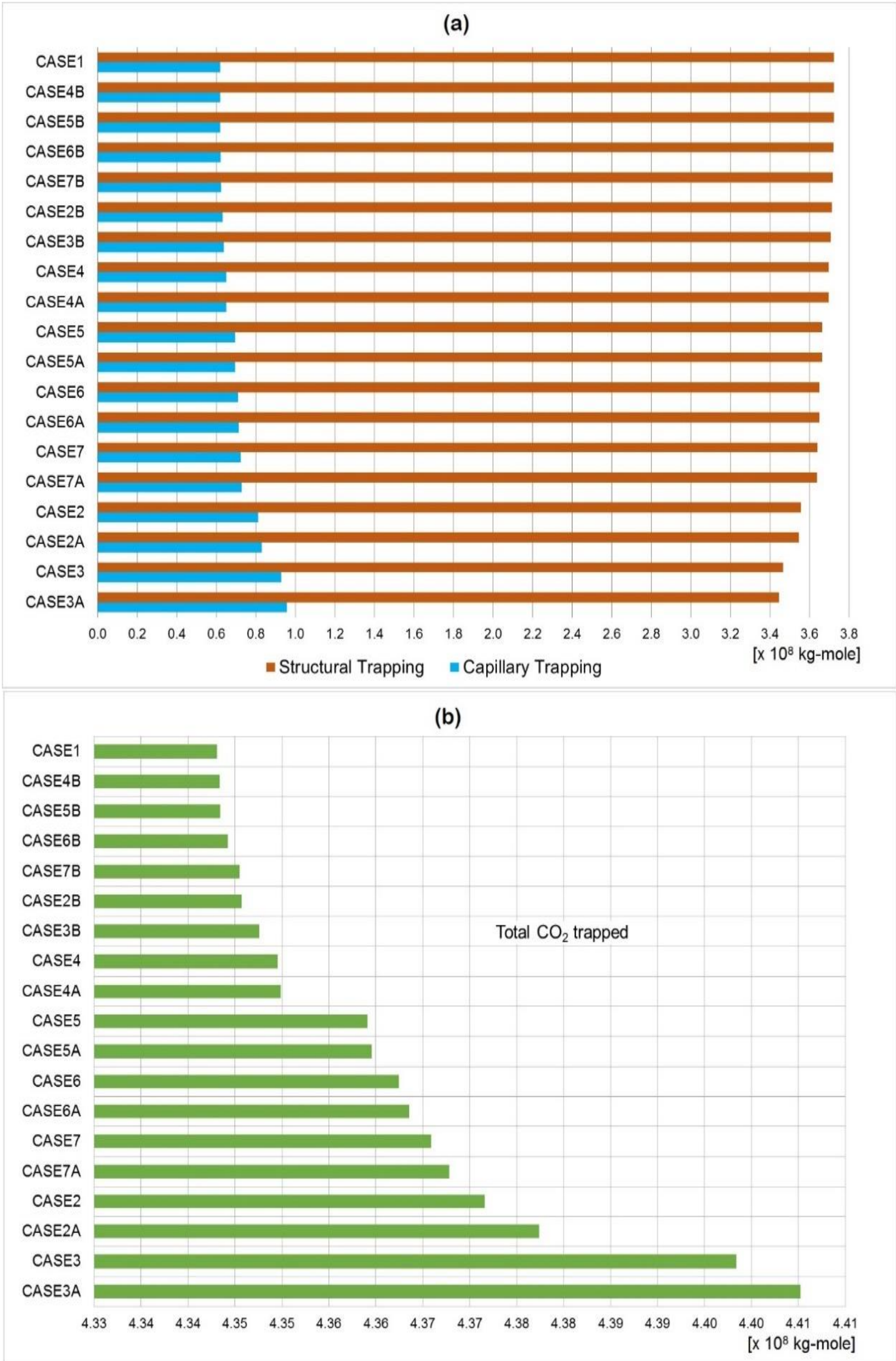

Figure 4.9: a) Quantification of the physical trapping mechanisms and b) the total CO_2 trapped, in order of increasing total trapping from top to bottom, at the end of the injection period.

4.4.3.3 Pressure evolution

To simulate the pressure evolution in the reservoir, an infinite lateral communication at both ends of the modelled domain is assumed. This is done to identify which cases of gradational contact at the transition zone and gradation in the reservoir would have the least impact on the structural integrity of the caprock. The assumption of an infinite-acting aquifer is reasonably based on the vast lateral extent of the Bunter sandstone rock unit which crops up onshore in Eastern England as the Sherwood Sandstone Group

(Brook et al. 2003). To assess the structrual trapping mechanism, the volume of mobile CO_2 lodged at the transition zone after 20 years of CO_2 injection is quantified and illustrated in Figure 4.10.

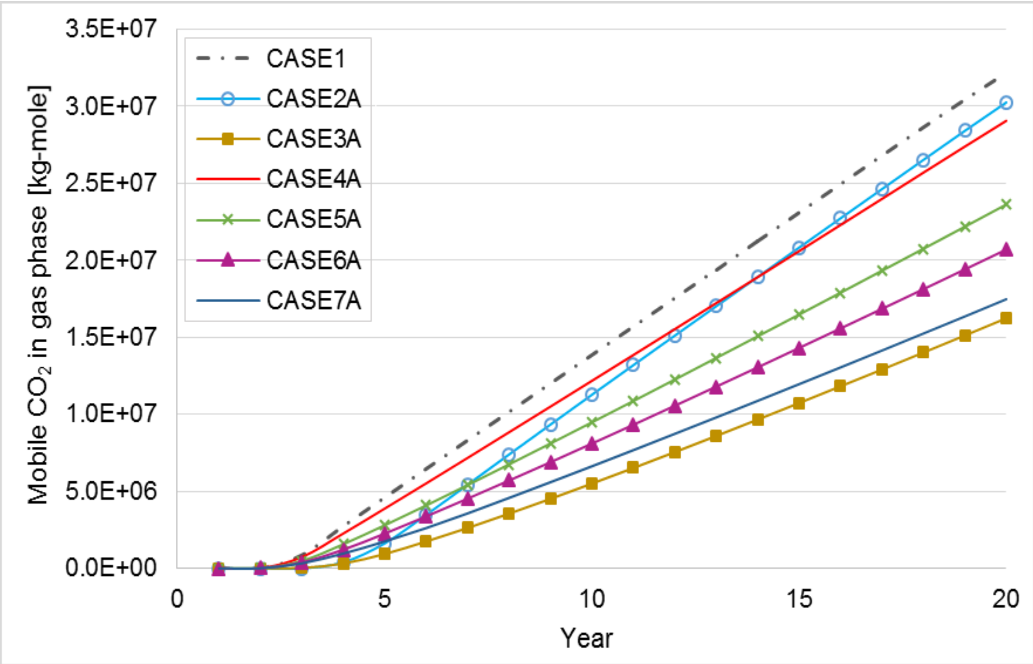

Figure 4.10: Mobile CO_2 in the reservoir-seal gradation zone of an aquifer with infinite lateral communication.

As illustrated in Section 4.3.2.2, the proportion of mobile CO_2 at the transition zone is influenced by the average particle-size within the rock matrix. This can be seen in a comparison between Case 3A and 2A where a decreasing particle-size, from the base to the top of Case 3A aquifer, progressively reduced the amount of free gas migrating vertically. Alternatively, the increasing particle-size from the base to the top of Case 2A propelled the vertical migration of CO_2 plume. Following the observations in Figure 4.9, Case 3A and 7A were chosen for respective analysis on the impact of a graded reservoir and a gradational contact at the reservoir-seal interface on the pressure distribution in the domain. These cases showed the lowest magnitude of buoyant force in the transition zone. Consequently, Case 1, 3A, and 7A were simulated in a version of Aquifer-2 that reflected the probable pore volume of the Bunter Sandstone Formation (Table 4.4).

Reservoir Formation Domain	***Reservoir Pore Volume (rm^3)***	***Reference***
Aquifer-2 (Infinite-acting)	4.83E+14	This study
Aquifer-2 (Bunter-estimation)	1.45E+12	This study
Bunter Sandstone	1.52E+12	Brook et al. (2003)
Bunter Sandstone	1.396 E+12	Holloway et al. (2006)

Table 4.4: Provisional figures for reservoir pore volume used in this study

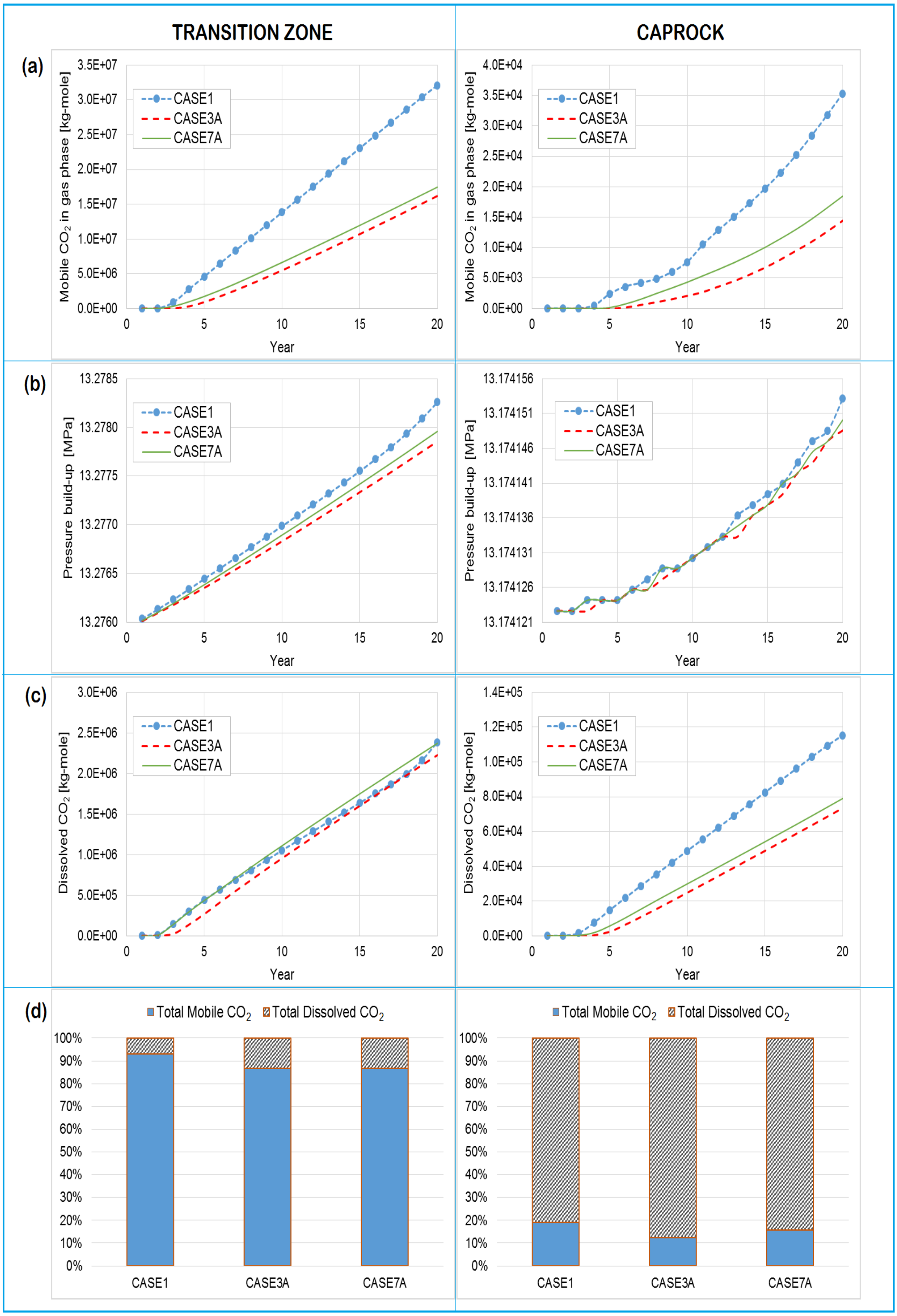

Figure 4.11: Time plots showing: a) mobile CO_2, b) pressure evolution, and c) CO_2 dissolution through the injection period; as well as d) the percentage volume of total dissolved and mobile CO_2 at the 20th year of injection, in the transition zone and the caprock respectively.

In the Bunter-estimate version of Aquifer-2, overpressure in the transition zone varied directly with the mass of free CO_2 in the strata. However, pressure evolution in the overlying caprock did not show such a correlation (Figure 4.11). This disparity was accounted for by the measure of capillary trapped CO_2 within each strata. This is because in pore spaces the incumbent aqueous phase will further dissolve immobilised CO_2 ganglia which can account for the pressure drop (Peters et al. 2015). In other words, the degree of CO_2 dissolution through residual trapping within a strata serves to counteract the impact of mobile CO_2 saturation on the pore fluid pressure (Figure 4.11d). Notwithstanding, the results suggest that pore pressure within caprocks superjacent to graded strata at the reservoir/seal interface will show a lower evolution profile in comparison to those that are further removed. This assumption, however, is mostly valid for a field-scale determination of pressure evolution within the caprock. Generally, higher capillary forces resulting from smaller pore geometry tend to thicken the horizontal gravity current as a result of the reduced effective permeability of the intruding CO_2 (Figure 4.12):

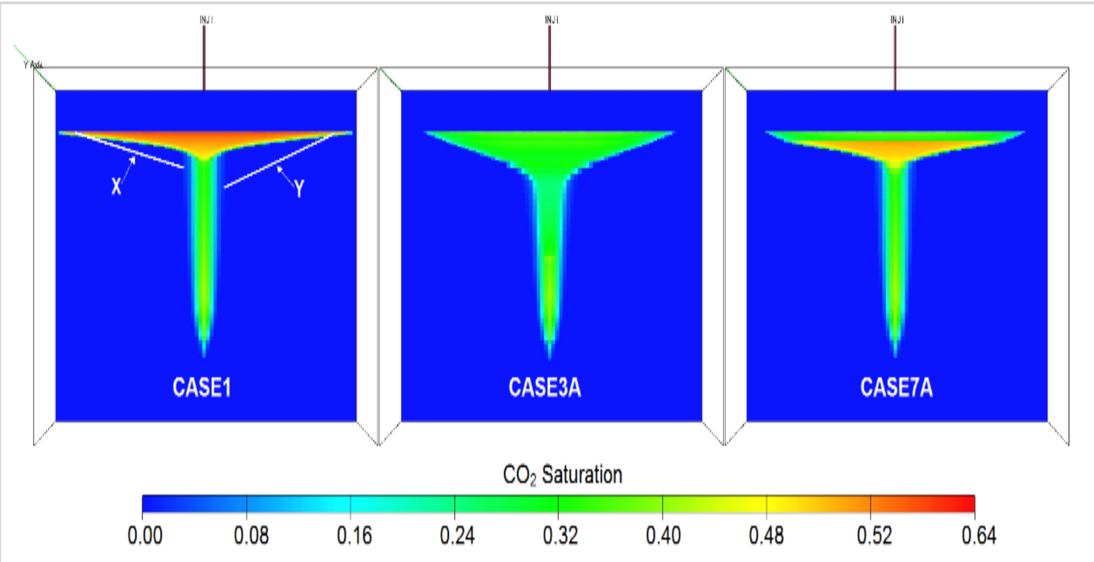

Figure 4.12: A depiction of CO_2 saturation in the 20th year of gas injection. NB: The curves X and Y in Case1 illustrate the trend for gravity current in Case7A and Case3A respectively.

This usually results in a larger capillary fringe, *i.e.* the region occupied by both phases. With constant CO_2 flux, the partial saturation of the non-wetting phase within the capillary fringe increases and thicker horizontal currents contact a greater region of the reservoir (Golding et al. 2013). This has an immediate effect on pressure evolution within the contact area as localised pore pressures increase while the capillary forces within the matrix immobilise the CO_2 ganglia. This phenomenon was notably observed around the injection well within the reservoir and the caprock at the end of the numerical simulation (Figure 4.13):

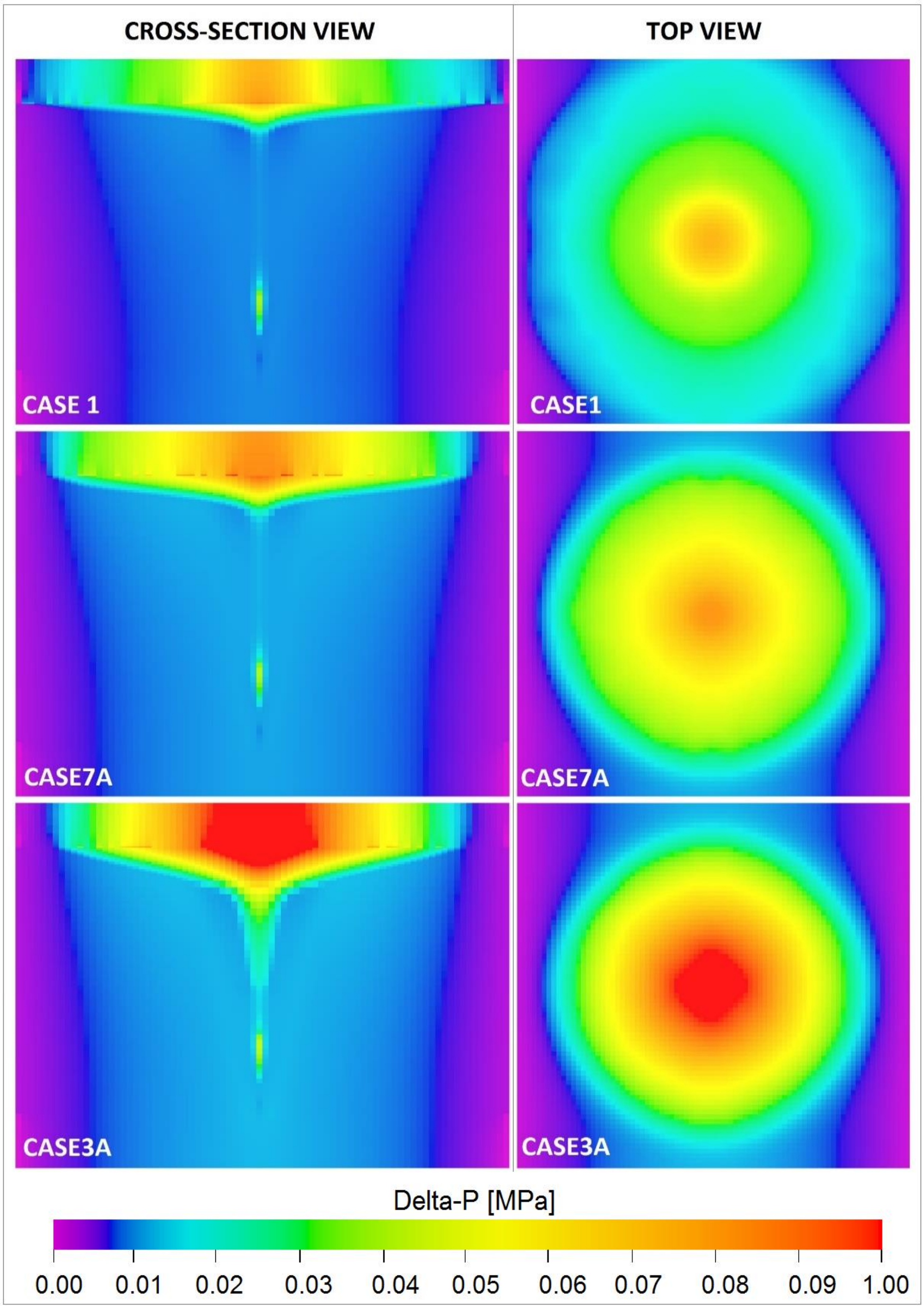

Figure 4.13: 2D illustration of pressure change in the 20th year of CO_2 injection

The reasoning is that within a thinning pore matrix, higher capillary forces correlate to a higher saturation of irreducible brine. The lateral continuity of such a matrix will result in little or no path being available for the migrating CO_2 plume to bypass the constricted strata, hence the gravity current expands beneath it. A consequence is the increased local capillary trapping of the gas within the strata, while the continous flux of the buoyant CO_2 plume results in CO_2 permeability though the region of highest gas concentration. The significance of a laterally continous reservoir-seal gradation zone within a semi-finite aquifer is a higher overpressure around the injection point, thus increasing the magnitude of pressure transmitted in the lower part of the caprock.

4.4 The dome-shaped structural model

The structural model adopted here is the heterogeneous 3D reservoir model developed with cemented sand layers and interbedded shale by James et al. (2016). This serves as an accurate representation of the Bunter aquifer where the 3D model covers an area of 25 km by 25 km (Figure 4.14). The 3D grid was built with a rotation of 45° and grid cells of 200m by 200m in the X, Y direction totalling 681,256 cells (n_i = 124, n_j = 134, n_k = 41) with 603,394 active cells. Grid cells modelled as cemented sands were inactive in the numerical simulation *i.e.* with zero pore volume. Table 4.5 summarises the model's layering scheme and the average modelled permeability and porosity values for sand facies in each reservoir zone.

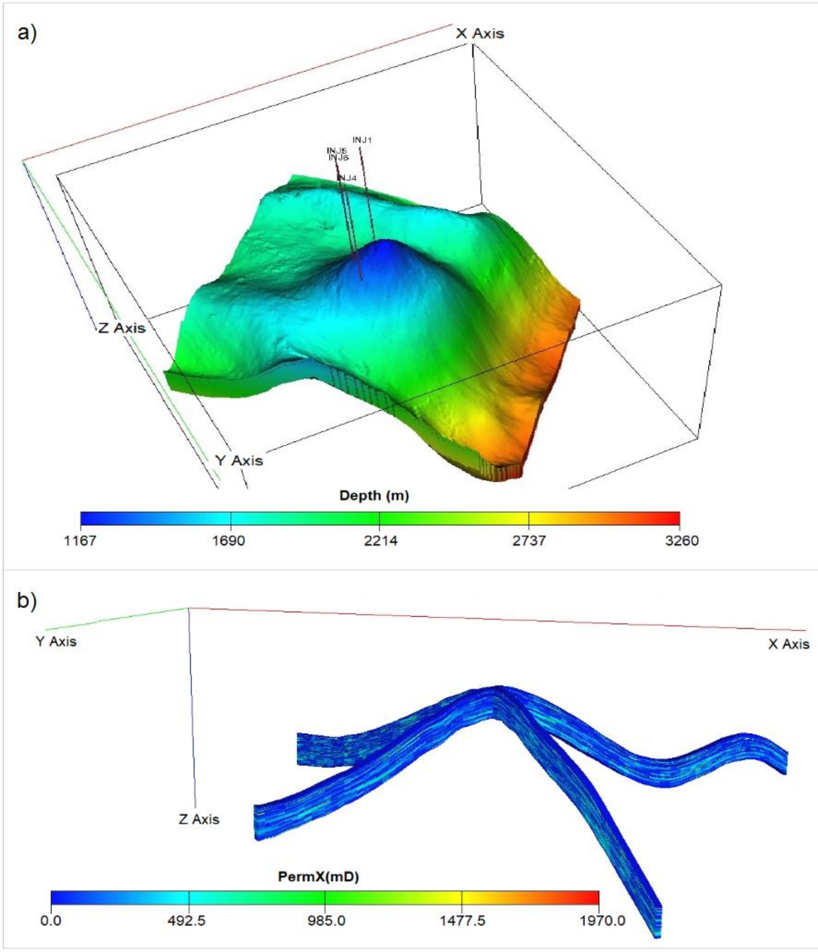

Figure 4.14: Illustration of the dome-shaped structural model developed by James et al. (2016) showing: a) the modelled area, and b) permeability distribution in a cross-section of the store unit.

Zones	***Average thickness (m)***	***Number of layers***	***Average K_h (mD)***	***Average porosity (-)***
Solling Claystone	10	1	0.0065	0.03
R.Zone 1	8	4	233	0.21
R.Zone 2	21	7	219	0.22
R.Zone 3	99	15	195	0.23
R.Zone 4	73	10	223	0.20
R.Zone 5	15	3	162	0.22
Basal Shale	3	1	0.0065	0.03

Table 4.5: Layering for the dome-shaped 3D model. [Adapted from James et al. (2016)]

James et al. (2016) modelled the Solling Claystone as a single sealing layer at the top of the structural model. The first layers in reservoir zones 3 and 4 were cemented sand and shale, respectively, acting as laterally continuous intra-reservoir seals. No fault was included in the 3D model since there was no clear evidence of faulting in the reservoir or primary caprock of the Bunter aquifer. The reservoir formation was modelled with an average sand porosity of 22%, an average sand permeability of 200 mD (maximum 1970 mD), and facies proportions shown in Table 4.6, using a Sequential Guassian Simulation method (Nowak and Verly 2005). The shale facies were assigned porosity and permeability values of 3% and 0.0065 mD, respectively.

Zones	***Sand***	***Shale***	***Cement***
R.Zone 1	0.87	0.03	0.10
R.Zone 2	0.81	0.12	0.07
R.Zone 3	0.80	0.11	0.09
R.Zone 4	0.93	0.06	0.01
R.Zone 5	0.53	0.47	0.00

Table 4.6: Modelled facies proportions. [Source: James et al. (2016)]

The model assumes an isothermal system, a uniform salinity, and a hydrostatically pressured aquifer with an initial reservoir pressure of 11.9 MPa and fracture pressure of 19.7 MPa at the crest of the structure, a depth of 1170 m TVDSS. Four vertical wells are located on the North West flank of the structure penetrating the full upper sandstone sequence and perforated in zones 3 & 4 to inject CO_2 at a combined rate of 7Mt/yr. The injection wells are deviated to maximise the sand-face contact in the store unit. Table 4.7 gives a summary of fluid and rock properties used.

Parameter	***Value***
Aquifer datum depth	1170 m TVDSS
Pressure at datum	11.9 MPa
Temperature	45ºC
Brine salinity	200,000 ppm
CO_2 density at datum	1.87 Kg/m^3
Brine density at datum	1152.16 Kg/m^3
Rock compressibility	4.93 x 10^{-6} 1/MPa
Sandstone Porosity (arithmetic average)	22%
Sandstone Permeability (arithmetic average)	200 mD
Average Kv/Kh ratio	0.36
Fracture pressure gradient	16.8 MPa/km
Bulk rock volume above spill point (~1737 TVDSS)	1.4 x 10^{10} m^3
Reservoir pore volume above spill point (~1737 TVDSS)	2.5 x 10^9 m^3

Table 4.7: Initial conditions and parameters for the dome-shaped structural model. [Adapted from James et al. (2016)]

$P_c - k_r - S_w$ relationships generated for the generic box model in Section 4.3 are utilised in the dome-shaped structural model *i.e.* claystone, sandstone, silty sandstone, muddy sandstone, clayey sandstone, and sandy siltstone. Schlumberger's (2015) ECLIPSE E100 Black Oil module is used for the dynamic simulation of GCS. Shariatipour et al. (2012) and Hassanzadeh et al. (2008) have showed the applicability of the Black Oil reservoir simulator for CO_2 storage in saline aquifers. This involves adapting the Black Oil fluid model to the PVT behaviour of CO_2-brine mixtures where CO_2 and brine properties are described using the gas-phase and oil-phase, respectively.

4.4.1 Sensitivity design

Dynamic simulation of GCS is conducted to observe the impact of heterogeneity in $P_c - k_r - S_w$ relationships, as well as various assumptions of relative permeability functions in the reservoir formation, on CO_2 injectivity and storage capacity. The sensitivity study is outlined in three modules in order to ascertain the effect of the cemented sand layer in the model on CO_2 storage performance. ***Module I*** includes a cemented sand layer situated at the top of R.Zone 3 in the structural model. ***Module II*** and ***III*** replaces the cemented sand layer with a shale layer and an uncemented sandstone layer, respectively. Sensitivity cases in Modules I, II and III are designated X, Y, and Z, respectively, and these cases are labelled according to the description in Table 4.8.

Case ID	***Description***
BASE 0	Sandstone $P_c - k_r - S_w$ functions in the entire reservoir formation
BASE 1	Silty Sandstone $P_c - k_r - S_w$ functions in the entire reservoir formation
BASE 2	Muddy Sandstone $P_c - k_r - S_w$ functions in the entire reservoir formation
BASE 3	Clayey Sandstone $P_c - k_r - S_w$ functions in the entire reservoir formation
BASE 4	Sandy Siltstone $P_c - k_r - S_w$ functions in the entire reservoir formation
CASE 1	Inclusion of $P_c - k_r - S_w$ heterogeneity in the reservoir formation according to permeability values of each grid block
CASE 2	Different $P_c - k_r - S_w$ functions assigned to each intra-reservoir zone

Table 4.8: Description of sensitivity cases in the study

The senstivity cases identified with the prefix BASE adopts a single $P_c - k_r - S_w$ function in all five reservoir zones, while those identified with CASE incorporates heterogeneity in $P_c - k_r - S_w$ functions within the reservoir formation. $P_c - k_r - S_w$ functions adopted in CASE1 are assigned based on average permeability value in each block as described in Table 4.9. Those adopted in CASE2 are based on the average permeability for each intra-reservoir zone (see Table 4.5) using the description of reservoir lithologies in Table 4.4. In other words, the relative permeability functions adopted for R.Zones 1, 2, 3, 4 and 5 are based on the vG-MC descriptions for sandstone, muddy sandstone, clayey sandstone, silty sandstone and sandy siltstone, respectively.

Range of permeability in model (mD)	***Lithology used to define $P_c - k_r - S_w$ functions***
>1600 and ≤1970	Sandstone (S)
>1200 and ≤1600	Silty Sandstone (SiS)
>800 and ≤1200	Muddy Sandstone (MS)
>400 and ≤800	Clayey Sandstone (CS)
≥1 and ≤400	Sandy Siltstone (SSi)
>0 and <1	Claystone (C)

Table 4.9: Description of $P_c - k_r - S_w$ functions in CASE1

4.4.2 Result and discussion

The rate of gas injection in the heterogeneous model was found to be identical for sensitivity cases in Module I & II. Cases in Module III showed a higher cumulative gas injection as a result of prolonged CO_2 injection within the maximum allowable pressure limit. This is attributed to the non-sealing intra Bunter baffle modelled in Module III which increases the pore space available for gas storage. The non-sealing layer at the top of R.Zone 3 prompts an easier dissipation of injection pressure in the store in comparison to Modules I & II with a sealing intra Bunter baffle. The increasing pressure also expands the pore volume that is available for gas injection thereby increasing the storage capacity. Figures 4.15, 4.16 & 4.17 present a summary of these observations using graphical illustrations of the cases designated with the prefix BASE.

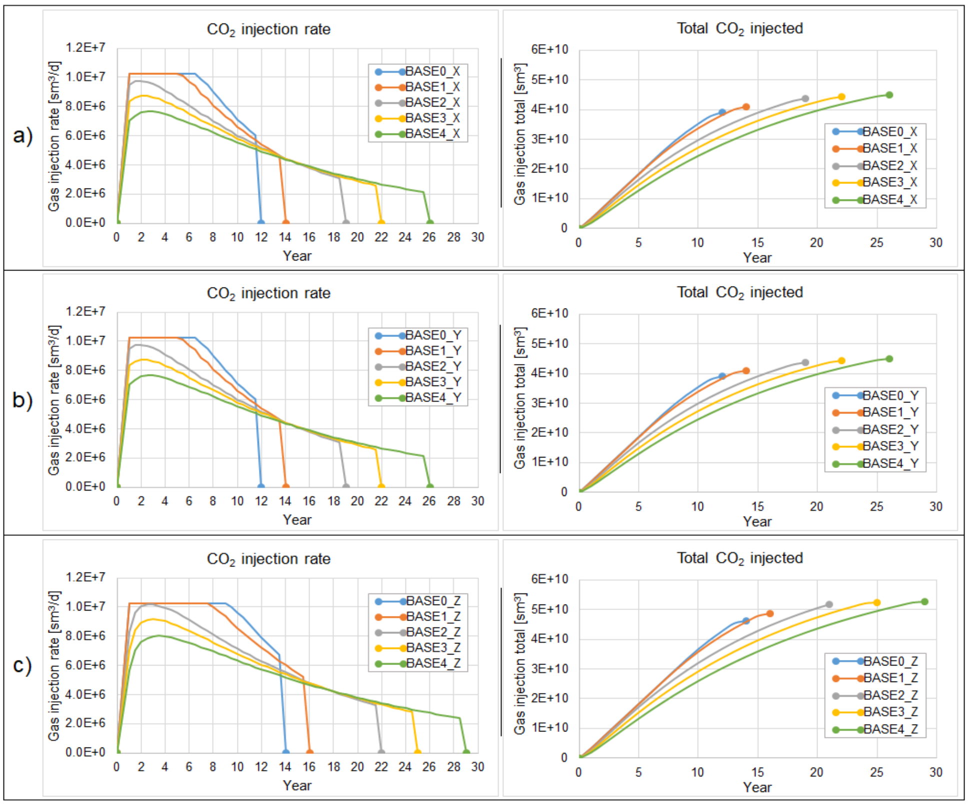

Figure 4.15: CO_2 injection rate and cumulative CO_2 injected for the structural model with a) a cemented sand layer, b) a shale layer, and c) an uncemented sand layer at the top of R.Zone 3

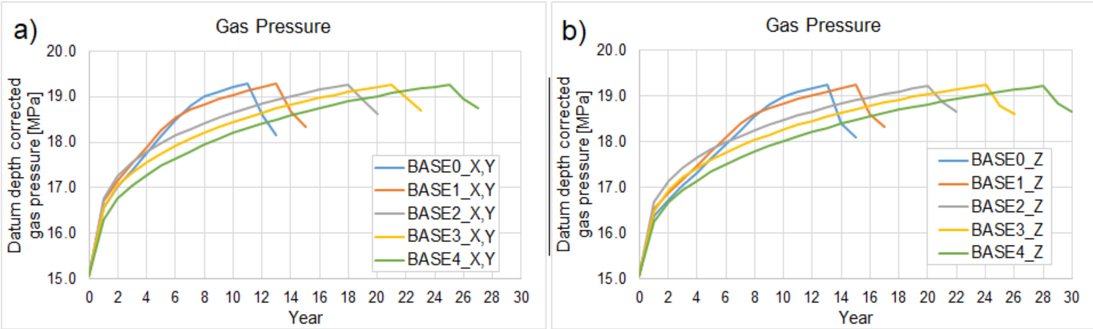

Figure 4.16: Datum corrected gas pressure for BASE cases in a) Module I & II, b) Module III.

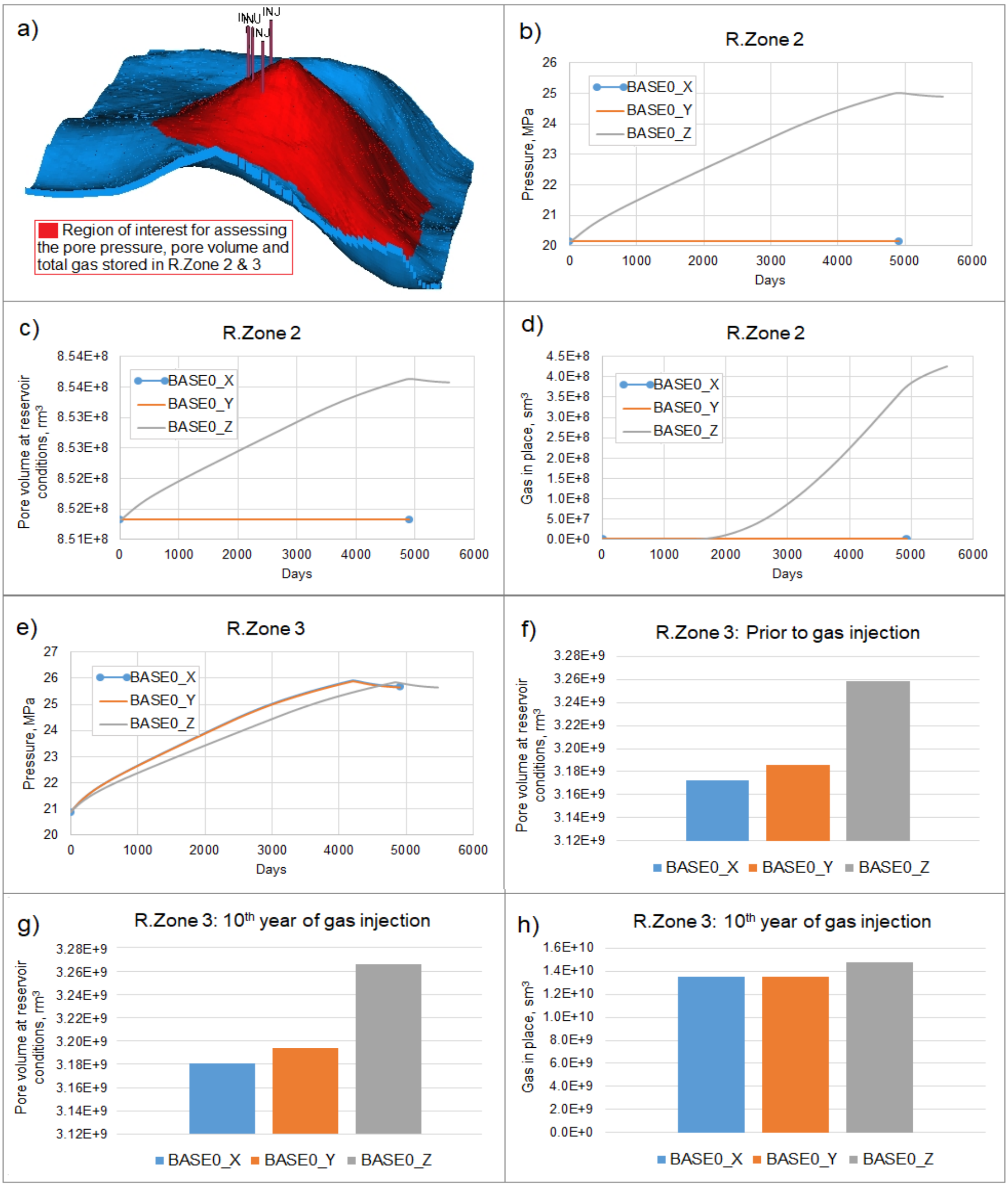

Figure 4.17: Graphical illustration of the pressure, volume, and storage capacity profile within R.Zone 2 & 3 as well as the Bunter dome showing the region of interest for these assessments .

The analysis of Figure 4.15 & 4.16 shows that relative permeability assumptions have a significant impact on pore pressure evolution and how much CO_2 can be injected in the store before the fracture constraint is reached. Referring back to Figure 4.8 in Section 4.3.2.2, the estimation of storage capacity of the BASE cases modelled herein is seen to be directly related to the relative permeability assumptions based on clast size. Here, total CO_2 injected is highest for the sandy siltstone storage unit (BASE4) and lowest for the sandstone unit (BASE0). This is because the migration of pressurised brine is faster in BASE0 than in BASE4, making pore pressure build-up faster in BASE0. Consequently, the pressure constraint is reached earlier resulting in a shorter injection life and reduced injection volume.

In Figure 4.17, an assessment of pore volume, pore pressure and storage capacity focuses on R.Zones 2 & 3 within the Bunter dome, as indicated in Figure 4.17a. The pore pressure evolution in R.Zone 2 of Module III results in an increase in the pore volume at reservoir conditions, while a constant pressure profile in the same zone for Modules I & II results in a constant volume profile. This is due to the pressure communication through the top layer of R.Zone 3, where pressurised brine readily migrates through a non-sealing layer as opposed to a sealing layer. The impact of pressure evolution on the reservoir pore volume is also seen in R.Zone 3 where pore volume increases as pressure increases in all three Modules (Figure 4.17f & g). Note that the additional pore space available in Module III, via the non-sealing intra Bunter baffle, increases the estimation of CO_2 storage in the store (Figure 4.17f & h). This was also seen for sensitivity cases with the prefix CASE in Figure 4.18 below.

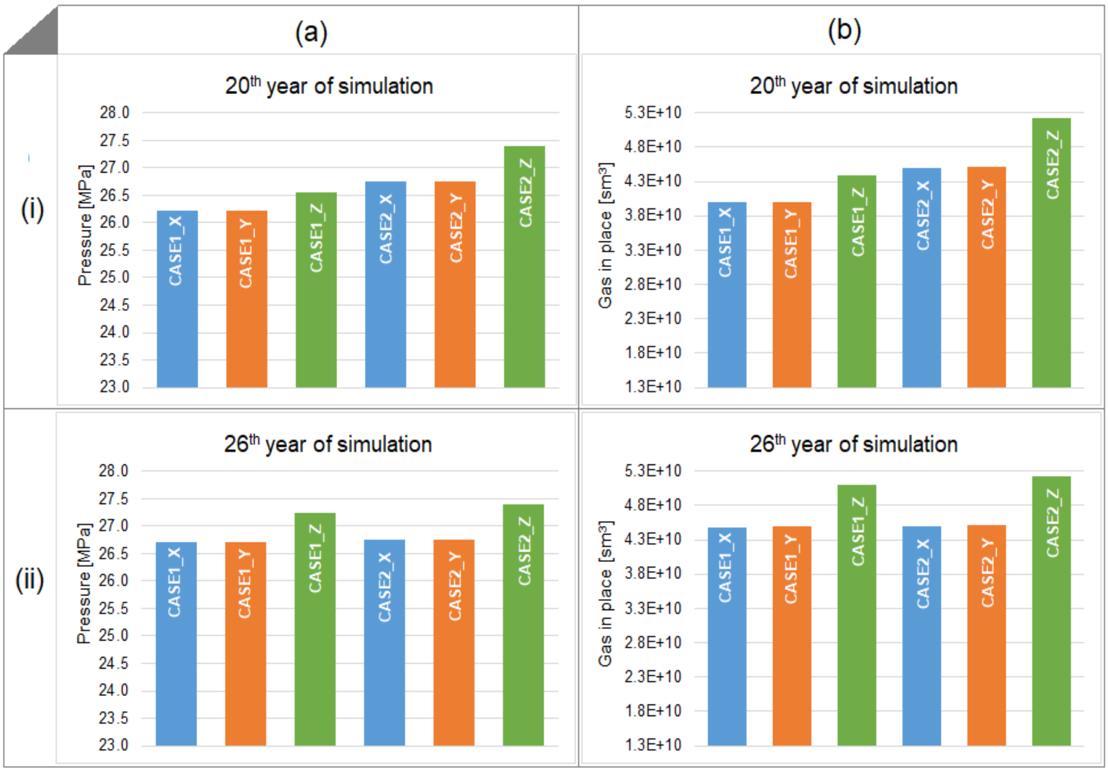

Figure 4.18: a) Pressure and b) CO_2 storage capacity in the reservoir formation for CASEs 1 & 2 at the (i) 20^{th} and (ii) 26^{th} year of simulation

In Figure 4.18, the impact of relative permeability distribution on pressure evolution in the reservoir is noticeable in the 20^{th} year of dynamic simulation. Here the homogeneous distribution of relative permeability functions in the reservoir zone (CASE2) favour pressure propagation over the heterogeneous distribution within each reservoir zone (CASE1). However, in the 26th year of simulation the pressure magnitude appears to be the same for both cases in each Module (Figure 4.18ii). This is attributed to a prolonged injection profile in CASE1 where CO_2 injection continued for six years beyond that of CASE2 (Figure 4.19a).

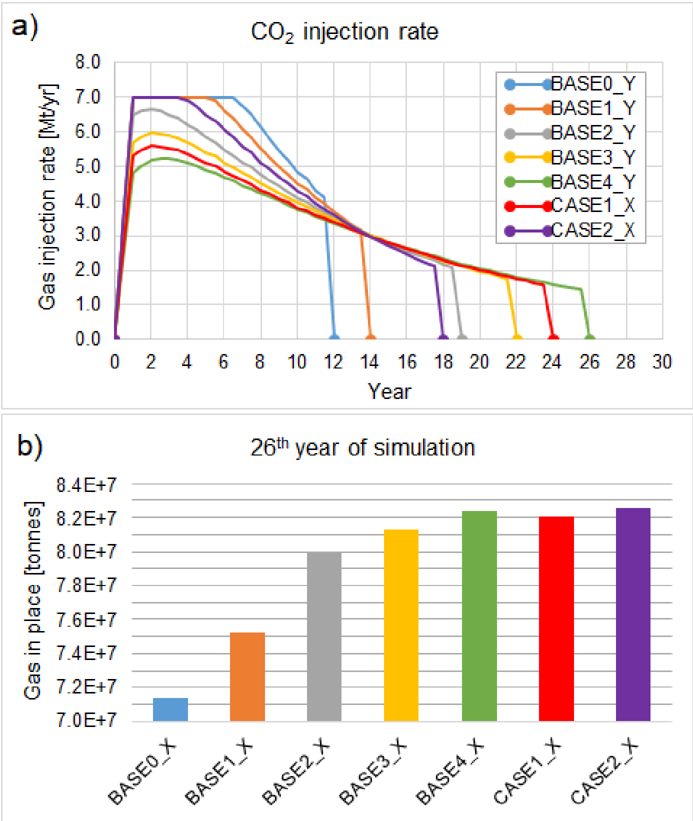

Figure 4.19: The a) injection profile, and b) total CO_2 stored in the 26th year of dynamic simulation of sensitivity cases in Module I.

Figure 4.19 presents a comparison of all sensitivity cases in Module I in order to assess the effect of P_c – k_r – S_w distribution scheme in the formation on CO_2 storage capacity estimation. The injection profile in CASE1 shows a closer similarity to that of BASE3 and BASE4 since the distribution of intrinsic permeability values in the model showed most of the values between 1 and 800 mD (see Figure 4.14b). Hence the harmonisation of diverse relative permeability functions within the reservoir unit, *i.e.* CASE1, could be essentially modelled using either BASE3 or 4 (refer to Table 4.8 & 4.9). When the total gas that can be injected within the allowable fracture pressure is assessed at the end of simulation, a closer match in the estimated volume of CO_2 stored is recorded for CASE1, CASE2 and BASE4 (Figure 4.19b). This indicates that the homogeneity of k_r – S_w functions in a storage formation can be effectively described using either approximations within intra-reservoir zones or a quantitive analysis of petrographic data in the entire storage unit.

4.5 Summary and conclusion

Numerical modelling of CO_2 geosequestration is to a large extent dependent on the quality of the quantitative knowledge of the geological descriptions used to construct the reservoir model. Through relating fluid and transport processes to primary sedimentary structures in siliciclastic formations, numerical simulation was employed to probe the effects of heterogeneous dynamic flow parameters on CO_2 storage performance. The results emphasise the significance of enhancing geological details in reservoir-specific models. Specifically, the importance of modelling heterogeneity in the capillary pressure and relative permeability functions. For CO_2 storage in geological formations, the reservoir injectivity and trapping mechanisms are sensitive to gradational changes at the reservoir-seal interface as well as within the reservoir. Clast-size gradation from coarser- to finer-grained sediments within the reservoir leads to more favorable capillary trapping scenarios for CO_2 sequestration, irrespective of the boundary conditions. Gradation further increases the opportunity for CO_2 dissolution during the injection phase. Hence, the presence of these structures is vital in numerical models that investigate the post-injection sequestration processes. The measure of how such sedimentary structures influence CO_2 storage will not be adequately determined if their description is based on the permeability and porosity data alone. This is based on the observation that the relative permeability data essentially dictates the effective permeability of fluids in a porous media. The presence of a gradational contact at the reservoir-seal interface can also influence storage security.

The analysis in this chapter showed that for an open aquifer, the lateral continuity of such structures will likely reduce the field-scale overpressure in the caprock by mitigating brine migration into the seal. However, this could also increase localised pore pressures centred on the injection point within the caprock. Such scenarios can lead to the hydraulic fracturing of structural traps within the injection point, especially at the base of the trapping unit (Rozhko et al. 2007). Gradation at the reservoir-seal interface may then be said to improve field-scale CO_2 storage security while also diminishing local-scale caprock integrity. This creates a paradoxical impact of gradation on structural trap integrity and further goes to highlight the importance of including such geological detail in numerical simulation studies.

Relative permeability is a key parameter that influences injectivity performance and the estimation of CO_2 storage capacity. Capacity can vary depending on which relative permeability assumptions were used in the storage formation. In the presence of intra reservoir baffles, non-sealing layers situated above the injection zones have the effect of providing access to more space for pressure dissipation to occur. This enables a prolonged period before the maximum allowable pressure limit is reached and an enhanced capacity estimation. However, the migration of pressurised brine through this space and subsequent storage of CO_2 highly depends on the relative permeability defined for the rock matrix. In conclusion, numerical analysis which disregards the sensitivity of geological detail in the model to multi-phase fluid transport processes will fail to sufficiently account for CO_2 storage performance. The next chapter considers the impact of capillary pressure and relative permeability heterogeneities on pressure response in the caprock during CO_2 injection.

CHAPTER 5[‡]

The effect of sedimentary heterogeneities in the sealing formation on pore pressure prediction

The observation of pressure dissipation across the storage and sealing formation is relevant for storage capacity and geomechanical analysis during CO_2 injection. This chapter evaluates the relevance of relative permeability variations in the sealing formation when modelling geological CO_2 sequestration processes. Numerical simulations herein focus on gradational changes in the lower part of the caprock, particularly how they affect pressure evolution within the entire sealing formation when represented by relative permeability functions. The caprock plays an important role in geological carbon sequestration (GCS) in terms of its structural integrity, thus investigating pressure evolution in these rocks during GCS permits the assessment of this property.

The results demonstrate the importance of pore size variations in the mathematical model adopted to generate the characteristic curves for GCS analysis. Gradational changes at the base of the caprock influence the magnitude of pressure that propagates vertically into the caprock from the aquifer, especially at the critical zone (*i.e.* the region overlying the CO_2 plume accumulating at the reservoir-seal interface). A higher degree of overpressure and CO_2 storage capacity was observed at the base of caprocks that showed gradation. These results illustrate the need to obtain reliable relative permeability functions for GCS, beyond just permeability and porosity data.

[‡] The content of this chapter has been extracted from the following paper:

Onoja, M.U., Williams, J.D.O., Vosper, H., and Shariatipour, S.M. (2019) Effect of sedimentary heterogeneities in the sealing formation on predictive analysis of geological CO_2 storage. *International Journal of Greenhouse Gas Control* **82**, 229–243. https://doi.org/10.1016/J.IJGGC.2019.01.013

The candidate set the scientific scope of the work, devised and developed the methodology, performed all data analysis and wrote the text. The co-authors provided guidance during the design of this part of the project and feedback on the manuscript.

Minor adaptations have been performed to streamline the layout of the thesis.

5.1 Introduction

CO_2 injection into an aquifer increases the pore pressure, producing an expansion of the aquifer and changing the effective stress field (Ducellier et al. 2011). Due to the coupled hydromechanical effect that occurs during injection, pressure propagates from the aquifer into the caprock deforming both formations (Handin et al. 1963). Strain acting laterally can increase lateral stresses while vertical strain can cause an extension at the top of the caprock close to the well. The overpressure-induced surface heave observed around injection wells at the In Salah CO_2 storage project in Algeria (Rutqvist et al. 2010) is an example of this vertical strain. Analysing caprock integrity usually relies on predictions from reservoir and geomechanical models, where the former provides pressure data for the latter.

The mechanisms for gas transport through mudrocks can be categorized as pressure-driven volume flow of mobile gas phase and transport of dissolved gas either by molecular diffusion or advective flux of brine. The importance of diffusive and advective transport mechanisms in mudrocks has been addressed by Schlömer and Krooss (1997), Krooss et al. (1992), and Busch et al. (2008). However, the pressure-driven volume flow (Darcy flow) is considered the most efficient transport mechanism (Amann-Hildenbrand et al. 2015). In CO_2/brine/rock systems, the pressure-driven flow of mobile gas phase entails the visco-capillary two-phase flow which describes the displacement of the wetting brine phase in the original porosity of the rock fabric by the non-wetting gas phase under the influence of capillary and viscous forces (Bear 1972). This pressure driven-flow could also result in gas flow along micro- and macro- fractures within the mudrock. The former describes dilatancy-controlled gas flow resulting from an inability of the mudrock to withstand persistent gas-pressures with a magnitude that surpasses the minimum principal stress acting on the rock mass (Horseman et al. 1996), while the latter describes gas flow initiated when the magnitude of gas pressure surpasses the sum of the minimum principal stress and the tensile strength of the rock (Valko and Economides 1997). In such scenarios, the capillary gas entry pressure becomes the controlling factor for the two-phase flow characteristics of a porous medium.

Caprocks possess a smaller pore throat matrix as well as a higher percentage of immobile water within the matrix than reservoir rocks. As such, the capillary entry pressure required to initiate gas flow in water saturated mud sealing rocks can be extremely large due to the presence of fine-grained clasts in these rocks (Harrington and Horseman 1999). Notwithstanding, the bulk gas flow at the reservoir-seal interface can initiate dilatant flow in the mudrock before the capillary entry pressure is exceeded. This can be achieved through the opening/widening of the interspaces of the clay matrix (e.g. Skurtveit et al. 2012, Horseman et al. 1999, Angeli et al. 2009). The aperture of these dilatant pathways are a function of the internal gas pressure and structural constraint within the clay, which can be attributed to the ability of water films within its fabric to conduct stress (Lambe 1960). Once gas flow is initiated in the porous media, its mobility is usually determined by the permeability of the formation and the $P_c - k_r - S_w$ relationships (Marschall et al. 2005). This suggests a functional dependency of pressure distribution within sedimentary formation on the rock's microstructural features, such as the pore size distribution or average grain size (Bihani and Daigle 2019). A number of numerical simulations on CO_2 injection into saline aquifer sandstones have utilised this function using a variety of approaches, e.g. the hydrodynamic behaviour of CO_2 (Doughty 2010), the combined effects of capillary pressure and salinity (Alkan et al. 2010), the effects of interlayer communication through seals (Birkholzer et al. 2009), the major trapping mechanism in Mt. Simon Sandstone Formation (Liu et al. 2011), the effects of well orientation (Okwen et al. 2011), and the effects of gridding (Yamamoto and Doughty 2011). Rutqvist and Tsang (2002) showed that hydromechanical changes in the caprock occur in the basal unit, especially near the injection well (injection zone). The authors described a sandstone aquifer beneath a shale caprock using a value of 0.457 to represent the vG's pore size distribution index [*m*] for both the reservoir and seal formations. Their simulation study, as well as those from aforementioned examples, overlooked the likely importance the interpretation of the parameter, *m*, will have on fluid dynamics in sedimentary formations.

5.2 Problem Statement

In petroleum literature, saline formations have not been investigated as much as oil and gas formations. A consequence of this is limited laboratory and field data results and greater uncertainty in the engineering designs for saline formations. For example, an analysis of the capillary sealing behaviour of N_2, CO_2, CH_4 obtained the lowest values for CO_2/brine/rock systems (Hildenbrand et al. 2004, Li et al. 2005), suggesting that sealing mudrocks that were effective for hydrocarbons may not have the same retention capacity for CO_2. Available laboratory and field data indicate that mudrock permeabilities vary by three orders of magnitude at a given porosity and this variance could be attributed to the pore throat size distribution as well as the clay content of the mudrock (Dewhurst et al. 1999, Yang and Aplin 2010). Generally, gas migration through the water-wet caprock will be initiated when the gas pressure in the reservoir exceeds the capillary entry pressure. Any resulting fracture-controlled flow of CO_2 will be influenced by its effective permeability, which is likely to be higher for silt-rich than clay-rich mudrocks (Dewhurst et al. 1998). A common practice in reservoir simulation is adopting a single $P_c - k_r - S_w$ curve for an entire mudrock column overlying a storage formation. This may not be ideal, especially for lithostratigraphic units such as the Mercia Mudstone Group (MMG) in the East Irish Sea, which is mainly composed of claystones and siltstones (Seedhouse and Racey 1997).

In an experimental investigation on the capillary sealing properties of nine high quality sealing mudrock samples, Amann-Hildendrand et al. (2013) observed that only a small proportion, *i.e.* a narrow horizontal band, of the rock fabric was exposed to the permeating fluid/CO_2 after the capillary entry pressure was exceeded. This was attributed to the dependency of the effective gas permeability on the capillary pressure curve. At the basin scale, the fraction of rock fabric exposed to the permeating CO_2 could be interpreted as the reservoir/seal interface. Since the capillary pressure-controlled properties are associated with the pore size distribution and wettability, the lithology and mineral composition of the mudrock at the reservoir/seal interface becomes important when estimating the capillary sealing efficiency of the caprock overlying potential CO_2 storage sites. The MMG, which overlies potential CO_2 storage formations such as the Sherwood Sandstone Group and its North Sea equivalent, the Bunter Sandstone Formation (Noy et al. 2012, Williams et al. 2018), serves as a good example. At the reservoir/seal interface, transitional lithologies commonly exist between the Sherwood Sandstone and the Mercia Mudstone (Newell and Shariatipour 2016, Seedhouse and Racey 1997, Shariatipour et al. 2016a). This lithology is characterised by interbedded claystone, siltstones and medium- to fine- grained sandstones of approximately equal proportions (Hobbs et al. 2002). Onshore UK, the transitional interface is referred to as the Tarporley Siltstone Formation which forms the basal formation of the Mercia Mudstone Group with gradational changes up to 60 m in the East Midlands Shelf, up to 220 m in the Cheshire Basin, and up to 70 m in the Stafford Basin (Howard et al. 2008). With Bennion and Bachu's (2008) demonstrating that relative permeabilities for *in situ* fluids within a storage location can follow different curves, the classical two-phase flow concept in mudrocks may need refining, with respect to the P_c – k_r – S_w functions in variable mudrock lithologies that could occur within a sealing formation. Shariatipour et al. (2016b) showed that a highly permeable layer at the reservoir-seal interface can contribute to pressure diffusion across the reservoir. The authors indicated that such permeability usually results from weathering, particularly at unconformity surface, and the reservoir-seal interface could be regarded as a continuing unit of the reservoir's top or the caprock's base. Hence, it becomes important that reservoir simulations for CO_2 sequestration adequately describe relative permeability functions at the top of the aquifer and/or the base of the caprock. This is because flow characteristics within either region could differ from the bulk properties of the entire corresponding formation. This chapter focuses on the impact of sedimentary heterogeneity, duly represented by intrinsic permeability and relative permeability functions, in the lower part of the caprock on pressure evolution within the sealing formation.

5.3 Model Characteristics

5.3.1 Model Description

A two-dimensional (2D) radially symmetric model domain with a radial extent of 6 km was chosen to represent the aquifer-caprock system and investigate the impact of boundary conditions, while ensuring that the mobile CO_2 plume during injection does not reach the lateral boundary of the domain. A storage formation, located at a depth of approximately 1000 m below the ground surface, is 200 m thick and bounded at the top by a 200 m thick caprock sealing unit. The upper and lower boundaries of the domain have no flow conditions. Two observation zones identified as Region 1 and Region 2 (see Figure 5.1) are used to represent the zones of reference above the perforated injection interval, as implemented for this study. A single vertical injection well is located at r = 0 with CO_2 injection operating over 20 years at a rate of 48 kg/s (*i.e.* annual rate of 1.5 million tonnes of CO_2). The aquifer is initially fully saturated, assuming a hydrostatic fluid pressure distribution and a salinity of 300,000 ppm. Isothermal conditions are modelled using a uniform temperature of 33°C. Schlumberger's (2015) ECLIPSE multiphase code is used for the dynamic simulation of supercritical CO_2 ($scCO_2$) displacing brine. The allowable bottom-hole-pressure (BHP) is set to 75% of a lithostatic pressure gradient assumed to be 22.5 MPa/km (after Noy et al., 2012). This is ~90% of the minimum horizontal stress magnitude in the East Irish Sea Basin as estimated by Williams et al. (2018).

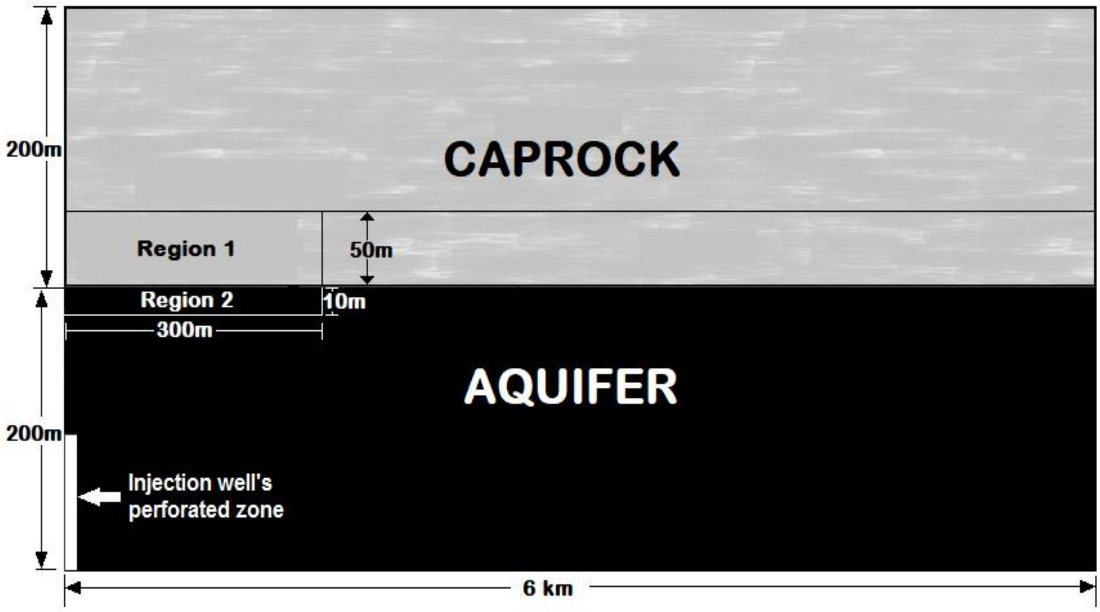

Figure 5.1: Schematic description of the model geometry in the r-z cross section, where Regions 1 and 2 are observation zones in the study. Not to scale.

In order to accurately approximate the magnitude of expected fluid pressure increase resulting from CO_2 injection, cells towards the top of the reservoir and at the base of the caprock are thinner. Within the reservoir-seal interval the thinnest cells are 0.01 m thick while the average cell thickness within the model is 1 m. The petrophysical properties of the aquifer are based on the Sherwood Sandstone Group of the South Morecambe gas field, East Irish Sea Basin (Bastin et al. 2003). Table 5.1 lists the assigned hydrogeological properties typical of a homogeneous saline aquifer that is suitable for GCS. The aquifer is assumed to be a fully water-wet sandstone formation with a maximum pore throat radius of 37 microns and CO_2/brine interfacial tension of 30 mN/m. The assumed value for maximum pore throat radius falls within the range of dominant pore throat sizes of Permo-Triassic sandstones in the United Kingdom (Bloomfield et al. 2001).

Parameter	***Aquifer***
Porosity, Ø (%)	14
Permeability (mD)	150
Permeability anisotropy	0.1
Gas entry pressure, P_e (kPa)	1.6
Irreducible brine saturation, S_{wr}	0.3
Pore compressibility (bar^{-1})	4.5×10^{-5}
Maximum relative permeability to CO_2, k_o	0.584

Table 5.1: Static parameters assumed in the modelled domain

5.3.2 Sensitivity study design

Using a set of simulation scenarios, this chapter aims to evaluate the degree to which a gradation at the base of a sealing caprock will affect the magnitude of pressure that propagates into the sealing formation as a result of $scCO_2$ injection in the underlying reservoir. For the purpose of this study, the 'transition zone' henceforth refers to the region of gradational changes at the lower part of the caprock. A set of graded orientation identified as coarse- to fine-, fine- to coarse-, and coarse- to fine- to coarse-textured sediments is constructed within a transition zone with varying thickness of 0.1m, 1m, 10m, 20m and 50m. A total of six different caprock lithologies, namely claystone, sandy claystone, mudstone, siltstone, sandy siltstone and clayey sandstone are used to help define flow characteristics within the caprock formation.

This study describes claystone, sandy claystone and mudstone as finer lithologies while siltstone, sandy siltstone and clayey sandstone are identified as coarser lithologies. All lithologies are modelled under the assumption of a single value for capillary entry pressure in all variations, *i.e.* 172 kPa. This assumes that each lithology type possesses the same diameter of largest pore throat on the exterior of the stratum in contact with the displacing fluid. The pore geometry parameter [*n*] then defines the variable capillary pressure curve for each lithological unit (Table 3.3). Residual CO_2 saturation, an important parameter for imbibition curves to model residual trapping, is not computed for the variable lithologies since the study is focused on the drainage cycle. Assumed values for residual brine saturation are based on Bennion and Bachu's (2008) experimentally measured relative permeability characteristics for supercritical CO_2 displacing brine from low permeable shale, carbonate and limestone rock samples. Endpoint CO_2 relative permeabilities are computed using Eq. 2.44, *i.e.* the relationship proposed by Standing (1975). The heterogeneous properties of the caprock lithologies are listed in Table 5.2, where a single porosity of 4.4% is assumed for the caprock lithologies with permeability values ranging from 2.23 x 10^{-4} mD to 7.88 x 10^{-5} mD, linearly characterised by their clay content. This hypothesis is supported by existing data that suggests a log-linear relationship between permeability and porosity over a wide range of mudstones with dataset of measured permeabilities spanning approximately 1 order of magnitude at a single porosity value provided the clay content and mean pore throat radius of the mudstones are known (Yang and Aplin 2007, 2010). Armitage et al. (2016) further demonstrated that the lower the clay content, the higher the permeability at the same porosity, and provided a compilation of Kv/Kh ratio for six Mercia Mudstone core samples which vary between 0.493 and 0.852. Based on this range, the permeability anisotropy in the caprock is assumed to be 0.5.

The coupled van Genutchen-Mualem-Corey (*vG-MC*) model (Eq. 3.1–3.4) is used to describe the retention behaviour of the rocks and the k_r of brine and CO_2.Tables of k_r–S relations used in the numerical simulations are shown in Figure 5.2. In accordance with the k_r–S functions computed for the caprock lithologies, claystone is regarded as the most compact lithology with the highest impedance on fluid flow, followed by sandy claystone then mudstone, siltstone, sandy siltstone and finally clayey sandstone. All properties of the reservoir are identical in all the sensitivity cases while the caprock lithologies within the basal transition zone are modelled with an equal fraction of thickness for each case. Sensitivity simulations conducted herein are listed in Table 5.3.

Caprock lithology	***vG-MC pore size index, m (where m = 1 – 1/n)***	***Intrinsic Permeability, K (mD)***	***Residual brine saturation (S_{wr})***	***Maximum relative permeability to CO_2 (k_o)***
Claystone	0.083	7.88×10^{-5}	0.605	0.128
Sandy Claystone	0.187	4.23×10^{-5}	0.595	0.141
Mudstone	0.237	1.72×10^{-5}	0.569	0.175
Siltstone	0.270	8.21×10^{-4}	0.558	0.191
Sandy Siltstone	0.291	5.37×10^{-4}	0.492	0.287
Clayey Sandstone	0.324	2.23×10^{-4}	0.476	0.312

Table 5.2: Heterogeneous properties of the caprock lithologies

Case ID	***CAPROCK***		
	Extensive top unit (m)	***Basal transition unit (m)***	***Lithology from the top to base***
BASE	200	0	Claystone
CASE1_0.1m	199.9	0.1	Claystone (Top unit) Sandy Claystone Mudstone Siltstone Sandy Siltstone Clayey Sandstone
CASE1_1m	199	1	
CASE1_10m	190	10	
CASE1_20m	180	20	
CASE1_50m	150	50	
CASE2_0.1m	199.9	0.1	Claystone (Top unit) Clayey Sandstone Sandy Siltstone Siltstone Mudstone Sandy Claystone
CASE2_1m	199	1	
CASE2_10m	190	10	
CASE2_20m	180	20	
CASE2_50m	150	50	
CASE3_0.1m	199.9	0.1	Claystone (Top unit) Sandy Claystone Mudstone Siltstone Sandy Siltstone Clayey Sandstone
CASE3_1m	199	1	
CASE3_10m	190	10	

CASE3_20m	180	20	Sandy Siltstone Siltstone Mudstone Sandy Claystone Claystone
CASE3_50m	150	50	
CASE4_0.1m	199.9	0.1	Claystone (Top unit) Sandy Siltstone Siltstone Mudstone Sandy Claystone Claystone Sandy Claystone Mudstone Siltstone Sandy Siltstone Clayey Sandstone
CASE4_1m	199	1	
CASE4_10m	190	10	
CASE4_20m	180	20	
CASE4_50m	150	50	

Table 5.3: Description of the primary sensitivity simulations conducted in the study. NB: The lithologies at the basal transition interface of cases1-4 have an equal fraction of thickness.

RESERVOIR SANDSTONE		
Sw	Krw	Krg
1.000	1	0
0.960	5.12E-01	2.26E-04
0.920	3.40E-01	1.75E-03
0.880	2.33E-01	5.74E-03
0.840	1.61E-01	1.32E-02
0.800	1.10E-01	2.49E-02
0.760	7.41E-02	4.16E-02
0.720	4.88E-02	6.38E-02
0.680	3.12E-02	9.18E-02
0.640	1.92E-02	1.26E-01
0.600	1.12E-02	1.66E-01
0.560	6.11E-03	2.12E-01
0.520	3.03E-03	2.64E-01
0.480	1.32E-03	3.21E-01
0.440	4.68E-04	3.83E-01
0.400	1.18E-04	4.48E-01
0.360	1.47E-05	5.17E-01
0.300	0	5.84E-01

CLAYEY SANDSTONE		
Sw	Krw	Krg
1.000	1	0
0.970	1.89E-01	1.14E-04
0.940	9.29E-02	8.83E-04
0.910	4.96E-02	2.89E-03
0.870	2.21E-02	8.35E-03
0.840	1.20E-02	1.51E-02
0.810	6.30E-03	2.44E-02
0.770	2.52E-03	4.12E-02
0.740	1.19E-03	5.73E-02
0.710	5.17E-04	7.65E-02
0.670	1.44E-04	1.07E-01
0.640	4.64E-05	1.33E-01
0.605	9.28E-06	1.67E-01
0.595	5.41E-06	1.77E-01
0.569	1.04E-06	2.05E-01
0.558	4.50E-07	2.17E-01
0.492	8.33E-12	2.93E-01
0.476	0	3.12E-01

SANDY SILTSTONE		
Sw	Krw	Krg
1.000	1	0
0.970	1.43E-01	1.15E-04
0.940	6.47E-02	8.91E-04
0.910	3.21E-02	2.91E-03
0.870	1.29E-02	8.40E-03
0.840	6.45E-03	1.51E-02
0.810	3.11E-03	2.44E-02
0.770	1.09E-03	4.12E-02
0.740	4.54E-04	5.73E-02
0.710	1.71E-04	7.64E-02
0.670	3.76E-05	1.06E-01
0.640	9.55E-06	1.32E-01
0.605	1.30E-06	1.65E-01
0.595	6.53E-07	1.75E-01
0.569	7.62E-08	2.02E-01
0.558	2.44E-08	2.14E-01
0.492	0	2.87E-01

SILTSTONE		
Sw	Krw	Krg
1.000	1	0
0.970	1.04E-01	1.15E-04
0.940	4.11E-02	8.89E-04
0.910	1.77E-02	2.89E-03
0.870	5.83E-03	8.27E-03
0.840	2.43E-03	1.48E-02
0.810	9.45E-04	2.38E-02
0.770	2.30E-04	3.97E-02
0.740	6.74E-05	5.48E-02
0.710	1.60E-05	7.23E-02
0.670	1.42E-06	9.94E-02
0.640	1.20E-07	1.22E-01
0.605	1.47E-09	1.50E-01
0.595	2.22E-10	1.59E-01
0.569	1.52E-14	1.81E-01
0.558	0.00E+00	1.91E-01

MUDSTONE		
Sw	Krw	Krg
1.000	1	0
0.970	7.09E-02	1.14E-04
0.940	2.49E-02	8.80E-04
0.910	9.64E-03	2.86E-03
0.870	2.71E-03	8.17E-03
0.840	9.86E-04	1.46E-02
0.810	3.29E-04	2.34E-02
0.770	6.25E-05	3.91E-02
0.740	1.45E-05	5.38E-02
0.710	2.55E-06	7.09E-02
0.670	1.28E-07	9.72E-02
0.640	5.46E-09	1.19E-01
0.605	1.25E-11	1.46E-01
0.595	6.79E-13	1.54E-01
0.569	0.00E+00	1.75E-01

SANDY CLAYSTONE		
Sw	Krw	Krg
1.000	1	0
0.970	3.25E-02	1.10E-04
0.940	8.88E-03	8.46E-04
0.910	2.66E-03	2.74E-03
0.870	5.11E-04	7.80E-03
0.840	1.33E-04	1.39E-02
0.810	3.00E-05	2.22E-02
0.770	2.94E-06	3.69E-02
0.740	3.56E-07	5.05E-02
0.710	2.65E-08	6.62E-02
0.670	2.21E-10	9.01E-02
0.640	7.25E-13	1.10E-01
0.605	3.52E-20	1.34E-01
0.595	0.00E+00	1.41E-01

CLAYSTONE		
Sw	Krw	Krg
1.000	1	0
0.970	1.48E-03	1.07E-04
0.940	1.32E-04	8.26E-04
0.910	1.19E-05	2.67E-03
0.870	3.56E-07	7.60E-03
0.840	1.81E-08	1.35E-02
0.810	6.19E-10	2.16E-02
0.770	2.89E-12	3.57E-02
0.740	2.03E-14	4.88E-02
0.710	4.06E-17	6.39E-02
0.670	2.88E-22	8.66E-02
0.640	6.49E-29	1.05E-01
0.605	0.00E+00	1.28E-01

Figure 5.2: k_r – S tables used in the study

5.4 Results and discussion

In order to compare the pressure profile for a caprock with a basal transition zone and one without, numerical simulations of CO_2 injection into an underlying homogenous aquifer are initiated within closed and open boundary conditions. Modelling of the closed and open systems entail no-flow conditions and flow conditions at the 6 km lateral boundary, respectively. Simulations are run within two different scenarios; the first defines sedimentary heterogeneities in the basal transition zone of the caprock using relative and intrinsic permeability values, herein identified as "***K + k_r***", while the second defines heterogeneity using only intrinsic permeability values, herein identified as "***only K***". This is done to compare the influence of parametric representation of heterogeneity on the predictive analysis of caprock pressurisation during CO_2 storage.

The results are analysed below:

5.4.1 Closed system

The CO_2 saturations within the reservoir for all the sensitivity cases of the model are practically identical and presented in Figure 5.3:

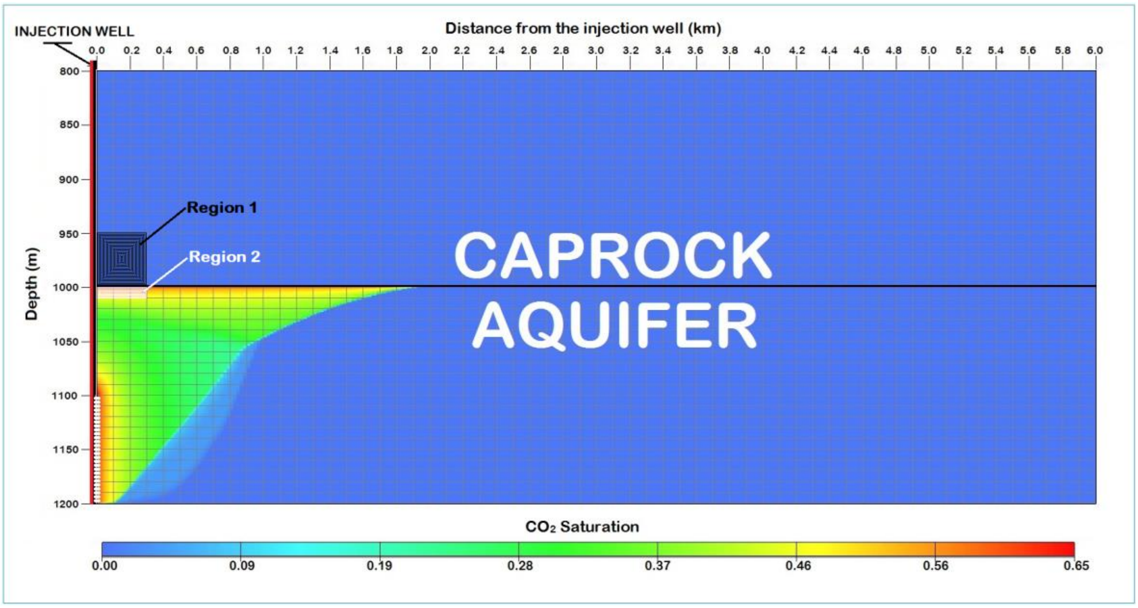

Figure 5.3: CO_2 distribution at the end of the 20-year injection period for all sensitivity cases

The absence of geological barriers to vertical flow within the aquifer enhances an upward migration of the buoyant plume to the top of the aquifer. Here the rising plume is restricted by the impervious caprock and spreads out laterally beneath the caprock. $scCO_2$ injection in the reservoir induces fluid pressure that increases monotonically with time (Figure 5.4). The results show a decline in the injection rate from approximately the 11^{th} year of CO_2 injection as the pore fluid pressure reaches the well control pressure. The rate of gas injection in the aquifer is the same and constant for all cases pre-decline. This is predictable since all cases possess the same aquifer properties. However, the post-decline of the injection rate shows a negligible difference in curvature among the following set of cases: (BASE; CASE3_50m; CASES with transition zone thickness of 0.1m & 1m), and (CASE1_10m, 20m; CASE2_10m, 20m, 50m; CASE3_10m, 20m; CASE4_10m, 20m), which is highlighted by the representative cases: BASE and CASE1_20m, respectively (Figure5.4b).

The variability in injection rate results from varying permeabilities at the base of the caprock which could enhance or diminish fluid flow through the porous matrix as the injected gas migrates to the top of the reservoir. The degree to which these cases enhance the cumulative injection of CO_2 within simulated parameters is shown in Figure 5.4a. However, an indistinguishable pressurisation profile is observed within Region 2 for all the cases (Figure 5.4c), suggesting the irrelevance of caprock heterogeneities on aquifer pressurisation during CO_2 injection.

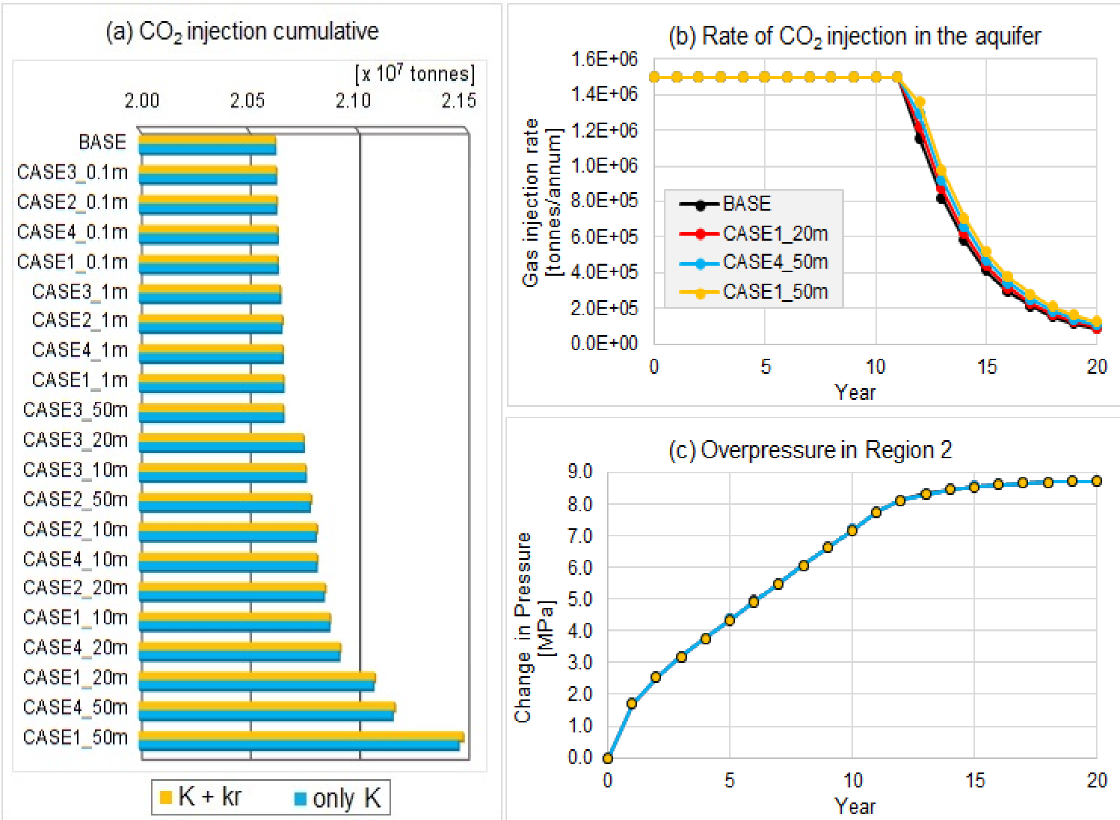

Figure 5.4: Plots showing a) cumulative CO_2 injected at the end of 20-year simulation, b) representative curves for CO_2 injection profile in the aquifer, and c) representative curve for pressure change in Region 2 for scenarios modelled with CLOSED boundary conditions.

5.4.1.1 Pressure evolution in the caprock

Overpressure (*i.e.* the change in pore pressure) occurs in the caprock formation due to the coupled hydromechanical effect that occurs during CO_2 injection into the underlying aquifer, resulting in the vertical displacement of overpressure from the storage formation to the seal formation (Niemi et al. 2017). Unlike the pore fluid pressure profile in Region 2 (Figure 5.4c), the increment of pore pressure in Region 1 over the injection period is not the same for all cases modelled. Pressure propagation in Region 1 is, however, slower than in Region 2 due to the contrast in permeability between the two formations.

The magnitude of overpressure reported in Region 1 for each description of sedimentary heterogeneities, *i.e.* "$K + k_r$" and "*only K*", show higher values for cases with defined heterogeneity in intrinsic permeability (K) and relative permeability (k_r) functions (Figure 5.5). This suggests a misrepresentation of heterogeneity in flow models when it is simply described by static petrophysical properties, such as porosity and permeability.

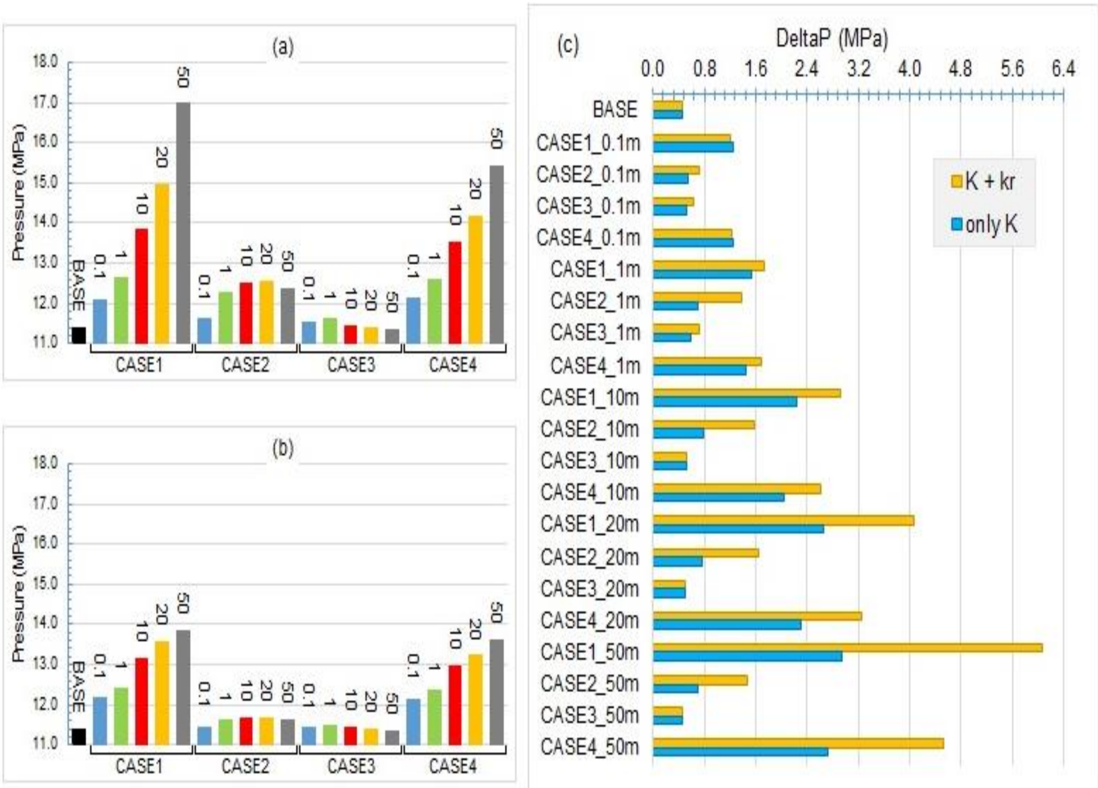

Figure 5.5: Average pressure in Region 1 at the 20th year of injection for caprock heterogeneities represented by a) $K + k_r$, b) only K, and (c) change in pressure for both scenarios.

Numerical output of pressure data in Region 1 for both scenarios is observed to have a wider range for peak pressure values in CASES 1 & 4 from the BASE case, in comparison to CASES 2 & 3. This is largely attributed to the sequence and width of coarser or finer lithologies at the lowest part of the transitional interface. This study refers to this phenomenon as the "stacked-width" *i.e.* the total thickness of coarse- or fine- textured strata occurring sequentially at the base of the caprock. The stacked-width for each case is shown in Table 5.4. A comparison of the average pressure in Region 1 for all cases, based on the stacked-width at the lowest part of the transitional interface, suggests that the type and width of stratum at the lowest part in caprock formation will dictate the rate of pressure diffusion into the sealing formation.

CASE	***Transition zone thickness (m)***	***Stacked-width***	
		Thickness (m)	***Description***
1	0.1	0.06	Coarser strata
	1	0.6	
	10	6	
	20	12	
	50	30	
4	0.1	0.03	
	1	0.3	
	10	3	
	20	6	
	50	15	
2	0.1	0.04	Finer strata
	1	0.4	
	10	4	
	20	8	
	50	20	
3	0.1	0.03	
	1	0.3	
	10	3	
	20	6	
	50	15	

Table 5.4: Stacked-width for coarser- or finer- strata for each case

In Figure 5.5 we see a corresponding trend between the degree of pressure propagation into the caprock and the stacked-width in both "K + k_r" and "*only K*" scenarios, with higher values highlighted for coarser stacked-widths. The influence of "stacked-width" is further illustrated in Figure 5.6, which describes pressure propagation along the caprock, at a reference depth of 990 m (*i.e.* 10 m above the reservoir-seal interface). This show that an increase in the stacked-width of coarser caprock lithologies, *i.e.* clayey sandstone, sandy siltstone and siltstone, has a direct influence on the magnitude of pressure that diffuses from the aquifer into the first few metres of the overlying caprock. In both scenarios, *i.e.* "K + k_r" and "*only K*", the pressure profile along the reference depth (*i.e.* -990 m) is commensurate in magnitude for caprock showing normal gradation (*i.e.* CASE 1 & 4) within 0.1m- and 1m-thick transition zones. Pressure curves for both cases become discernible within transition zones ≥ 10m.

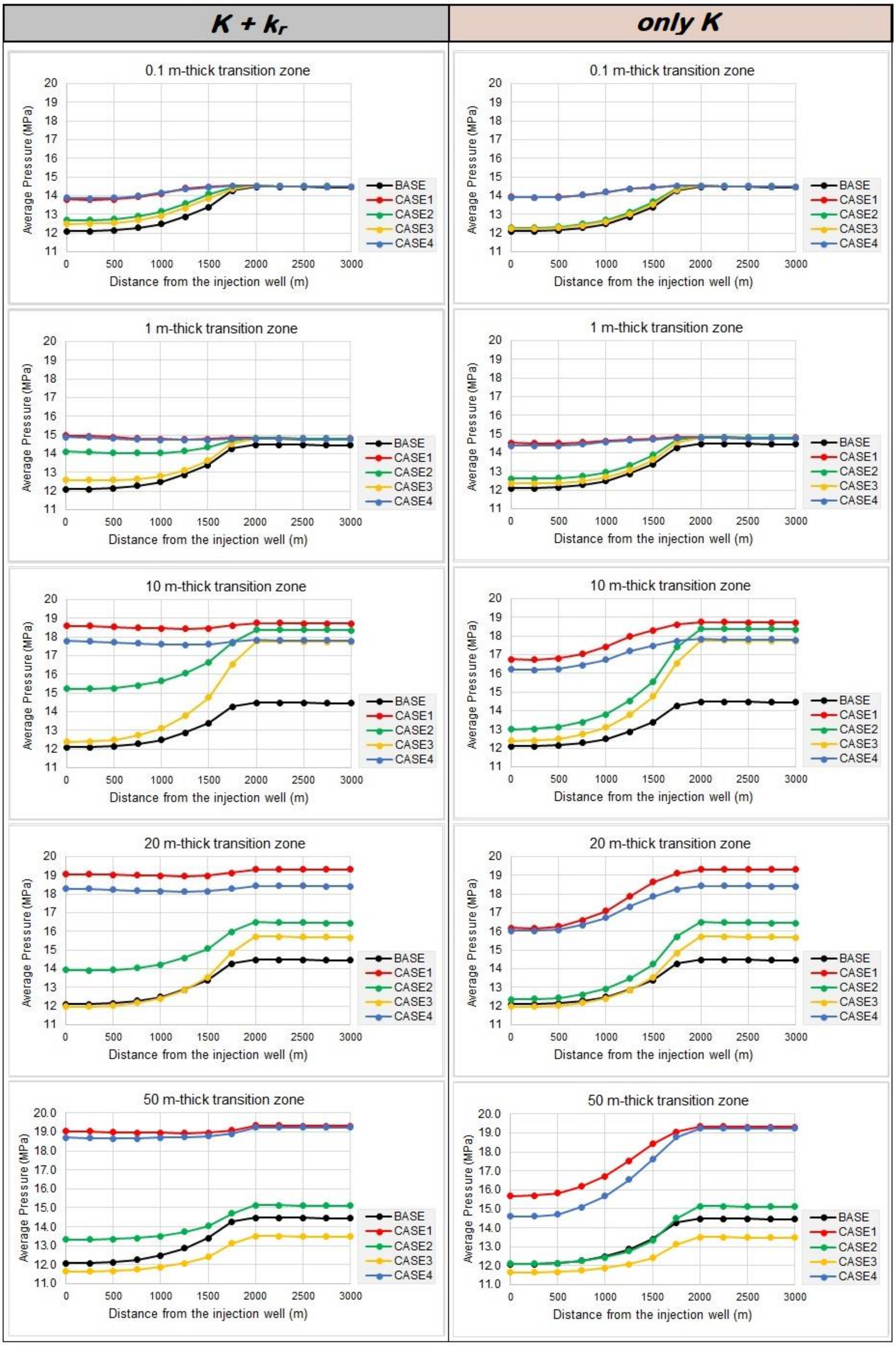

Figure 5.6: Pressure profile along the caprock (depth = 990 m) of a CLOSED-system for varying transition zone thickness in caprock heterogeneities represented by "$K + k_r$" and "only K"

The pressure profiles within the injection zone (*i.e.* $r \leq 500$ m) for both cases differ distinctively from a caprock with no basal transition zone (*i.e.* BASE case). Magnitudes of pressure for CASE 1 & 4 are also higher than CASE 2 & 3 (*i.e.* caprocks showing reverse gradation) within the injection zone for all transition zones depicted. This demonstrates the capacity to which normal gradation at the base of the caprock influences the pressure character during gas injection, indicating the precedence of normal grading effects over inverse grading effects on pressure propagation. The reverse gradation at the base of the caprock (CASE 2 & 3) also show pressure profiles within the injection zone that differ from the BASE curve. These pressure curves, however, tend to converge towards the BASE curve more readily for "*only K"* scenarios than for "$K + k_r$" scenarios. Consequently, the exclusion of relative permeability heterogeneities during such modelling exercise could easily give the notion that reverse gradation in the transition zone has negligible effects on caprock pressurisation in comparison to the absence of a basal transition zone. This further emphasises the significance of relative permeability functions in reservoir simulations. Over the 20-year $scCO_2$ injection period, the modelling exercise indicates that the average pressure along the reference depth (*i.e.* -990 m) is lower in the region overlying the injection zone (*i.e.* $r \leq 500$ m) for individual cases in "$K + k_r$" and "*only K*" scenarios. Corresponding pressure profile for each case peaks at about 2000 m from the injection well and maintains an approximately constant value beyond this range along the reference depth in the caprock. This trend is attributed to the column height of the CO_2 plume accumulating in the underlying aquifer, which serves as an inhibiting factor to pressure diffusion into the overlying caprock in the closed system (Figure 5.7):

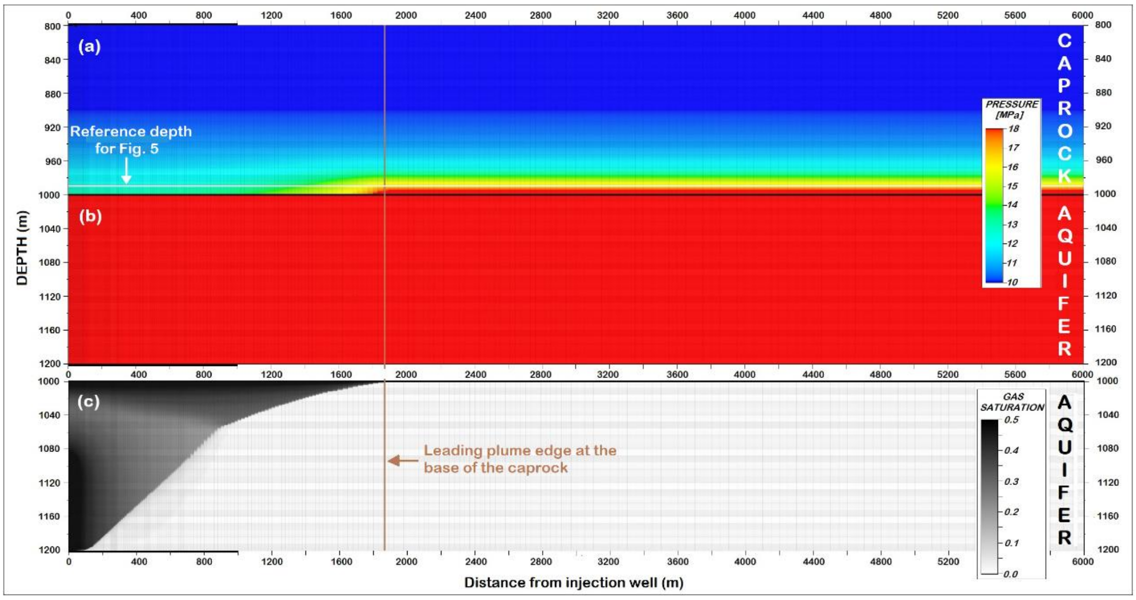

Figure 5.7: 2D visualisation of the BASE case at the end of the 20-year gas injection showing (a) pressure distribution in the caprock, (b) average pressure in the aquifer, and (c) CO_2 saturation in the aquifer.

In analysing caprock integrity for such hydraulic systems, the caprock above the plume is a critical zone for shear failure (Vilarrasa 2014). Figure 5.6 and 5.7 show the leading edge of CO_2 plume in the aquifer coincides with the maximum values for fluid pore pressure along the reference depth in the overlying caprock formation. Qualitatively, the height of continous CO_2 plume in contact with the reservoir-seal interface vary inversely with overpressure at the lower part of the caprock. In other words, the thickness of a bouyant CO_2 plume in contact with the caprock's base serves to abate any pressure diffusion into the overlying caprock. This suggests that CO_2 injection in such a closed-system will inadvertently enhance the caprock integrity, specifically at the injection region of the caprock's basal stratum/strata (which is equivalent to Region 1 in this study). The observation that Region 1 is less susceptible to shear failure during injection-induced pressurisation of the caprock can be explained by Figure 5.8:

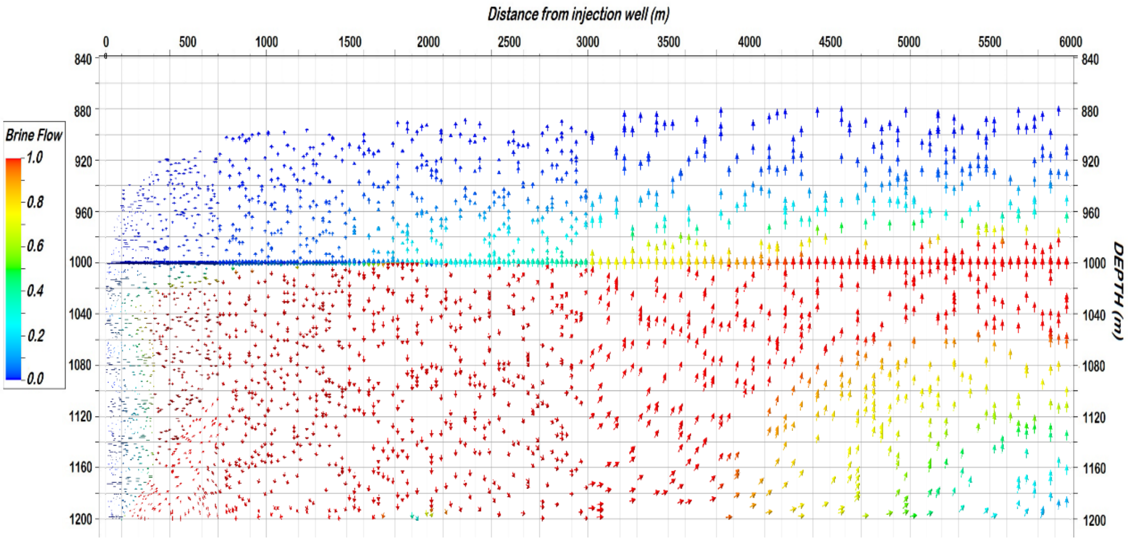

Figure 5.8: Volumetric brine flow vectors at the 20th year of gas injection in the CLOSED-system. N.B.: Colour scale is the relative flow rate where 1 is the highest and 0 is the lowest. Arrows are fitted to the grid cells, resulting in reduced visibility in smaller grid cells located between 0 and 2000m.

Figure 5.8 illustrates brine flow vectors in the modelled domain of a closed system at the end of the injection period. Here, lateral brine flow is restricted at the 6km boundary of the domain resulting in the cycling of brine within the aquifer. This cycling is dominated by buoyancy effects towards the 6km lateral boundary, and gravity effects on the near end of the model close to the injection well. These accounts for higher pore pressures portrayed on the right half of plots in Figure 5.6. Nevertheless, transitional strata at the lower part of the caprock show varying effects on the magnitude of pressure that bleeds into the caprock as detailed in Section 5.4.1.2. Dueto these observations, the next section only examines results for *"K + kr"* scenario.

5.4.1.2 Effects of basal transition zone on overpressure in the caprock

For the 0.1 m-thick transition zone the contrast in Region 1's overpressure between cases with graded and non-graded strata show values no greater than 0.8 MPa for the former (*i.e.* CASE 1 – 4) over the latter (*i.e.* BASE case). This indicates that a transition zone of 0.1 m thickness has a minimal effect on pressure change in the injection zone at the base of the caprock. As the transition zone thickens, the contrast in overpressure between the BASE and the cases showing normal gradation (*i.e.* CASE 1 and 4) also increases (Figure 5.9). For cases that show reverse gradation, CASE 2 attains maximum overpressure values for the 1 m-thick transition zones and maintains this constant pressure profile within thicker transition zones. CASE 3 shows slight deviation from the BASE's pressure curve in transition zones ≤ 1 m and converges to the BASE curve for transition zones ≥ 10 m.

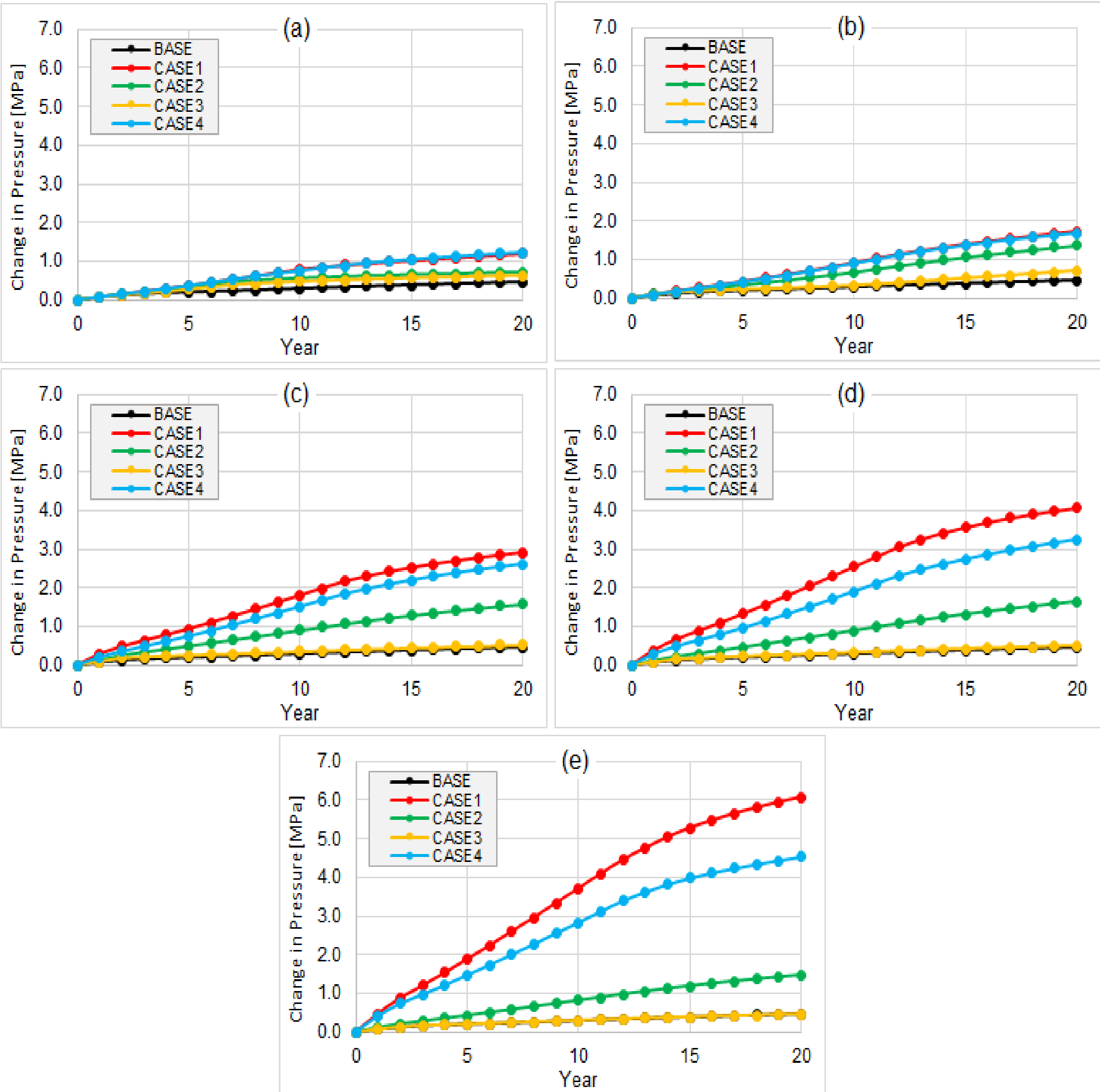

Figure 5.9: Overpressure in Region 1 for cases with graded beds in a) 0.1 m-, b) 1 m-, c) 10 m-, d) 20 m-, and e) 50 m-thick transition zone.

The equivalent pressure profiles for BASE and CASE 3 indicate that the strata within 1 m of the caprock's base are very important in analysing the structural integrity of caprock during CO_2 sequestration. Recall that in CASE 3 there are ten graded beds that transition from the most compact caprock stratum (*i.e.* claystone) at the base, unlike CASE 2 where five graded beds transition from the sandy claystone (Table 5.3). During the fluid injection, the least permeable 1m-thick claystone at the base of the caprock is crucial in mitigating the vertical displacement of fluid that would have otherwise occur in a more permeable stratum at the caprock's base.

Results portrayed in Section 5.4.1 indicate that the type, orientation, and thickness of strata at the lower part of the caprock play a major role in the measure of overpressure within this critical zone. The degree to which these strata affect pressure evolution within the entire formation hinges on their flow characteristics, as duly represented by k_r functions. Figure 5.9 implies that pressure evolving from the aquifer permeates the first 0.1 m of the most compact sealing lithology before the well control pressure is reached (Section 5.4.1) and will progressively increase if and when it vertically propagates through less compact layers. CASE 2 suggests that compact sandy claystone is more effective at a thickness ≥ 2m.

CASE 1 & 4 show greater deviation from the BASE's overpressure profile in comparison to their inverse counterparts. This is due to the ease of pressure communication through the least compact clayey sandstone situated at the base of the transition zone, resulting in higher overpressure in CASE 1 where the least compact layer is thicker than that in CASE 4.

5.4.2 Open system

Here the lateral boundary at 6km is open for fluids to escape the model domain. Simulation results show CO_2 saturation, gas injection rate, and pressure profile in the aquifer to be also almost identical (Figure 5.10). Unlike the closed system, there is no decline in injection rate due to pressure communication beyond the 6 km boundary. This accounts for the decline in overpressure within Region 2 after an initial increase at the onset of gas injection (Figure 5.10b), and corresponds to the aquifer connectivity for lateral brine migration beyond the 6 km boundary portrayed in Figure 5.11.

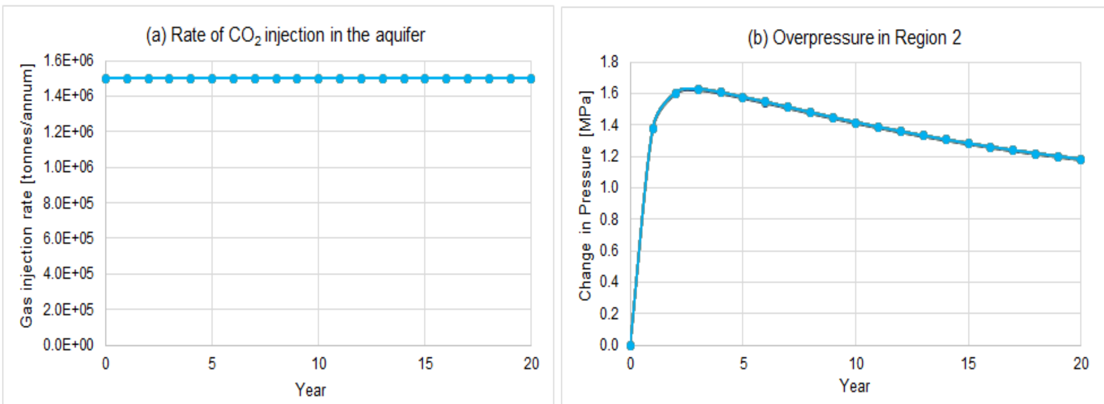

Figure 5.10: Representative curve(s) for a) CO_2 injection rate, b) Change in pore pressure within Region 2, for cases modelled with OPEN boundary conditions

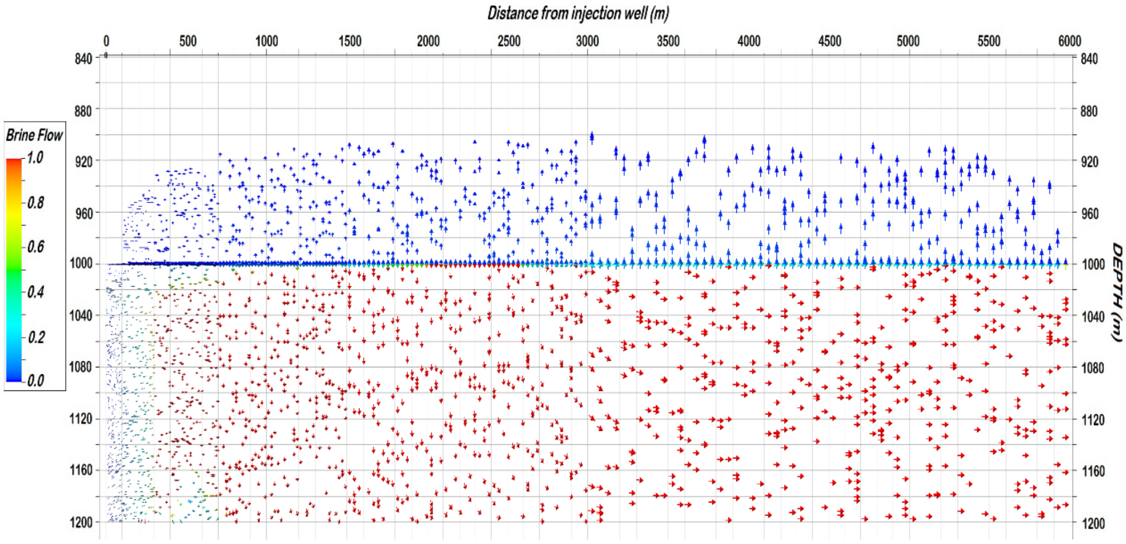

Figure 5.11: Volumetric brine flow vectors at the 20th year of gas injection in the OPEN-system. N.B.: Colour scale is the relative flow rate where 1 is the highest and 0 is the lowest. Arrows are fitted to the grid cells, resulting in reduced visibility in smaller grid cells located between 0 and 2000m.

Pressure also builds-up in the caprock of the open system as a response to CO_2 injection in the underlying aquifer. However, the aquifer connectivity and vast pressure communication beyond the 6 km lateral boundary results in considerably smaller magnitude of brine flow and hence pressure diffusion into the caprock of the open system. This also explains why the pressure profiles for all cases along -990 m in "*K + kr*" and "*only K*" scenarios are identical (Figure 5.12). Pressurisation at the reference depth corresponds to the degree of fluid expansion within the restricted pore space, which is higher for coarser strata than finer ones. Thus, the presence of a transition zone will have varying effects on pressure propagation, regardless of the boundary conditions.

Figure 5.12 shows that for all cases modelled in an open aquifer, the injection zone at the base of the caprock is critical for integrity, which is as expected for $scCO_2$ injection scenarios. The pressure diffusion into the caprock is supported by the vertical continuity of migrating CO_2 plume in contact with the reservoir/seal interface (Figure 5.13). This contradicts the trend seen in the closed system and is attributed to the overall flow dynamics as seen in Figure 5.11, which enhances the vertical displacement of brine at the injection zone.

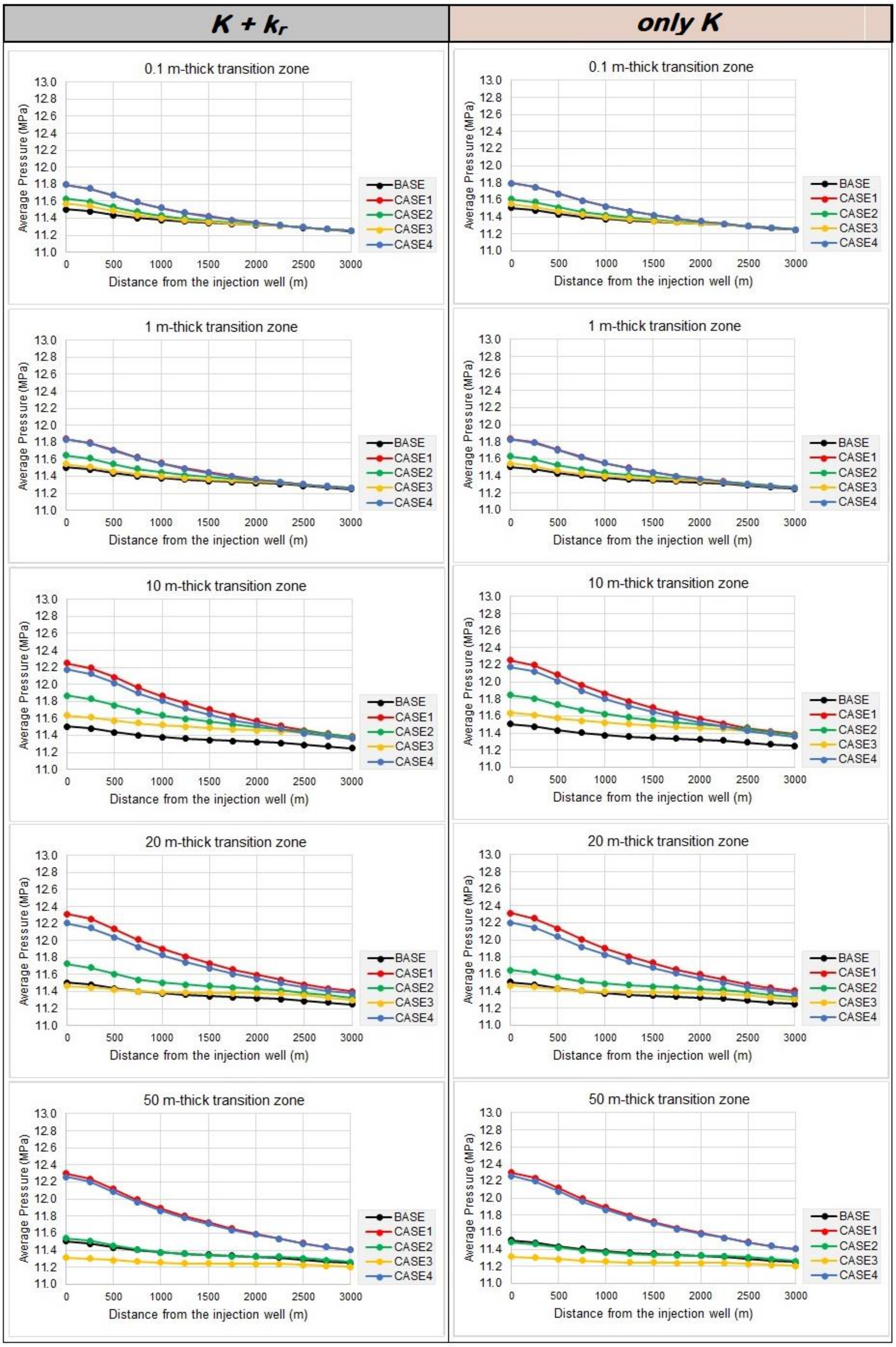

Figure 5.12: Pressure profile along the caprock (depth = 990 m) of an OPEN-system for varying transition zone thickness in caprock heterogeneities represented by "K + k_r" and "only K".

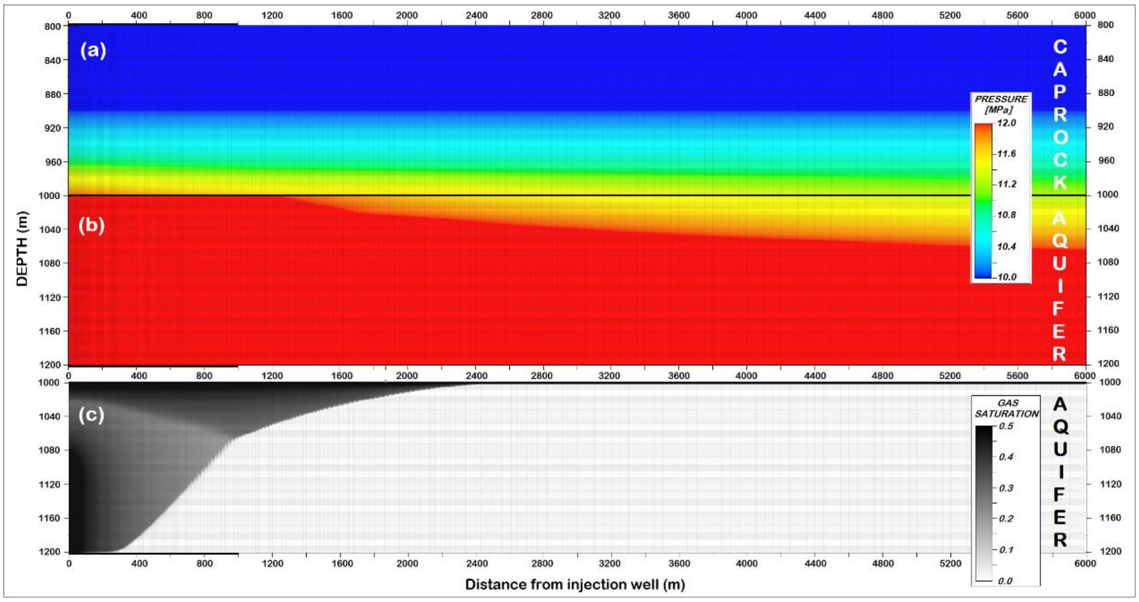

Figure 5.13: 2D visualisation of the Base case at the end of the 20-year injection showing (a) pressure distribution in the caprock, (b) average pressure in the aquifer, and (c) CO_2 saturation in the aquifer.

5.4.3 Open vs Closed system

The presence of a basal transition zone in the caprock is seen to have varying effects on pressurisation in the caprock within closed and open systems. Overpressure in the caprock is, however, higher for closed systems due to restricted brine flow beyond the lateral edge of the model. This is because brine, which serves as a conduit for pressure migration, is pushed up into the caprock at a higher degree for closed systems. Pressure change in the caprock will usually occur in the lower part of the seal. Figure 5.14 shows the impact of a laterally continuous transition zone showing normal gradation on the height to which overpressure occurs in the injection zone at the lower part of the caprock. This reinforces the argument that such occurrence may undermine the structural integrity of the caprock during CO_2 sequestration. The presence of a transition zone showing gradational changes can also increase the CO_2 storage capacity of the formation. At the end of the 20-year injection period, CO_2 migrates into the caprock and fills the interstices between pores of the rock grains.

Based on dynamic material-balance computation by the simulation software, results indicate that the magnitude of pressure change in the caprock is directly related to the quantity of free CO_2 within the caprock (Figure 5.15). This is because the hydraulic system in a storage formation is limited by the compression of fluid in the modelled domain, hence the available volume for storage of CO_2 in the caprock is provided by the expansion of the formation in response to injection pressure. This storage capacity is dependent on the sustainable pressure build-up that a given formation seal system can tolerate without geomechanical degradation. This would suggest that for confined reservoirs that show gradation in the sealing formation, higher overpressure within the limit of the fracture pressure in the transition zone will lead to further compression of the fluid, resulting in higher storage capacity of the porous media in comparison to open reservoirs. In numerical simulations, this assertion is mostly applicable for gradational changes that are duly accounted for by k_r functions in the reservoir model.

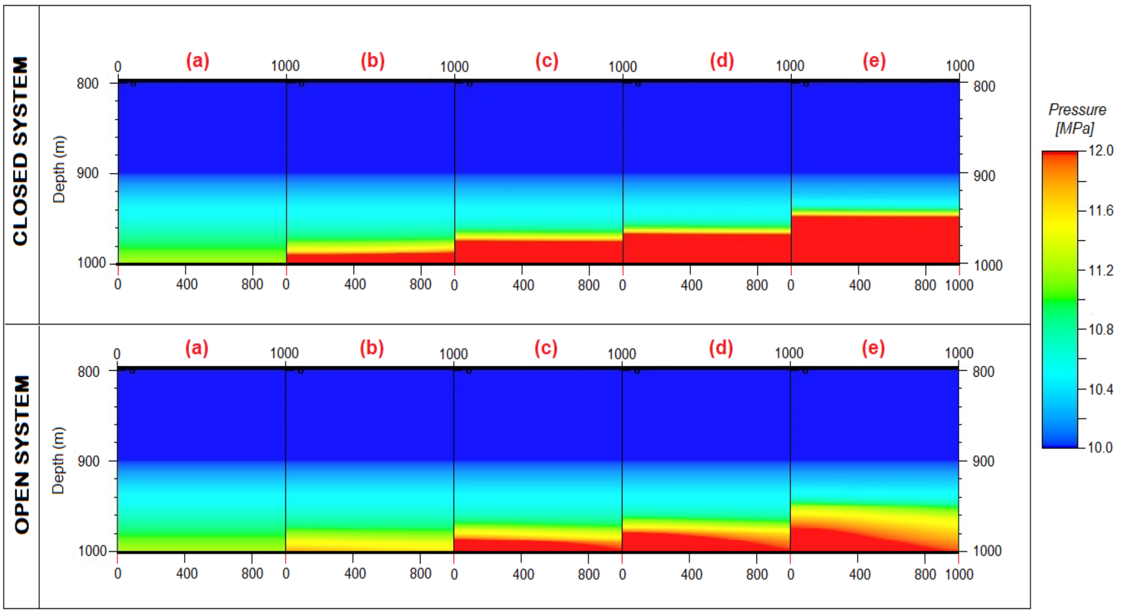

Figure 5.14: Pressure distribution in the caprock between the injection well and 1000m in a) all cases before CO_2 injection, and b) the BASE case, c) CASE1_10m, d) CASE1_20m, e) CASE1_50m at the end of CO_2 injection.

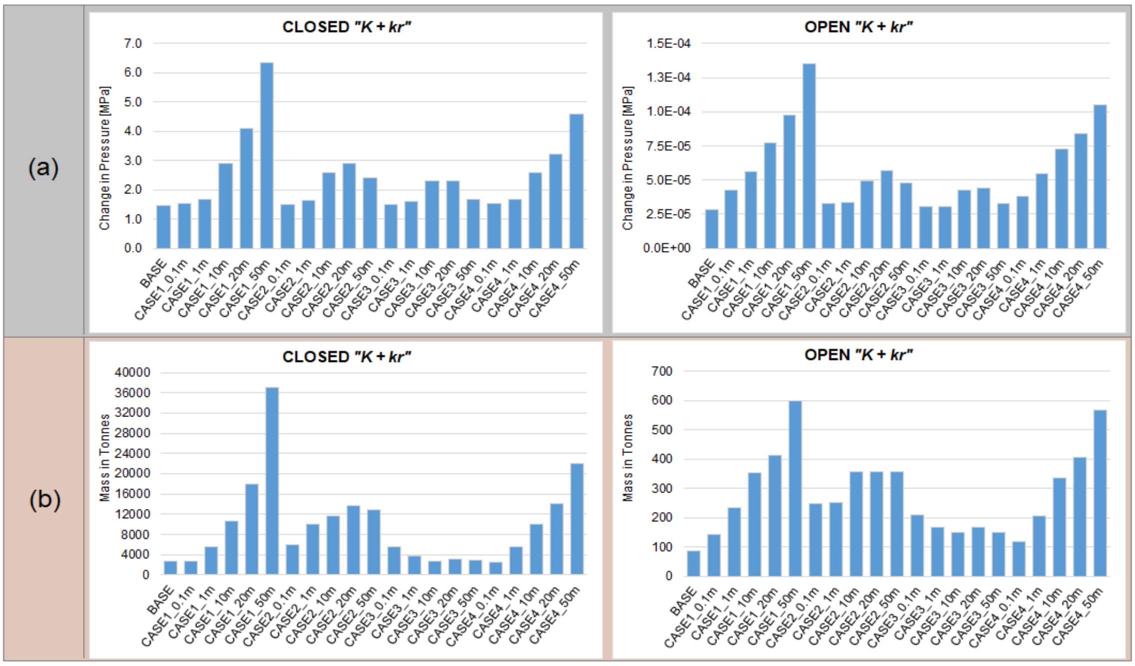

Figure 5.15: Comparison of simulated outputs in the caprock of the CLOSED- and OPEN-system for a) overpressure, and b) quantity of CO_2 in free form.

To check the applicability of the pressure profile for closed systems confined at 6km boundary (Figure 5.7) to systems with lateral boundaries beyond 6 km, numerical simulations are conducted for a representative example of 1m-thick basal transition zone in modelled domains with radial boundaries of 10 km, 25 km, 50 km, and 100 km (Figure 5.16). The results illustrate that closed boundaries ≤ 10 km tend to support the pressurisation regime described in Section 5.4.1.1 while those at distances ≥ 25 km describe pressure profiles similar to open flow systems. This can be attributed to the considerably larger pore volume now available for brine flow within lateral boundaries beyond 25 km. Regardless of boundary conditions, transitional strata at the base of a caprock show pressure profiles for the seal that differ from those without a basal transition zone.

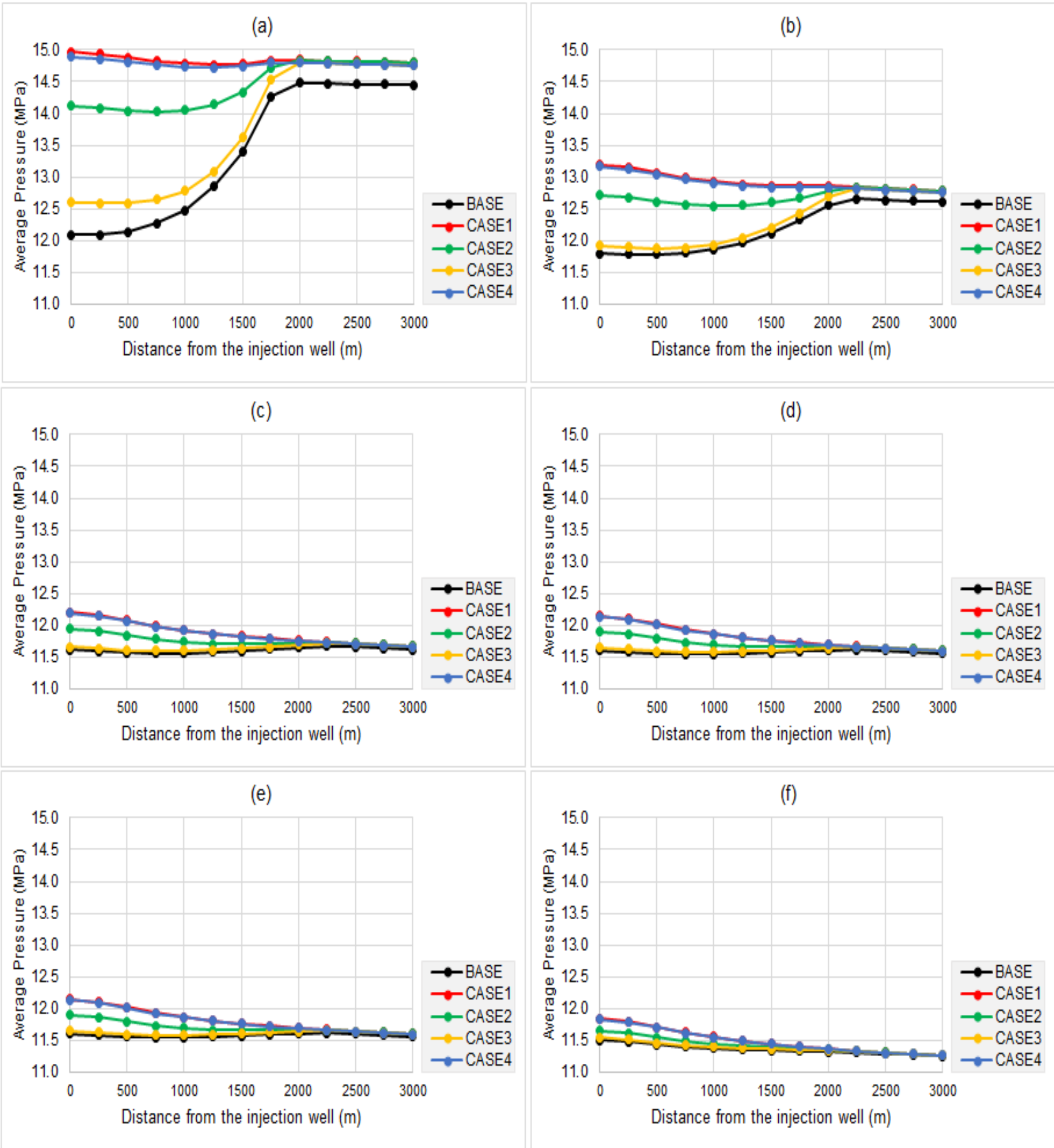

Figure 5.16: Pressure profile along the caprock (depth = 990 m) for 1m-thick transition zone in radial domains modelled with no flow conditions at a) 6 km, b) at 10 km, c) 25 km, d) 50 km, e) 100 km, and flow conditions at f) 6 km from the injection well.

5.5 Summary and conclusion

The goal of this modelling study was to explore how a basal transition zone in a sealing formation will affect CO_2 sequestration, using relative permeability functions to describe various lithologies within the model. Multi-phase flow characteristics for different siliciclastic lithologies were obtained using the pore size distribution index to compute constitutive models for the P_c – k_r – S_w relationship. This study used the information on pressure distribution within the sealing formation to highlight the impact of gradational changes in the caprock's base on its structural integrity and storage capacity. The magnitude of pressure distribution was determined through numerical simulation of the multiphase flow and multicomponent transport of CO_2 and brine in a hypothetical saline aquifer. An inference from the results is that the presence of a basal transition zone, with a thickness that transverses the region where overpressure is expected to occur in the caprock, is significant for storage capacity estimation as well as failure analysis. These results emphasise the relevance of relative permeability functions in reservoir simulations, as well as the impact of representing varying flow characteristics resulting from gradational changes, should they occur, on a subsequent geomechanical analysis.

Injection overpressure only affects the first few metres of the lower part of the whole caprock. Consequently, the presence of gradational changes at the base of the seal may allow more pressure bleed-off into the caprock. This pressure build-up in excess of the initial hydrostatic pressure will cause a higher loading at the critical zone for seals with a basal transition unit than those without. Hence, the additional stress change at the base of the seal, which will otherwise be unaccounted for in a caprock without a basal transition unit, could lead to rock failure (Orlic et al. 2011). However, based on the magnitude of pressure change observed from the simulations, it is not possible to come to a general conclusion concerning the influence of the transition zone on caprock integrity. Nevertheless, the additional stress change observed at the critical zone will need to be taken into consideration during hydromechanical analysis. Additionally, the pressure build-up resulting from CO_2 injection in porous geological media changes the stress field and induces an expansion of the media. As such, the appropriate representation of flow characteristics in modelled lithologies is vital in evaluating the dynamic storage capacity of CO_2. This highlights the need for adequate representation of small-scale geological heterogeneities in large-scale CO_2 sequestration modelling. The next chapter applies the P_c – k_r – S_w relationship in investigating the impact of sedimentary heterogeneities resulting from thin shale baffles and high permeability channels in the reservoir unit on the analysis of dynamic modelling.

CHAPTER 6[§]

Influence of argillite baffles on the flow properties of storage units

Predicting CO_2 plume migration is an important aspect for CCS and sedimentary heterogeneities such as interbedded argillite (fine-grained sedimentary rock composed predominantly of indurated clay particles) in the storage unit can control the buoyant migration of CO_2. This chapter documents a Darcy flow modelling approach to investigate different aspects of CO_2 drainage in a sandstone formation with interbedded argillaceous (*i.e.* mudstone) units. The numerical simulation is based on the Sleipner Gas Field storage unit where several thin argillite layers occur within the sandstone of the Utsira Formation. With respect to forward modelling simulations that have used Sleipner Formation as a case study, it is noted that previous attempts to numerically calibrate the CO_2 plume migration to time-lapse seismic dataset using software governed by Darcy flow physics achieved poor results. This study does not try to history-match the spatial distribution of gravity currents, *i.e.* the flow of a density-driven invading fluid through porous media at Sleipner's Utsira Formation, but rather presents the effect of modelling heterogeneities in the dynamic flow properties, when describing sedimentary heterogeneity in the rock fabric, on subsequent Darcy flow analysis. CO_2-brine buoyant displacement pattern is simulated using the ECLIPSE 'black oil' simulator within a two-dimensional (2D) axisymmetric geometry and a three-dimensional (3D) Cartesian coordinate system. This investigation focused on two key parameters affecting CO_2 migration mobility, namely relative permeability and capillary forces. Examination of these parameters indicate that there is a scope for a revision of the basic premise for modelling flow properties in the interbedded mudstones and the top sand wedge at the Sleipner Field when using Darcy flow simulators.

[§] The content of this chapter has been extracted from the following paper:

Onoja, M.U., and Shariatipour, S.M. (2019) Assessing the impact of relative permeability and capillary heterogeneity on Darcy flow modelling of CO_2 storage in Utsira Formation. *Greenhouse Gases: Science and Technology*. https://doi.org/10.1002/ghg.1932

The candidate set the scientific scope of the work, devised and developed the methodology, performed all data analysis and wrote the text. The co-author provided guidance during the design of this part of the project and feedback on the manuscript.

Minor adaptations have been performed to streamline the layout of the thesis

6.1 Introduction

The presence of high permeability channels, herein referred to as ‘thief zones’, and mudstone baffles can result from sedimentological processes such as variation in grain size and sorting (Honarpour et al. 1990). Such heterogeneities are a source of uncertainty in plume migration as they influence fluid flow paths and the position of flow units within the storage formation. Bear (1972) defined the concept of flow unit as the representative elementary volume (REV) or mappable portion of the reservoir which possess analogous petrophysical properties that affect fluid flow and differ from other sections of the reservoir rock volume. The accurate characterisation of flow units in a reservoir formation helps to reduce the uncertainty in CO_2 sequestration and oil production forecast (Al-Menhali et al. 2014, Haldorsen and Damsleth 1993). A typical reservoir rock with mudstone intervals contains varying amount of clay minerals (Fertl and Chilingarian 1990), which can result in different flow units for CO_2 storage. The Paluxy Formation in Alabama, Mississippi (Koperna et al. 2017) and the Utsira Formation in the Norwegian North Sea (Arts et al. 2004) are good examples of sandstones with interbedded mudstones.

The Utsira Formation is a saline aquifer that lies at a depth of 800 m below sea level (mbsl) and is 200 – 300m thick in the Sleipner area. It is overlain by 50 – 100m thick ‘shale’ of the Nordland Group acting as the primary reservoir caprock and underlain by the Hordaland Group (Figure 6.1). Geophysical well logs acquired around the Sleipner area show laterally extensive thin beds of argillite within the Utsira Formation, about 1 – 1.5 m thick, and a 5 – 6.5 m thick argillaceous layer separating an eastward thickening sand body, commonly referred to as the ‘sand wedge’, from the underlying Utsira Sand (Zweigel et al. 2004). These interbedded mudstone layers are characterised by spikes of higher gamma readings that are similar to those of the overlying Nordland Shale. The Utsira Sand is mostly unconsolidated and largely uncemented with no evidence of faults. It has an average porosity of 36% and a permeability range from 1000 and 8000 mD (Zweigel et al. 2004).

CO_2 injection began in the Sleipner reservoir unit in 1996 at an average annual rate of 1 Mt. A time-lapse monitoring programme was initiated in 1994 to monitor the migration and dispersal of the CO_2 plume. Interpretations of the seismic reflection surveys show that by 1999, three years after injection commenced, the Sleipner CO_2 plume had breached the mudstone barriers within the Utsira Sand and ascended from the injection point to the reservoir-caprock interface via nine reflective layers (Figure 6.2). In Figure 6.2a, the vertical zones within the plume, annotated by C, are interpreted as the main conduit for CO_2 upward migrated and referred to as chimneys (Chadwick, R.A. et al. 2004). Of all nine layers, the top layer is imaged most clearly by the seismic surveys. This top layer of CO_2 accumulation is the sand wedge (Figure 6.1b) and it is regarded as the main determinant of storage integrity in the medium to longer term (Chadwick and Noy 2010). A north-trending linear propagation of the layer is particularly prominent and corresponds to CO_2 migrating northwards along a linear ridge at the reservoir top (Figure 6.3).

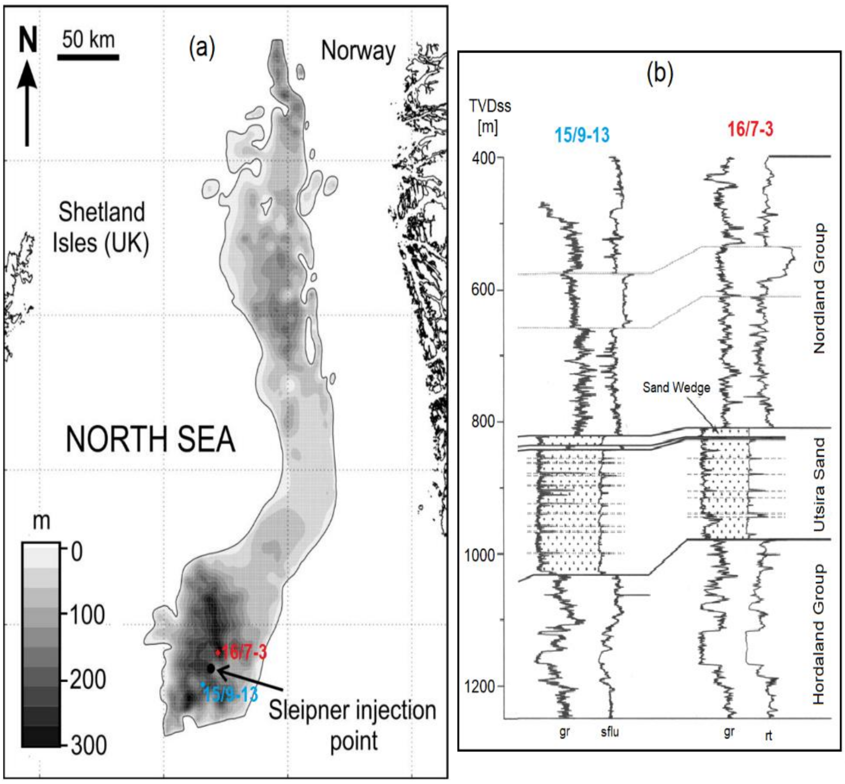

Figure 6.1. a) Isopach map of the Utsira Sand showing the Sleipner injection point and two surround wells and b) representative geophysical well logs showing the Utsira Sand characterised by generally low gamma-ray and low resistivity values. [Adapted from Chadwick et al. (2005)*].*

The nature of the CO_2 supply to the sand wedge and the distribution of CO_2 plume within it depends on the transport properties of Utsira mudstones and the sand wedge, respectively. Explanations for the observed growth of the CO_2 plume in the topmost layer include:

a) the unlikelihood that CO_2 migration through the mudstones is entirely governed by visco-capillary Darcy flow but rather via some form of pathway flow (Harrington et al. 2009), and
b) the presence of high permeability channels within this layer with a preferential north-south flow direction (see Figure 6.4).

Suggestions on the origin of pathway flow include faulting or minor collapse induced by fluidisation within the main feeder chimney identified in Figure 6.2a (Hermanrud et al. 2007), and the presence of 'holes' in the Utsira mudstones possibly due to erosion or sand mobilisation (Zweigel et al. 2004). Regardless of the origin of these pathways, the flow property of the mudstones plays a vital role in moderating the upward migration rate of the CO_2 plume (Boait et al. 2011). For instance, the relative permeability to CO_2 in the mudstone baffles is likely to increase as they become more saturated with CO_2 (Chadwick and Noy 2010). The influence of channelling in the top sand wedge on the CO_2 plume migration has been investigated by Williams and Chadwick (2017), Cowton et al. (2018) and Hodneland et al. (2019) through the effects of permeability heterogeneity, plume temperature, and concentration of impurities. This approach yielded a better match between the observed and calculated CO_2-water contact (CWC) for most of the sand wedge but failed to match the observed migration rate of CO_2 along the prominent northern ridge.

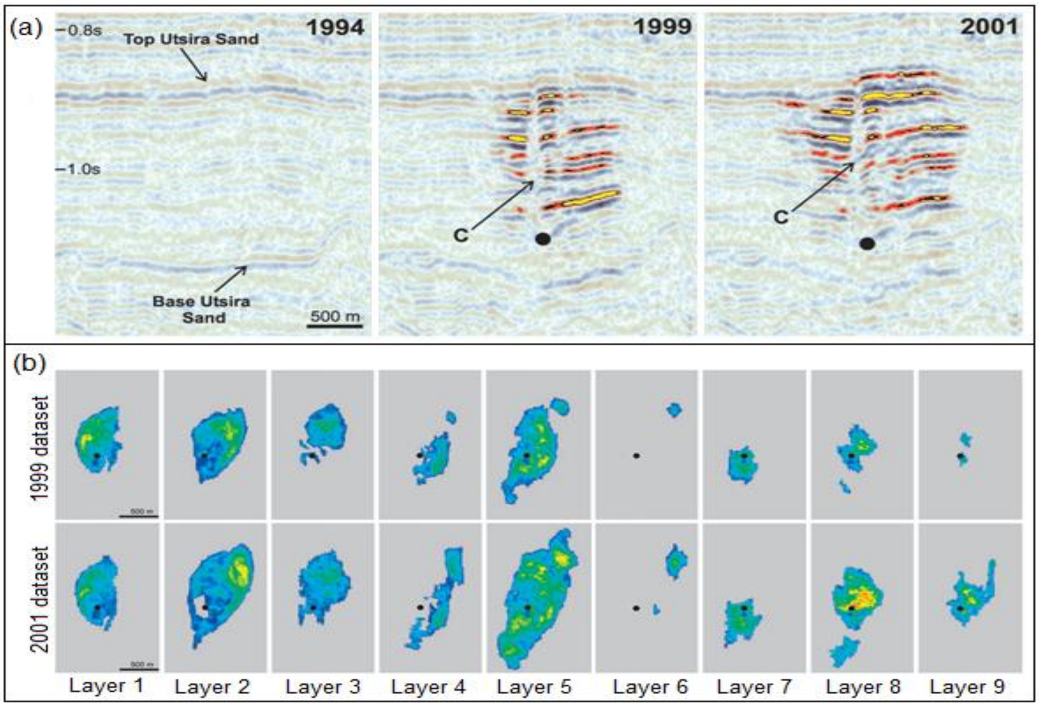

Figure 6.2: a) Time-lapse seismic images of the CO_2 plume N-S inline through 1994 (prior to injection), 1999 and 2001 datasets with C denoting the main chimney and the solid circle depicting the injection point. b) Absolute amplitude maps of the interpreted layers showing plume development in the 1999 and 2001 seismic surveys. Black disc denotes injection point. [Adapted from Chadwick et al. (2005)*].*

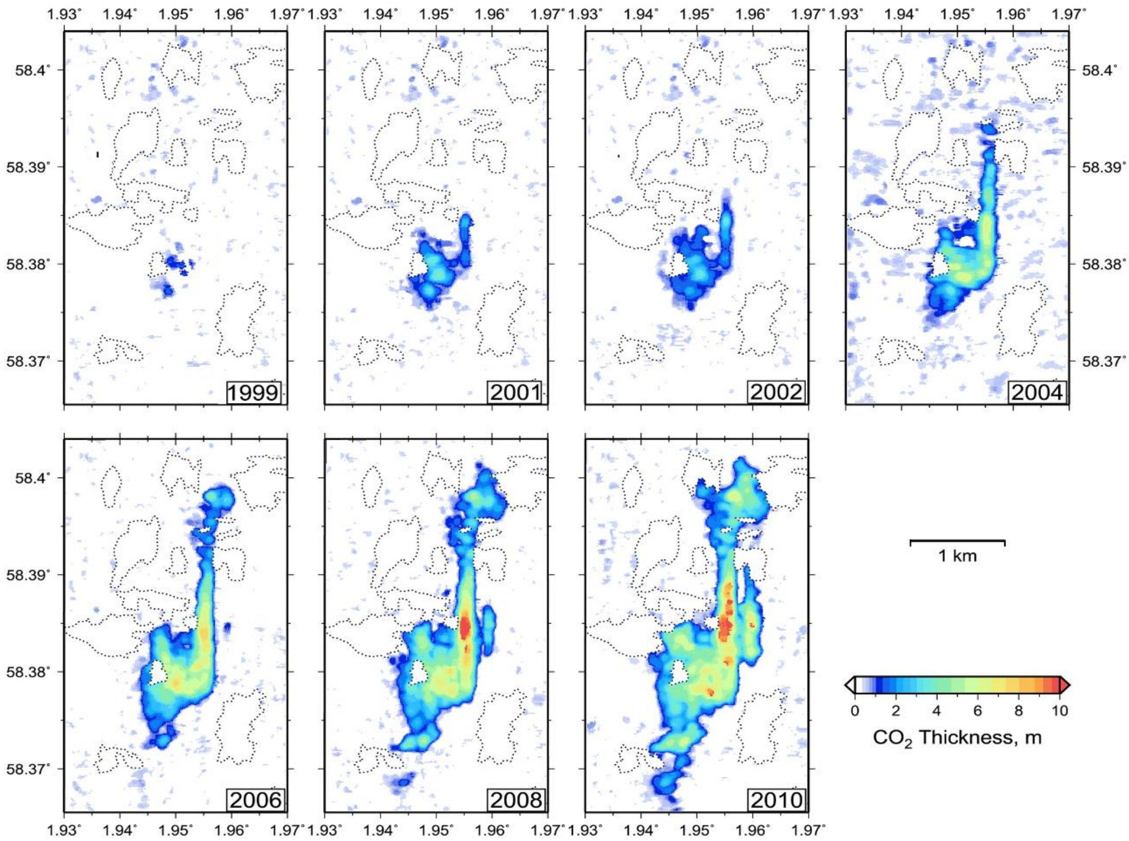

Figure 6.3: The mapped distribution of CO_2 in the uppermost layer beneath the caprock (Layer 9) as interpreted from 4D time-lapse seismic. [Source: Cowton et al. (2016)]

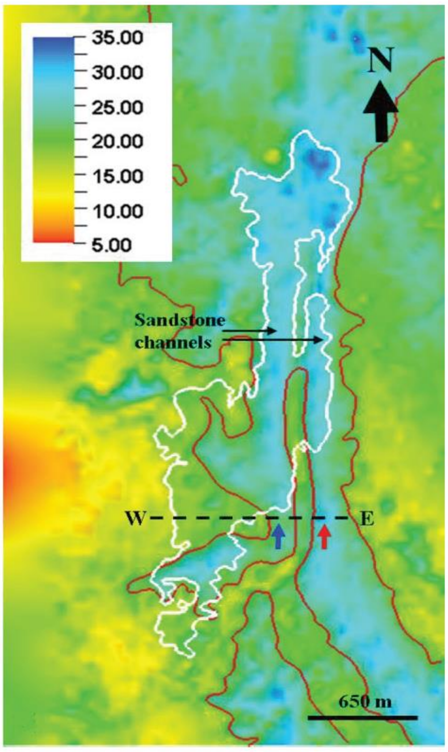

Figure 6.4: Shaded isochore map (ms) of the top sand-wedge from seismic mapping. Cold colours denote thicker reservoir (channels) with the blue and red arrows show individual channels. Warm colours highlight thinning in the reservoir above mud diapirs. The red polygon outlines a 20 ms isochore. The white polygon delineates the margins of the topmost CO_2 layer in 2010. The dotted line shows the location of the seismic section. [Source: Williams and Chadwick (2017)]

The seismic time-lapse datasets have been applied using various simulation approaches to assess uncertainties that exist and approximate history match at the Sleipner storage formation (Cavanagh and Haszeldine 2014, Boait et al. 2011, Singh et al. 2010, Bickle et al. 2007). These include the pressure performance (Chadwick et al. 2012), the reactive transport in Layer 9 (Zhang et al. 2017, Gaus et al. 2005), and a greater emphasis on the quantification of CO_2 plume (White et al. 2018, Dupuy et al. 2017, Cowton et al. 2016, Ghosh et al. 2015, Chadwick and Noy 2015, Romdhane et al. 2014). Zhu et al.'s (2015) history matching of CO_2 plume migration in the Utsira Formation, through simulating sensitivity on pressure, temperature, intrinsic permeability, relative permeability curves, feeders, spill rates and methane (CH_4) content in the CO_2 stream, concluded that the CO_2 plume extent is only sensitive to permeability anisotropy, temperature and CH_4 content. However, the concept of relative permeability sensitivity was not elaborated on in the text and requires further clarification. Additionally, the lack of sensitivity to relative permeability as established in Singh et al. (2010) was based on a steady-state upscaling of $k_r – S_w$ curves using the viscous-limit assumption. The term 'viscous-limit' is used to describe viscous-dominated displacements where fluids are transported in response to an applied external force *i.e.* the viscous force. The magnitude of the viscous force is mainly dependent on the pressure gradient and the fluid viscosities, and not the fluid and rock interactions *i.e.* capillary forces. Consequently, this chapter investigates the sensitivity of CO_2 plume to relative permeability based on the capillary-limit assumption. This process employs the establishment of casual relationships between the pore-size parameter and the P_c – k_r – S_w curves to characterise the dynamic flow state of interbedded mudstone units and high permeability sand channels in a reservoir formation. To this end, the current study is especially interested in two key performance measures:

i) How the P_c – k_r – S_w functions of the intra-sand mudstones influence the maximum vertical migration distance of CO_2 from the injection point to the top of the reservoir, and
ii) How the k_r – S_w functions within 'thief zones' in the sand wedge influence the plume footprint area.

The flow simulations presented in this study are based around the time-lapse seismic monitoring programme at the Sleipner Field. This is to enable the exploration of the performance measures stated above in the numerical simulation of CO_2 injection in a sandstone aquifer interbedded with laterally continuous mudstones. It is important to stress that this study does not attempt to reproduce observed fluxes of CO_2 plume derived from the seismic data but to investigate the impact of capillary-limit relative permeability curves in the interbedded mudstone and high permeability sand channels on the growth of CO_2 plume.

6.2 Numerical flow simulation

The flow simulations employ two modelling scenarios to review and analyse the performance measures identified in the preceding section. The first case study simulates the Darcy flow of CO_2 through saturated porous media using an axisymmetric model (Section 6.2.1) while the second case study investigates the temporal evolution of the topmost CO_2 layer in three-dimensions using the Sleipner Benchmark model of the topmost reservoir layer or 'sand wedge' (Section 6.2.2).

6.2.1 First Case Study

An ECLIPSE100 flow model using a radial axisymmetric mesh that incorporates the properties of the Utsira Formation is used to simulate the growth of CO_2 plume. The model is kept relatively simple to allow multiple model scenarios to be run within a reasonable computation time. The outer boundary of the model is set at radius of 6 km to accommodate the lateral spread of the CO_2 plume during the injection period. Horizontally, cell dimensions start at 2.5 m at the axis expanding to 5 m between radial distances of 100 m and 200 m, 10 m between 200 m and 400 m, 20 m between 400 m and 800 m, 30 m between 800 m and 1500 m with further expansion thereafter reaching 50 m at the outer boundary. The modelled reservoir domain is 220 m thick and contains seven thin mudstones which should allow up to eight spreading layers of CO_2. The vertical spacing of the mudstones match the estimated spacing between the mapped reflections (Haukaas et al. 2013) and are described in Figure 6.5. *Capillary Pressure – Relative Permeability – Wetting Saturation* (P_c – k_r – S_w) relations (Figure 6.6) are computed using the van Genuchten-Mualem-Corey (vG-MC) function described in Chapter 3. Assumptions for the reservoir sand include an average permeability and porosity of 2000 mD and 0.36, respectively; and P_c – k_r – S_w relations based on a capillary entry pressure [P_e] of 0.00172 MPa, a residual wetting saturation [S_{wr}] of 0.3, and a pore geometry parameter [n] of 2.28.

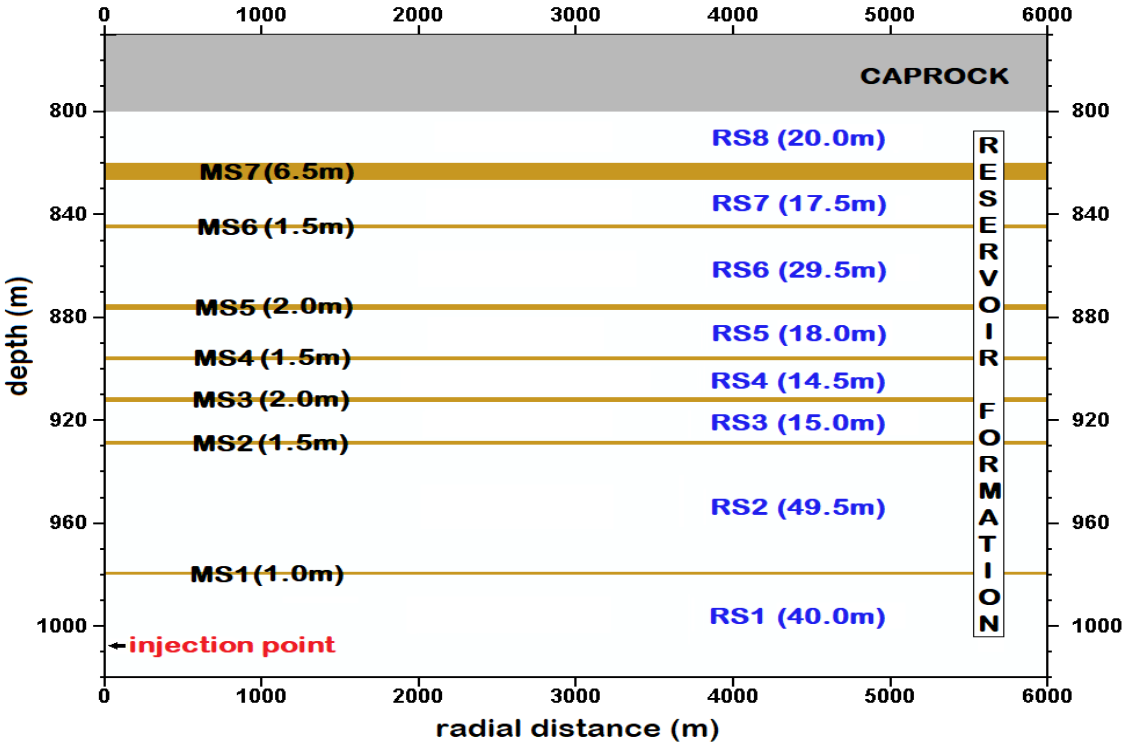

Figure 6.5: Schematic description of the model geometry in the r-z cross section showing the reservoir zones [RS1 – RS8] and the interbedded mudstone layers [MS1 – MS7] as well as their thicknesses in bracket. Not to scale.

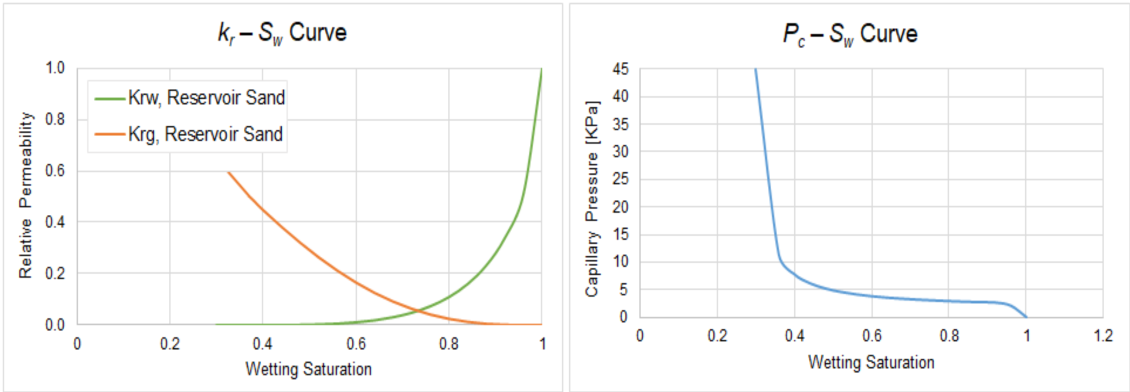

Figure 6.6: P_c – k_r – S_w relationship for the reservoir sand

In the modelled domain a single vertical injection well is located at *r = 0* with CO_2 injection at an annual rate of 1 million tonnes for twenty years. The injection rate applied herein is based on the average injection rate at the onset of CO_2 injection in the Sleipner Field (Chadwick et al. 2005). Two flow scenarios are modelled in the numerical flow simulation. At the outset, CO_2 migration through the mudstones is inferred to occur by viscous-dominated Darcy flow along discrete pathways. These pathways are assumed to originate at *r = 0* of each intra-sand mudstones with a constant aperture of 2.5 m. This was adopted as the only position for holes in the thin shale layers since previous research by Cavanagh and Haszeldine (2014) confirmed that the CO_2 stacked layers are insensitive to variations in the precise position of holes in the shale layers. It is noted that the viscous force usually dominates the displacement process at the field scale and its magnitude is dependent on the applied pressure gradient (*i.e.* externally applied force) and the fluid viscosities (Odsæter et al. 2015). The second scenario assumes CO_2 migration through the mudstones is strictly by capillary-dominated Darcy flow. Capillary forces dominate the displacement process in the pore scale. Breakthrough pressures and $P_c – S_w$ curves for porous media manifest the capillary forces at the interface between CO_2 and brine in the pore throats of the porous media. The sensitivity analysis of both scenarios is expected to provide insights into the buoyant migration of supercritical CO_2 across low permeability mudstone baffles and barriers within a sandstone reservoir.

6.2.1.1 Pathway flow analysis

Initial flow properties of the mudstones are based upon a capillary entry pressure of 1.72 MPa for the Nordland Shale (Harrington et al. 2009). The permeability of intra-sand mudstones are considered to be ultra-low with an intrinsic permeability value of 0.001 mD and a porosity of 0.35, after the Nordland Group caprock. The $P_c – k_r – S_w$ function of the thin mudstones is computed using a pore geometry parameter [n] of 1.41 and a residual wetting saturation [S_w] of 0.605. Pathways in the interbedded mudstones are represented by either increased permeability values, $P_c – k_r – S_w$ functions for the reservoir sand, or both in some cases.

Flow simulation indicates that the injected supercritical CO_2 ($scCO_2$) ascends due to the gravity segregation resulting from the density contrast between the invading gas and *in situ* brine. The flow properties of each reservoir are constant with an average permeability of 2000 mD, which implies that capillary forces within the sand units are not an issue for the mobility of the plume. However, in the presence of intra-sand argillite units, as is the case here, if the capillary pressure [P_c] of the invading fluid does not exceed the entry pressure of the thin mudstone layer the fluid will pond beneath the capillary barrier and migrate laterally along its topography until a spill-point or an opening for vertical migration is reached. The assumption of vertically aligned pathways in the mudstone layers invariably serves as a conduit for viscous-driven Darcy flow to produce a multi-layered CO_2 plume in the reservoir formation (see Chadwick et al. 2006, and Hermanrud et al. 2009). In the first instance, the sensitivity cases described in Table 6.1 highlights the sensitivity of the CO_2 plume contact area to the flow properties of these pathways. A qualitative insight into the plume dynamics is provided through two distinctive elements: the vertical migration of the plume, where the mobility of the gas through each sand layer is mainly a function of the pathway's flow properties, and the amount of free gas within layers of reservoir sand at the end of simulation.

CASE ID	***Description***
P0	- Presence of capillary forces in the intra-sand mudstones. - Pathway in the mudstones based on intrinsic permeability value of 70 mD and $P_c – k_r – S_w$ function for reservoir sand (where the capillary pressure, P_e, is 1.72 KPa, the residual wetting saturation, S_w, is 0.3 and pore geometry parameter, n, is 2.28).
P1	- Presence of capillary forces in the intra-sand mudstones. - Pathway based on only intrinsic permeability value of 70 mD.

P2	- Absence of capillary forces in the intra-sand mudstones. - Pathway based on intrinsic permeability value of 70 mD.
P3	- Absence of capillary forces in the intra-sand mudstones. - Pathway based on intrinsic permeability value of 70 mD and $k_r – S_w$ function for reservoir sand, where $P_c = 0$.
P4	- Presence of capillary forces in the intra-sand mudstones. - Pathway based on only $P_c – k_r – S_w$ function for reservoir sand.
P5	- Presence of capillary forces in the intra-sand mudstones. - No pathway. Flow properties of thin argillites are the same as the caprock.

Table 6.1: Description of cases modelled for pathway flow analysis

In Figure 6.7, a comparison of the sensitivity cases in pairs, *i.e.* P0 vs P1, P2 vs P3, and P4 vs P5, support the proposition that the relative permeability functions could serve to enhance or retard the mobility of non-wetting fluid through the aperture. This is irrespective of the presence or absence of capillary forces in the pathway. Although pathways modelled by the intrinsic permeability value alone promote the development of a multi-layer plume, the inclusion of the relative permeability curve for a less compact lithology improves the mobility of gas through the aperture. This serves to increase the quantity of CO_2 in each overlying layer and shows that the relative permeability function of the pathway in the thin argillite layers, especially the first argillaceous layer, is fundamental to fluid flow through the reservoir. This is highlighted in Figure 6.8 where cases P0 and P3, modelled with the same effective permeability for pathway flow, show the ease of gravity drainage from RS1 into overlying reservoir zones: RS2, RS3 and RS8.

The sensitivity of pathway flow to capillary forces and relative permeability is emphasised in Figure 6.7c. In this illustration for cases P4 and P5, the mudstones act as impermeable barriers that lead to the accumulation of a single layer of CO_2 beneath the first mudstone (MS1) in the reservoir formation. The presence of pathway flow in P4, modelled via $P_c – k_r – S_w$ functions of the reservoir sand where the capillary entry pressure is 1.72 KPa, allows the buoyant migration of CO_2 through the first mudstone layer (MS1) into the overlying sand layer, unlike case P5 (see Figure 6.8b). This identifies two main hypotheses:

i) The capillary forces acting in a porous media can significantly impede the rate of CO_2 migration through it; and

ii) At an intrinsic permeability value of 0.001 mD and a capillary entry pressure of 1.72 MPa, the relative permeability distribution along a 1 m thick laterally extensive argillite layer becomes an important feature for assessing fluid migration through the flow barrier.

In the absence of capillary forces, as seen in cases P2 and P3, the pathway flow becomes a function of the effective permeability of the aperture. Figure 6.8d further illustrates the relevance of relative permeability functions in the transport properties of the aperture when comparing cases P2 and P3. The sandstone $k_r – S_w$ curves modelled into the vertically aligned pathways in case P3 resulted in the increase of CO_2 volume flow to the top of the reservoir *i.e.* RS8.

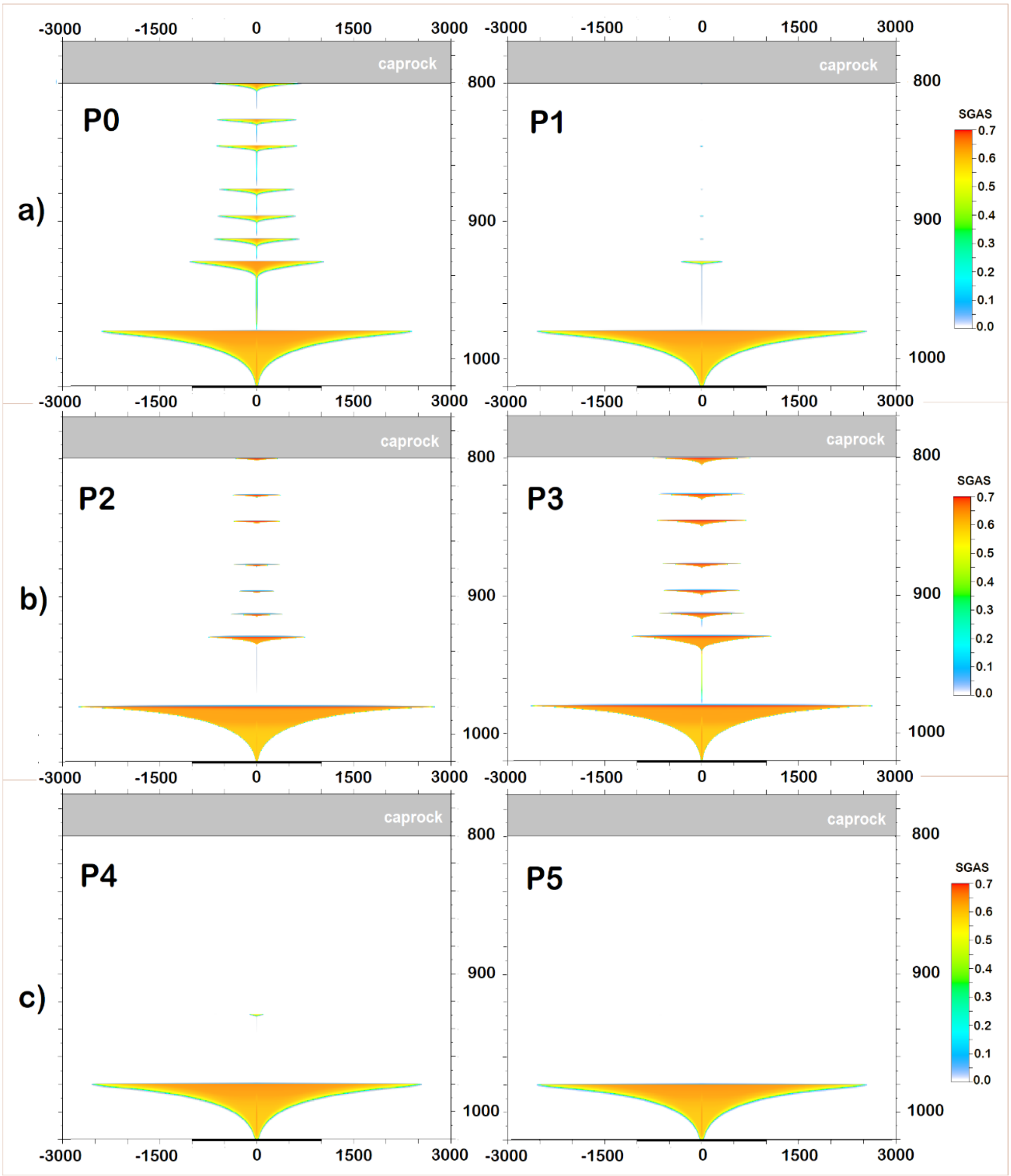

Figure 6.7: Comparison of CO_2 plume distribution at the end of simulation for cases a) P0 & P1, b) P2 & P3, and c) P4 & P5.

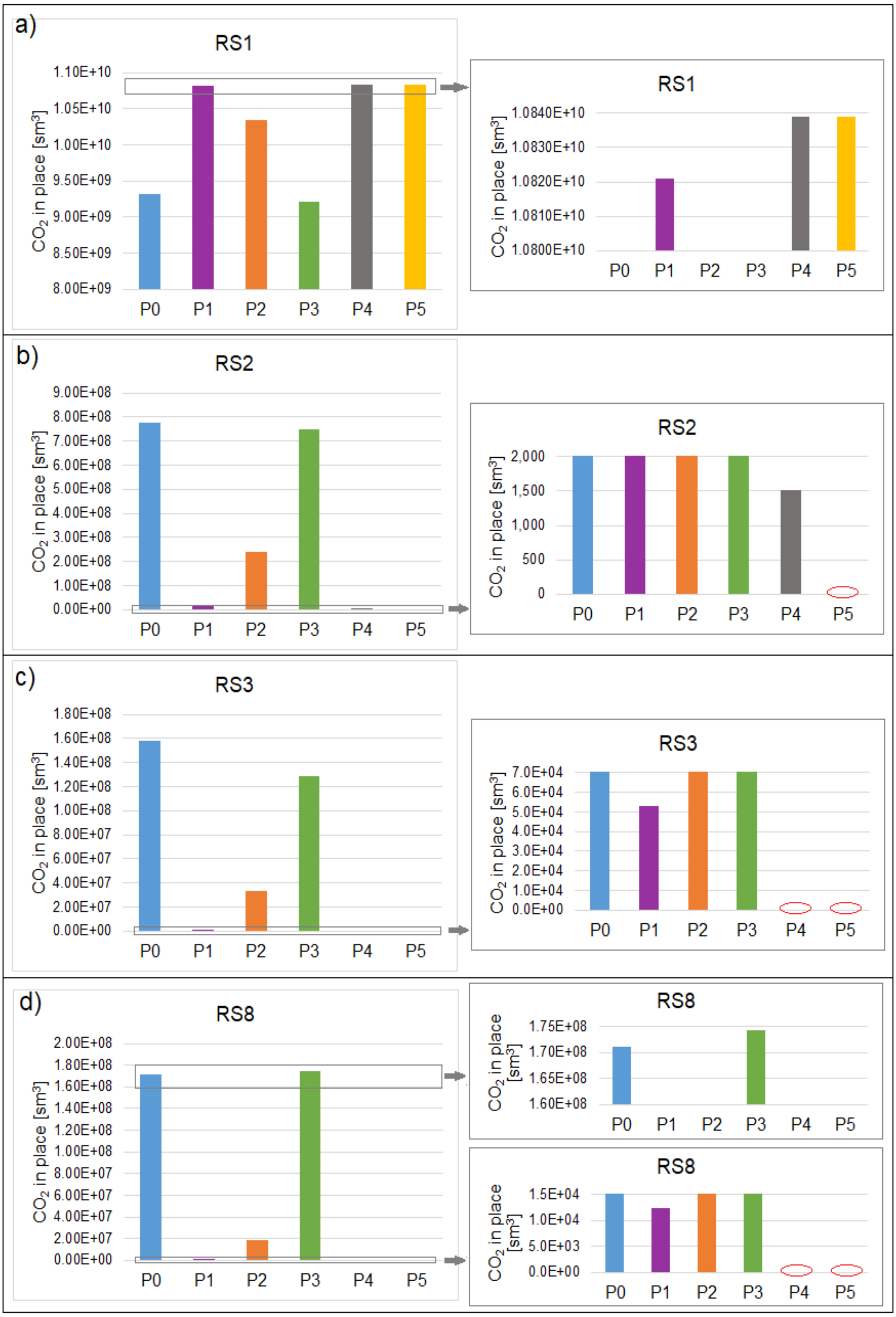

Figure 6.8: Volume of CO_2 in place in reservoir zones a) 1, b) 2, c) 3 and d) 8 at the end of simulation. NB: Red circles in 6.8c & d depict zero CO_2 accumulation in the respective case.

6.2.1.2 Capillary flow analysis

In this section, CO_2 migration through the intra-sand mudstones is assumed to occur by capillary-limit flow. The permeability and capillary entry pressure of the intra-sand mudstones play a key role in moderating the rate of upward migration of CO_2 through the reservoir. These properties are adjusted so that the flow simulation matches the arrival of CO_2 at the top of the reservoir in the third year of injection, as detected by the time-lapse seismic monitoring programme at Sleipner site (Chadwick et al. 2005). The assumed permeability of the mudstones for this analysis was empirically derived under viscosity-dominated Darcy flow where the mudstone layers are modelled without $P_c - S_w$ functions, *i.e.* the absence of capillary forces. The resulting permeability value of 30 mD employed in the sensitivity analysis of Darcy flow physics is based on the observation of plume migration to the top unit of the reservoir (RS8) in the third year of CO_2 injection (Figure 6.9).

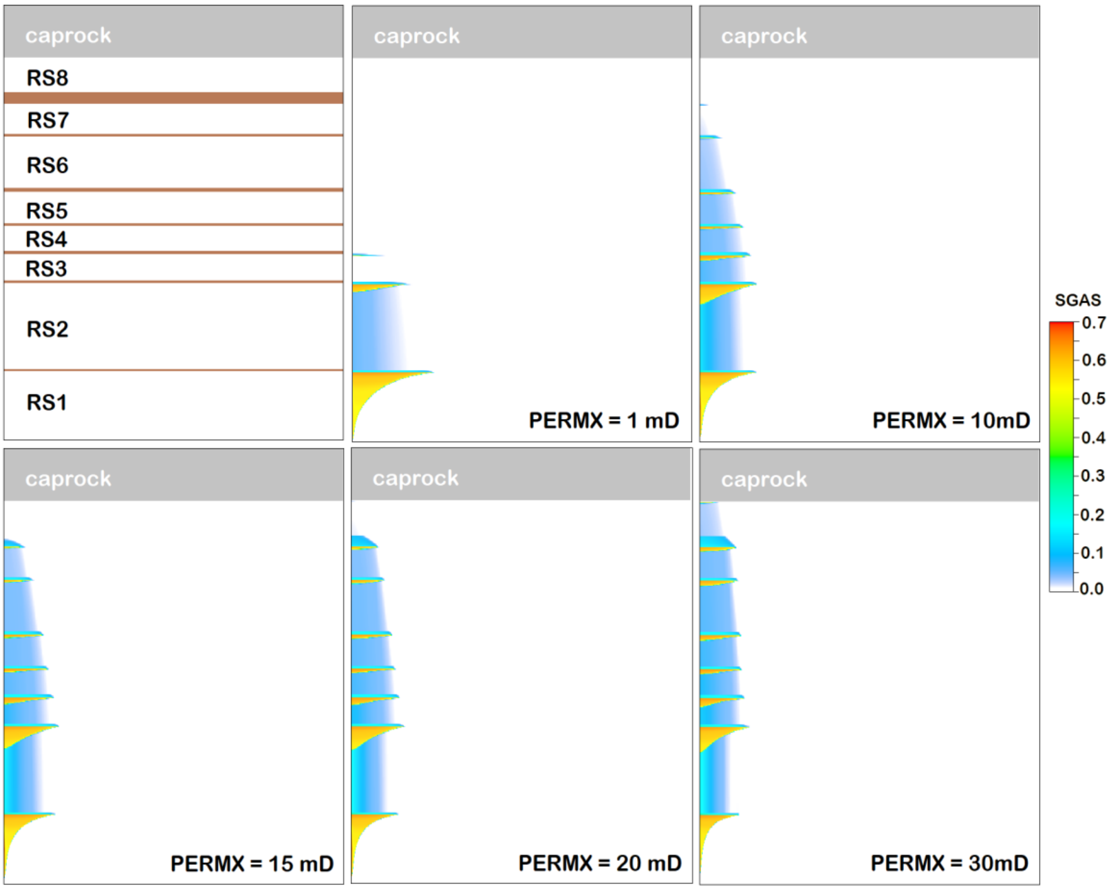

Figure 6.9: Multi-layered CO_2 plume migration for viscosity-dominated flow through reservoir argillite units with varying permeabilities. NB: PERMZ = PERMX x 0.1

It is worth noting that the plume morphology at the Sleipner site indicates that column heights of trapped CO_2 plume are low and a capillary entry pressure of 1.72 MPa may not be applicable to the Utsira mudstones (Cavanagh and Haszeldine 2014). To this end, a capillary entry pressure value three orders of magnitude less than 1.72 MPa was used for the thin argillite layers. This value was chosen by iteration to match the arrival time of CO_2 at the top of a reservoir formation in the third year of CO_2 injection, when the interbedded mudstones are assigned a permeability of 30 mD. Figure 6.10 supports the hypothesis that the buoyant movement of the non-wetting phase is strongly influenced by the capillary forces in the intra-sand mudstone units. In instances where the P_c of the CO_2 plume exceeds the mudstone entry pressure, the plume breaches the mudstone layer and migrates vertically until another capillary barrier is reached. The essential feature is that the total driving force for invading fluid flow is just about adequate to overcome the semi-permeable mudstone resistance afforded by a capillary entry pressure of 1.72 KPa. Cavanagh and Haszeldine (2014) attribute the possibility of such uncharacteristically low threshold pressures to the occurrence of micron-thick fractures in the mudstones. The Darcy flow model in Figure 6.10d portrays the pattern of pooling, breaching and vertical migration of CO_2, which matches the observed plume distribution in Sleipner. This model is identified as the base case, designated as S0, for an analysis on the sensitivity of buoyant plume migration to $P_c - k_r - S_w$ functions in the thin mudstones. Other sensitivity cases are defined in Table 6.2, while Figure 6.11 illustrates the descriptive $P_c - k_r - S_w$ curves applied herein.

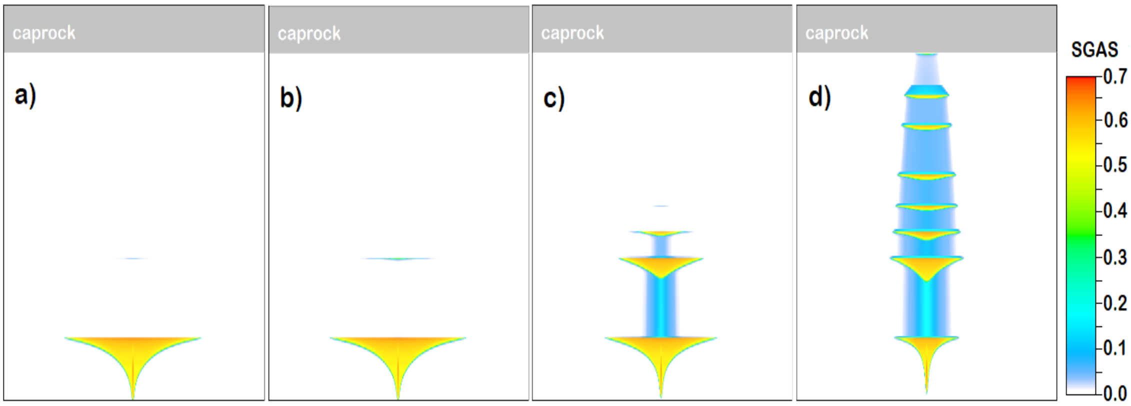

Figure 6.10: Buoyant migration of $scCO_2$ through intra-sand mudstone units modelled with capillary entry pressure of a) 1720 KPa, b) 172 KPa, c) 17.2 KPa and d) 1.72 KPa

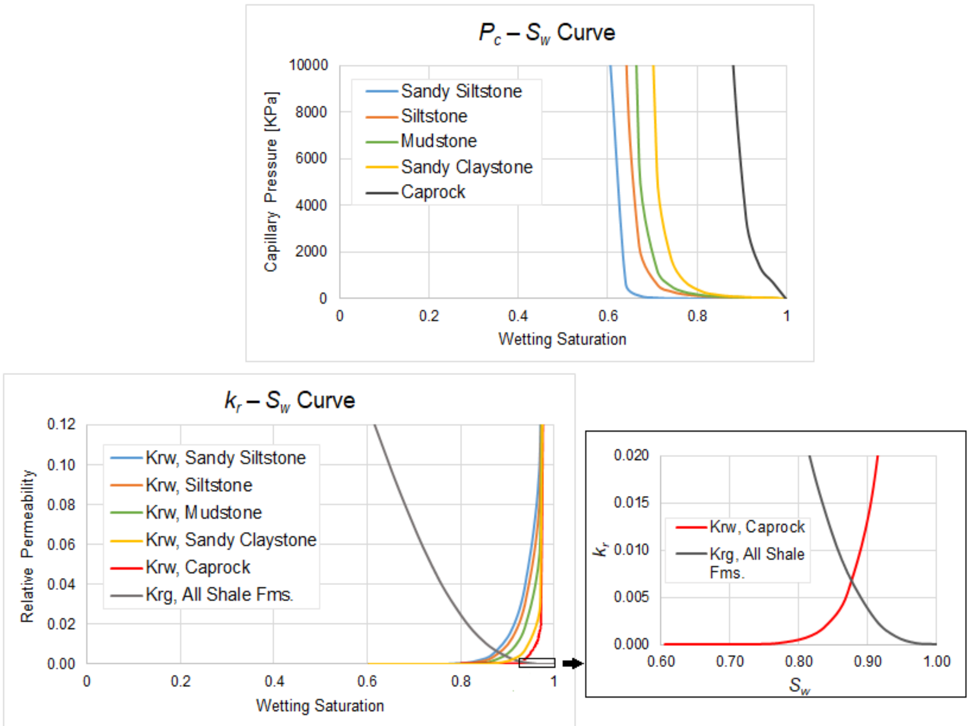

Figure 6.11: $P_c - k_r - S_w$ relationship for the various argillaceous units

CASE ID	Description of intra-sand argillite layers M1 – M6
S0	All Sandy Siltstone
S1	All Siltstone
S2	All Mudstone
S3	According to plume thickness in the 2001 Sleipner data set (Figure 6.2b) under the following assumptions: M1 = Sandy Siltstone, M2 = Siltstone, M3 = Mudstone, M4 = Sandy Siltstone, M5 = Sandy Claystone, and M6 = Siltstone.

Table 6.2: Description of sensitivity cases modelled for capillary-dominated Darcy flow analysis. NB: P_c – k_r – S_w description for M7 is equivalent to the 'sandy siltstone' for all cases modelled.

As CO_2 injection proceeds, the gas propagates under gravity along the horizontal semi-permeable argillaceous layers. Results of a 20-year injection period show that the volume of CO_2 plume pooling beneath the capillary barrier is essentially dependent on the transport properties of the semi-permeable strata above it (Figure 6.12). Sandy siltstone, which provides the least resistance to buoyant CO_2 migration, results in a higher degree of gas percolation through the sand enriched argillite, as opposed to the siltstone and mudstone. This is evident in the plume saturation profile in RS1 and RS2, *i.e.* Figure 6.12 a & b, where the thin argillite layers in cases S0, S1 and S2 are modelled as sandy siltstone, siltstone and mudstone, respectively, using the transport properties curve map in Figure 6.11. With a constant injection rate and an equivalent volume of CO_2 injected in all three cases, the loss of CO_2 plume in RS1 results in a higher concentration of mass at the front end of plume evolution in RS2. This gives a greater chance for the gravity current to advance through the overlying argillite layers. However, the likelihood of such occurrence is entirely dependent on the magnitude of capillary force in the overlying argillite layer that counteracts the buoyant force in the migrating plume. Such equilibrium between the capillary force and the buoyant force is described by the Young-Laplace equation (Hobson 1954). This equation relates the gravitational column height of buoyant fluid to the capillarity of the porous media using the expression below:

$$\Delta\rho g h = \frac{2\sigma \cos\theta}{R} \tag{6.1}$$

where $\Delta\rho g h$ is quantified as the buoyancy force counteracted by the capillary force, P_c. $\Delta\rho$ is described as the density contrast between the wetting and non-wetting fluid, g is the gravitational constant, h is the column height of buoyant plume, σ is the interfacial tension between the fluid phases, Θ is the wetting angle, and R is the pore throat radius.

As injection proceeds in cases S0, S1 and S2, pathways emerge for CO_2 percolation through the thin argillite layers. These pathways are a function of CO_2 breakthrough pressure and the column height of plume beneath each argillaceous layer. At a constant CO_2 pressure in the reservoir, the CO_2 breakthrough pressure for each argillaceous unit varies according the resistant force acting within the argillite layer. The mass of gravity current that then advances through each argillaceous unit is attributed to the column height of plume beneath that argillite layer. Hence, the case modelled with the least resistant force in each argillaceous unit, *i.e.* S0, show preferential migration of the plume to the top of the formation, *i.e.* RS8 (Figure 6.12g). This is due to the greater magnitude of buoyant force acting, with respect to the resistant force, at the top of each underlying reservoir unit, in contrast to cases S1 and S2. Case S3 elaborates on this theory where the volume profile of CO_2 plume that migrates through the first argillite (MS1) is akin to that of case S0 (Figure 6.12a). This is because the capillary forces acting within MS1 is the same in both cases.

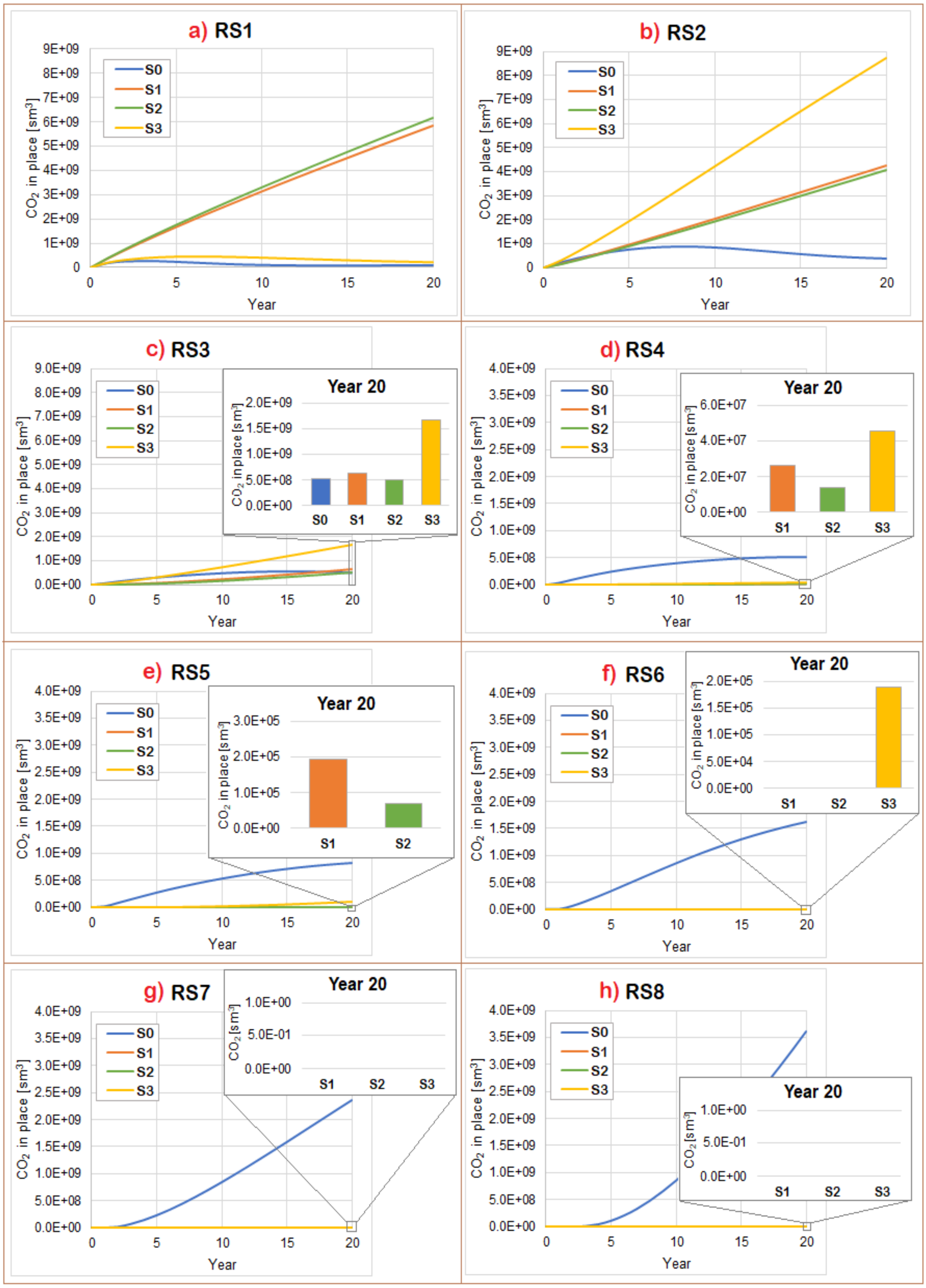

Figure 6.12: Profile of CO_2 emplaced during the injection period in a) RS1, b) RS2, as well as the volume of CO_2 emplaced at the end of injection in c) RS3, d) RS4, e) RS5, f) RS6, g) RS7, and h) RS8

As the buoyant plume migrates through MS2, a divergence in the volume profile for cases S0 and S3 in RS2 is evident and sets in due to the greater ease of CO_2 percolation to the overlying sand unit in the former (Figure 6.12b). Eventually, the varying capillary forces acting within the overlying argillite layers in case S3, which create a higher resistance to buoyant plume migration than the ones in case S0, results in shorter vertical migration through the reservoir formation (Figure 6.12g). This shows that the number of layered CO_2 plumes resulting from horizontally persistent thin argillite units in a homogeneous sandstone is highly dependent on the capillary force acting within each unit.

The main feature captured by the modelled cases is the impact of the relative permeability and capillary pressure curves on the buoyant drainage of CO_2 through the thin argillite layers. The introduction of variance in capillary pressure curves at the same capillary entry pressure gives rise to local scale capillary forces that may lead to partially saturated currents of CO_2 in the pore matrix of the argillaceous layer. Likewise, varying the relative permeability curves also affects the effective permeability of the intra-sand argillite layers. Thus, the rate of plume advancement is dependent, not just on the capillary entry pressure, but also on the correlated structure of the rock fabric's local capillary curve and the relative permeability to the invading fluid.

6.2.2 Second Case Study

Judging from the plume migration trend at Sleipner, where CO_2 plume reaches the top layer by the third year of the CO_2 injection and steadily increases through the ensuing years of injection (see Figure 6.3), it seems most of the injected CO_2 will accumulate at the top layer in the longer term. Hence, the sensitivity of the topmost accumulation to high permeability channels or thief zones within the sand wedge should prove to be a pointer for the longer-term behaviour of the plume. This is done using the benchmark model constructed for Sleipner's uppermost sand wedge, commonly referred to as the Sleipner Layer 9 Benchmark Model (Figure 6.13). Singh et al. (2010) defined input parameters derived from best estimates to provide an accurate rock and fluid property dataset for the model, including the anticipated injection rate in the sand wedge that replicates the volume profile of CO_2 within it. Refer to Appendix A of Singh et al. (2010) for the benchmark model assumptions and input parameters.

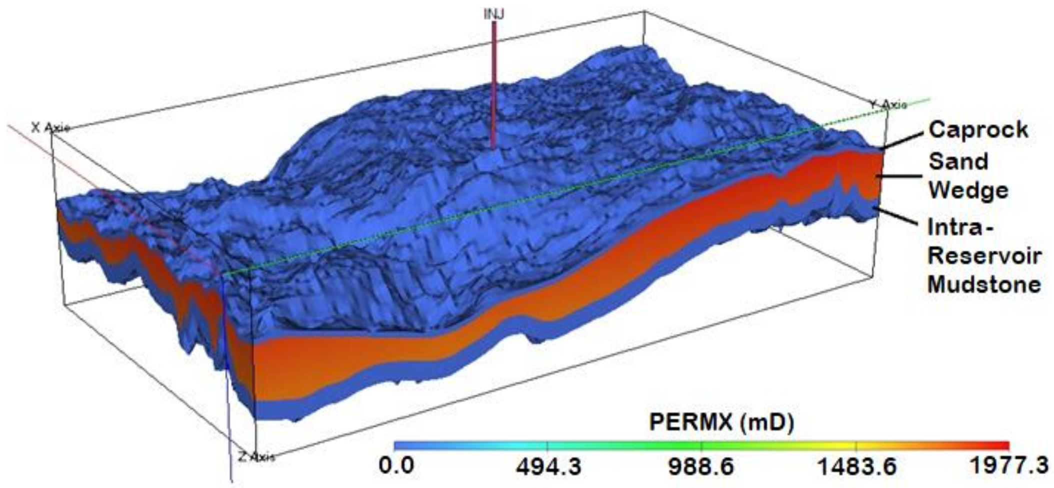

Figure 6.13: Sleipner Layer 9 Benchmark Model showing estimated horizontal permeability.

This study employs relative permeability functions to describe thief zones within the sand wedge. It differs from Williams and Chadwick's (2017) approach which uses absolute permeability to describe the thief zones. The base case for the sensitivity study in this section uses the laboratory-measured $k_r – S_w$ curve obtained from Singh et al. (2010). This is fitted to the vG-MC model using a pore geometry value [*m*] of 0.95, a brine relative permeability end-point of 0.54, a CO_2 relative permeability end-point of 0.75, a critical and connate brine saturation of 0.386 and 0.11, respectively, and a critical and connate CO_2 saturation of 0.02 and 0.0, respectively. The average permeability and porosity of the sand wedge sand are assumed to be 2000 mD and 0.36, respectively, with a permeability anisotropy of 0.1. The Sleipner Layer 9 Benchmark Model has a grid resolution of 50 m in the XY direction and 1 m in the Z direction (Singh et al. 2010).

Cases for analysing the influence of channelling in the top sand wedge on the CO_2 plume migration through the effects of relative permeability heterogeneity are defined in Table 6.3. Different relative permeability curves are computed using varying pore geometry values in Table 6.3 while keeping the end-point of relative permeability to the immiscible fluids and their saturation values constant. Laboratory-measured P_c data for Utsira Sand (Williams et al. 2018) is used and held constant for all the sensitivity cases. ECLIPSE 100 'black oil simulator' is used to simulate CO_2 injection in the Benchmark model for 11 years to replicate the distribution of CO_2 in the upper layer from 1999 to 2009 using Singh et al.'s (2010) injection rate assumptions. Figure 6.14 shows the capillary pressure and injection profile used in the study, as well as the regions for channelling in the benchmark model. The northerly and southerly channels are modelled into the top half of the reservoir column to accommodate CO_2 gravity currents that are expected to spread radially from the injection point. This is because a common feature of Darcy flow simulations for CO_2 injection in a homogeneous saline formation is the predictable coning of CO_2 plume away from the injection location (Cavanagh and Nazarian 2014).

Case ID	***Description of 'thief zones'***
C0	Base case where m = 0.95
C1	m = 0.96
C2	m = 0.97
C3	m = 0.98
C4	m = 0.99
C5	m = 0.91
C6	m = 0.85
C7	m = 0.81
C8	m = 0.75
C9	m = 0.71
C10	m = 0.65

Table 6.3: Description of cases that investigate the sensitivity of temporal evolution of CO_2 in the topmost layer to relative permeability functions in the high permeability channels.

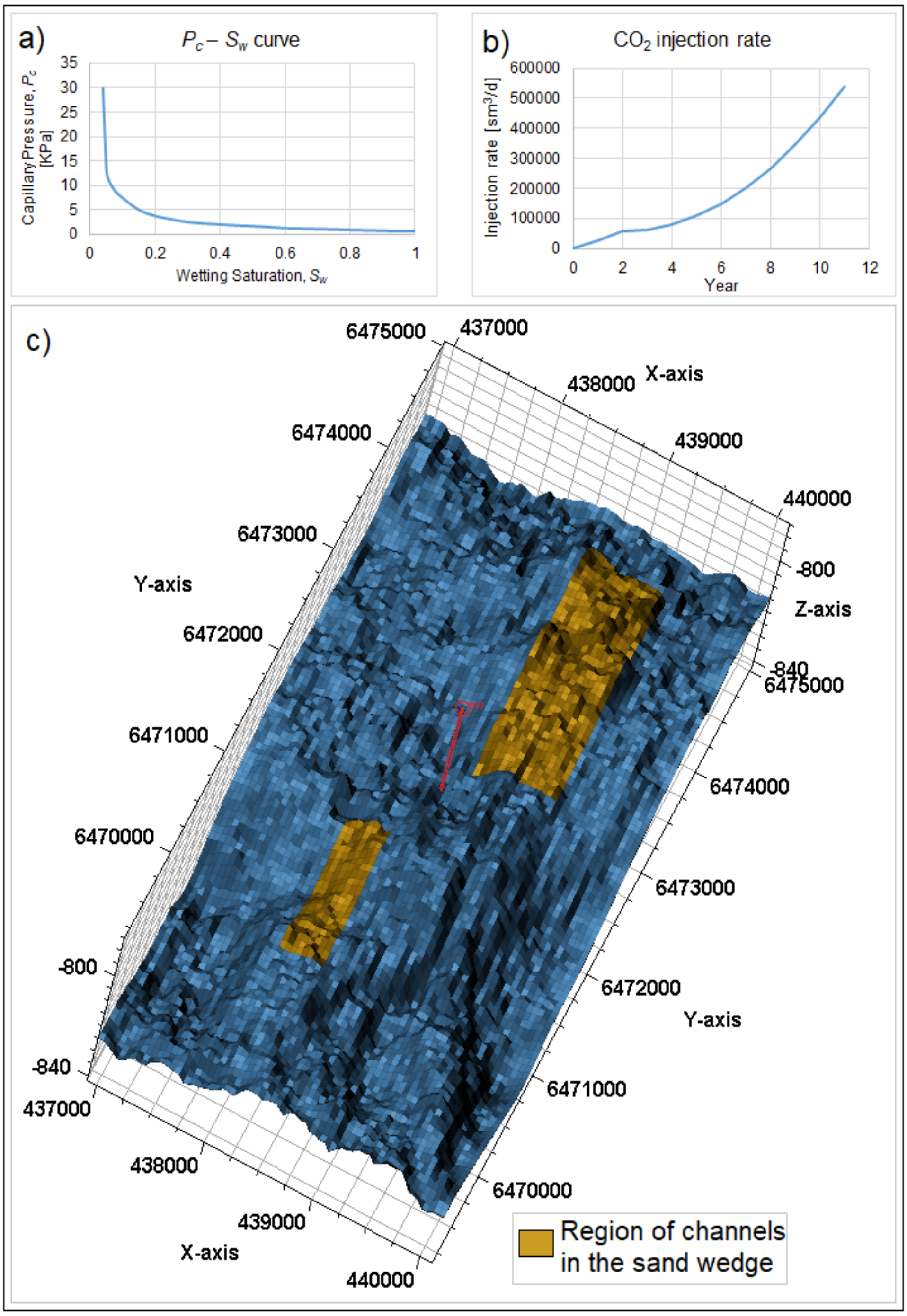

Figure 6.14: Illustration of the a) capillary pressure curve for Utsira Sand, b) the injection profile, and c) the regions for channelling in the Sleipner Layer 9 Benchmark Model.

6.2.2.1 Pressure-driven analysis

Figure 6.15 illustrates the CO_2-water contact observed in the top layer of the sand wedge at the end of the simulation run. None of the simulation outcome displayed the observed morphology of CO_2 plume at the top of the sand wedge in the seismic data set (Figure 6.15). Cavanagh (2013) has shown that a long period for pressure compensation post CO_2 injection would allow black oil simulation to attain equilibrium, thus improving the plume distribution when calibrating flow simulations to the time-lapse seismic observations. Regardless, the history matching of the plume morphology in the sand wedge is not within the scope of this study.

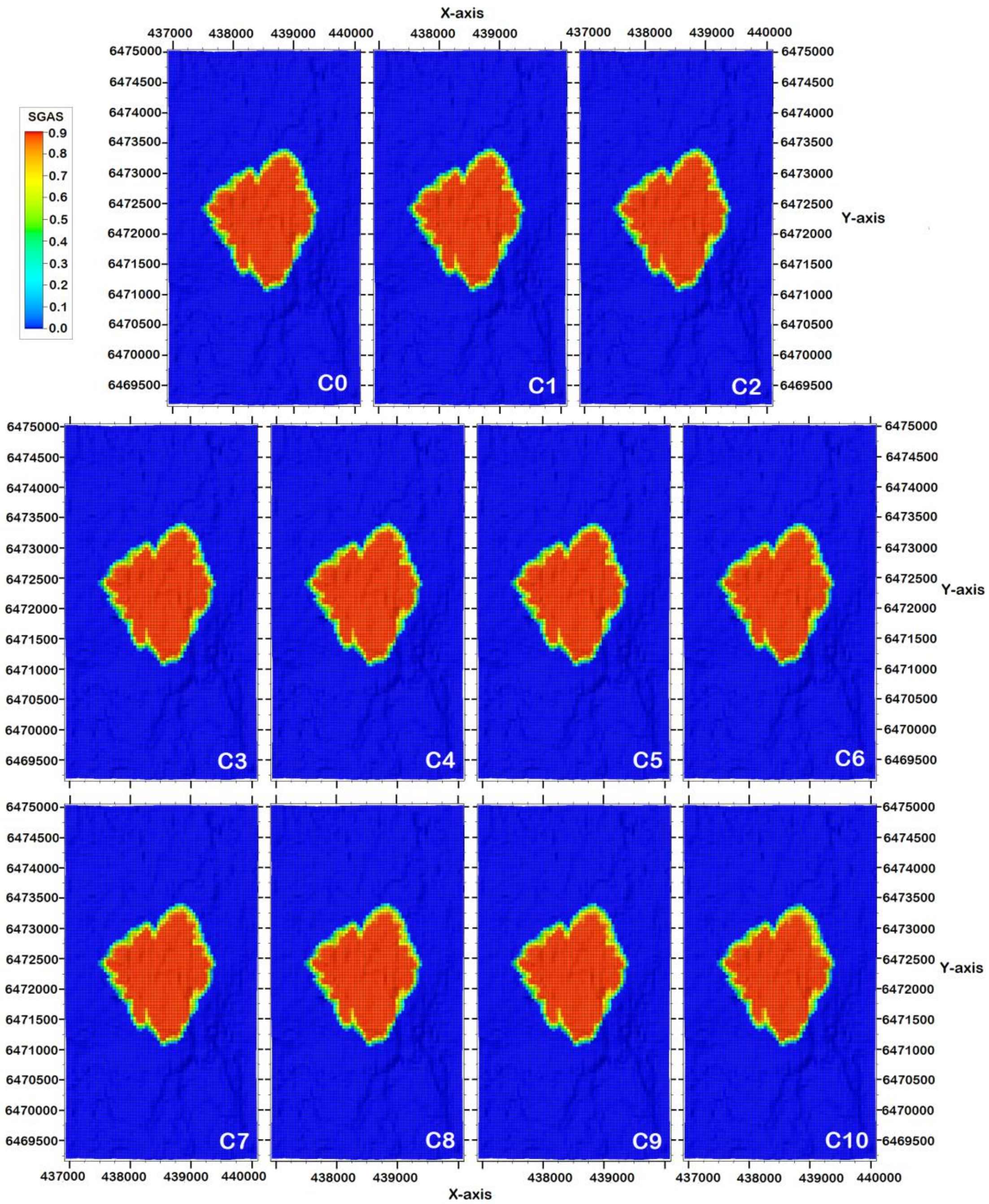

Figure 6.15: CO_2 plume morphology in the top layer of the sand wedge at the end of simulation

At first glance, Figure 6.15 showed identical morphology in the northerly and southerly plume extensions for all cases. However, on closer inspection of the grid blocks (at an expanded scale of 500%) the comparable area of plume extension only applied to the following cases: C0, C1, C2, C3, & C4; C5 & C6; C7 & C8; and C9 & C10. This could be attributed to the values of *m* for the cases in each grouping, where *m* becomes equivalent when it is rounded up to one decimal place (see Table 6.3). As a result, the effect of the relative permeability curve on fluid flow is negligible. Building on this narrative, cases C0, C6, C8 and C10 were selected as representative cases for each grouping to further examine the plume extension in the northerly and southerly channels (Figure 6.16). Recall that the simulation resolution of each grid block is 50 x 50 x 1 m.

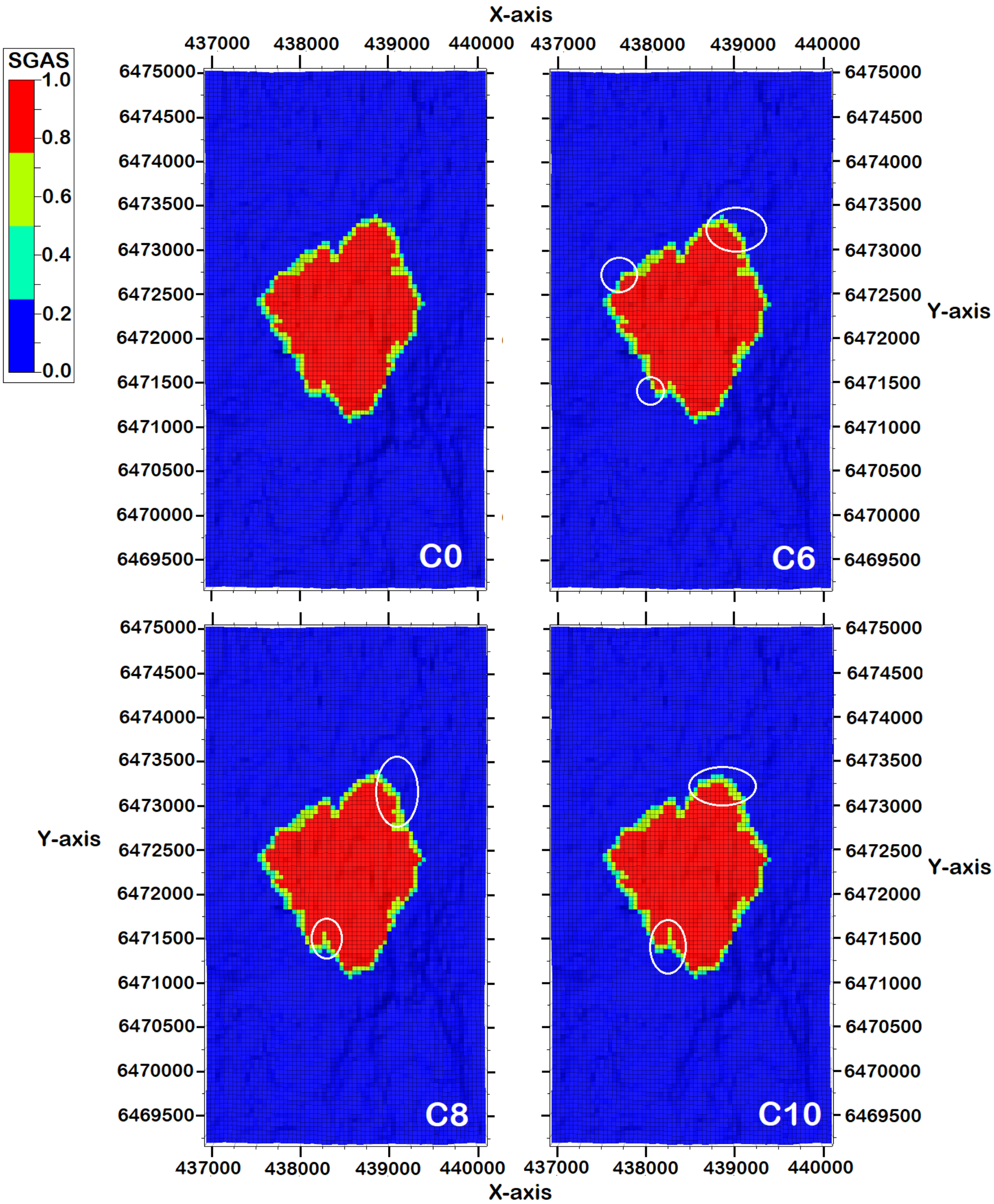

Figure 6.16: CO_2 plume morphology in the top layer of the sand wedge for the representative cases. NB: The white circles on C6, C8 and C10 are used to highlight the regions of plume shortening in comparison to the base case, C0.

In Figure 6.16, Case C0 was found to show the largest plume extension while C10 showed the least. This is readily attributed to the value of *m*, where higher values would portray a higher relative permeability to CO_2. The volume of CO_2 that migrates to the northerly and southerly channels was quantified and illustrated in Figure 6.17 for the four cases: C0, C6, C8, and C10. At the end of CO_2 injection, the mass of CO_2 in the both the norther region [NR] and the souther region [SR] was largest for C0 and followed a downward trend for case C6 through to C10. This would suggest that the chanelling of gravity currents at the top of the reservoir is sensitive to relative permeability functions, however insignificant it may seem. The inclusion of heterogeneity in the capillary pressure functions could further highlight the sensitivity at this scale. These functions have already been shown to be essential in assessing the rate of CO_2 leakage seepage in pathway flow (Section 6.2.1.1).

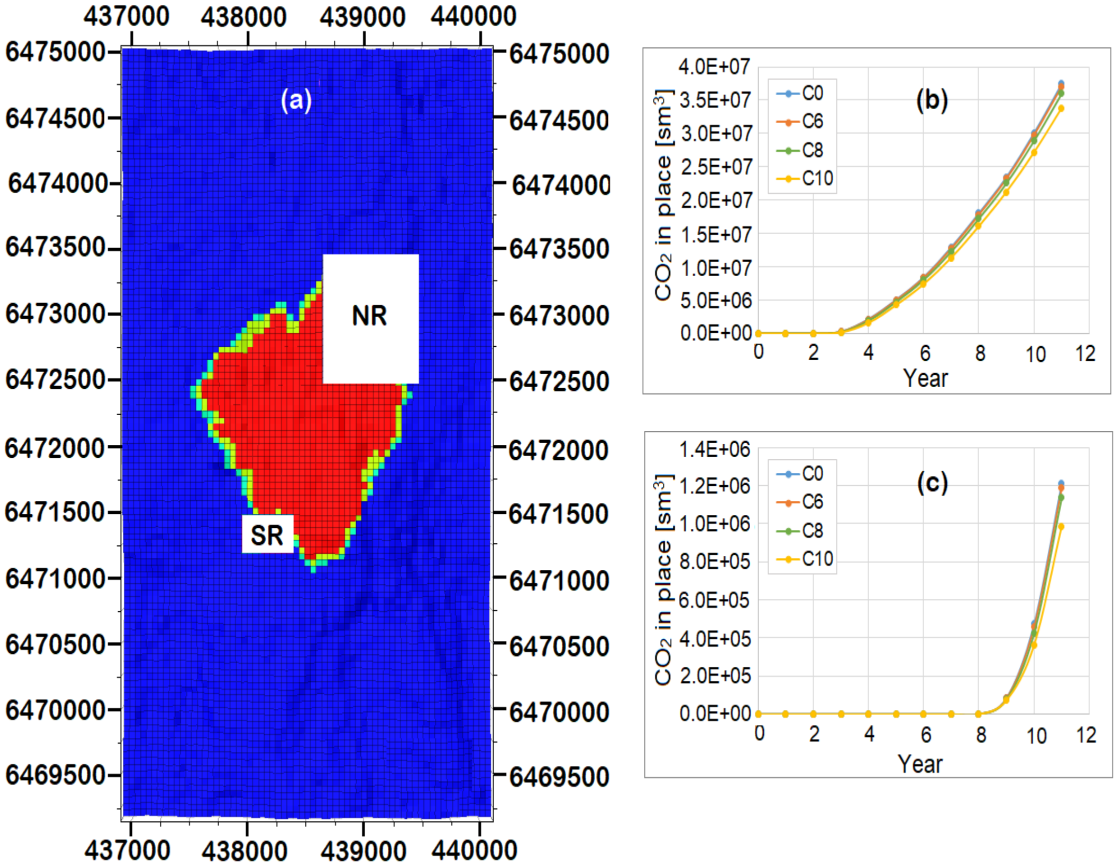

Figure 6.17: a) The description of the regions in the top layer of the sand wedge where the volume profile of CO_2 is assesed for b) the northern region, NR and c) the southern region, SR, during the simulation period.

Reflecting on 'channelling investigations' by Williams and Chadwick (2017) and Cowton et al. (2018), a better calibration of the migration rate at the northern ridge in Darcy flow simulators could be afforded by introducing heterogeneity in capillary pressure and relative permeability functions incorporated in the top sand wedge. It is common that grid resolution limitations may reduce sensitivity to relative permeability functions and capillary forces in numerical models due to numerical errors. As illustrated by Nilsen et al. (2011:3807), "the large size of coarse grid results in a large difference between the average of the non-linear relative permeability functions and the relative permeability functions evaluated in the average saturation". Refining the simulation grid will help to diminish numerical errors due to poor discretisation. Hence, high-resolution models can be used to easily capture the effects of such functions and support a Darcy-based modelling approach. A downside to using high-resolution models, however, is the computational efficiency of forward modelling within reasonable time scales using full flow physics. This has resulted in the use of less complex simulators and/or analytical methods that adopt a vertically averaged formulation of the governing equations of multiphase flow (e.g. Gasda et al. 2009, Doster et al.

2013, Nilsen et al. 2017, and Cowton et al. 2018). This usually entails modelling the gravity current in its simplest form based on the Vertical Equilibrium (VE) pseudo functions introduced by Coats et al. (1971). The VE concept assumes gravity forces alone are the driving forces towards equilibrated (segregated) vertical fluid distributions. This implies that the phase hydrostatic potential is independent of depth within a cell and relative permeabilities are calculated using segregated saturation functions in the vertical dimension (Schlumberger 2017). This may seem ideal for simulation studies in the Utsira 'sand wedge' since predictions suggest that the plume migration could be primarily buoyancy-driven and not pressure-driven (Singh et al. 2010, Cavanagh 2013). With migration proceeding further away from the injection area, the CO_2 plume becomes thinner, making numerical errors due to poor vertical discretisation more important (Nilsen et al. 2011). Under the assumption that fluid flow predominates in the horizontal direction, VE models utilise the large aspect ratio of CO_2 gravity current to reduce the complexity of flow simulations in 3D and increase computational efficiency (Cowton et al. 2018).

6.2.2.2 Gravity-segregated analysis

The gravity-segregated flow can be modelled in ECLIPSE using the VE option, where the degree of fluid segregation is specified using mixing parameters 'VEFRAC' and VEFRACP' for the relative permeability and capillary pressure, respectively (Schlumberger 2017). Using the VE option, simulation outcome for the sensitivity cases described in Table 6.3, where relative permeability variations are specified for the rock fabric in high permeability channels, showed no difference to the plume contact area when total fluid segregation is assumed. This is because when VEFRAC equals unity, the simulation disregards the relative permeability curves specified for the rock fabric in high permeability channels and only uses the VE relative permeability curves in the run. However, the VE option allows for an increase in mobility as both phases become relatively mobile in low saturations. The resulting spread in horizontal current becomes a function of the degree of fluid segregation assumed. The higher the degree of fluid segregation, the faster the spread in horizontal current along the topography of the capillary barrier (Figure 6.18). Figure 6.19 shows the outline of gas flow in a three-dimensional space where the largest plume contact area is discernible for the assumption of total fluid segregation. Even though the CO_2-water contact in the VE models do not match Sleipner's time-lapse seismic data, they illustrate better northerly and southerly plume distribution than the full Darcy flow physics simulated herein (Figure 6.20).

The plume distribution trend seen in Figure 6.20 argues for the value of VE models when calibrating petrophysical properties to history-match the plume spread in Utsira's top sand unit. In the context of sensitivity to relative permeability curves, an assumption of partial fluid segregation when using the VE option in ECLIPSE affords the modelling of CO_2 plume sensitivity to rock curves in the simulation. More importantly, high-resolution modelling using the VE option is computationally efficient. To quote Singh et al. (2010:10), "as long as high resolution models which include gravity segregation are used, good matches to field observations can be obtained using conventional black-oil simulators".

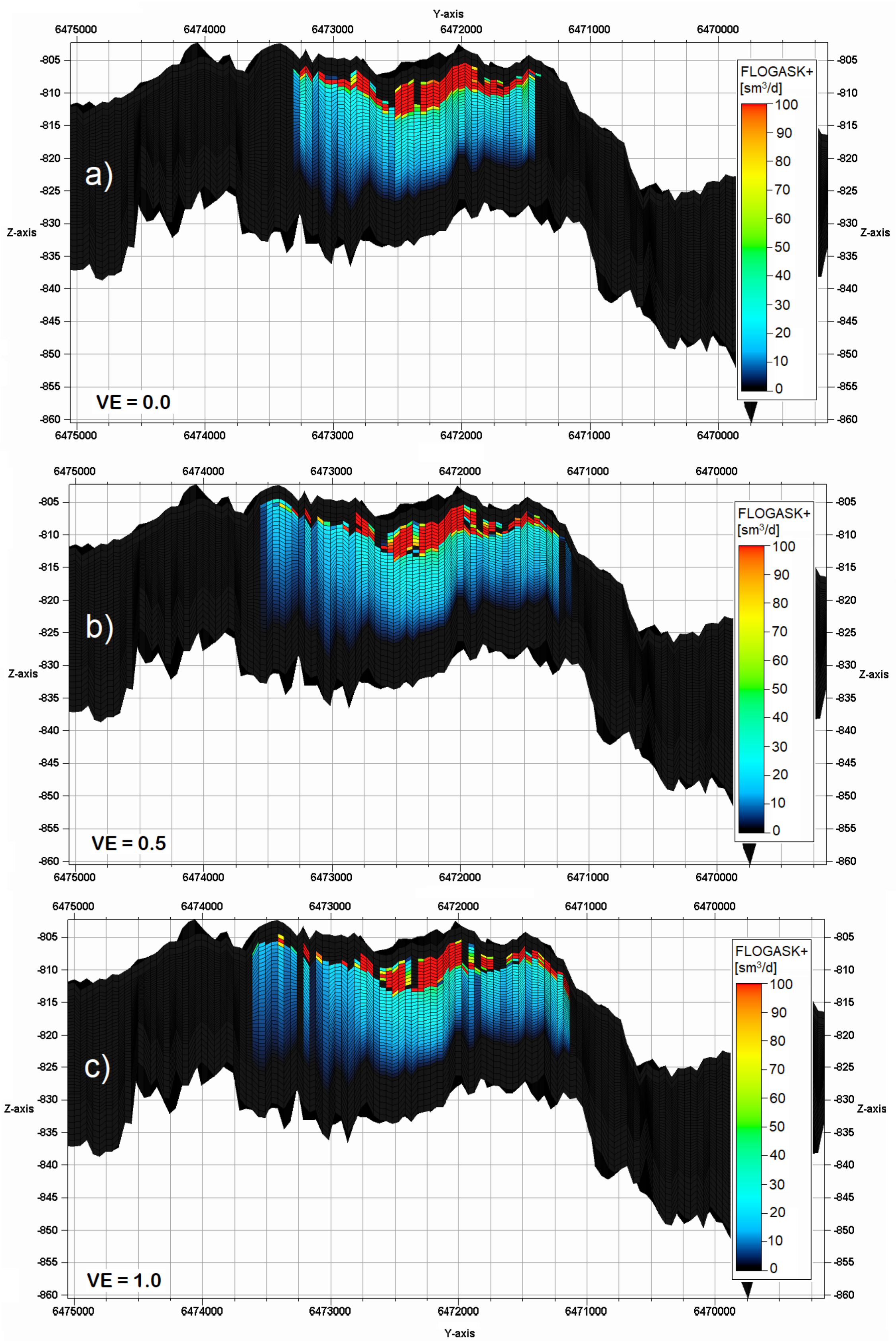

Figure 6.18: Gravity current in a cross section of the numerical domain for a VE model with a mixing fraction of a) 0.0, b) 0.5 and c) 1.0 at the end of CO_2 injection

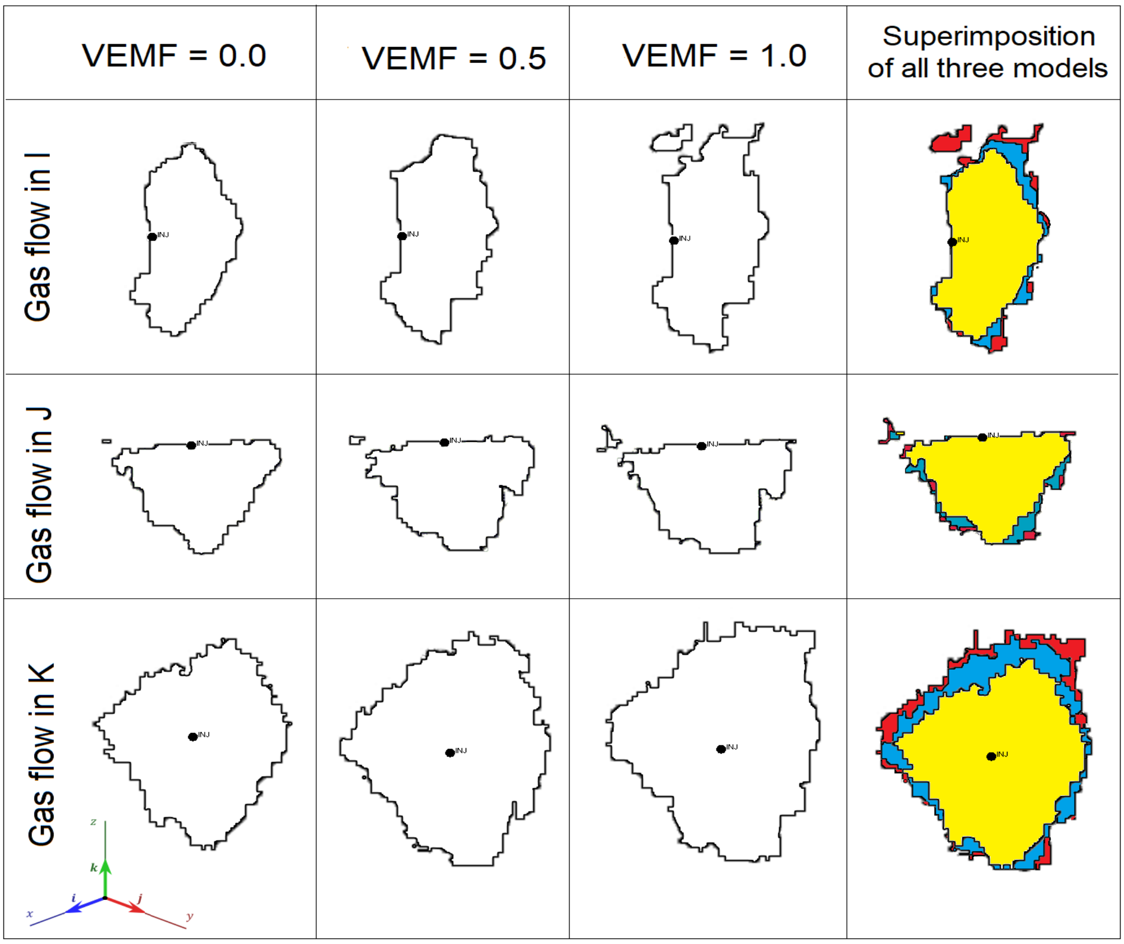

Figure 6.19: Schematic of saturated gas at the end of simulation in the three-dimensional space for the Vertical Equilibrium Mixing Fraction (VEMF) of 0.0, 0.5 and 1.0 with colour code for superimposed models illustrated as yellow, blue and red, respectively. Black disc indicates the injection point.

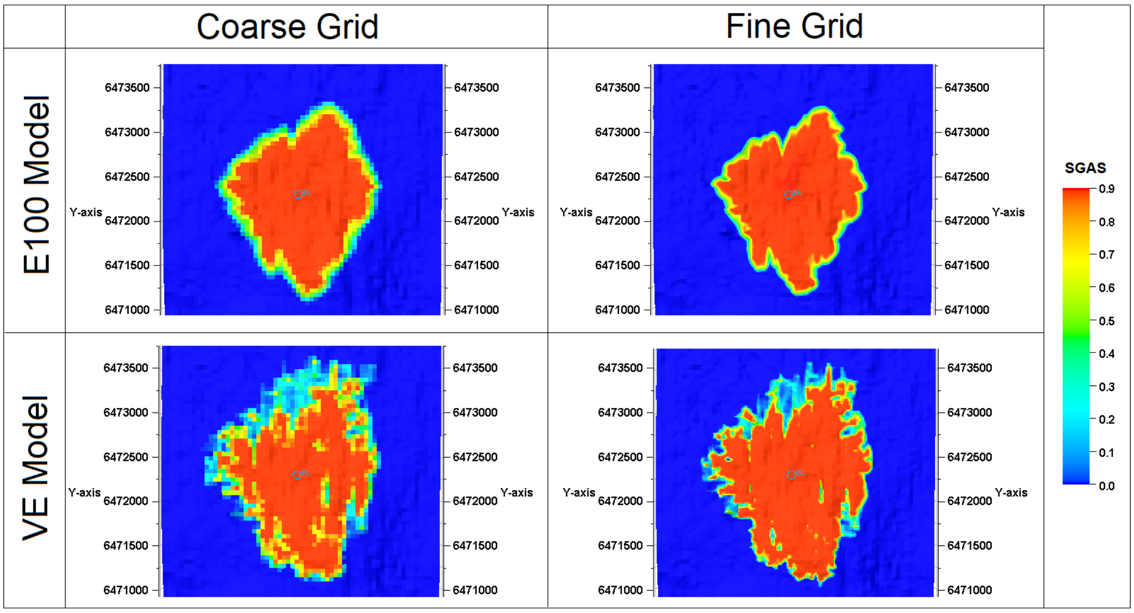

Figure 6.20: Results of flow simulation in the benchmark model for coarse and fine grids in E100 and VE models

6.3 Summary and conclusion

The first investigative study in this chapter presented an axisymmetric geometry for a fixed-volume release of supercritical CO_2 into a saline formation with intra-sand mudstone baffles in cases that describe drainage of the fluid through:

i) Viscous-limit pathways in the interbedded mudstone layers, and

ii) Capillary-limit percolation in semi-permeable mudstone layers.

The models developed were simplified but provided valuable insight into the effects of relative permeability and capillary functions on the propagation of gravity-dominated displacement flow in porous rocks. The flow modelling approach presented here suggest that the semi-permeable thin argillite layers have an atypically low capillary entry pressure of 1.72 KPa that enables the rapid vertical migration of CO_2 from the base to the top of the reservoir formation. The possibility of such low threshold pressures has been attributed to the occurrence of micron-fractures in the argillite layer, probably induced, prior to CO_2 injection, by transient fluid overpressure during rapid deglaciation at Sleipner (Cavanagh and Haszeldine 2014). The local capillary forces and relative permeability to the invading fluid were found to play a key role in moderating the rate of buoyant migration through the reservoir, including buoyant migration through pathways in laterally extensive mudstone layers. Results show that capillary forces within semi-permeable barriers in a storage formation regulates the degree of CO_2 mass that breaches the capillary barriers, while the rate of leakage in the gravity current passing through the barrier is a function of its relative permeability to the invading fluid..

The second investigation considered the sensitivity of plume extension to relative permeability functions in flow channels within the top sand unit of Utsira Formation. This assumed visco-capillary Darcy flow as the dominant process in modelling the distribution of CO_2 in the Sleipner benchmark model. Simulation outcome was found to vary from the observed CO_2-water contact in the seismic data. The poor performance of Darcy flow physics to simulate seismically-observed fluxes at the Utsira Formation, e.g. Chadwick et al. (2006), Hermanrud et al. (2009), Singh et al. (2010) and Cavanagh (2013), has been attributed to the underlying governing equation of Darcy's law which requires pressure gradient-driven viscous flow in permeable media. Nevertheless, Cavanagh (2013) observed that a pressure-compensated modelling approach improves the performance of Darcy flow models in matching the observed distribution of CO_2 at Sleipner. Most importantly, incorporating detailed depositional heterogeneity of the top sand wedge into Darcy flow models have resulted in a closer history match in CO_2 plume distribution (Williams and Chadwick 2017). However, including heterogeneity in relative permeability and capillary functions when modelling depositional heterogeneity is easily overlooked in the simulation of CO_2 geo-sequestration. Although the sensitivity of the CO_2 plume morphology, particularly within the channels in the top sand wedge, to relative permeability functions seemed insignificant in this study, including relative permeability heterogeneity in simulation studies, where and when applicable, should not be ignored. This is because the introduction of relative permeability variations opens up the possibility of investigating uncertainties in model space by facilitating a Darcy modelling approach.

CHAPTER 7

Summary, Conclusions and Recommendations

7.1 Overview of the research

In characterising reservoir units, reservoir engineers consider rock and fluid properties that can help predict fluid behaviour (Tiab and Donaldson 2015) and this requires using all available sources of reservoir data, including the capillary pressure and relative permeability functions. In this thesis, a numerical simulator based on traditional multi-phase Darcy-flow physics was used for the forward modelling of two-phase flow in CO_2–brine–rock systems. This was done in order to investigate the effect of sedimentary heterogeneities at the grain scale on CO_2 geosequestration at the field scale. The main focus was on CO_2/brine transport processes in siliciclastic formations using the descriptive functions of the multiphase flow parameters *i.e.* relative permeability (k_r) and capillary pressure (P_c) curves. A number of investigative studies were conducted in a bid to understand the effect of multi-phase fluid flow on CO_2 sorage and security. The main aim was to examine the impact of the exclusion of heterogeneities in P_c and k_r on the predictive analysis of CO_2 geosequestration. This is because heterogeneity in P_c and k_r are routinely neglected in reservoir simulations of CO_2 storage, mainly because the experimental methods for determining these functions are quite tedious and time consuming. Regardless, empirical models such as the Brooks-Corey (BC) and the van Genuchten (vG) models allows the implemention of these functions in multi-phase physics simulators employed for CO_2 storage.

In the first instance, an empirical parametrisation scheme that describes the capilllary presure – relative permeability – wetting saturation ($P_c – k_r – S_w$) relationship, when computed using the van Genuchten (vG) model, was proposed for clastic rocks. The $P_c – k_r – S_w$ relationship was duly implemented in the vG model through statistical data on the pore gemetry index (PGI) for various clastic sediments and a description of the capilllary entry pressure (P_e) in the empirical model (*see* Chapter 3). Using numerical simulation of CO_2 storage in saline aquifers, the study identified the pore geometry index as a very crucial parameter in the predictive analysis of CO_2 storage performance. The parameterisation scheme was then used as a formative tool for describing P_c and k_r heterogeneities that could arise from sedimentary structures in clastic reservoir formations and their subsequent impact on CO_2/brine transport processes in a porous medium.

Chapter 4 analysed the impact of gradation in the reservoir as well as a gradational contact at the reservoir-seal interface on CO_2 storage and security. The chapter highlighted the importance of enhancing the geological detail in such sedimentary structure, especially through P_c and k_r functions, in reservoir-specific models. The presence of gradation at the reservoir-seal contact affected the CO_2 storage performance during the predictive analysis. Clast-size gradation from coarse- to fine-grained sediments was found to improve the capillary trapping of injected CO_2 and increase the dissolution of the gas in brine. For open-boundary aquifers, the lateral continuity of such sedimentary structures could improve field-scale CO_2 storage security while also diminishing the caprock integrity around the injection well(s). This was noted as an interesting contradiction on the impact of a gradational contact at the reservoir-seal interface on the structural trapping integrity of the caprock, thus emphasising the importance of including such geological detail in the dynamic properties during numerical simualtion. The chapter also considered the sensitivity of CO_2 injectivity and storage capacity to factors such as tightly cemented flow barriers within the reservoir formation. While coarser sediments favoured reservoir injectivity, the presence of a laterally continous cemented sand mitigated the vertical propagation of pore pressure. This resulted in a ‘pressure box’ beneath the cemented layer where pore pressure rapidy increased until its curtailment by the maximum allowable bottom hole pressure, through reduction in the CO_2 injection rate. Results showed that relative permeability assumptions have a significant impact on pore pressure evolution within the reservoir as well as the quantity of CO_2 that can be injected in the store before the fracture constraint is reached.

Using the Mercia Mudstone as a case study, Chapter 5 examined the effect of a clast-size transition zone in the caprock’s base on pore pressure propagation within the seal. The pressure-driven volume flow has been considered as a very efficient transport mechanism for *in situ* fluid flow through mudrocks (Amann-Hildenbrand et al. 2015), and once gas flow is initiated in the porous media its mobility is then determined by the permeability of the formation and the $P_c – k_r – S_w$ relationship (Marschall et al. 2005). Rutqvist and Tsang (2002) have already showed that hydromechanical changes in the caprock occur in the basal unit, especially near the injection well (*i.e.* the critical zone). In this study, an additional stress change resulting from a laterally-continuous transition zone at the caprock’s base was observed in the critical zone of the seal. In subsequent geomechanical analysis, such detail in stress change would need to be accounted for to ascertain the structural integrity of sealing formations during CO_2 injection. The study confirmed the influence of the $P_c – k_r – S_w$ relationship on pressure distribution in the caprock during CO_2 injection. This reinforces the argument for the adequate representation of small-scale heterogeneities in large-scale forward modelling of CO_2 storage.

Finally, Chapter 6 documented a Darcy flow modelling approach to investigate aspects of CO_2 drainage in a sandstone formation with interbedded mudstones, using the Utsira Formation from Sleipner as a case study. The numerical simulations considered the sensitivity of the migrating CO_2 plume to relative permeability and capillary pressure functions. This was done without attempting a history-match of the observed CO_2/brine contact in Sleipner’s time-lapse seismic dataset. Contrary to prior observations by Singh et al. (2010) and Zhu et al. (2015) on the lack of plume sensitivity to relative permeability within the Utsira Formation, results in this study showed plume-migration sensitivity to k_r functions within sedimentary structures such as fluid-flow pathways and high-permeability channels. For history matching exercises at the Sleipner storage site using Darcy-flow simulators, improved calibration of the migration rate at the northerly ridge can be afforded by modelling relative permeability and capillary presssure heterogeneities that arise form high permeability channels. Higher-resolution numerical models can then be used to easily capture the sensitivity of plume migration to the variability in k_r and P_c curves. The investigations herein showed that the introduction of k_r and P_c heterogeneities in forward modelling exercises increases the efficiency of a Darcy modelling approach when investigating uncertainties using a representative elementary volume (REV).

7.2 Research contributions

One of the practical contributions of this research is the detailed insight provided by the three case studies. The case studies reveal that heterogeneity in relative permeability and capillary pressure functions should be linked to performance forecasting of CO_2 sequestration. This implies that for effective implementation of computational simulation to assess CO_2 storage performance, emphasis should be placed on understanding the impact of variability in capillary pressure and relative permeability curves within a representative elementary volume (REV). Another practical contribution is the framework for computing different capillary pressure and relative permeability curves, with respect to clastic formations, in order to gain an understanding of the interplay between capillary forces and viscous forces during continuum-scale numerical simulations. This will help to increase accuracy in the description of heterogeneity during numerical simulations and, hopefully, the subsequent analysis on multi-phase fluid flow and transport in porous media.

To date, and within available literature, no conceptual description/development of a model that describes multiphase flow-parameter heterogeneity in sedimentary rocks has been suggested for numerical analysis of multiphase fluid flow and transport processes. The results in this thesis indicate that the characterisation of the storage dynamic behaviour and risk assessment can be improved by consideration of multiphase flow-parameter heterogeneity. Since the degree of reservoir heterogeneity is the most important factor affecting fluid flow behavior in the reservoir, the parameterisation scheme can guide reservoir engineers to effectively assign capillary pressure and relative permeability heterogeneities in forward modelling exercises. This is because numerical models that disregard the sensitivity of geological detail to multi-phase fluid transport processes will fail to sufficiently account for CO_2 storage performance. To this end, the parameterisation scheme can be used as a practical tool for reservoir simulation studies. This has the potential to improve the reliable prediction of CO_2 storage performance and associated processes concerned with subsurface extraction from, and/or disposal in, porous media e.g. nuclear waste disposal, geothermal energy, hydrocarbon production and groundwater extraction. In the sparse availability of detailed laboratory data for k_r and P_c, implementing the parametrisation scheme proposed for siliciclastic formations in predictive modelling workflows should improve the assessment of any potential storage complex with significant sedimentary structures. As field development proceeds and a wide range of laboratory data become available, this approach to relative permeability generation could also enable the rapid incorporation of these data into a field wide model.

7.3 Recommendations for future work

The application of mathematical models in subsurface engineering has aided in the understanding of complex geological systems, such as reservoir geometry and associated spatial heterogeneity. Fine-scale heterogeneities in the subsurface formation have been shown to be capable of significantly affecting CO_2 migration at the large-scale. It is essential to be able to anticipate and predict their effects during the forward modelling of CO_2/brine transport processes. However, little experimental data are currently available on $scCO_2$-brine flow characteristics in deep saline aquifers. This is mainly due to the fact that constitutive capillary and relative permeability functions are highly site specific and experimental validation is time consuming. Consequently, predictive reservoir models will continue to depend upon empirical models to characterise $P_c - k_r - S_w$ relationships, and hence the need for improved parameterisation of the empirical model. To this end, the parameterisation scheme proposed in Chapter 3 can be implemented to describe the hydraulic behaviour of sandstone and mudstone when using either the Brooks-Corey or van Genuchten model.

Future works should focus on laboratory studies to validate the curves implemented in this study. This should entail an appropriate documentation of the petrography data during the experimental measurement of capillary pressure and relative permeability of a clastic rock sample. Pending the availability of a collective pool of experimental data that will give precision to the boundaries of pore geometry index (PGI) for various clastic rocks, utilising state-of-the-art three-dimensional (3D) printing and computational techniques to validate and refine this multiphase flow-parameter model should be considered. This could be possible through X-Ray Computed Tomography (CT) visualisation followed by the digital reconstruction of core samples, then subsequent non-destructive laboratory measurement of multiphase fluid flow parameters in the artificial (3D printed) porous media, as well as numerical modelling and simulations of multiphase flow physics in the pore-, core-, and field-scale. In the longer term, a validated and refined multiphase flow-parameter model can be incorporated into simulation tools where fluid and transport in porous media are the key processes. This will enable the efficient computation of sedimentary heterogeneities in field-scale analysis and such high-quality software will be an invaluable platform to interact with the end users.

This thesis acknowledges that the numerical analysis on the effect of small-scale heterogeneities on large-scale analysis of CO_2 storage in porous media conducted herein used simplifying assumptions, that:

a) the variation in the constitutive functions only depend on the average grain size, and
b) the small-scale heterogeneities in the model space are, in most part, defined by laterally continuous sedimentary structures.

As a result, there is room for further investigation by considering the effects of additional factors such as patchy distribution of these heterogeneities, impermeable faults, and leaky well bores on changes in hydraulic properties. For instance, faults are important in compartmentalising reservoirs and modifying the depositional continuity (Bouvier et al. 1989). The increased knowledge of fault-induced reservoir compartmentalisation and communication can influence how primary sedimentary structures define reservoir flow processes (Zulqarnain et al. 2018). Also, subsequent diagenetically precipitated materials post particle deposition can form patches of cemented sand which constitute flow barriers within the reservoir. This thesis has shown that laterally continous cementation not only constitutes barriers to flow but may also form pressure seals which can impact on the reservoir injectivity. Hence, detailed sedimentary and petrographic analyses, including the fine-scale examination of well data and reservoir-specific models are required to adequately predict CO_2 storage performance. Further studies should model other features like faults with different transmissibility and patchy sedimentary structures in order to understand their influence. The development of reservoir depositional models could prove useful for studies that anticipate and predict the effects of depositional heterogeneities in site-specific analysis.

Possible alteration of capillary pressure and relative permeability functions in CO_2 rich systems should also be considered, including the susceptibility of these functions to thermal properties of the storage formation and transport processes during CO_2 injection (Wang et al. 2019, Tsuji et al. 2019). Additionally, upscaling of the capillary pressure and relative permeability curves for regional-scale studies should also be considered. The coarse models should preserve the most important flow characteristics and sub-grid heterogeneity hence appropriate multiscale upscaling techniques such as the Pore-Volume-Weighted (PVW) method (Barker and Thibeau 1997), the Transmissibility-Potential-Weighted (TPW) method (Darman et al. 1999), and Hewett and Archer (1997) stream-tubes approach should be examined.

References

Aarnes, J.E., Kippe, V., Lie, K.-A., and Rustad, A.B. (2007) 'Modelling of Multiscale Structures in Flow Simulations for Petroleum Reservoirs'. in *Geometric Modelling, Numerical Simulation, and Optimization*, 307–360.

Abaci, S., Edwards, J.S., and Whittaker, B.N. (1992) 'Relative Permeability Measurements for Two Phase Flow in Unconsolidated Sands'. *Mine Water and the Environment* 11 (2), 11–26.

Aimard, N., Lescanne, M., Mouronval, G., and Prebende, C. (2007) 'The CO_2 Pilot at Lacq: An Integrated Oxycombustion CO_2 Capture and Geological Storage Project in the South West of France'. in *International Petroleum Technology Conference* held 4-6 December 2007 at Dubai, U.A.E: Society of Petroleum Engineers.

Al-Khdheeawi, E.A., Vialle, S., Barifcani, A., Sarmadivaleh, M., and Iglauer, S. (2017) 'Impact of Reservoir Wettability and Heterogeneity on CO_2-Plume Migration and Trapping Capacity'. *International Journal of Greenhouse Gas Control* 58. 142–158.

Al-Menhali, A., Reynolds, C., Lai, P., Niu, B., Nicholls, N., Crawshaw, J.P., and Krevor, S. (2014) 'Advanced Reservoir Characterization for CO_2 Storage'. in *International Petroleum Technology Conference* held 19-22 January 2014 at Doha, Qatar: Society of Petroleum Engineers.

Al-Mutairi, S.M., Abu-Khamsin, S.A., Okasha, T.M., and Hossain, M.E. (2014) 'An Experimental Investigation of Wettability Alteration during CO_2 Immiscible Flooding'. *Journal of Petroleum Science and Engineering* 120, 73–77.

Ali, K., Anwar-ul-Haq, Bilal, S., and Siddiqi, S. (2006) 'Concentration and Temperature Dependence of Surface Parameters of Some Aqueous Salt Solutions'. *Colloids and Surfaces A: Physicochemical and Engineering Aspects* 272 (1–2), 105–110.

Alkan, H., Cinar, Y., and Ãœlker, E.B. (2010) 'Impact of Capillary Pressure, Salinity and In Situ Conditions on CO_2 Injection into Saline Aquifers'. *Transport in Porous Media* 84 (3), 799–819.

Amaefule, J.O. and Handy, L.L. (1982) 'The Effect of Interfacial Tensions on Relative Oil/Water Permeabilities of Consolidated Porous Media'. *Society of Petroleum Engineers Journal* 22 (03), 371–381.

Amann-Hildenbrand, A., Bertier, P., Busch, A., and Krooss, B.M. (2013) 'Experimental Investigation of the Sealing Capacity of Generic Clay-Rich Caprocks'. *International Journal of Greenhouse Gas Control* 19, 620–641.

Amann-Hildenbrand, A., Krooss, B.M., Harrington, J., Cuss, R., Davy, C., Skoczylas, F., Jacops, E., and Maes, N. (2015) 'Gas Transfer Through Clay Barriers'. in *Natural and Engineered Clay Barriers*. ed. by Tournassat, C., Steefel, C., Bourg, I., and Bergaya, F. vol. 6. Amsterdam, Netherlands: Elsevier Ltd., 227–267.

Angeli, M., Soldal, M., Skurtveit, E., and Aker, E. (2009) 'Experimental Percolation of Supercritical CO_2 through a Caprock'. in *Greenhouse Gas Control Technologies 9* vol. 1 (1). 3351–3358.

Aplin, A.C., Fleet, A.J., and Macquaker, J.H.S. (1999) *Muds and Mudstones: Physical and Fluid-Flow Properties*. vol. 158. London; Tulsa, OK: Geological Society; USA distributor, AAPG Bookstore.

Arif, M., Al-Yaseri, A.Z., Barifcani, A., Lebedev, M., and Iglauer, S. (2016) 'Impact of Pressure and Temperature on CO_2–brine–mica Contact Angles and CO_2–brine Interfacial Tension: Implications for Carbon Geo-Sequestration'. *Journal of Colloid and Interface Science* 462, 208–215.

Armitage, P.J., Worden, R.H., Faulkner, D.R., Butcher, A.R., and Espie, A.A. (2016) 'Permeability of the Mercia Mudstone: Suitability as Caprock to Carbon Capture and Storage Sites'. *Geofluids* 16 (1), 26–42.

Arts, R., Eiken, O., Chadwick, A., Zweigel, P., van der Meer, L., and Zinszner, B. (2004) 'Monitoring of CO_2 Injected at Sleipner Using Time-Lapse Seismic Data'. *Energy* 29 (9–10), 1383–1392.

Ashraf, M. (2014) 'Geological Storage of CO_2: Heterogeneity Impact on the Behavior of Pressure'. *International Journal of Greenhouse Gas Control* 28, 356–368.

Bachu, S. (2013) 'Drainage and Imbibition CO_2/Brine Relative Permeability Curves at in Situ Conditions for Sandstone Formations in Western Canada'. *Energy Procedia* 37, 4428–4436.

Bachu, S. (2008) 'CO_2 Storage in Geological Media: Role, Means, Status and Barriers to Deployment'. *Progress in Energy and Combustion Science* 34 (2), 254–273.

Bachu, S. (2003) 'Screening and Ranking of Sedimentary Basins for Sequestration of CO_2 in Geological Media in Response to Climate Change'. *Environmental Geology* 44 (3), 277–289.

Bachu, S. (2000) 'Sequestration of CO_2 in Geological Media: Criteria and Approach for Site Selection in Response to Climate Change'. *Energy Conversion and Management* 41 (9), 953–970.

Bachu, S. and Adams, J.J. (2003) 'Sequestration of CO_2 in Geological Media in Response to Climate Change: Capacity of Deep Saline Aquifers to Sequester CO_2 in Solution'. *Energy Conversion and Management* 44 (20), 3151–3175.

Bachu, S. and Bennion, B. (2008) 'Effects of In-Situ Conditions on Relative Permeability Characteristics of CO_2-Brine Systems'. *Environmental Geology* 54 (8), 1707–1722.

Bachu, S., Gunter, W.D., and Perkins, E.H. (1994) 'Aquifer Disposal of CO_2: Hydrodynamic and Mineral Trapping'. in *Energy Conversion and Management* 35 (4). 269–279.

Bardon, C. and Longeron, D.G. (1980) 'Influence of Very Low Interfacial Tensions on Relative Permeability'. *Society of Petroleum Engineers Journal* 20 (05), 391–401.

Barker, J.W. and Thibeau, S. (1997) 'A Critical Review of the Use of Pseudorelative Permeabilities for Upscaling'. SPE Reservoir Engineering 12 (02), 138–143.

Bastin, J.C., Boycott-Brown, T., Sims, A., and Woodhouse, R. (2003) 'The South Morecambe Gas Field, Blocks 110/2a, 110/3a, 110/7a and 110/8a, East Irish Sea'. *Geological Society, London, Memoirs* 20 (1), 107–118.

Bear, J. (1972) *Dynamics of Fluids in Porous Media*. New York: American Elsevier Publishing Company.

Bennion, D.B. and Bachu, S. (2008) 'Drainage and Imbibition Relative Permeability Relationships for Supercritical CO_2/Brine and H_2S/Brine Systems in Intergranular Sandstone, Carbonate, Shale, and Anhydrite Rocks'. *SPE Reservoir Evaluation and Engineering* 11, 487–496.

Bennion, D.B. and Bachu, S. (2006) 'Dependence on Temperature, Pressure, and Salinity of the IFT and Relative Permeability Displacement Characteristics of CO_2 Injected in Deep Saline Aquifers'. in *SPE Annual Technical Conference and Exhibition* held 24-27 Spetember 2006 at San Antonio, Texas: Society of Petroleum Engineers.

Benson, S., Hingerl, F., Zuo, L., Pini, R., Niu, B., Reynolds, C., Krevor, S., Calvo, R., and Niemi, A. (2015) *Relative Permeability for Multi-Phase Flow in CO_2 Storage Reservoirs. Part II: Resolving Fundamental Issues and Filling Data Gaps* [online] available from < http://decarboni.se/sites/default/files/publications/193438/relative-permeability-multi-phase-flow-co2-storage%20reservoirs-part-ii-resolving-fundamental-issues-filling-data-gaps.pdf> [28 November 2018]

Benson, S., Pini, R., Reynolds, C., and Krevor, S. (2013) *Relative Permeability Analyses to Describe Multi-Phase Flow in CO_2 Storage Reservoirs* [online] available from <http://hub.globalccsinstitute.com/sites/default/files/publications/111691/relative-permeability-analysis-describe-multi-phase-flow-co2-storage-reservoirs.pdf> [21 August 2018]

Benson, S.M. and Cole, D.R. (2008) 'CO_2 Sequestration in Deep Sedimentary Formations'. *Elements* 4 (5), 325–331.

Benson, S.M. and Surles, T. (2006) 'Carbon Dioxide Capture and Storage: An Overview With Emphasis on Capture and Storage in Deep Geological Formations'. *Proceedings of the IEEE* 94 (10), 1795–1805.

Benton, M.J., Cook, E., and Turner, P. (2002) *Permian and Triassic Red Beds and the Penarth Group of Great Britain*. Geological. Peterborough: Joint Nature Conservation Committee

Bergman, P.D. and Winter, E.M. (1995) 'Disposal of Carbon Dioxide in Aquifers in the U.S.' in *Energy Conversion and Management* 36 (6). 523–526.

Beygi, M.R., Delshad, M., Pudugramam, V.S., Pope, G.A., and Wheeler, M.F. (2015) 'Novel Three-Phase Compositional Relative Permeability and Three-Phase Hysteresis Models'. *SPE Journal* 20 (01), 21–34.

Bickle, M., Chadwick, A., Huppert, H.E., Hallworth, M., and Lyle, S. (2007) 'Modelling Carbon Dioxide Accumulation at Sleipner: Implications for Underground Carbon Storage'. *Earth and Planetary Science Letters* 255 (1–2), 164–176.

Bihani, A. and Daigle, H. (2019) 'On the Role of Spatially Correlated Heterogeneity in Determining Mudrock Sealing Capacity for CO_2 Sequestration'. *Marine and Petroleum Geology* 106, 116–127.

Bikkina, P.K. (2012) 'Reply to the Comments on "Contact Angle Measurements of CO_2–water–quartz/Calcite Systems in the Perspective of Carbon Sequestration"'. *International Journal of Greenhouse Gas Control* 7, 263–264.

Bikkina, P.K. (2011) 'Contact Angle Measurements of CO_2–water–quartz/Calcite Systems in the Perspective of Carbon Sequestration'. *International Journal of Greenhouse Gas Control* 5 (5), 1259–1271.

Birkholzer, J.T., Oldenburg, C.M., and Zhou, Q. (2015) 'CO_2 Migration and Pressure Evolution in Deep Saline Aquifers'. *International Journal of Greenhouse Gas Control* 40, 203–220.

Birkholzer, J.T., Zhou, Q., and Tsang, C.-F. (2009) 'Large-Scale Impact of CO_2 Storage in Deep Saline Aquifers: A Sensitivity Study on Pressure Response in Stratified Systems'. *International Journal of Greenhouse Gas Control* 3 (2), 181–194.

Bjørlykke, K. (2010) *Petroleum Geoscience: From Sedimentary Environments to Rock Physics*. Berlin Heidelberg: Springer-Verlag

Bloomfield, J.P., Gooddy, D.C., Bright, M.I., and Williams, P.J. (2001) ‘Pore-Throat Size Distributions in Permo-Triassic Sandstones from the United Kingdom and Some Implications for Contaminant Hydrogeology’. *Hydrogeology Journal* 9 (3), 219–230

Blunt, M.J. (2000) ‘An Empirical Model for Three-Phase Relative Permeability’. *SPE Journal* 5 (04), 435–445.

Blunt, M.J., Bijeljic, B., Dong, H., Gharbi, O., Iglauer, S., Mostaghimi, P., Paluszny, A., and Pentland, C. (2013) ‘Pore-Scale Imaging and Modelling’. *Advances in Water Resources* 51, 197–216.

Boait, F., White, N., Chadwick, A., Noy, D., and Bickle, M. (2011) ‘Layer Spreading and Dimming within the CO_2 Plume at the Sleipner Field in the North Sea’. *Energy Procedia* 4, 3254–3261.

Boggs, S. (2009) *Petrology of Sedimentary Rocks*. 2nd edn. Cambridge: Cambridge University Press.

Boggs, S. (2006) *Principles of Sedimentology and Stratigraphy*. 4th edn. New Jersey, USA: Pearson Prentice Hall.

Bouvier, J.D., Kaars-Sijpesteijn, C.H., Kluesner, D.F., Onyejekwe, C.C., and Van Der Pal, R.C. (1989) ‘Three-Dimensional Seismic Interpretation and Fault Sealing Investigations, Nun River Field, Nigeria’. *AAPG Bulletin* 73 (11), 1397–1414.

Brook, M., Shaw, K., Vincent, C., and Holloway, S. (2003) *Storage Potential of the Bunter Sandstone in the UK Sector of the Southern North Sea and the Adjacent Onshore Area of Eastern England*. vol. CR/03/154. Nottingham: British Geological Survey.

Brooks, R.H. and Corey, A.T. (1964) ‘Hydraulic Properties of Porous Media’. *Hydrology Papers* 3, 1–27.

Broseta, D., Tonnet, N., and Shah, V. (2012) ‘Are Rocks Still Water-Wet in the Presence of Dense CO_2 or H_2S?’ *Geofluids* 12 (4), 280–294.

Brown, A. (2000) ‘Evaluation of Possible Gas Microseepage Mechanisms’. *AAPG Bulletin* 84 (11), 1775–1789.

BSI (1990) *British Standard Methods of Test for Soils for Civil Engineering Purposes. BS 1377: Part 1-9*. British Standards Institution.

Buckley, S.E. and Leverett, M.C. (1942) 'Mechanism of Fluid Displacement in Sands'. *Transactions of the AIME* 146 (1), 107–116.

Burdine, N.T. (1953) 'Relative Permeability Calculations From Pore Size Distribution Data'. *Journal of Petroleum Technology* 5 (3), 71–78.

Burnside, N.M. and Naylor, M. (2014) ‘Review and Implications of Relative Permeability of CO_2/Brine Systems and Residual Trapping of CO_2’. *International Journal of Greenhouse Gas Control* 23, 1–11.

Burton, M., Kumar, N., and Bryant, S.L. (2009) ‘CO_2 Injectivity into Brine Aquifers: Why Relative Permeability Matters as Much as Absolute Permeability’. *Energy Procedia* 1 (1), 3091–3098.

Busch, A., Alles, S., Gensterblum, Y., Prinz, D., Dewhurst, D.N., Raven, M.D., Stanjek, H., and

Krooss, B.M. (2008) ‘Carbon Dioxide Storage Potential of Shales’. *International Journal of Greenhouse Gas Control* 2 (3), 297–308.

Cameron, D.A. and Durlofsky, L.J. (2012) ‘Optimization of Well Placement, CO_2 Injection Rates, and Brine Cycling for Geological Carbon Sequestration’. *International Journal of Greenhouse Gas Control* 10, 100–112.

Carlson, F.M. (1981) ‘Simulation of Relative Permeability Hysteresis to the Nonwetting Phase’. in *SPE Annual Technical Conference and Exhibition* held 4-7 October 1981 at San Antonio, Texas: Society of Petroleum Engineers.

Carman, P.C. (1956) *Flow of Gases through Porous Media*. New York: Academic Press Inc.

Carsel, R.F. and Parrish, R.S. (1988) ‘Developing Joint Probability Distributions of Soil Water Retention Characteristics’. *Water Resources Research* 24 (5), 755–769.

Cavanagh, A. (2013) ‘Benchmark Calibration and Prediction of the Sleipner CO_2 Plume from 2006 to 2012’. *Energy Procedia* 37, 3529–3545.

Cavanagh, A. and Nazarian, B. (2014) ‘A New and Extended Sleipner Benchmark Model for CO_2 Storage Simulations in the Utsira Formation’. *Energy Procedia* 63, 2831–2835.

Cavanagh, A.J. and Haszeldine, R.S. (2014) ‘The Sleipner Storage Site: Capillary Flow Modeling of a Layered CO_2 Plume Requires Fractured Shale Barriers within the Utsira Formation’. *International Journal of Greenhouse Gas Control* 21, 101–112.

Chadwick, R.A., Holloway, S., Brook, M.S., and Kirby, G.A. (2004) ‘The Case for Underground CO_2 Sequestration in Northern Europe’. *Geological Society Special Publications* 233, 17–23.

Chadwick, A., Noy, D., Lindeberg, E., Arts, R., Eiken, O., and Williams, G. (2006) ‘Calibrating Reservoir Performance with Time-Lapse Seismic Monitoring and Flow Simulations of the Sleipner CO_2 Plume’. in *GHGT-8: 8th International Conference on Greenhouse Gas Control Technologies* held 19-22 June 2006 at Trondheim, Norway: Oxford, Elsevier, 1–6.

Chadwick, R.A., Arts, R., and Eiken, O. (2005) ‘4D Seismic Quantification of a Growing CO_2 Plume at Sleipner, North Sea’. *Geological Society, London, Petroleum Geology Conference Series* 6 (1), 1385–1399.

Chadwick, R.A., Arts, R., Eiken, O., Kirby, G.A., Lindeberg, E., and Zweigel, P. (2004) ‘4D Seismic Imaging of an Injected CO_2 Plume at the Sleipner Field, Central North Sea’. *Geological Society, London, Memoirs* 29 (1), 311–320.

Chadwick, R.A. and Noy, D.J. (2015) ‘Underground CO_2 Storage: Demonstrating Regulatory Conformance by Convergence of History-Matched Modeled and Observed CO_2 Plume Behavior Using Sleipner Time-Lapse Seismics’. *Greenhouse Gases: Science and Technology* 5 (3), 305–322.

Chadwick, R.A. and Noy, D.J. (2010) ‘History-Matching Flow Simulations and Time-Lapse Seismic Data from the Sleipner CO_2 Plume’. *Geological Society, London, Petroleum Geology Conference series* 7 (1), 1171–1182.

Chadwick, R.A., Williams, G.A., Williams, J.D.O., and Noy, D.J. (2012) ‘Measuring Pressure Performance of a Large Saline Aquifer during Industrial-Scale CO_2 Injection: The Utsira Sand, Norwegian North Sea’. *International Journal of Greenhouse Gas Control* 10, 374–388.

Chalbaud, C.A., Robin, M., and Egermann, P. (2006) ‘Interfacial Tension Data and Correlations of Brine-CO_2 Systems under Reservoir Conditions'. in *SPE Annual Technical Conference and Exhibition* held 24-27 September 2006 at San Antonio, Texas: Society of Petroleum Engineers.

Chen, Z.A. and Ruth, D.W. (1995) 'Measurement And Interpretation Of Centrifuge Capillary Pressure Curves-the SCA Survey Data'. *The Log Analyst* 36 (5), 21-33.

Chierici, G.L. (1984) 'Novel Relations for Drainage and Imbibition Relative Permeabilities'. *Society of Petroleum Engineers Journal* 24 (03), 275–276.

Chiquet, P., Daridon, J.-L., Broseta, D., and and Thibeau, S. (2007) 'CO_2/Water Interfacial Tensions under Pressure and Temperature Conditions of CO_2 Geological Storage'. *Energy Conversion and Management* 48 (3), 736–744.

Christoffersen, K.R. and Whitson, C.H. (1995) 'Gas/Oil Capillary Pressure of Chalk at Elevated Pressures'. *SPE Formation Evaluation* 10 (3), 153–159.

Chun, B.-S. and Wilkinson, G.T. (1995) 'Interfacial Tension in High-Pressure Carbon Dioxide Mixtures'. *Industrial & Engineering Chemistry Research* 34 (12), 4371–4377.

Clarkson, C.R., Qanbari, F., and Williams-Kovacs, J.D. (2016) 'Semi-Analytical Model for Matching Flowback and Early-Time Production of Multi-Fractured Horizontal Tight Oil Wells'. *Journal of Unconventional Oil and Gas Resources* 15, 134–145.

Class, H., Ebigbo, A., Helmig, R., Dahle, H.K., Nordbotten, J.M., Celia, M.A., Audigane, P., Darcis, M., Ennis-King, J., Fan, Y., Flemisch, B., Gasda, S.E., Jin, M., Krug, S., Labregere, D., Naderi Beni, A., Pawar, R.J., Sbai, A., Thomas, S.G., Trenty, L., and Wei, L. (2009) 'A Benchmark Study on Problems Related to CO_2 Storage in Geologic Formations'. *Computational Geosciences* 13 (4), 409–434.

Coats, K.H. (1987) 'Reservoir Simulation'. in *Petroleum Engineering Handbook* ed. by Howard B. Bradley. Richardson, Texas: Society of Petroleum Engineers, 1840.

Coats, K.H., Dempsey, J.R., and Henderson, J.H. (1971) 'The Use of Vertical Equilibrium in Two-Dimensional Simulation of Three-Dimensional Reservoir Performance'. *Society of Petroleum Engineers Journal* 11 (01), 63–71.

Corey, A.T. (1954) 'The Interrelation between Gas and Oil Relative Permeabilites'. *Producers Monthly* 19, 38–41.

Cowton, L.R., Neufeld, J.A., White, N.J., Bickle, M.J., White, J.C., and Chadwick, R.A. (2016) 'An Inverse Method for Estimating Thickness and Volume with Time of a Thin CO_2-Filled Layer at the Sleipner Field, North Sea'. *Journal of Geophysical Research: Solid Earth* 121 (7), 5068–5085.

Cowton, L.R., Neufeld, J.A., White, N.J., Bickle, M.J., Williams, G.A., White, J.C., and Chadwick, R.A. (2018) 'Benchmarking of Vertically-Integrated CO_2 Flow Simulations at the Sleipner Field, North Sea'. *Earth and Planetary Science Letters* 491, 121–133.

Dance, T. (2013) 'Assessment and Geological Characterisation of the CO2CRC Otway Project CO_2 Storage Demonstration Site: From Prefeasibility to Injection'. *Marine and Petroleum Geology* 46, 251–269.

Darling, T. (2005) *Well Logging and Formation Evaluation*. Houston, Texas: Elsevier, Gulf Professional Publishing.

Darman, N.H., Sorbie, K.S., and Pickup, G.E. (1999) 'The Development of Pseudo Functions for Gravity-Dominated Immiscible Gas Displacements'. in *SPE Reservoir Simulation*

Symposium held 14-17 February 1999 at Houston, Texas: Society of Petroleum Engineers.

Debbabi, Y., Jackson, M.D., Hampson, G.J., and Salinas, P. (2017) 'Capillary Heterogeneity Trapping and Crossflow in Layered Porous Media'. *Transport in Porous Media* 120 (1), 183–206.

Dewhurst, D.N., Aplin, A.C., Sarda, J.-P., and Yang, Y. (1998) 'Compaction-Driven Evolution of Porosity and Permeability in Natural Mudstones: An Experimental Study'. *Journal of Geophysical Research: Solid Earth* 103 (B1), 651–661.

Dewhurst, D.N., Yang, Y., and Aplin, A.C. (1999) 'Permeability and Fluid Flow in Natural Mudstones'. *Geological Society, London, Special Publications* 158 (1), 23–43.

DOE - Fossil Energy (2017) *DOE Announces Major Milestone Reached for Illinois Industrial CCS Project* [online] available from <https://www.energy.gov/fe/articles/doe-announces-major-milestone-reached-illinois-industrial-ccs-project> [10 August 2018]

Doster, F., Nordbotten, J.M., and Celia, M.A. (2013) 'Impact of Capillary Hysteresis and Trapping on Vertically Integrated Models for CO_2 Storage'. in *Computational Methods in Geologic CO_2 Sequestration* 62 (Part C), 465–474.

Doughty, C. (2010) 'Investigation of CO_2 Plume Behavior for a Large-Scale Pilot Test of Geologic Carbon Storage in a Saline Formation'. *Transport in Porous Media* 82 (1), 49–76.

Doughty, C., Freifeld, B.M., and Trautz, R.C. (2008) 'Site Characterization for CO_2 Geologic Storage and Vice Versa: The Frio Brine Pilot, Texas, USA as a Case Study'. *Environmental Geology* 54 (8), 1635–1656.

Doveton, J.H. (1991) 'Lithofacies and Geochernical-Facies Profiles from Modern Wireline Logs - New Subsurface Templates for Sedimentary Modeling'. in *Sedimentary Modelling: Computer Simulations and Methods for Improved Parameter Definition*. ed. by Franseen, E.K., Watney, W.L., St. Kendall, C.G., and Ross, W. Kansas: Kansas Geological Survey Bulletin 233, 101–110.

Dria, D.E., Pope, G.A., and Sepehrnoori, K. (1993) 'Three-Phase Gas/Oil/Brine Relative Permeabilities Measured Under CO_2 Flooding Conditions'. *SPE Reservoir Engineering* 8 (02), 143-150.

Duan, Z. and Sun, R. (2003) 'An Improved Model Calculating CO_2 Solubility in Pure Water and Aqueous NaCl Solutions from 273 to 533 K and from 0 to 2000 Bar'. *Chemical Geology* 193 (3–4), 257–271.

Ducellier, A., Seyedi, D., and Foerster, E. (2011) 'A Coupled Hydromechanical Fault Model for the Study of the Integrity and Safety of Geological Storage of CO_2'. *Energy Procedia* 4, 5138–5145.

Dullien, F.A.L. (1991) *Porous Media: Fluid Transport and Pore Structure.* 2nd edn. Academic Press.

Dupuy, B., Romdhane, A., Eliasson, P., Querendez, E., Yan, H., Torres, V.A., and Ghaderi, A. (2017) 'Quantitative Seismic Characterization of CO_2 at the Sleipner Storage Site, North Sea'. *Interpretation* 5 (4), SS23-SS42.

Durlofsky, L.J. (2005) 'Upscaling and Gridding of Fine Scale Geological Models for Flow Simulation'. in *8th International Forum on Reservoir Simulation*. held 20-24 June 2005 at Iles Borromees, Stresa, Italy.

Ebigbo, A., Class, H., and Helmig, R. (2007) 'CO_2 Leakage through an Abandoned Well:

Problem-Oriented Benchmarks'. *Computational Geosciences* 11 (2), 103–115.

Eichel, H., Helmig, R., Neuweiler, I., and Cirpka, O.A. (2005) 'Upscaling of Two-Phase Flow Processes in Porous Media'. in *Upscaling Multiphase Flow in Porous Media*. ed. by Das D. and Hassanizadeh S. Berlin/Heidelberg: Springer-Verlag, 237–257.

Eiken, O., Ringrose, P., Hermanrud, C., Nazarian, B., Torp, T.A., and Høier, L. (2011) 'Lessons Learned from 14 Years of CCS Operations: Sleipner, In Salah and Snøhvit'. *Energy Procedia* 4, 5541–5548.

Elewaut, E., Koelewijin, D., van der Straaten, R., Baily, H., Holloway, S., Barbier, J., Lindeberg, E., Moller, H., and Gaida, K. (1996) 'Inventory of the Theoretical CO_2 Storage Capacty of the European Union and Norway'. in *The Underground Disposal of Carbon Dioxide. Final Report of Joule II Project No. CT92-0031*. ed. by Holloway, S. Keyworth, Nottingham: British Geological Survey, 16–115.

Ennis-King, J.P. and Paterson, L. (2005) 'Role of Convective Mixing in the Long-Term Storage of Carbon Dioxide in Deep Saline Formations'. *SPE Journal* 10 (03), 349–356.

Espinet, A., Shoemaker, C., and Doughty, C. (2013) 'Estimation of Plume Distribution for Carbon Sequestration Using Parameter Estimation with Limited Monitoring Data'. *Water Resources Research* 49 (7), 4442–4464.

Espinoza, D.N. and Santamarina, J.C. (2017) 'CO_2 Breakthrough—Caprock Sealing Efficiency and Integrity for Carbon Geological Storage'. *International Journal of Greenhouse Gas Control* 66, 218–229.

Espinoza, D.N. and Santamarina, J.C. (2010) 'Water-CO_2-Mineral Systems: Interfacial Tension, Contact Angle, and Diffusion-Implications to CO_2 Geological Storage'. *Water Resources Research* 46 (7), 1–10.

Fabricius, I.L., Fazladic, L.D., Steinholm, A., and Korsbech, U. (2003) 'The Use of Spectral Natural Gamma-Ray Analysis in Reservoir Evaluation of Siliciclastic Sediments: A Case Study from the Middle Jurassic of the Harald Field, Danish Central Graben'. *Geological Survey of Denmark and Greenland Bulletin* 1, 349–366.

Farokhpoor, R., Bjørkvik, B.J.A., Lindeberg, E., and Torsæter, O. (2013) 'Wettability Behaviour of CO_2 at Storage Conditions'. *International Journal of Greenhouse Gas Control* 12, 18–25.

Fatt, I. and Dykstra, H. (1951) 'Relative Permeability Studies'. *Journal of Petroleum Technology* 3 (09), 249–256.

Fertl, W.H. and Chilingarian, G. V. (1990) 'Type and Distribution Modes of Clay Minerals from Well Logging Data'. *Journal of Petroleum Science and Engineering* 3 (4), 321–332.

Figueroa, J.D., Fout, T., Plasynski, S., McIlvried, H., and Srivastava, R.D. (2008) 'Advances in CO_2 Capture Technology—The U.S. Department of Energy's Carbon Sequestration Program'. *International Journal of Greenhouse Gas Control* 2 (1), 9–20.

Fleet, M., Gurton, R., and Taggart, I. (2004) 'The Function of Gas-Water Relative Permeability Hysteresis in the Sequestration of Carbon Dioxide in Saline Formations'. in *SPE Asia Pacific Oil and Gas Conference and Exhibition*. held 18-20 October 2004 at Perth, Australia: Society of Petroleum Engineers.

Flemming, B.W. (2000) 'A Revised Textural Classification of Gravel-Free Muddy Sediments on the Basis of Ternary Diagrams'. *Continental Shelf Research* 20 (10). 1125–1137.

Fredlund, D.G. and Xing, A. (1994) ‘Equations for the Soil-Water Characteristic Curve’. *Canadian Geotechnical Journal* 31 (4), 521–532.

Freund, P. and Ormerod, W.G. (1997) ‘Progress toward Storage of Carbon Dioxide’. *Energy Conversion and Management* 38, S199–S204.

Fuentes, C., Haverkamp, R., and Parlange, J.Y. (1992) ‘Parameter Constraints on Closed-Form Soilwater Relationships’. *Journal of Hydrology* 134 (1–4), 117–142.

Fulcher, R.A., Ertekin, T., and Stahl, C.D. (1985) ‘Effect of Capillary Number and Its Constituents on Two-Phase Relative Permeability Curves’. *Journal of Petroleum Technology* 37 (02), 249–260.

Gasda, S.E., Nordbotten, J.M., and Celia, M.A. (2009) ‘Vertical Equilibrium with Sub-Scale Analytical Methods for Geological CO_2 Sequestration’. *Computational Geosciences* 13 (4), 469–481.

Gates, J.I. and Lietz, W.T. (1950) ‘Relative Permeabilities of California Cores by the Capillary - Pressure Method’. in *Spring Meeting of the Pacific Coast District, Drilling and Production Practice* held 1 May 1950 at Los Angeles: American Petroleum Institute, 285–302.

Gaus, I., Azaroual, M., and Czernichowski-Lauriol, I. (2005) ‘Reactive Transport Modelling of the Impact of CO_2 Injection on the Clayey Cap Rock at Sleipner (North Sea)’. *Chemical Geology* 217 (3–4), 319–337.

GCCSI (2018) *Project Database: Large-Scale CCS Facilities* [online] available from <http://www.globalccsinstitute.com/projects/large-scale-ccs-projects> [10 August 2018]

van Genuchten, M.T. (1980) ‘A Closed Form Equation for Predicting the Hydraulic Conductivity of Unsaturated Soils’. *Soil Science Society of America Journal* 44 (5), 892–898.

van Genuchten, M.T. and Nielsen, D.R. (1985) ‘On Describing and Predicting the Hydraulic Properties of Unsaturated Soils’. *Annales Geophysicae* 3 (5), 615–628.

Gershenzon, N.I., Ritzi, R.W., Dominic, D.F., Mehnert, E., Okwen, R.T., and Patterson, C. (2017) ‘CO_2 Trapping in Reservoirs with Fluvial Architecture: Sensitivity to Heterogeneity in Permeability and Constitutive Relationship Parameters for Different Rock Types’. *Journal of Petroleum Science and Engineering* 155, 89–99.

Ghosh, R., Sen, M.K., and Vedanti, N. (2015) ‘Quantitative Interpretation of CO_2 Plume from Sleipner (North Sea), Using Post-Stack Inversion and Rock Physics Modeling’. *International Journal of Greenhouse Gas Control* 32, 147–158.

Giorgis, T., Carpita, M., and Battistelli, A. (2007) ‘2D Modeling of Salt Precipitation during the Injection of Dry CO_2 in a Depleted Gas Reservoir’. in *Geologic Carbon Sequestration and Methane Hydrates Research from the TOUGH Symposium 2006* 48 (6), 1816–1826.

Golding, M.J., Huppert, H.E., and Neufeld, J.A. (2013) ‘The Effects of Capillary Forces on the Axisymmetric Propagation of Two-Phase, Constant-Flux Gravity Currents in Porous Media’. *Physics of Fluids* 25 (36602), 1–18.

Golding, M.J., Neufeld, J.A., Hesse, M.A., and Huppert, H.E. (2011) ‘Two-Phase Gravity Currents in Porous Media’. *Journal of Fluid Mechanics* 678, 248–270.

Gor, G.Y., Elliot, T.R., and Prévost, J.H. (2013) ‘Effects of Thermal Stresses on Caprock Integrity during CO_2 Storage’. *International Journal of Greenhouse Gas Control* 12. 300–309.

Gozalpour, F., Ren, S.R., and Tohidi, B. (2005) ‘CO_2 EOR and Storage in Oil Reservoir’. *Oil &*

Gas Science and Technology - Rev.IFP 60 (3), 537–546.

van de Graaff, W.J.E. and Ealey, J.P. (1989) ‘Geological Modelling for Simulation Studies’. *AAPG Bulletin* 73 (11), 1436–1444.

Haldorsen, H.. and Damsleth, E. (1993) ‘Challenges in Reservoir Characterization’. *AAPG Bulletin* 77 (4), 541–551.

Haldorsen, H.H. (1986) ‘Simulator Parameter Assignment and the Problem of Scale in Reservoir Engineering’. in *Reservoir Characterization* ed. by Lake, L.W. and Carroll, H.B. Orlando, Florida: Academic Press, 293–340.

Handin, J., Hager, R., Freidman, M., and Feather, J. (1963) ‘Experimental Deformation of Sedimentary Rocks Under Confining Pressure: Pore Pressure Tests’. *AAPG Bulletin* 47 (5), 717–755.

Hansen, G., Hamouda, A.., and Denoyel, R. (2000) ‘The Effect of Pressure on Contact Angles and Wettability in the Mica/Water/n-Decane System and the Calcite+Stearic Acid/Water/n-Decane System’. *Colloids and Surfaces A: Physicochemical and Engineering Aspects* 172 (1–3), 7–16.

Hansen, O., Gilding, D., Nazarian, B., Osdal, B., Ringrose, P., Kristoffersen, J.B., Eiken, O., and Hansen, H. (2013) ‘Snøhvit: The History of Injecting and Storing 1 Mt CO_2 in the Fluvial Tubåen Fm’. *Energy Procedia* 37, 3565–3573.

Harrington, J.F. and Horseman, S.T. (1999) ‘Gas Transport Properties of Clays and Mudrocks’. *Geological Society, London, Special Publications* 158 (1), 107.

Harrington, J.F., Noy, D.J., Horseman, S.T., Birchall, D.J., and Chadwick, R.A. (2009) ‘Laboratory Study of Gas and Water Flow in the Nordland Shale, Sleipner, North Sea’. in *Carbon Dioxide Sequestration in Geological Media – State of the Science. AAPG Studies in Geology 59*. ed. by Grobe, M., Pashin, J.C., and Dodge, R.L. Tulsa, OK: AAPG Special Volumes, 521–543.

Harvey, A., Parry, W.T., Bellows, J., Gallagher, J., and Harwood, R. (2014) *ASME International Steam Tables for Industrial Use.* 3rd edn*.* New York: ASME Press.

Hassanizadeh, S.M. and Gray, W.G. (1993) ‘Toward an Improved Description of the Physics of Two-Phase Flow’. *Advances in Water Resources* 16 (1), 53–67.

Hassanzadeh, H., Pooladi-Darvish, M., Elsharkawy, A.M., Keith, D.W., and Leonenko, Y. (2008) ‘Predicting PVT Data for CO_2–brine Mixtures for Black-Oil Simulation of CO_2 Geological Storage’. *International Journal of Greenhouse Gas Control* 2 (1), 65–77.

Hassler, G.L. and Brunner, E. (1945) 'Measurement of Capillary Pressures in Small Core Samples'. *Transactions of the AIME* 160 (01), 114–123.

Haukaas, J., Nickel, M., and Sonneland, L. (2013) ‘Successful 4D History Matching of the Sleipner CO_2 Plume’. in *75th EAGE Conference & Exhibition Incorporating SPE EUROPEC 2013* held 10-13 June 2013 at London, UK: European Association of Geoscientists and Engineers.

Hebach, A., Oberhof, A., Dahmen, N., Kögel, A., Ederer, H., and and Dinjus, E. (2002) ‘Interfacial Tension at Elevated Pressures-Measurements and Correlations in the Water + Carbon Dioxide System’. *Journal of Chemical & Engineering Data* 47 (6), 1540–1546.

Held, R.J. and Celia, M.A. (2001) ‘Modeling Support of Functional Relationships between Capillary Pressure, Saturation, Interfacial Area and Common Lines’. *Advances in Water*

Resources 24 (3–4), 325–343.

Helmig, R., Niessner, J., Flemisch, B., Wolff, M., and Fritz, J. (2010) 'Efficient Modeling of Flow and Transport in Porous Media Using Multiphysics and Multiscale Approaches'. in *Handbook of Geomathematics*. Berlin, Heidelberg: Springer Berlin Heidelberg, 417–457.

Hermanrud, C., Andresen, T., Eiken, O., Hansen, H., Janbu, A., Lippard, J., Bolås, H.N., Simmenes, T.H., Teige, G.M.G., and Østmo, S. (2009) 'Storage of CO_2 in Saline Aquifers–Lessons Learned from 10 Years of Injection into the Utsira Formation in the Sleipner Area'. *Energy Procedia* 1 (01), 1997–2004.

Hermanrud, C., Zweigel, P., Eiken, O., Lippard, J., and Andresen, T. (2007) 'CO_2 Flow in the Utsira Formation: Inferences Made from 4D Seismic Analysis in the Sleipner Area'. in *AAPG and AAPG European Region Energy Conferenceand Exhibition* held 18-21 November 2007 at Athens, Greece: American Association of Petroleum Geologists.

Hewett, T.A. and Archer, R.A. (1997) 'Scale-Averaged Effective Flow Properties for Coarse-Grid Reservoir Simulation'. in *SPE Reservoir Simulation Symposium* held 8-11 June 1997 at Dallas, Texas: Society of Petroleum Engineers.

Hildenbrand, A., Schlömer, S., Krooss, B.M., and Littke, R. (2004) 'Gas Breakthrough Experiments on Pelitic Rocks: Comparative Study with N_2, CO_2 and CH_4'. *Geofluids* 4 (1), 61–80.

Hingerl, F.F., Yang, F., Pini, R., Xiao, X., Toney, M.F., Liu, Y., and Benson, S.M. (2016) 'Characterization of Heterogeneity in the Heletz Sandstone from Core to Pore Scale and Quantification of Its Impact on Multi-Phase Flow'. *International Journal of Greenhouse Gas Control* 48, 69–83.

Hiscott, R.N. (1978) 'Grading, Graded Bedding'. in *Sedimentology. Encyclopedia of Earth Science*. Dordrecht: Springer Netherlands, 535–538.

Hitchon, B., Gunter, W.D., Gentzis, T., and Bailey, R.T. (1999) 'Sedimentary Basins and Greenhouse Gases: A Serendipitous Association'. *Energy Conversion and Management* 40 (8). 825–843.

Hobbs, P.R.N., Hallam, J.R., Forster, A., Entwisle, D.C., Jones, L.D., Cripps, A.C., Northmore, K.J., Slef, S.J., and Meakin, J.L. (2002) *Engineering Geology of British Rocks and Soils - Mudstones of the Mercia Mudstone Group*. British Geological Survey Research Report, RR/01/02. Keyworth, Nottingham: NERC.

Hobson, G.D. (1954) *Some Fundamentals of Petroleum Geology*. London: Oxford University Press.

Hodneland, E., Gasda, S., Kaufmann, R., Bekkvik, T.C., Hermanrud, C., and Midttømme, K. (2019) 'Effect of Temperature and Concentration of Impurities in the Fluid Stream on CO_2 Migration in the Utsira Formation'. *International Journal of Greenhouse Gas Control* 83, 20–28.

Holloway, S., Vincent, C.J., Bentham, M.S., and Kirk, K.L. (2006) 'Top-down and Bottom-up Estimates of CO_2 Storage Capacity in the United Kingdom Sector of the Southern North Sea Basin'. *Environmental Geosciences* 13 (2), 71–84.

Holt, T., Jensen, J.-I., and Lindeberg, E. (1995) 'Underground Storage of CO_2 in Aquifers and Oil Reservoirs'. *Energy Conversion and Management* 36 (6–9), 535–538.

Holtz, M.H. (2002) 'Residual Gas Saturation to Aquifer Influx: A Calculation Method for 3-D Computer Reservoir Model Construction'. in *SPE Gas Technology Symposium*

30 April–2 May 2002 at Calgary, Alberta, Canada: Society of Petroleum Engineers.

Honarpour, M., Koederitz, L., and Harvey, H. (1986) *Relative Permeability of Petroleum Reservoirs*. 1st edn. Boca Raton, Florida: CRC Press, Inc.

Honarpour, M. and Mahmood, S.M. (1988) 'Relative-Permeability Measurements: An Overview'. *Journal of Petroleum Technology* 40 (08), 963–966.

Honarpour, M.M., Schatzinger, R.A., Szpakiewicz, M.J., Jackson, S.R., Sharma, B., Tomutsa, L., and Chang, M.M. (1990) *Integrated Methodology for Constructing a Quantified Hydrodynamic Model for Application to Clastic Petroleum Reservoirs*. NIPER-439 Report. Bartlesville, OK: National Institute for Petroleum and Energy Research.

Horseman, S.T., Harrington, J.F., and Sellin, P. (1999) 'Gas Migration in Clay Barriers'. *Engineering Geology* 54 (1), 139–149.

Horseman, S.T., Higgo, J.J.W., Alexander, J., and Harrington, J.F. (1996) *Water, Gas and Solute Movement through Argillaceous Media*. Nuclear Energy Agency Report, CC-96/1. Paris, France: Organisation for Economic Co-Operation and Development.

Hovorka, S.D., Meckel, T.A., Trevino, R.H., Lu, J., Nicot, J.-P., Choi, J.-W., Freeman, D., Cook, P., Daley, T.M., Ajo-Franklin, J.B., Freifeild, B.M., Doughty, C., Carrigan, C.R., Brecque, D. La, Kharaka, Y.K., Thordsen, J.J., Phelps, T.J., Yang, C., Romanak, K.D., Zhang, T., Holt, R.M., Lindler, J.S., and Butsch, R.J. (2011) 'Monitoring a Large Volume CO_2 Injection: Year Two Results from SECARB Project at Denbury's Cranfield, Mississippi, USA'. *Energy Procedia* 4, 3478–3485.

Howard, A.S., Warrington, G., Ambrose, K., and Rees, J.G. (2008) *A Formational Framework for the Mercia Mudstone Group (Triassic) of England and Wales*. British Geological Survey Research Report, RR/08/04, Keyworth, Nottingham: NERC.

Hubbert, M.K. (1956) 'Darcy's Law and the Field Equations of the Flow of Underground Fluids'. *Transactions of the AIME* 207, 222–239.

Hubbert, M.K. (1953) 'Entrapment of Petroleum under Hydrodynamic Conditions'. *AAPG Bulletin* 37 (8), 1954–2026.

Iglauer, S., Mathew, M.S., and Bresme, F. (2012) 'Molecular Dynamics Computations of Brine–CO_2 Interfacial Tensions and Brine–CO_2–Quartz Contact Angles and Their Effects on Structural and Residual Trapping Mechanisms in Carbon Geo-Sequestration'. *Journal of Colloid and Interface Science* 386 (1), 405–414.

Iglauer, S., Pentland, C.H., and Busch, A. (2015) 'CO_2 Wettability of Seal and Reservoir Rocks and the Implications for Carbon Geo-Sequestration'. *Water Resources Research* 51 (1), 729–774.

Ingram, R.L. (1953) 'Fissility of Mudrocks'. *Geological Society of America Bulletin* 64 (8), 869–878.

IPCC (2014) *Climate Change 2014: Mitigation of Climate Change. Contribution of Working Group III to the Fifth Assessment Report of the Intergovernmental Panel on Climate Change*. ed. by Edenhofer, O., Pichs-Madruga, R., Minx, J., Sokona, Y., Farahani, E., Kadner, S., Seyboth, K., Adler, A., Baum, I., Brunner, S., Eickemeier, P., Kriemann, B., Savolainen, J., Schlömer, S., von Stechow, C., and Zwickel, T. Cambridge, United Kingdom: Cambridge University Press.

IPCC (2005) *IPCC Special Report on Carbon Dioxide Capture and Storage. Prepared by Working Group III of the Intergovernmental Panel on Climate Change*. ed. by Metz O.

Davidson, H. C. de Coninck, M. Loos, and L. A. Meyer, B. Cambridge, United Kingdom: Cambridge University Press

Ippisch, O., Vogel, H.-J., and Bastian, P. (2006) 'Validity Limits for the van Genuchten–Mualem Model and Implications for Parameter Estimation and Numerical Simulation'. *Advances in Water Resources* 29 (12), 1780–1789.

Irons, J.A., Weismiller, R.A., and Petersen, G.W. (1989) 'Soil Reflectance'. in *Theory and Applications of Remote Sensing*. ed. by Asrar, G. Washington D.C.: John Wiley & Sons, 66–106.

James, A., Baines, S., and McCollough, S. (2016) *D10: WP5A – Bunter Storage Development Plan*. ETI Report, 10113ETIS-Rep-13-03. Loughborough: Energy Technologies Institute.

Jansen, D., Gazzani, M., Manzolini, G., Dijk, E. van, and Carbo, M. (2015) 'Pre-Combustion CO_2 Capture'. *International Journal of Greenhouse Gas Control* 40, 167–187.

Juanes, R., Spiteri, E.J., Orr, F.M., and Blunt, M.J. (2006) 'Impact of Relative Permeability Hysteresis on Geological CO_2 Storage'. *Water Resources Research* 42 (12), 1–13.

Jung, J.-W. and Wan, J. (2012) 'Supercritical CO_2 and Ionic Strength Effects on Wettability of Silica Surfaces: Equilibrium Contact Angle Measurements'. *Energy & Fuels* 26 (9), 6053–6059.

Kang, S.M., Fathi, E., Ambrose, R.J., Akkutlu, I.Y., and Sigal, R.F. (2011) 'Carbon Dioxide Storage Capacity of Organic-Rich Shales'. *SPE Journal* 16 (04), 842–855.

Katahara, K.W. (1995) 'Gamma Ray Log Response in Shaly Sands'. *The Log Analyst* 36 (04), 50–71

Kelkar, M., Perez, G., and Chopra, A. (2002) *Applied Geostatistics for Reservoir Characterization*. Richardson, TX: Society of Petroleum Engineers.

Killough, J.E. (1976) 'Reservoir Simulation With History-Dependent Saturation Functions'. *Society of Petroleum Engineers Journal* 16 (01), 37–48.

Kim, K.-Y., Han, W.S., Oh, J., Kim, T., and Kim, J.-C. (2012) 'Characteristics of Salt-Precipitation and the Associated Pressure Build-Up during CO_2 Storage in Saline Aquifers'. *Transport in Porous Media* 92 (2), 397–418.

Koide, H., Tazaki, Y., Noguchi, Y., Nakayama, S., Iijima, M., Ito, K., and Shindo, Y. (1992) 'Subterranean Containment and Long-Term Storage of Carbon Dioxide in Unused Aquifers and in Depleted Natural Gas Reservoirs'. *Energy Conversion and Management* 33 (5), 619–626.

Kolditz, O., Bauer, S., Beyer, C., Böttcher, N., Dietrich, P., Görke, U.-J., Kalbacher, T., Park, C.-H., Sauer, U., Schütze, C., Shao, H., Singh, A., Taron, J., Wang, W., and Watanabe, N. (2012) 'A Systematic Benchmarking Approach for Geologic CO_2 Injection and Storage'. *Environmental Earth Sciences* 67 (2), 613–632.

Koperna, G.J., Pashin, J., and Walsh, P. (2017) *SECARB Commercial Scale CO_2 Injection and Optimization of Storage Capacity in the Southeastern United States*. Final Scientific/Technical Report, SP102717. Pittsburgh, US: USDOE

Kopp, A., Class, H., and Helmig, R. (2009) 'Investigations on CO_2 Storage Capacity in Saline Aquifers'. *International Journal of Greenhouse Gas Control* 3 (3), 263–276.

Koschel, D., Coxam, J.-Y., Rodier, L., and Majer, V. (2006) 'Enthalpy and Solubility Data of CO_2 in Water and NaCl(Aq) at Conditions of Interest for Geological Sequestration'. *Fluid Phase*

Equilibria 247 (1–2), 107–120.

Kovscek, A.R. and Cakici, M.D. (2005) ‘Geologic Storage of Carbon Dioxide and Enhanced Oil Recovery. II. Cooptimization of Storage and Recovery’. *Energy Conversion and Management* 46 (11), 1941–1956.

Krause, M., Krevor, S., and Benson, S.M. (2013) ‘A Procedure for the Accurate Determination of Sub-Core Scale Permeability Distributions with Error Quantification’. *Transport in Porous Media* 98 (3), 565–588.

Krevor, S., Blunt, M.J., Benson, S.M., Pentland, C.H., Reynolds, C., Al-Menhali, A., and Niu, B. (2015) ‘Capillary Trapping for Geologic Carbon Dioxide Storage – From Pore Scale Physics to Field Scale Implications’. *International Journal of Greenhouse Gas Control* 40, 221–237.

Krevor, S.C.M., Pini, R., Zuo, L., and Benson, S.M. (2012) ‘Relative Permeability and Trapping of CO_2 and Water in Sandstone Rocks at Reservoir Conditions’. *Water Resources Research* 48 (2), W02532.

Krooss, B.M., Leythaeuser, D., and Schaefer, R.G. (1992) ‘The Quantification of Diffusive Hydrocarbon Losses through Cap Rocks of Natural Gas Reservoirs – a Re-Evaluation’. *The American Association of Petroleum Geologists Bulletin* 76 (3), 403–406.

Kuila, U. and Prasad, M. (2013) ‘Specific Surface Area and Pore-Size Distribution in Clays and Shales’. *Geophysical Prospecting* 61 (2), 341–362.

Kuo, C.-W. and Benson, S.M. (2015) ‘Numerical and Analytical Study of Effects of Small Scale Heterogeneity on CO_2/Brine Multiphase Flow System in Horizontal Corefloods’. *Advances in Water Resources* 79, 1–17.

Lambe, T.W. (1960) ‘A Mechanistic Picture of Shear Strength in Clay’. in *Research Conference on Shear Strength of Cohesive Soils* held June 1960 at University of Colorado, Boulder, Colorado, United States: American Society of Civil Engineers.

Land, C.S. (1968) ‘Calculation of Imbibition Relative Permeability for Two- and Three-Phase Flow From Rock Properties’. *Society of Petroleum Engineers Journal* 8 (02), 149–156.

Larsen, J.A. and Skauge, A. (1998) ‘Methodology for Numerical Simulation With Cycle-Dependent Relative Permeabilities’. *SPE Journal* 3 (02), 163–173.

Leij, F.J., Russell, W.B., and Lesch, S.M. (1997) ‘Closed-Form Expressions for Water Retention and Conductivity Data’. *Ground Water* 35 (5), 848–858.

Lenhard, R.J. and Oostrom, M. (1998) ‘A Parametric Model for Predicting Relative Permeability-Saturation-Capillary Pressure Relationships of Oil–Water Systems in Porous Media with Mixed Wettability’. *Transport in Porous Media* 31 (1), 109–131.

Lenhard, R.J. and Parker, J.C. (1987) ‘A Model for Hysteretic Constitutive Relations Governing Multiphase Flow: 2. Permeability-Saturation Relations’. *Water Resources Research* 23 (12), 2197–2206.

Lenhard, R.J., Parker, J.C., and Mishra, S. (1989) ‘On the Correspondence between Brooks-Corey and van Genuchten Models’. *Journal of Irrigation and Drainage Engineering* 115 (4), 744–751.

Leong, E.C. and Rahardjo, H. (1997) ‘Review of Soil-Water Characteristic Curve Equations’. *Journal of Geotechnical and Geoenvironmental Engineering* 123 (12), 1106–1117.

Leverett, M.C. (1941) 'Capillary Behavior in Porous Solids'. *Transactions of the AIME* 142 (01), 152–169.

Li, B., Tchelepi, A.H., and Benson, M.S. (2013) 'The Influence of Capillary Entry Pressure Representation on CO_2 Solubility Trapping'. *Energy Procedia* 37, 3808–3815.

Li, K. and Horne, R.N. (2002) 'Experimental Verification of Methods to Calculate Relative Permeability Using Capillary Pressure Data'. in *SPE Western Regional/AAPG Pacific Section Joint Meeting* held 20-22 May 2002 at Anchorage, Alaska: Society of Petroleum Engineers.

Li, S., Dong, M., Li, Z., Huang, S., Qing, H., and Nickel, E. (2005) 'Gas Breakthrough Pressure for Hydrocarbon Reservoir Seal Rocks: Implications for the Security of Long-Term CO_2 Storage in the Weyburn Field'. *Geofluids* 5 (4), 326–334.

Li, X., Boek, E.S., Maitland, G.C., and Trusler, J.P.M. (2012) 'Interfacial Tension of (Brines + CO_2): $CaCl_2$(Aq), $MgCl_2$(Aq), and Na_2SO_4(Aq) at Temperatures between (343 and 423) K, Pressures between (2 and 50) MPa, and Molalities of (0.5 to 5) Mol·kg^{-1}'. *Journal of Chemical & Engineering Data* 57 (5), 1369–1375.

Li, Z., Galindo-Torres, S., Yan, G., Scheuermann, A., and Li, L. (2018) 'A Lattice Boltzmann Investigation of Steady-State Fluid Distribution, Capillary Pressure and Relative Permeability of a Porous Medium: Effects of Fluid and Geometrical Properties'. *Advances in Water Resources* 116, 153–166.

Lichtner, P.C., Hammond, G.E., Lu, C., Karra, S., Bisht, G., Andre, B., Mills, R., and Kumar, J. (2015) *PFLOTRAN User Manual: A Massively Parallel Reactive Flow and Transport Model for Describing Surface and Subsurface Processes.* Technical Report. Los Alamos, US: USDOE.

Lin, C.-C. and Chen, Y.-W. (2011) 'Performance of a Cross-Flow Rotating Packed Bed in Removing Carbon Dioxide from Gaseous Streams by Chemical Absorption'. *International Journal of Greenhouse Gas Control* 5 (4), 668–675.

Liu, F., Lu, P., Zhu, C., and Xiao, Y. (2011) 'Coupled Reactive Flow and Transport Modeling of CO_2 Sequestration in the Mt. Simon Sandstone Formation, Midwest U.S.A.' *International Journal of Greenhouse Gas Control* 5 (2). 294–307.

Lucia, F.J. (2007) 'Petrophysical Rock Properties'. in *Carbonate Reservoir Characterization.* 2nd edn. Berlin, Heidelberg: Springer Berlin Heidelberg, 1–27.

MacMinn, C.W., Szulczewski, M.L., and Juanes, R. (2011) 'CO_2 Migration in Saline Aquifers. Part 2. Capillary and Solubility Trapping'. *Journal of Fluid Mechanics* 688, 321–351.

Macquaker, J.H.S. and Adams, A.E. (2003) 'Maximizing Information from Fine-Grained Sedimentary Rocks: An Inclusive Nomenclature for Mudstones'. *Journal of Sedimentary Research* 73 (5), 735–744.

Mahadevan, J. (2012) 'Comments on the Paper Titled "Contact Angle Measurements of CO_2–water-Quartz/Calcite Systems in the Perspective of Carbon Sequestration": A Case of Contamination?' *International Journal of Greenhouse Gas Control* 7, 261–262.

Marschall, P., Horseman, S., and Gimmi, T. (2005) 'Characterisation of Gas Transport Properties of the Opalinus Clay, a Potential Host Rock Formation for Radioactive Waste Disposal'. *Oil & Gas Science and Technology - Rev.IFP* 60 (1), 121–139.

Mathias, S.A., Gluyas, J.G., González Martínez de Miguel, G.J., Bryant, S.L., and Wilson, D. (2013) 'On Relative Permeability Data Uncertainty and CO_2 Injectivity Estimation for Brine Aquifers'. *International Journal of Greenhouse Gas Control* 12, 200–212.

McCaffery, F.G. (1972) 'Measurement of Interfacial Tensions And Contact Angles At High Temperature And Pressure'. *Journal of Canadian Petroleum Technology* 11 (03), 26–32.

Meckel, T.A., Bryant, S.L., and Ravi Ganesh, P. (2015) 'Characterization and Prediction of CO_2 Saturation Resulting from Modeling Buoyant Fluid Migration in 2D Heterogeneous Geologic Fabrics'. *International Journal of Greenhouse Gas Control* 34. 85–96.

van der Meer, L.G.H. (1992) 'Investigations Regarding the Storage of Carbon Dioxide in Aquifers in the Netherlands'. *Energy Conversion and Management* 33 (5–8), 611–618.

Middleton, R.S., Keating, G.N., Stauffer, P.H., Jordan, A.B., Viswanathan, H.S., Kang, Q.J., Carey, J.W., Mulkey, M.L., Sullivan, E.J., Chu, S.P., Esposito, R., and Meckel, T.A. (2012) 'The Cross-Scale Science of CO_2 Capture and Storage: From Pore Scale to Regional Scale'. *Energy & Environmental Science* 5 (6), 7328–7345.

Mishra, S., Oruganti, Y.D., Gupta, N., Ganesh, P.R., McNeil, C., Bhattacharya, I., and Spitznogle, G. (2014) 'Modeling CO_2 Plume Migration Based on Calibration of Injection and Post-Injection Pressure Response at the AEP Mountaineer Project'. *Greenhouse Gases: Science and Technology* 4 (3), 331–356.

Morel-Seytoux, H.J., Meyer, P.D., Nachabe, M., Tourna, J., van Genuchten, M.T., and Lenhard, R.J. (1996) 'Parameter Equivalence for the Brooks-Corey and Van Genuchten Soil Characteristics: Preserving the Effective Capillary Drive'. *Water Resources Research* 32 (5), 1251–1258.

Mori, H., Trevisan, L., and Illangasekare, T.H. (2015) 'Evaluation of Relative Permeability Functions as Inputs to Multiphase Flow Models Simulating Supercritical CO_2 Behavior in Deep Geologic Formations'. *International Journal of Greenhouse Gas Control* 41, 328–335.

Mualem, Y. (1976) 'A New Model for Predicting the Hydraulic Conductivity of Unsaturated Porous Media'. *Water Resources Research* 12 (3), 513–522.

Nazeer, A., Abbasi, S.A., and Solangi, S.H. (2016) 'Sedimentary Facies Interpretation of Gamma Ray (GR) Log as Basic Well Logs in Central and Lower Indus Basin of Pakistan'. *Geodesy and Geodynamics* 7 (6). 432–443.

Newell, A.J. (2017) 'Evolving Stratigraphy of a Middle Triassic Fluvial-Dominated Sheet Sandstone: The Otter Sandstone Formation of the Wessex Basin (UK)'. *Geological Journal* 53 (05), 1954-1972.

Newell, A.J. and Shariatipour, S.M. (2016) 'Linking Outcrop Analogue with Flow Simulation to Reduce Uncertainty in Sub-Surface Carbon Capture and Storage: An Example from the Sherwood Sandstone Group of the Wessex Basin, UK'. in *The Value of Outcrop Studies in Reducing Subsurface Uncertainty and Risk in Hydrocarbon Exploration and Production*. ed. by Bowman, M. and Jordan, C.J. Geological Society of London, 231–246.

Nguyen, B.N., Hou, Z., Bacon, D.H., Murray, C.J., and White, M.D. (2016) 'Three-Dimensional Modeling of the Reactive Transport of CO_2 and Its Impact on Geomechanical Properties of Reservoir Rocks and Seals'. *International Journal of Greenhouse Gas Control* 46, 100–115.

Niemi, A., Bear, J., and Bensabat, J. (2017) *Geological Storage of CO_2 in Deep Saline Formations*. Dordrecht, Netherlands: Springer.

Nilsen, H.M., Herrera, P.A., Ashraf, M., Ligaarden, I., Iding, M., Hermanrud, C., Lie, K.-A., Nordbotten, J.M., Dahle, H.K., and Keilegavlen, E. (2011) 'Field-Case Simulation of CO_2 -Plume Migration Using Vertical-Equilibrium Models'. *Energy Procedia* 4, 3801–3808.

Nilsen, H.M., Krogstad, S., Andersen, O., Allen, R., and Lie, K.-A. (2017) 'Using Sensitivities and Vertical-Equilibrium Models for Parameter Estimation of CO_2 Injection Models with Application to Sleipner Data'. *Energy Procedia* 114, 3476–3495.

Nordbotten, J M, Celia, M.A., and Bachu, S. (2005) 'Injection and Storage of CO_2 in Deep Saline Aquifers: Analytical Solution for CO_2 Plume Evolution During Injection'. *Transport in Porous Media* 58 (3), 339–360.

Nordbotten, J.M., Celia, M.A., and Bachu, S. (2004) 'Analytical Solutions for Leakage Rates through Abandoned Wells'. *Water Resources Research* 40 (W04204).

Nordbotten, Jan M., Celia, M.A., Bachu, S., and Dahle, H.K. (2005) 'Semianalytical Solution for CO_2 Leakage through an Abandoned Well'. *Environmental Science & Technology* 39 (2), 602–611.

Nowak, M. and Verly, G. (2005) 'The Practice of Sequential Gaussian Simulation'. in *Geostatistics Banff 2004. Quantitative Geology and Geostatistics, Vol 14* ed. by Leuangthong, O. and Deutsch, C. V. Dordrecht, Netherlands: Springer, 387–398.

Noy, D.J., Holloway, S., Chadwick, R.A., Williams, J.D.O., Hannis, S.A., and Lahann, R.W. (2012) 'Modelling Large-Scale Carbon Dioxide Injection into the Bunter Sandstone in the UK Southern North Sea'. *International Journal of Greenhouse Gas Control* 9, 220–233.

O'Meara, D.J., Hirasaki, G.J., and Rohan, J.A. (1992) 'Centrifuge Measurements of Capillary Pressure: Part 1-Outflow Boundary Condition'. *SPE Reservoir Engineering* 7 (01), 133–142.

Obi, E.-O.I. and Blunt, M.J. (2006) 'Streamline-Based Simulation of Carbon Dioxide Storage in a North Sea Aquifer'. *Water Resources Research* 42 (3), 1–13.

Odsæter, L.H., Berg, C.F., and Rustad, A.B. (2015) 'Rate Dependency in Steady-State Upscaling'. *Transport in Porous Media* 110 (3), 565–589.

Okasha, T.M. and Alshiwaish, A. (2009) 'Effect of Brine Salinity on Interfacial Tension in Arab-D Carbonate Reservoir, Saudi Arabia'. in *SPE Middle East Oil and Gas Show and Conference* held 15-18 March 2009 at Manama, Bahrain: Society of Petroleum Engineers.

Okwen, R., Stewart, M., and Cunningham, J. (2011) 'Effect of Well Orientation (Vertical vs. Horizontal) and Well Length on the Injection of CO_2 in Deep Saline Aquifers'. *Transport in Porous Media* 90 (1), 219–232.

Oostrom, M., White, M.D., Porse, S.L., Krevor, S.C.M., and Mathias, S.A. (2016) 'Comparison of Relative Permeability–Saturation–Capillary Pressure Models for Simulation of Reservoir CO_2 Injection'. *International Journal of Greenhouse Gas Control* 45, 70–85.

Orlic, B., Heege, J. ter, and Wassing, B. (2011) 'Assessing the Integrity of Fault- and Top Seals at CO_2 Storage Sites'. *Energy Procedia* 4, 4798–4805.

Orsini, P., Cantucci, B., and Quattrocchi, F. (2014) 'Large-Scale Numerical Modelling of CO_2 Injection and Containment Phases for an Italian Near-Coast Reservoir Using PFLOTRAN'. *Energy Procedia* 51, 334–343.

Padurean, A., Cormos, C.-C., Cormos, A.-M., and Agachi, P.-S. (2011) 'Multicriterial Analysis of Post-Combustion Carbon Dioxide Capture Using Alkanolamines'. *International Journal of Greenhouse Gas Control* 5 (4), 676–685.

Peng, D.-Y. and Robinson, D.B. (1976) 'A New Two-Constant Equation of State'. *Industrial & Engineering Chemistry Fundamentals* 15 (1), 59–64.

Perrin, J.-C. and Benson, S. (2010) ‘An Experimental Study on the Influence of Sub-Core Scale Heterogeneities on CO_2 Distribution in Reservoir Rocks’. *Transport in Porous Media* 82 (1), 93–109.

Perrot, P. (1998) *A to Z of Thermodynamics*. New York: Oxford University Press.

Peters, E., Egberts, P.J.P., Loeve, D., and Hofstee, C. (2015) ‘CO_2 Dissolution and Its Impact on Reservoir Pressure Behavior’. *International Journal of Greenhouse Gas Control* 43, 115–123.

Pettijohn, F.J. (1957) *Sedimentary Rocks*. 2nd edn. New York: Harper.

Pettijohn, F.J., Potter, P.E., and Siever, R. (1972) *Sand and Sandstone*. New York: Springer-Verlag.

Picard, M.D. (1971) ‘Classification of Fine-Grained Sedimentary Rocks’. *Journal of Sedimentary Research* 41 (1), 179–195.

Poe, B.D. (2014) ‘Production Performance Evaluation of Wells Completed in Unconventional Reservoirs Using Capillary Pressure Data and Relative Permeability Effects’. in *SPE Annual Technical Conference and Exhibition* held 27-29 October 2014 at Amsterdam, Netherlands: Society of Petroleum Engineers.

Pommer, M. and Milliken, K. (2015) ‘Pore Types and Pore-Size Distributions across Thermal Maturity, Eagle Ford Formation, Southern Texas’. *AAPG Bulletin* 99 (09), 1713–1744.

Potter, P.E., Maynard, J.B., and Depetris, P.J. (2005) *Mud and Mudstones: Introduction and Overview*. Berlin, Heidelberg: Springer-Verlag Berlin Heidelberg.

Potter, P.E., Maynard, J.B., and Pryor, W.A. (1980) *Sedimentology of Shale: Study Guide and Reference Source*. New York: Springer-Verlag.

Preston, C., Monea, M., Jazrawi, W., Brown, K., Whittaker, S., White, D., Law, D., Chalaturnyk, R., and Rostron, B. (2005) ‘IEA GHG Weyburn CO_2 Monitoring and Storage Project’. *Fuel Processing Technology* 86 (14–15), 1547–1568.

Pruess, K. (2005) *ECO2N: A TOUGH2 Fluid Property Module for Mixtures of Water, NaCl, and CO_2*. Technical Report, LBNL-57952. Berkeley, CA: Lawrence Berkeley National Laboratory.

Pruess, K. and Müller, N. (2009) ‘Formation Dry-out from CO_2 Injection into Saline Aquifers: 1. Effects of Solids Precipitation and Their Mitigation’. *Water Resources Research* 45 (W03402).

Pruess, K. and Nordbotten, J. (2011) ‘Numerical Simulation Studies of the Long-Term Evolution of a CO_2 Plume in a Saline Aquifer with a Sloping Caprock’. *Transport in Porous Media* 90 (1), 135–151.

Purcell, W.R. (1949) 'Capillary Pressures - Their Measurement Using Mercury and the Calculation of Permeability Therefrom'. *Journal of Petroleum Technology* 1 (02), 39–48.

Rapoport, L.A. and Leas, W.J. (1951) ‘Relative Permeability to Liquid in Liquid-Gas Systems’. *Journal of Petroleum Technology* 3 (03), 83–98.

Rasmusson, K., Tsang, C.-F., Tsang, Y., Rasmusson, M., Pan, L., Fagerlund, F., Bensabat, J., and Niemi, A. (2015) ‘Distribution of Injected CO_2 in a Stratified Saline Reservoir Accounting for Coupled Wellbore-Reservoir Flow’. *Greenhouse Gases: Science and Technology* 5 (4), 419–436.

Redlich, O. and Kwong, J.N.S. (1949) 'On the Thermodynamics of Solutions. V. An Equation of State. Fugacities of Gaseous Solutions.' *Chemical Reviews* 44 (1), 233–244.

Reeves, P.C. and Celia, M.A. (1996) 'A Functional Relationship Between Capillary Pressure, Saturation, and Interfacial Area as Revealed by a Pore-Scale Network Model'. *Water Resources Research* 32 (8), 2345–2358.

Reitsma, S. and Kueper, B.H. (1994) 'Laboratory Measurement of Capillary Pressure-Saturation Relationships in a Rock Fracture'. *Water Resources Research* 30 (4), 865–878.

Rhys, G.H. (1974) *A Proposed Standard Lithostratigraphic Nomenclature for the Southern North Sea and an Outline Structural Nomenclature for the Whole of the (UK) North Sea*. Rep. Inst. Geol. Sci., 74/8. London: HM Stationery Office.

Richardson, J.G., Kerver, J.K., Hafford, J.A., and Osoba, J.S. (1952) 'Laboratory Determination of Relative Permeability'. *Journal of Petroleum Technology* 4 (08), 187–196.

Rock, L., O'brien, S., Tessarolo, S., Duer, J., Bacci, V.O., Hirst, B., Randell, D., Helmy, Mo., Blackmore, J., Duong, C., Halladay, A., Smitth, N., Dixit, T., Kassam, S., and Yaychuk, M. (2017) 'The Quest CCS Project: 1st Year Review Post Start of Injection'. *Energy Procedia* 114, 5320–5328.

Romdhane, A., Querendez, E., and Ravaut, C. (2014) 'CO_2 Thin-Layer Detection at the Sleipner Field with Full Waveform Inversion: Application to Synthetic and Real Data'. *Energy Procedia* 51, 281–288.

Rose, W. and Bruce, W.A. (1949) 'Evaluation Of Capillary Character In Petroleum Reservoir Rock'. *Journal of Petroleum Technology* 1 (05), 127–142.

Rozhko, A.Y., Podladchikov, Y.Y., and Renard, F. (2007) 'Failure Patterns Caused by Localized Rise in Pore-Fluid Overpressure and Effective Strength of Rocks'. *Geophysical Research Letters* 34 (L22304).

Rubin, E.S., Yeh, S., Antes, M., Berkenpas, M., and Davison, J. (2007) 'Use of Experience Curves to Estimate the Future Cost of Power Plants with CO_2 Capture'. *International Journal of Greenhouse Gas Control* 1 (2), 188–197.

Rutqvist, J., Birkholzer, J.T., and Tsang, C.-F. (2008) 'Coupled Reservoir–geomechanical Analysis of the Potential for Tensile and Shear Failure Associated with CO_2 Injection in Multilayered Reservoir–caprock Systems'. *International Journal of Rock Mechanics and Mining Sciences* 45 (2), 132–143.

Rutqvist, J. and Tsang, C.-F. (2002) 'A Study of Caprock Hydromechanical Changes Associated with CO_2-Injection into a Brine Formation'. *Environmental Geology* 42 (2), 296–305.

Rutqvist, J., Vasco, D.W., and Myer, L. (2010) 'Coupled Reservoir-Geomechanical Analysis of CO_2 Injection and Ground Deformations at In Salah, Algeria'. *International Journal of Greenhouse Gas Journal* 4 (2). 225–230.

Saadatpoor, E., Bryant, S.L., and Sepehrnoori, K. (2010) 'New Trapping Mechanism in Carbon Sequestration'. *Transport in Porous Media* 82 (1), 3–17.

Sakurai, K., Watanabe, N., Ishibashi, T., Tsuchiya, N., Ohsaki, Y., Tamagawa, T., and Yagi, M. (2013) 'Oil-Water Relative Permeability Curves for Fractures in Granite and Limestone at Different Intrinsic Permeabilities'. in *19th Formation Evaluation Symposium of Japan* held 26-27 September 2013 at Chiba, Japan: Society of Petrophysicists and Well-Log Analysts.

Saraji, S., Piri, M., and Goual, L. (2014) 'The Effects of SO_2 Contamination, Brine Salinity, Pressure, and Temperature on Dynamic Contact Angles and Interfacial Tension of Supercritical CO_2/Brine/Quartz Systems'. *International Journal of Greenhouse Gas Control* 28, 147–155.

Sarmadivaleh, M., Al-Yaseri, A.Z., and Iglauer, S. (2015) 'Influence of Temperature and Pressure on Quartz–Water–CO_2 Contact Angle and CO_2–Water Interfacial Tension'. *Journal of Colloid and Interface Science* 441, 59–64.

Scheffknecht, G., Al-Makhadmeh, L., Schnell, U., and Maier, J. (2011) 'Oxy-Fuel Coal Combustion—A Review of the Current State-of-the-Art'. *International Journal of Greenhouse Gas Control* 5, S16–S35.

Schlömer, S. and Krooss, B.M. (1997) 'Experimental Characterisation of the Hydrocarbon Sealing Efficiency of Cap Rocks'. *Marine and Petroleum Geology* 14 (5), 565–580.

Schlumberger (2017) *ECLIPSE Technical Description*.

Schlumberger (2016) *Petrel E&P Software Platform*.

Seedhouse, J.K. and Racey, A. (1997) 'Sealing Capacity of the Mercia Mudstone Group in the East Irish Sea Basin: Implications for Petroleum Exploration'. *Journal of Petroleum Geology* 20 (3), 261–286.

Selley, R.C. and Sonnenberg, S.A. (2014) *Elements of Petroleum Geology*. 3rd edn. Academic Press.

Senior, C.L., Morris, W., and Lewandowski, T.A. (2013) 'Emissions and Risks Associated with Oxyfuel Combustion: State of the Science and Critical Data Gaps'. *Journal of the Air & Waste Management Association* 63 (7), 832–843.

Seyyedi, M., Sohrabi, M., and Farzaneh, A. (2015) 'Investigation of Rock Wettability Alteration by Carbonated Water through Contact Angle Measurements'. *Energy and Fuels* 29 (9), 5544–5553.

Shariatipour, Seyed M, Mackay, E.J., and Pickup, G.E. (2016) 'An Engineering Solution for CO_2 Injection in Saline Aquifers'. *International Journal of Greenhouse Gas Control* 53. 98–105.

Shariatipour, Seyed M., Pickup, G.E., and Mackay, E.J. (2016a) 'Simulations of CO_2 Storage in Aquifer Models with Top Surface Morphology and Transition Zones'. *International Journal of Greenhouse Gas Control* 54 (Part 1), 117–128.

Shariatipour, Seyed M., Pickup, G.E., and Mackay, E.J. (2016b) 'Investigation of CO_2 Storage in a Saline Formation with an Angular Unconformity at the Caprock Interface'. *Petroleum Geoscience* 22 (2), 203–210.

Shariatipour, S.M., Pickup, G.E., and Mackay, E.J. (2014) 'The Effect of Aquifer/Caprock Interface on Geological Storage of CO_2'. in *Energy Procedia* 63, 5544–5555.

Shariatipour, S., Pickup, G.E., Mackay, E.J., and Heinemann, N. (2012) 'Flow Simulation of CO_2 Storage in Saline Aquifers Using Black Oil Simulator'. in *Carbon Management Technology Conference* held 7-9 February 2012 at Orlando, Florido, USA: Carbon Management Technology Conference.

Shell (2011) *UK Carbon Capture and Storage Demonstration Competition. UKCCS-KT-S7.19-Shell-002, SCAL Report*. ScottishPower CCS Consortium.

Shepard, F.P. (1954) 'Nomenclature Based on Sand-Silt-Clay Ratios'. *Journal of Sedimentary Research* 24 (3), 151–158.

Singh, V.P., Cavanagh, A., Hansen, H., Nazarian, B., Iding, M., and Ringrose, P.S. (2010) ‘Reservoir Modeling of CO_2 Plume Behavior Calibrated Against Monitoring Data From Sleipner, Norway’. in *SPE Annual Technical Conference and Exhibition* held 19-22 September 2010 at Florence, Italy: Society of Petroleum Engineers.

Skurtveit, E., Aker, E., Soldal, M., Angeli, M., and Wang, Z. (2012) ‘Experimental Investigation of CO_2 Breakthrough and Flow Mechanisms in Shale’. *Petroleum Geoscience* 18 (1), 3–15.

Smith, S.A., Beddoe, C.J., Mibeck, B.A.F., Heebink, L. V, Kurz, B.A., Peck, W.D., and Jin, L. (2017) ‘Relative Permeability of Williston Basin CO_2 Storage Targets’. *Energy Procedia* 114, 2957–2971.

Soave, G. (1972) ‘Equilibrium Constants from a Modified Redlich-Kwong Equation of State’. *Chemical Engineering Science* 27 (6), 1197–1203.

Spain, D.R. and Conrad, C.P. (1997) ‘Quantitative Analysis of Top-Seal Capacity: Offshore Netherlands, Southern North Sea’. *Geologie En Mijnbouw* 76 (3), 217–226.

Span, R. and Wagner, W. (1996) ‘A New Equation of State for Carbon Dioxide Covering the Fluid Region from the Triple-Point Temperature to 1100 K at Pressures up to 800 MPa’. *Journal of Physical and Chemical Reference Data* 25 (6), 1509–1596.

Spiteri, E.J., Juanes, R., Blunt, M.J., and Orr, F.M. (2008) ‘A New Model of Trapping and Relative Permeability Hysteresis for All Wettability Characteristics’. *SPE Journal* 13 (03), 277–288.

Spycher, N., Pruess, K., and Ennis-King, J. (2003) ‘CO_2-H_2O Mixtures in the Geological Sequestration of CO_2. I. Assessment and Calculation of Mutual Solubilities from 12 to 100°C and up to 600 Bar’. *Geochimica et Cosmochimica Acta* 67 (16), 3015–3031.

Standing, M.B. (1975) *Notes on Relative Permeability Relationships* [online] available from <http://www.pe.tamu.edu/blasingame/data/z_zCourse_Archive/P620_11B/P620_Reference/P620_Supplementary_Materials_(09C)/PDF_Txt_Standing_Kr_Notes_(1973).pdf> [18 May 2018]

Stow, D.A. V (1981) ‘Fine-Grained Sediments: Terminology’. *Quarterly Journal of Engineering Geology and Hydrogeology* 14 (4), 243–244.

Szymkiewicz, A. (2013) *Modelling Water Flow in Unsaturated Porous Media: Accounting for Nonlinear Permeability and Material Heterogeneity*. Berlin Heidelberg: Springer-Verlag.

Temam, R. (1979) *Navier-Stokes Equations: Theory and Numerical Analysis*. 2nd edn. ed. by J.L. Lions, G. Papanicolaou, and R.T. Rockafellar. North Holland: Elsevier Science.

Thomas, L.P. and Holliday, D.W. (1982) *Southampton No.1 (Western Esplanade) Geothermal Well: Geological Well Completion Report*. London: Institute of Geological Sciences.

Thomeer, J.H.M. (1960) ‘Introduction of a Pore Geometrical Factor Defined by the Capillary Pressure Curve’. *Journal of Petroleum Technology* 12 (03), 73–77.

Tiab, D. and Donaldson, E.C. (2015) *Petrophysics: Theory and Practice of Measuring Reservoir Rock and Fluid Transport Properties*. 4th edn. Oxford, UK: Gulf Professional Publishing.

Treiber, L.E. and Owens, W.W. (1972) ‘A Laboratory Evaluation of the Wettability of Fifty Oil-Producing Reservoirs’. *Society of Petroleum Engineers Journal* 12 (06), 531–540.

Tsuji, T., Ikeda, T., and Jiang, F. (2019) ‘Evolution of Hydraulic and Elastic Properties of Reservoir Rocks Due to Mineral Precipitation in CO_2 Geological Storage’. *Computers and*

Geosciences 126, 84–95.

UKCCSRC (2012) *CO_2 Storage* [online] available from <https://www.geos.ed.ac.uk/ukccsrc/what-is-ccs/storage.html> [18 January 2019]

USDA (1987) *Soil Mechanics Level I, Module 3: USDA Textural Soil Classification*. Soil Conservation Service: United States Department of Agriculture.

Valko, P. and Economides, M.J. (1997) *Hydraulic Fracture Mechanics*. New York: John Wiley.

Valle, L.M., Rodríguez, R., Grima, C., and Martínez, C. (2018) 'Effects of Supercritical CO2 Injection on Sandstone Wettability and Capillary Trapping'. *International Journal of Greenhouse Gas Control* 78, 341–348.

Versteeg, P. and Rubin, E.S. (2011) 'A Technical and Economic Assessment of Ammonia-Based Post-Combustion CO_2 Capture at Coal-Fired Power Plants'. *International Journal of Greenhouse Gas Control* 5 (6), 1596–1605.

Vialle, S., Druhan, J.L., and Maher, K. (2016) 'Multi-Phase Flow Simulation of CO_2 Leakage through a Fractured Caprock in Response to Mitigation Strategies'. *International Journal of Greenhouse Gas Control* 44, 11–25.

Vilarrasa, V. (2014) 'Impact of CO_2 Injection through Horizontal and Vertical Wells on the Caprock Mechanical Stability'. *International Journal of Rock Mechanics and Mining Sciences* 66, 151–159.

Vogel, T. and Cislerova, M. (1988) 'On the Reliability of Unsaturated Hydraulic Conductivity Calculated from the Moisture Retention Curve'. *Transport in Porous Media* 3 (1), 1–15.

Vogel, T., Van Genuchten, M.T., and Cislerova, M. (2000) 'Effect of the Shape of the Soil Hydraulic Functions near Saturation on Variably-Saturated Flow Predictions'. *Advances in Water Resources* 24 (2), 133–144.

van der Waals, J.D. (1910) *The Equation of State for Gases and Liquid* [online lecture] Nobel Lectures, Physics 1901-1921. available from <https://www.nobelprize.org/prizes/physics/1910/waals/lecture/> [31 August 2018]

Wall, T., Liu, Y., Spero, C., Elliott, L., Khare, S., Rathnam, R., Zeenathal, F., Moghtaderi, B., Buhre, B., Sheng, C., Gupta, R., Yamada, T., Makino, K., and Yu, J. (2009) 'An Overview on Oxyfuel Coal Combustion—State of the Art Research and Technology Development'. *Chemical Engineering Research and Design* 87 (8), 1003–1016.

Wang, S., Edwards, I.M., and Clarens, A.F. (2013) 'Wettability Phenomena at the CO_2–Brine–Mineral Interface: Implications for Geologic Carbon Sequestration'. *Environmental Science & Technology* 47 (1), 234–241.

Wang, Y., Zhang, L., Soong, Y., Dilmore, R., Liu, H., Lei, H., and Li, X. (2019) 'From Core-Scale Experiment to Reservoir-Scale Modeling: A Scale-up Approach to Investigate Reaction-Induced Permeability Evolution of CO_2 Storage Reservoir and Caprock at a U.S. CO_2 Storage Site'. *Computers and Geosciences* 125, 55–68.

Wen, G. and Benson, S.M. (2019) 'CO_2 Plume Migration and Dissolution in Layered Reservoirs'. *International Journal of Greenhouse Gas Control* 87, 66–79.

Wentworth, C.K. (1922) 'A Scale of Grade and Class Terms for Clastic Sediments'. *The Journal of Geology* 30 (5), 377–392.

White, J.C., Williams, G., Chadwick, A., Furre, A.-K., and Kiær, A. (2018) 'Sleipner: The Ongoing Challenge to Determine the Thickness of a Thin CO_2 Layer'. *International Journal* *of Greenhouse Gas Control* 69, 81–95.

White, M.D., Bacon, D.H., McGrail, B.P., Watson, D.J., White, S.K., and Zhang, Z.F. (2012) *STOMP Subsurface Transport Over Multiple Phases: STOMP-CO2 and STOMP-CO2e Guide: Version 1.0*. Richland, WA (United States): USDOE.

Wickstrom, L.H., Venteris, E.R., Slucher, E.R., Carter, K.M., Mcdonald, J., Rupp, J.A., Greb, S.F., Baum, G.R., Harrison, W.B., and Hohn, M.E. (2006) 'Geologic Storage Options and Capacities for Carbon Dioxide Sequestration in the Midwest Regional Carbon Sequestration Partnership (MRCSP)'. in *Fifth Annual Conference on Carbon Capture and Sequestration-DOE/NETL* held 8-11 May 2006 at Alexandria, Virginia: National Energy Technology Laboratory.

Williams, G.A. and Chadwick, R.A. (2017) 'An Improved History-Match for Layer Spreading within the Sleipner Plume Including Thermal Propagation Effects'. *Energy Procedia* 114, 2856–2870.

Williams, G.A., Chadwick, R.A., and Vosper, H. (2018) 'Some Thoughts on Darcy-Type Flow Simulation for Modelling Underground CO_2 Storage, Based on the Sleipner CO_2 Storage Operation'. *International Journal of Greenhouse Gas Control* 68, 164–175.

Williams, J.D.O., Gent, C.M.A., Fellgett, M.W., and Gamboa, D. (2018) 'Impact of in Situ Stress and Fault Reactivation on Seal Integrity in the East Irish Sea Basin, UK'. *Marine and Petroleum Geology* 92, 685–696.

Williams, J.D.O., Jin, M., Bentham, M., Pickup, G.E., Hannis, S.D., and Mackay, E.J. (2013) 'Modelling Carbon Dioxide Storage within Closed Structures in the UK Bunter Sandstone Formation'. *International Journal of Greenhouse Gas Control* 18, 38–50.

Wollenweber, J., Alles, S., Busch, A., Krooss, B.M., Stanjek, H., and Littke, R. (2010) 'Experimental Investigation of the CO_2 Sealing Efficiency of Caprocks'. *International Journal of Greenhouse Gas Control* 4 (2), 231–241.

Wood, B.D., Radakovich, K., and Golfier, F. (2007) 'Effective Reaction at a Fluid–solid Interface: Applications to Biotransformation in Porous Media'. *Advances in Water Resources* 30 (6–7), 1630–1647.

Wösten, J.H.M. and van Genuchten, M.T. (1988) 'Using Texture and Other Soil Properties to Predict the Unsaturated Soil Hydraulic Functions'. *Soil Science Society of America Journal* 52 (6), 1762.

Xu, T., Kharaka, Y.K., Doughty, C., Freifeld, B.M., and Daley, T.M. (2010) 'Reactive Transport Modeling to Study Changes in Water Chemistry Induced by CO_2 Injection at the Frio-I Brine Pilot'. *Chemical Geology* 271 (3–4), 153–164.

Yamamoto, H. and Doughty, C. (2011) 'Investigation of Gridding Effects for Numerical Simulations of CO_2 Geologic Sequestration'. *International Journal of Greenhouse Gas Control* 5 (4). 975–985.

Yang, Y. and Aplin, A.C. (2010) 'A Permeability–porosity Relationship for Mudstones'. *Marine and Petroleum Geology* 27 (8), 1692–1697.

Yang, Y. and Aplin, A.C. (2007) 'Permeability and Petrophysical Properties of 30 Natural Mudstones'. *Journal of Geophysical Research: Solid Earth* 112 (B3206), 1–14.

Yoshida, N., Levine, J.S., and Stauffer, P.H. (2016) 'Investigation of Uncertainty in CO_2 Reservoir Models: A Sensitivity Analysis of Relative Permeability Parameter Values'. in *International Journal of Greenhouse Gas Control* 49. 161–178.

Young, T. (1805) 'III. An Essay on the Cohesion of Fluids'. *Philosophical Transactions of the Royal Society of London* 95, 65–87.

Zhang, D. and Song, J. (2014) 'Mechanisms for Geological Carbon Sequestration'. *Procedia IUTAM* 10, 319–327.

Zhang, G., Lu, P., Ji, X., and Zhu, C. (2017) 'CO_2 Plume Migration and Fate at Sleipner, Norway: Calibration of Numerical Models, Uncertainty Analysis, and Reactive Transport Modelling of CO_2 Trapping to 10,000 Years'. *Energy Procedia* 114, 2880–2895.

Zhang, M., Zhang, Y., and Lichtner, P. (2017) 'Evaluating Model Complexity in Simulating Supercritical CO_2 Dissolution, Leakage, Footprint, and Reservoir Pressure for Three-Dimensional Hierarchical Aquifer'. *International Journal of Greenhouse Gas Control* 64, 284–299.

Zhang, N., He, M., Zhang, B., Qiao, F., Sheng, H., and Hu, Q. (2016) 'Pore Structure Characteristics and Permeability of Deep Sedimentary Rocks Determined by Mercury Intrusion Porosimetry'. *Journal of Earth Science* 27 (4), 670–676.

Zhao, J., Kang, Q., Yao, J., Viswanathan, H., Pawar, R., Zhang, L., and Sun, H. (2018) 'The Effect of Wettability Heterogeneity on Relative Permeability of Two-Phase Flow in Porous Media: A Lattice Boltzmann Study'. *Water Resources Research* 54 (2), 1295–1311.

Zhou, Q., Birkholzer, J.T., Mehnert, E., Lin, Y.-F., and Zhang, K. (2010) 'Modeling Basin- and Plume-Scale Processes of CO_2 Storage for Full-Scale Deployment'. *Ground Water* 48 (4), 494–514.

Zhou, Q., Birkholzer, J.T., Tsang, C.-F., and Rutqvist, J. (2008) 'A Method for Quick Assessment of CO2 Storage Capacity in Closed and Semi-Closed Saline Formations'. *International Journal of Greenhouse Gas Control* 2 (4). 626–639.

Zhu, C., Zhang, G., Lu, P., Meng, L., and Ji, X. (2015) 'Benchmark Modeling of the Sleipner CO_2 Plume: Calibration to Seismic Data for the Uppermost Layer and Model Sensitivity Analysis'. *International Journal of Greenhouse Gas Control* 43, 233–246.

Zulqarnain, M., Zeidouni, M., and Hughes, R.G. (2018) 'Implications of Fault Structure Heterogeneities, Dissolution and Capillary Trapping Mechanisms for CO_2 Storage Integrity'. *International Journal of Greenhouse Gas Control* 76, 53–61.

Zweigel, P., Arts, R., Lothe, A.E., and Lindeberg, E.B.G. (2004) 'Reservoir Geology of the Utsira Formation at the First Industrial-Scale Underground CO_2 Storage Site (Sleipner Area, North Sea)'. *Geological Society, London, Special Publications* 233 (1), 165–180.

Appendix A

```
i=1;
SOF2d =zeros(15,2,200);
SGFNd =zeros(15,3,200);
SOF2i =zeros(13,2,200);
SGFNi =zeros(13,3,200);
for n=1.01:0.01:3;

%DRAINAGE
 jd=1;

 for sw=0.3:0.05:1;
 m=1-1/n;
 lan=m/(1-m)*(1-0.5^(1/m));
 sew=(sw-0.3)/(1-0.3);
 pc(jd)=0.01622/sew^(1/lan);
 krw(jd)=sew^0.5*(1-(1-
sew^(1/m))^m)^2;
 krg(jd)=0.623*(1-sew)^2*(1-sew^2);
 sw(jd)=sw;

 SOF2d (jd,1,i)=sw(jd);
 SOF2d (jd,2,i)=krw(jd);
 SGFNd (16-jd,1,i)=1-sw(jd);
 SGFNd (16-jd,2,i)=krg(jd);
 SGFNd (16-jd,3,i)=pc(jd);

 jd=jd+1;

end

%IMBIBITION
 ji=1;

 for sw=0.3:0.024:0.588;
 m=1-1/n;
 lan=m/(1-m)*(1-0.5^(1/m));
 sew=(sw-0.3)/(0.588-0.3);
 pc(ji)=0.01622/sew^(1/lan);
 krw(ji)=sew^0.5*(1-(1-
sew^(1/m))^m)^2;
 krg(ji)=0.623*(1-sew)^2*(1-sew^2);
 sw(ji)=sw;

 SOF2i (ji,1,i)=sw(ji);
 SOF2i (ji,2,i)=krw(ji);
 SGFNi (14-ji,1,i)=1-sw(ji);
 SGFNi (14-ji,2,i)=krg(ji);
 SGFNi (14-ji,3,i)=pc(ji);

 ji=ji+1;

end
```

```
%% …CONTINUATION
%% print_file
cd file_location;
fid=fopen('kr.inc','w');

fprintf(fid,'SGFN \n');

SGFNd_T=transpose(SGFNd(:,:,i));
fprintf(fid,'%f %f %f\r\n',SGFNd_T);
fprintf(fid,'\n/');
fprintf(fid,'\n');

SGFNi_T=transpose(SGFNi(:,:,i));
fprintf(fid,'%f %f %f\r\n',SGFNi_T);
fprintf(fid,'\n/');
fprintf(fid,'\n');
fprintf(fid,'SOF2 \n');

SOFTd_T=transpose(SOF2d(:,:,i));
fprintf(fid,'%f %f\r\n',SOFTd_T);
fprintf(fid,'\n/');
fprintf(fid,'\n');
SOFTi_T=transpose(SOF2i(:,:,i));
fprintf(fid,'%f %f\r\n',SOFTi_T);
fprintf(fid,'\n/');
fclose(fid);

%% RUN
nn=num2str(n);
foldername=['n_' nn '.data'];
mkdir(foldername)
copyfile('BASE.data',foldername)
copyfile('MULTPV.inc',foldername)
copyfile('PROPS_FLUID.INC',foldername)
copyfile('summary.inc',foldername)
copyfile('TRANX.inc',foldername)
copyfile('TRANZ.inc',foldername)
copyfile('kr.inc',foldername)
copyfile('$eclipse.bat',foldername)
cd(['./' foldername])
movefile('BASE.data',foldername)
input_file=foldername;
[~, fName, ext] =
fileparts(input_file);
aaa=['$eclipse.bat ' fName];
system(aaa);

i=i+1;

end
```

Algorithm A1: MATLAB-code used to compute $P_c - k_r - S_w$ data and initialise reservoir simulation in E100

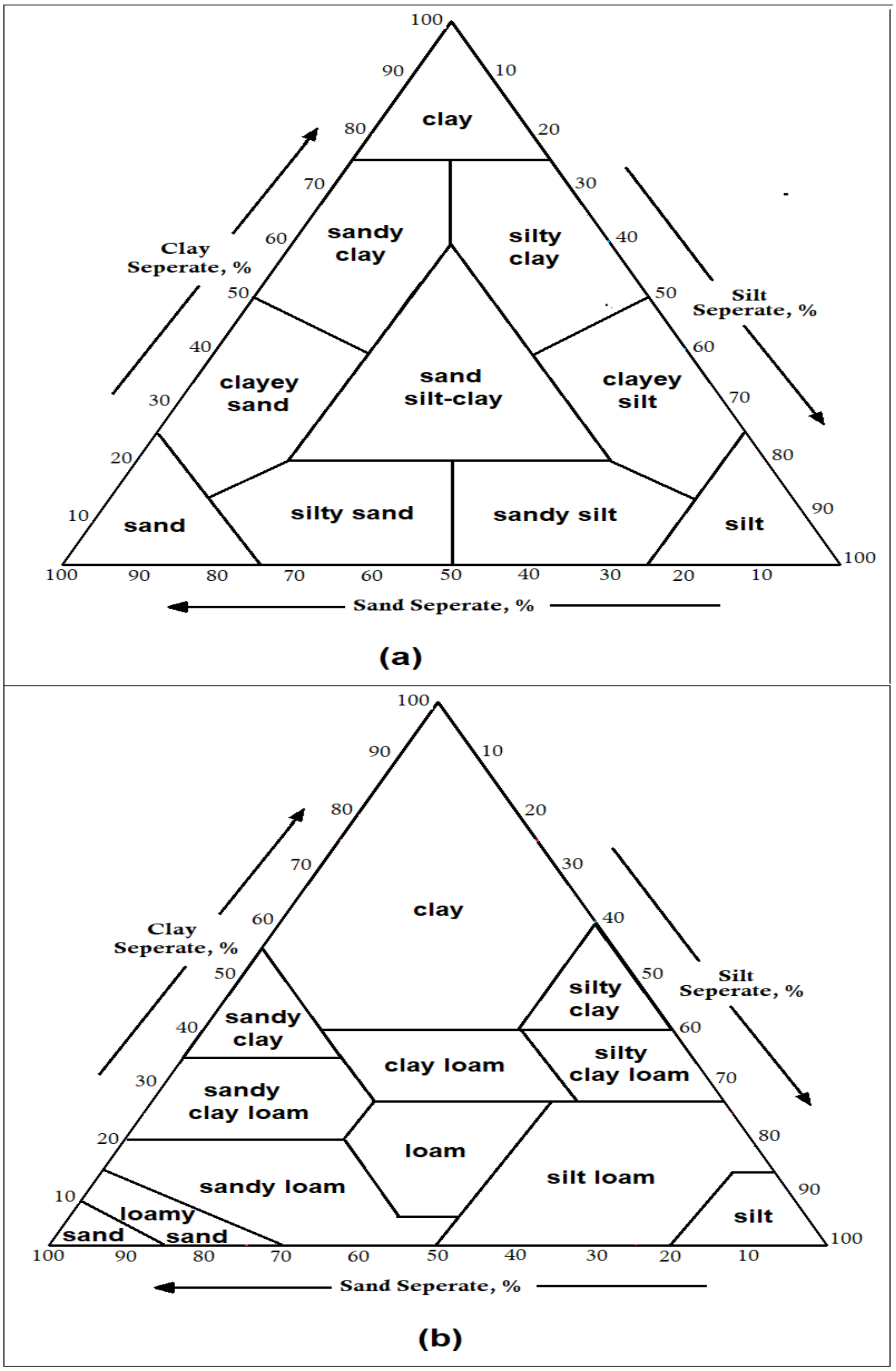

Figure A1: Ternary diagram of (a) the recommended conceptual scheme for the nomenclature of mixed clastic sediments, and (b) USDA's soil textural classification.